Kent Academic Repository

Irons, Hannah (2016) ***Experimental Implications of the Entanglement Transition in Clustered Quantum Materials.*** **Doctor of Philosophy (PhD) thesis, University of Kent,.**

University of Kent

Doctoral Thesis

Experimental Implications of the Entanglement Transition in Clustered Quantum Materials

---

Author:
Hannah Irons

Supervisor:
Dr. Jorge Quintanilla

A thesis submitted in fulfilment of the requirements
for the degree of Doctor of Philosophy

in the

Functional Materials Group
School of Physical Sciences

July 2016

Declaration of Authorship

I, Hannah IRONS, declare that this thesis titled, 'Experimental Implications of the Entanglement Transition in Clustered Quantum Materials' and the work presented in it are my own. I confirm that:

- This work was done wholly or mainly while in candidature for a research degree at this University.
- Where any part of this thesis has previously been submitted for a degree or any other qualification at this University or any other institution, this has been clearly stated.
- Where I have consulted the published work of others, this is always clearly attributed.
- Where I have quoted from the work of others, the source is always given. With the exception of such quotations, this thesis is entirely my own work.
- I have acknowledged all main sources of help.
- Where the thesis is based on work done by myself jointly with others, I have made clear exactly what was done by others and what I have contributed myself.

Signed: ____

Date: ____

“I want to stand as close to the edge as I can without going over. Out on the edge you see all kinds of things you can’t see from the center.”

Kurt Vonnegut

UNIVERSITY OF KENT

Abstract

Faculty Name
School of Physical Sciences

Doctor of Philosophy

Experimental Implications of the Entanglement Transition in Clustered Quantum Materials

by Hannah Irons

Clustered quantum materials provide a new platform for the experimental study of many-body entanglement. Here we address a simple model featuring N interacting spins in a transverse field. The field can induce an entanglement transition (ET). We calculate the magnetisation, low-energy gap and neutron-scattering cross-section and find that the ET has distinct signatures, detectable at temperatures as high as 10% of the interaction strength. Unlike a quantum critical point, the signatures of the ET are stronger for *smaller* clusters.

Acknowledgements

No one thinks that doing a PhD is going to be easy but nothing could really prepare me for how lost I felt. Not just at the beginning of it, but maybe for the entire thing. I've come to accept this as a normal reaction to studying quantum entanglement. Upon reaching the end of my PhD, I can be grateful for the things that I have learned, the research that has led down some interesting paths and the people around me. In these acknowledgements there are many people I wish to take the time to thank for their contributions to my work, my life and accomplishments.

First and foremost, I would like to thank my supervisor Dr. Jorge Quintanilla. Jorge's enthusiasm for everything he does is infectious and is probably the best quality you can have in a supervisor. His guidance in this project has been paramount to it's success and he has helped me to develop as a well-balanced researcher. Along with my supervisor, I am grateful to the collaboration and their years of leg work into the entanglement transition before I joined to explore finite-sized systems. These people include, my secondary supervisor: Toby Perring and guidance from Luigi Amico and Gabriel Aeppli and the funding bodies SEPnet and the ISIS neutron facility.

Throughout my PhD I was encouraged to attend schools and conferences and to network around with other people doing interesting work. I met some great people and would like to thank, in particular, James Vale and Greg Oliver (and that curve ball he threw at me last September after my seminar in Birmingham, that lead me to look at my molecular magnets in a whole new way). With additional gratitude towards Chris Hooley who taught me how to use the reduced density matrix.

At Kent Uni there are many people to acknowledge; to the academic staff: Sam Carr, Paul Strange and Silvia Ramos who have helped me with calculations, find helpful sources or preparing for presentations. The administration staff have always been approachable and quick to help, with special acknowledgments to Helen West and Ann Austin. Of course, I must also thank the student support at Kent, having made many friends during my time here; thanking Bruno Tomasello, Marc Williams, Jimmel Stewart, Phil Whittlesea, Erin Donovan, Radu Stancu and Manuel Marques.

I would like to acknowledge my parents and sisters, who may not understand a thing about what I do but have been emotionally supportive. My mum warned me about doing a PhD, she was concerned that I might 'use up' all my brain power and have none left for the rest of my life. With reflection, she was right and everyone should listen to their mother before doing a PhD.

Lastly, my most heartfelt gratitude goes to Chris Costa, my fiancee. Without his ongoing support I do not honest believe I would have made it to the end. Having recently finished his own PhD, the support Chris offered was sincere, and having someone believe in you because they've done it too is all the more genuine. So, thank you Doctor Costa from the future Doctor Costa and the exciting year we've got ahead of us.

PS. The real final acknowledgments are to my cats: Jack and Arthur and their numerous journeys across my keyboard.

Contents

List of Figures

List of Tables

Abbreviations

CMT	**C**ondensed **M**atter **T**heory
QM	**Q**uantum **M**echanics
QI	**Q**uantum **I**nformation
QPT	**Q**uantum **P**hase **T**ransition
QCP	**Q**uantum **C**ritical **P**oint
ET	**E**ntanglement **T**ransition
EPR	**E**instein **P**odolsky **R**osen
OBC	**O**pen **B**oundary **C**onditions
PBC	**P**eriodic **B**oundary **C**onditions
LRO	**L**ong **R**ange **O**rder
INS	**I**nelastic **N**eutron **S**cattering

Chapter 1

Introduction

This thesis is part of a collaborative effort between experimentalists and theorists into understanding and detecting a phenomenon known as the entanglement transition. The authors role in the collaboration was to use analytical and numerical methods to describe the behaviour of small finite-sized systems in relation to their entanglement and the entanglement transition. The main goal was to predict neutron scattering results for these models and to comment on a feasible temperature scale for experimentation. This chapter outlines the motivations behind this project and gives a chapter summary.

1.1 Motivation

The motivation behind any research project is a simple desire to learn more about an interesting topic. This is subjective to an extent, but for many scientists in many different fields a system undergoing some great behavioral change is a platform for interesting an exciting physics [13] [14] [15]. This project and the collaborative efforts in connection with it are founded on the goal of experimentally realising the entanglement transition. The entanglement transition, described in Chapter 2, is a new kind of quantum transition that is yet to be found experimentally and has very little theory developed around it [9] [12] . The entanglement transition is the change of the type of entanglement present in a system that occurs at a point where the system becomes semi-classical and breaks the entanglement entirely [16] [17] [18]. Being able to detect this type of transition is a complex problem, tackled within the collaboration using a process of theory and experimental methods working in harmony [8]. Firstly, as discussed in Chapter 2, identifying entanglement in a system has its own challenges, and secondly, the measures used to quantify the amount of entanglement in a system are theoretical measures that do not relate well to global experimental techniques [15] [19] [20] [21] [22] [23]. One of the other biggest challenges faced in this project is to find this phenomenon at temperatures that could be experimentally achievable. Quantum phenomena can be very sensitive to thermal fluctuations, having the underlying quantum behaviour destroyed by even relatively low temperatures.

The beginnings of the theory around the entanglement transition comes from the techniques developed in the recent field of Quantum Information being applied to known systems in condensed matter physics [16]. Quantum Information treats information as a resource, this concept has opened up this field as one of the most innovated and exciting areas in recent times [24]. Entanglement plays a key role in the techniques developed in Quantum Information mostly in the form of entangled qubits. By applying these to more complex but solvable models in condensed matter, shine a new light into both of these fields. Papers from Wootters and collaborators began by exploring the distribution of entanglement in small systems of three qubits and developed a method of quantifying the amount of entanglement called concurrence (also described in Chapter 2)[19] [20] [21]. It is seen in this project that finite-sized calculations can offer a great insight into these more complex systems and the distribution of entanglement [9].

Quantum Information and finite-sized calculations in this thesis have helped us understand better an unusual behaviour seen in 1D antiferromagnetic chains called factorisation. First described by Kurmann et al. in 1982, factorisation occurs in the ordered antiferromagnetic phase of 1D chains with an applied external field where, at a particular value of the field, the ground state of the system spontaneously looses all quantum fluctuations [18]. The spins remain antiferromagnetic with long range order but without any fluctuations, which can be observed with the absolute value of the correlation functions showing a perfect flatness [25]. Factorisation is introduced in Chapter 3 with results for the correlation functions in Chapter 5. It is the factorisation field where the entanglement transition occurs. Quantum Information has shown that below the factorisation field the chains are antiferromagnetically entangled and above the transition they are ferromagnetically entangled. At the transition because the system becomes classical and the ground state becomes separable, there is zero entanglement. The transition in the thermodynamic limit takes place entirely in the antiferromagnetically ordered phase, and by tuning the anisotropy between the interactions in the spin chain it is accepted that the entanglement transition is an entirely separate phenomenon from critically that induces the phase transition in the chains to being ferromagnetically aligned with the applied field.

This project predicts experimental neutron scattering results for a class of small molecular magnets, as of yet the collaboration hasn't conducted any experiments based on these results but being able to experimentally detect the entanglement transition is one of the most important motivations behind the work presented in this thesis. Being able to use neutron scattering experiments to identify the entanglement transition for the first time would be a step towards using entangled states in some sort of application. Quantum Information is already paving the way in using entanglement in innovative and practical way such as Quantum Key Distribution (QKD) for security and encryption purposes [15] [26] [16]. Using entanglement and the entanglement transition in molecular magnets is still very far away, but it starts with understanding the theory and the mechanism of the transition and this thesis manages to give real predictions in finding the entanglement transition at achievable temperatures. Producing molecular magnets in itself is a new and innovative field, and together with the progress being made into entanglement gives a very promising future for the interesting concepts and physics studied in this thesis.

1.2 Chapter Summary

The thesis is organised in the following way; with the relevant background chapters discussing entanglement and the models used in this project with a commentary on the application of these models to real materials and experiments. The results chapters then progress with the complexity of the models used starting with a simple, but insightful, dimer system, and then building up larger finite-sized systems, whilst discussing the trends towards the thermodynamic limit. The final results chapter is the accumulation of the goals of the project by detailing the results of finding the entanglement transition in small magnetic molecules at finite temperatures using the neutron scattering cross-section.

Chapter 2 presents the development of entanglement from its conceptualisation and its place in quantum mechanics to being able to identify it in a real system and then quantifies the amount of entanglement in a system. The EPR paradox from Einstein, Poldoski and Rosen from the 1930's best encapsulates the exciting time around the formation of quantum mechanics and the philosophical discussions between scientists on how to interpret the strange behaviour that was being discovered in quantum systems. The concept of entanglement is tightly connected to other quantum concepts accepted by the Copenhagen Interpretation that describe uncertainty and duality other statistical and probabilistic techniques. Chapter 2 outlines the postulates that the EPR paradox makes, the consequences of the thought experiment to how best describe the effects of entanglement using an alternative model. This alternative model developed by Einstein was a Hidden Variables model that says that quantum mechanical systems have a set of unknown parameters that dictate the results of certain measurements. With these concepts explained, the chapter uses them to work through examples of measurements on entangled pairs to build a Bell's Inequality [27]. Bell's Inequality is a testable threshold that can be experimentally broken by an entangled system.

The second half of Chapter 2 focuses on newer developments made to the field of entanglement by its reevaluation in the recent field of Quantum Information. The core of this is to treat entanglement as a resource for information, when applied to real systems this leads to being able to theoretically quantify the amount of entanglement in a given system. Here, two central ways of quantifying entanglement are described; these are von Neumann Entropy that uses the idea that an entangled state contains more information and therefore has a higher entropy; and concurrence that uses the spin-flip transformation of a particular state to project a state onto it's transformed orthogonal counterpart and describe the amount of overlap between them [21]. Lastly, as the goal of this project is to identify the entanglement transition, the chapter briefly discusses phase transitions, quantum critical points and the criterion for the entanglement transition.

Chapter 3 is the second background chapter and gives the Hamiltonians for all the models and variation of the models used in this thesis and is referred to throughout the thesis. The focus of this project is using the 1D anisotropic XY-model Hamiltonian for antiferromagnetic spin chains, this can be adjusted to the isotropic XY-model and the other end of the scale, to the Ising model. This model is used because of an unusual occurrence in these antiferromagnetic chains to factorise at a particular field

[18]. Factorisation and its connection to the entanglement transition is explained in chapter 3. The anisotropic XY-model Hamiltonian is used for finite-sized calculations predominantly but a commentary on the thermodynamic limit is made in this chapter and Chapter 5. With periodic boundary conditions this model can even be applied to molecular magnets in ring formations. Chapter 3 also provides a literature review on the type of real materials and crystals that the models and ideas presented in the project can be applied to. There is particular attention paid to molecular magnets in the literature as another recent field that is opening up exciting avenues for interesting behaviour that can be chemically tunable [7] [28]. In very recent publications scientists are starting to explore entanglement in some molecular systems and the effects of doping different ions [29] [30] [4].

The next three chapters collect the results and conclusions of this project. Chapter 4 serves as a template, outline the process of studying these models starting with a simple dimer model. The dimer has the advantages of being easily solved with a small Hilbert space making it easier to look directly at the eigen states to understand better the behaviour of the system. The process starts with solving the system and studying the energy spectrum, here a level crossing between the two lowest energy levels coincides with the calculated factorisation field. By looking directly at the eigen states that correspond to the lowest energy values it is shown that one is the antiferromagnetically entangled singlet and the other a ferromagnetically entangled state. The ground state changes from the antiferromagnetically entangled state to the ferromagnetically entangled state at the level crossing at the factorisation field. At this point any linear combination of the states is a valid eigen state and it can be shown that a linear combination can be found that shows the states to be separable and thus unentangled. The chapter concludes by calculating concurrence for the dimer [2].

Chapter 5 expands on the previous chapter, using the same process of exact diagonalisation to solve larger finite-sized systems for open and periodic boundary conditions. Results are detailed for even numbered finite-sized systems from 4 spins to in some calculations for 12 spins being the computational limit for exact diagonalisation. As with the dimer before, the energy spectra are calculated for the models and level crossings observed in the ground state. The larger the system the more level crossings there are between the two lowest states [31], care is taken to prove that it is only the last level crossing that causes the system to factorise. This is done explicitly for the 4 spin system where it is still possible to directly study the components of the states. For larger systems the correlation functions are used to study the effect of the level crossings, showing a complete 'flatness' in the correlations at the factorisation field. These calculations are extended into some finite temperature calculations to test the robustness of the effects of the level crossing. This chapter also explores criticality and implications for the thermodynamic limit. It concludes by calculating concurrence for a systems from 4 spins to 12 spins for open and periodic boundary conditions.

The last results chapter uses everything learned in previous chapters and applied it to modeling small molecular rings, with particular focus to the plaquette of 4 spins and the hexagon of 6 spins. This chapter is about the experimental implications of the entanglement transition, as such the results calculated are for measurable quantities, including magnetisation and most importantly, the magnetic neutron scattering cross section [12]. The entanglement transition in the plaquette and hexagon show a clear change in the spectral weight of the scattering function when passing through the factorisation field. The scattering function can be split into its component parts depending on the direction of the correlation function that it consists of. For example, the scattering function for the correlations in the xx, yy, zz or xy directions can be calculated separately and it can be seen where the antiferromagnetic and ferromagnetic peaks from the whole scattering function originate from. Using this it can be seen that before the transition the scattering function is predominantly made up of antiferromagnetic interactions and after it it is dominated by ferromagnetic interactions aligned with the direction of the applied field. This chapter also tests how robust the features of the entanglement transition are for different system sizes for a range of low temperatures, finding that typically the transition is still visible around 10% of the interaction energy J.

Lastly, Chapter 6 explores a different way of modeling small molecules such as the plaquette and Hexagon. This method takes into consideration any cross-term interacts that might arise in the 2D geometry of the small rings. Though both models and Hamiltonians used in describing the plaquette and hexagon systems are valid the alternative one would consider a molecule whose orbitals overlap in way that would cause cross-term interactions between the x and y directions between neighbouring ions. This section is not completed to the same level as the anisotropic XY-model approach, but highlights some interesting physics present in these models.

Chapter 7 provides a summary of the work presented in this thesis and comments on the key results and conclusions in respect to the main objectives of the project. This chapter will also comment on further work based on the foundations that this collaboration has made with the hopes that the next level of this work would involve experimentation on real quantum spin clusters.

Chapter 2

The Entanglement Transition

Since its conceptualisation in the mid 1930's, entanglement has had a complicated and controversial history. Quantum mechanics (QM) has evolved with the concepts involved in entanglement inherent in its framework. In contrast to classical mechanics, entanglement provides a platform in QM in which to ask some fundamental questions, questions that in classical mechanics seem redundant. The crux of this is that in a quantum mechanical system most properties can be directly measured. Instead, it is a theory based on ensembles and probability, which brings the act of measurement upon a system under scrutiny.

This chapter looks to introduce entanglement and its importance to the early stages of development for quantum mechanics. Here, the EPR (Einstein-Podolsky-Rosen) paradox is used as a narrative to describe the complex ideas behind entanglement and why it has a controversial history. At the time, two interpretations of QM were formulated; one being the, now accepted, Copenhagen Interpretation and the other based on Locality and a Local Hidden Variables model. Resolution came for physicists regarding entanglement when Bell's inequalities were formed and later when real experiments were conducted.

Entanglement has seen a resurgence of interest since the late 1990's when Wootters and colleagues put forth the principles behind quantifying the amount of entanglement in a spin system [19] [20] [21]. Since then several developments have been made in quantifying entanglement in different ways, in particular von Neumann entropy which is outlined in this chapter as it demonstrates the main ideas that are then built upon in many of the other methods [15]. When quantifying entanglement in this thesis, concurrence is calculated as it is a commonly utilised quantity and a fairly straight-forward method. Concurrence is also outlined in this chapter with addition examples set out in detail, in Chapters 4 and 5.

Lastly, this project is centered around the entanglement transition, thus this chapter will describe what that means and how the entanglement transition is different from a typical phase transition.

2.1 Entanglement

Entanglement is a purely quantum mechanical phenomenon with no analogous behaviour seen in classical mechanics. A quantum mechanical system, including an entangled system, has a strong relationship with measurement. The act of measurement on a QM system can not be fully separated from it, having a significant effect on the outcome of the system. In a classical object it is possible to measure the length of that object with relative certainty, without changing it. For a quantum mechanical object, like a photon, it is possible to either measure its position or its wavelength (to obtain its momentum). A photon exhibits wave particle duality which has been well demonstrated using a set of Young slits experiments. The general set-up of the experiment sends individual photons towards two appropriately distanced slits and then the photons are individually recorded by an array of detectors past the slits. Each photon behaves like a wave when passing through the slits, which allows it to interfere with itself. Statistically this forms a wave diffraction pattern on the detectors. In addition, the photons behave like localised particles on arrival at the detector. Indeed, it is possible, by placing an additional detector at one of the slits , to determine which of the two slits a particular photon went through. However, when this is done the diffraction pattern is lost.

The Young slits experiments are a powerful way to describe interesting phenomena such as duality, uncertainty, non-commuting parameters and the effect measurement can have on a quantum mechanical system. The type of measurement dictates whether the photon behaves like a wave or a particle and the accuracy of the measurement relate to the uncertainty in Heisenberg's uncertainty principle given below;

$$\Delta x \Delta p \geq \frac{\hbar}{2}. \tag{2.1}$$

Position x and momentum p are non-commutable quantities. If one parameter is measured with high accuracy then the other can not be measured with any accuracy. In a strict sense, this means that if one parameter is measured accurately then it is not just that the other is immeasurable but that it has no physical meaning at the moment of measurement and can never be recorded simultaneously. For the photon, this is understandable, if its momentum is measured then the photon is exhibiting wave behaviour and a wave has no local position to measure.

Entanglement is the principle that one part of an entangled system can have a physical influence on another part of that system without interacting with it and even when they are beyond each others' local environment i.e. a measurement taken independent of the distance between them. This apparently instantaneous transfer of information contradicts relativity and caused concern for physicists at the time. In the 1930's Einstein, Podolsky and Rosen developed a thought experiment that became known as the EPR paradox, to clarify the restricting nature of quantum mechanics. They proposed that QM was "incomplete" and that the idea that measurable quantities could be non-commuting or physically unknowable could be circumvented by a more complete theory. Einstein developed a model of hidden variables that were able to describe unknown parameters that exist before measurement.

2.1.1 The EPR Paradox

The EPR paradox is a thought experiment, devised in the early years of QM. When navigating this bizarre and new area of physics the EPR paradox was based on two principles that show the core difference between classical and quantum physics. The first condition reads

" ... every element of the physical reality must have a counterpart in the physical theory." [32]

In classical physics, this statement is straight forward: the direct measurement of the length of a piece of string with high certainty is its length as a physical property. In a

QM system measuring the length of something with a strong certainty is not a direct measurement. An electron's 'length' does not have much meaning, it is usually taken as a point particle with the accuracy of its length more associated with its position. As seen in equation 2.1 the accuracy of its measured position has a profound effect on the system, which is addressed in the second hypothesis:

"... if without in anyway disturbing the system, we can predict with certainty (i.e. with a probability equal to unity) the value of a physical quantity, then there exists an element of reality corresponding to that quantity." [32]

This statement essentially says that the act of measuring a system should not change the system. The Copenhagen Interpretation of QM contradicts this, as was described above using Young's Slits experiments as an example. Einstein developed his local hidden variables (LHV) model to explain such phenomena and still obey the conditions for the EPR paradox [33]. Einstein devised what he thought of as a more complete quantum theory that was more fundamental than what statistical mechanics could provide. Hidden variables were the supposed statistical and otherwise unknowable quantities of a system [15]. Additionally, they described the outcome of a measurement without the need of the measurement being performed.

The EPR paradox can be summerised using a pair of specially prepared spin particles as an example. A particle with a zero spin decays into two equal and opposing particles. In order to conserve spin they must have opposing spin in the same given direction. They must conserve momentum also and travel in opposite directions. They are then separated by an arbitrary long distance that removes them from each others' local environment. If these particles are entangled then they can behave 'non-locally' regardless of distance, this means that one particle can affect the other. The consequence of this 'action at a distance' is that it implies an instantaneous transfer of information that could be interpreted to break causality.

The two separated particles are labeled particle A and B, with their spin direction referred to spin A and B. If measured in the same direction the spins will always anti-align, which would be the same for an entangled pair or a classically anti-correlated pair. If the spins are measured in different directions then if they are entangled. The first measurement taken, say on spin A, will directly influence the spin of spin B. Before a measurement the spin of both particles is undefined. LHV model is used to explain the unusual behaviour of entangled particles by saying that there is a set of variables that describe all measured outcomes. This is best explained in an example using the Bell Inequalities, demonstrated in the following section.

2.1.2 Bells Inequalities

In 1964 J.S Bell formulated a family of inequalities to mathematically represent the EPR paradox using a model that incorporated Local Hidden Variables. The inequality, if broken would indicate that the measured system could not be described using the LHV model but were an entangled pair. This was the first method that scientists could use as a foundation to test the existence of entanglement [27]. The inequalities produce a probabilistic limit on the statistical measurement of a string of paired particles. An experiment can be set up where a source emits pairs of equal and spin opposing particles. Each pair of spin A and spin B are measured separately in any direction α, β and γ (not necessarily orthogonal). Before the particles are measured their respective spins are undefined in any direction. A possible scenario for any measurement outcome is given a subscript label i where table 2.1 maps out all possible scenarios with N_i giving the number of times scenario i will be realised, statistically, when the experiment is measured a number of independent ways . If the particles are measured in the same direction then the outcome will always be an anti-aligned arrangement of spins [34] [15] [35].

Label	Number of Scenario i realised	Particle A	Particle B
1	N_1	$(\uparrow_\alpha\uparrow_\beta\uparrow_\gamma)$	$(\downarrow_\alpha\downarrow_\beta\downarrow_\gamma)$
2	N_2	$(\uparrow_\alpha\uparrow_\beta\downarrow_\gamma)$	$(\downarrow_\alpha\downarrow_\beta\uparrow_\gamma)$
3	N_3	$(\uparrow_\alpha\downarrow_\beta\uparrow_\gamma)$	$(\downarrow_\alpha\uparrow_\beta\downarrow_\gamma)$
4	N_4	$(\uparrow_\alpha\downarrow_\beta\downarrow_\gamma)$	$(\downarrow_\alpha\uparrow_\beta\uparrow_\gamma)$
5	N_5	$(\downarrow_\alpha\uparrow_\beta\uparrow_\gamma)$	$(\uparrow_\alpha\downarrow_\beta\downarrow_\gamma)$
6	N_6	$(\downarrow_\alpha\uparrow_\beta\downarrow_\gamma)$	$(\uparrow_\alpha\downarrow_\beta\uparrow_\gamma)$
7	N_7	$(\downarrow_\alpha\downarrow_\beta\uparrow_\gamma)$	$(\uparrow_\alpha\uparrow_\beta\downarrow_\gamma)$
8	N_8	$(\downarrow_\alpha\downarrow_\beta\downarrow_\gamma)$	$(\uparrow_\alpha\uparrow_\beta\uparrow_\gamma)$

TABLE 2.1: All possible measurement scenarios are given a label from 1 to 8 that corresponds to the number of times the scenario is realised N_i. Each scenario has a predetermined planned for particle A that has the anti-aligned measurement for particle B for any direction of measurement α, β and γ. These scenarios can be used to calculate the probability of a given outcome when particles A and B are measured in different directions.

Any measurement recorded for the pairs of spins have a probability that can be deduced from table 2.1. For example, a measurement has occurred on a pair of spins. Spin A was measured in the α direction and was found to be in the state $|\uparrow_\alpha\rangle$ and spin B was measured in the γ direction and also found to be in the state $|\uparrow_\gamma\rangle$. This corresponds to scenarios N_2 and N_4. The probability of this measurement is written as follows, with the notation $P(A, B)$ for the measurement on spin A and B;

$$P(\uparrow_\alpha, \uparrow_\gamma) = \frac{N_2 + N_4}{\sum_{i=1}^{8} N_i}. \tag{2.2}$$

Any measurement can be used to construct a probability and can be combined to form an inequality on the basis that the combined probability of two possible orientations of spin is greater than just one possible orientation of the spin. [36]. With all possible scenarios included and the sum of all scenarios equal to one then a more general inequality can be constructed for spin A and spin B [32];

It is said that the spins are undefined until measured for both a Quantum Mechanical outcome and using Einstein's LHV model. By describing the paired systems using LHV it is effectively saying that before the spins are measured, they have a predisposed plan to point in an agreed arrangement dependent on the direction measured. This allowed the spins to always point opposite to each other without information traveling between them and angular momentum remaining conserved. This hidden plan is characterised by a set of parameters called λ and assumes that the probabilities of the measured results are independent of the directional choices made on either particle and also independent of actually being measured at all [22]

For example if the hidden variables have a given plan for spin A to always measure a positive spin regardless of direction represented i.e. $(\uparrow_\alpha\uparrow_\beta\uparrow_\gamma)$ then the plan for spin B is $(\downarrow_\alpha\downarrow_\beta\downarrow_\gamma)$. This can be seen on table 2.1 labeled $i = 1$. For this case any direction measured will give an anti-aligned result $\uparrow\downarrow$. But λ is random with an even probability distribution, so that all plans for the spins are valid and as equally likely. Another plan for spin A may be $(\uparrow_\alpha\uparrow_\beta\downarrow_\gamma)$ and Spin B has $(\downarrow_\alpha\downarrow_\beta\uparrow_\gamma)$ (labeled 2) and so on until all possible plans are accounted for so that:

$$\int \rho(\lambda)\, d\lambda = 1. \tag{2.3}$$

If the plan mentioned above, with the label 2 if taken and all possible pairs of measurements are taken it can be seen how many measurements obey the conservation of spin or not.

Direction for A	Direction for B	measurement	Conserved
α	α	$\vert\uparrow\downarrow\rangle$	✓
α	β	$\vert\uparrow\downarrow\rangle$	✓
α	γ	$\vert\uparrow\uparrow\rangle$	×
β	α	$\vert\uparrow\downarrow\rangle$	✓
β	β	$\vert\uparrow\downarrow\rangle$	✓
β	γ	$\vert\uparrow\uparrow\rangle$	×
γ	α	$\vert\downarrow\downarrow\rangle$	×
γ	β	$\vert\downarrow\downarrow\rangle$	×
γ	γ	$\vert\downarrow\uparrow\rangle$	✓

TABLE 2.2: Hidden Variables model for scenario N_2 where all combinations of the directions of measurement is considered. The table then states whether spin has been conserved with a tick or a cross symbol.

Table 2.2 lists all the possible measurement outcomes for plan N_2 which conserves spin $\frac{5}{9}$ of the times. This can be done for all plans described by hidden variables, continuing with the labels introduced in table 2.1; 1 and 8 conserve spin $\frac{9}{9}$ always; and $2 \to 7$ conserve spin $\frac{5}{9}$ of the times. This gives a probability for anti aligned spins to be $\frac{2}{3}$.

The same measurement set up can be applied to a pair of anti-correlated spins that are represented by an entangled wavefunction:

$$|\psi(A,B)\rangle = \frac{1}{\sqrt{2}}\Big[|\uparrow\rangle_A \otimes |\downarrow\rangle_B - |\downarrow\rangle_A \otimes |\uparrow\rangle_B\Big]. \tag{2.4}$$

This is an entangled singlet that represents an anti-correlated dependence between spin A and spin B. If either spin is measured then the whole wavefunction collapses and the spin on the other particle can be known without further measurement. For example, when spin A is measured to be $|\uparrow\rangle$ then the second term in the singlet can not be true and the configuration left is $|\uparrow\downarrow\rangle$ thus without measuring it, it is known that spin B is $|\downarrow\rangle$.

Before the three directions α, β and γ are discussed a simple set up where spin A is measured first in the z direction and spin B is measured at an angle θ in respect to A, is demonstrated. This arrangement is shown in Figure 2.1, where S denotes a spin measurement.

When the measurement for spin B is performed in the z direction, i.e when $\theta = 0$ then the measurement in vector form is $|\downarrow\rangle_z = \left[\begin{smallmatrix}0\\1\end{smallmatrix}\right]$. The xz plane is chosen to perform the spin

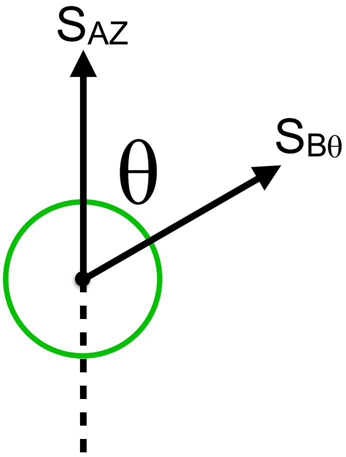

FIGURE 2.1: The measured direction of particle A is set as the z direction and is measured first. The direction of the measurement particle B is dependent on θ and is measured after particle A. If the system is entangled then the measurement on particle A will give information on the spin direction of particle B dependent on the angle θ.

measurements in. A component measured in this plane can be written in the following way (as outlined in Rae's Quantum Mechanics textbook [37]):

$$\begin{aligned}\hat{S}_\theta &= \hat{S}_z \cos\theta + \hat{S}_x \sin\theta \\ &= \frac{\hbar}{2}\begin{pmatrix}\cos\theta & \sin\theta \\ \sin\theta & -\cos\theta\end{pmatrix}.\end{aligned} \tag{2.5}$$

This matrix has the eigenvalues $\pm\frac{1}{2}\hbar$ with the corresponding eigenvectors:

$$\begin{aligned}Ev_1 &= \begin{pmatrix}\cos\frac{\theta}{2} \\ \sin\frac{\theta}{2}\end{pmatrix} \\ Ev_2 &= \begin{pmatrix}-\sin\frac{\theta}{2} \\ \cos\frac{\theta}{2}\end{pmatrix}\end{aligned} \tag{2.6}$$

The measurement for spin B can be written as a linear combination of the eigen vectors where the coefficients must coincide with a down measurement in the z direction, in the θ basis, thus:

$$\begin{pmatrix}0 \\ 1\end{pmatrix} = \sin\frac{\theta}{2}\begin{pmatrix}\cos\frac{\theta}{2} \\ \sin\frac{\theta}{2}\end{pmatrix} + \cos\frac{\theta}{2}\begin{pmatrix}-\sin\frac{\theta}{2} \\ \cos\frac{\theta}{2}\end{pmatrix}. \tag{2.7}$$

Using this it is possible to construct the probabilities of each possible result given spin A is measured first. Given spin A measured in the z direction yields $|\uparrow\rangle$ then dependent on θ the probability that spin B gives the measurement $|\uparrow\rangle$ also is $P_{\uparrow\uparrow}(\theta) = \sin^2\frac{\theta}{2}$. Correspondingly the probability of a $|\downarrow\rangle$ result for spin B is $P_{\uparrow\downarrow}(\theta) = \cos^2\frac{\theta}{2}$. This makes sense, as an example, for $\theta = \frac{\pi}{3}$ then $P_{\uparrow\uparrow} = \frac{1}{4}$ and $P_{\uparrow\downarrow} = \frac{3}{4}$, given the appropriate sample size. The same is worked out for spin A being measured as $|\downarrow\rangle$ and all possible measurements are provided:

$$\begin{aligned}
P_{\uparrow\uparrow}(\theta) &= \sin^2\frac{\theta}{2} \\
P_{\uparrow\downarrow}(\theta) &= \cos^2\frac{\theta}{2} \\
P_{\downarrow\uparrow}(\theta) &= \cos^2\frac{\theta}{2} \\
P_{\downarrow\downarrow}(\theta) &= \sin^2\frac{\theta}{2}.
\end{aligned} \tag{2.8}$$

For this simple arrangement, the probability is only dependent on the direction that spin B given by θ. Bell's inequality describes this arrangement quantum mechanically and is given as [22] [23];

$$P_{\uparrow\uparrow}(\theta) + P_{\uparrow\downarrow}(\theta) + P_{\downarrow\uparrow}(\theta) - P_{\downarrow\downarrow}(\theta) \leq 2. \tag{2.9}$$

In this form for the set up described and shown in Figure 2.1 the inequality can not be broken as it reduces down to $\cos^2\frac{\theta}{2} \leq 1$, which is always obeyed. Thus even a quantum mechanical interpretation can not describe an entangled state for two directions of measurement. When all three possible directions are included and spin A can be measured in any one of those directions then many examples of Bell's Inequalities can be constructed that can be broken. Allowing for a range of directions to be measured is what helps to define what is entangled and what system is just strongly correlated. Wootters states;

"... one of the primary distinctions between quantum entanglement and ordinary correlation [is that] entangled particles exhibit a correlation not just for one measurement but for a whole class of mutually exclusive measurements. [19]"

His paper discusses measurements mutually exclusive in being 'up' and 'down' or 'left' and 'right'. This section will conclude with an entangled example being worked through using a more general form to the angles being measured with a suitable range of angles that would show entanglement, being derived.

Unlike with LHVM, where the measurements are predetermined but hidden, the results for an entangled pair without hidden variables is affected by the relationship between the directions of measurements: α, β and γ. There is no need for these directions to be orthogonal to each other, and for this example they will be put in the xz plane as before, with the angles $\theta_{\alpha\beta}, \theta_{\beta\gamma}$ and $\theta_{\alpha\gamma}$ showing their configuration as demonstrated in Figure. 2.2.

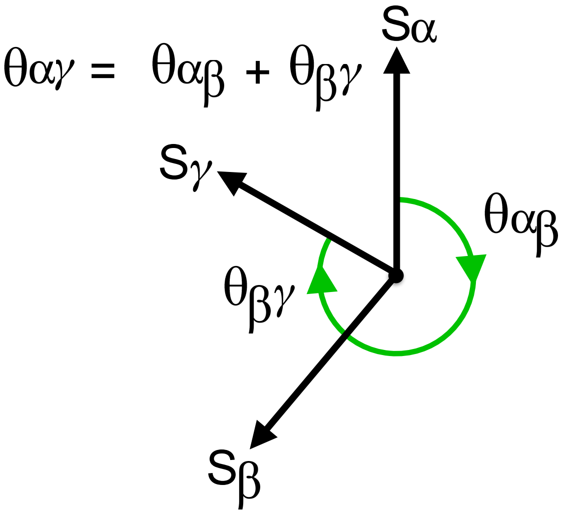

FIGURE 2.2: In this measurement arrangement particle A is still measured first but can be in any direction. The directions α, β and γ need not be orthogonal to each other and in this example are in the same 2D plane. The relationship between the angles and their directions are indicated in the figure.

The directions of the measurements and the angles between them shown in Figure. 2.2 are arbitrary but whether or not a particular arrangement can be shown to break Bell's Inequality and indicate an entangled pair is not. It should be said, that when Bell's Inequality is broken the system must be entangled but if it is not broken it can not be said that it is not entangled (as demonstrated by the above example). The inequality is a limit for a system to behave classically. The process now is to build up an example of a Bell's Inequality that represents three possible measurement directions for entangled singlets. This is achieved using Table. 2.1 and listing probabilities of all possible outcomes. An example for this is given by Eq. 2.2 for $P(\uparrow_\alpha, \uparrow_\gamma)$. There are six possible pairs of measurements that yield an $|\uparrow\uparrow\rangle$ result for all directions, and four possible different states, this equates to 24 possible combinations of measurements.

Using the example for a $|\uparrow\downarrow\rangle$ result, the probabilities are listed below:

$$\begin{aligned}
P(\downarrow_\alpha,\uparrow_\beta) = P(\downarrow_\beta,\uparrow_\alpha) &= \frac{N_7+N_8}{\sum_{i=1}^{8} N_i} \\
P(\downarrow_\alpha,\uparrow_\gamma) = P(\downarrow_\gamma,\uparrow_\alpha) &= \frac{N_6+N_8}{\sum_{i=1}^{8} N_i} \\
P(\downarrow_\beta,\uparrow_\gamma) = P(\downarrow_\gamma,\uparrow_\beta) &= \frac{N_4+N_8}{\sum_{i=1}^{8} N_i}. \qquad (2.10)
\end{aligned}$$

The same process can be applied to all other probabilities [1]. It is logical that the combined probability of two measurement results is greater than the probability of another, it follows from Eqs. 2.2 and 2.10:

$$\frac{N_7+N_8+N_2+N_4}{\sum_{i=1}^{8} N_i} \geq \frac{N_4+N_8}{\sum_{i=1}^{8} N_i}, \qquad (2.11)$$

which can be written in terms of its probabilities to form an example of a Bell's Inequality that represents this system and can be tested:

$$P(\downarrow_\alpha,\uparrow_\beta) + P(\uparrow_\alpha,\uparrow_\gamma) - P(\downarrow_\beta,\uparrow_\gamma) \geq 0. \qquad (2.12)$$

Using the arrangement that $\theta_{\alpha\gamma} = \theta_{\alpha\beta} + \theta_{\beta\gamma}$ and the probabilities discussed in Eq. 2.8 the inequality can be written in terms of the angles between the measurement directions and it is possible to explore possible experimental set-ups that can show entanglement:

$$\cos^2\frac{\theta_{\alpha\beta}}{2} + \sin^2\frac{\theta_{\alpha\beta}+\theta_{\beta\gamma}}{2} - cos^2\frac{\theta_{\beta\gamma}}{2} \geq 0. \qquad (2.13)$$

This inequality can be broken and the function can go negative for certain values of θ. Figure. 2.3 fixes $\theta_{\beta\gamma} = 100°$ or $\frac{5}{9}\pi$ rads and plots Eq.2.13 as a function $f(\theta)$ of $\theta_{\alpha\beta}$. It can be seen that for most part the inequality is obeyed, but there is a small section of angles that would experimentally imply entanglement. Figure. 2.4 shows the dependence of both angles on the inequality. As it is only the negative regions of the function that of are interest in detecting entanglement any part of the function that is ≥ 0, and therefore obeys the inequality, is capped at zero and plotted in yellow. This allows the negative regions to stand out as two dark triangular regions that relate to possible experimental set-up that would detect entanglement if present.

---

[1] In general; for anti-aligned pairs the probabilities $P(\uparrow_i,\downarrow_j) = P(\uparrow_j\downarrow_i)$ and $P(\downarrow_i,\uparrow_j) = P(\downarrow_j\uparrow_i)$ always, but for aligned pairs $P(\uparrow_i,\uparrow_j) \neq P(\uparrow_j\uparrow_i)$ and $P(\downarrow_i,\downarrow_j) \neq P(\downarrow_j\downarrow_i)$.

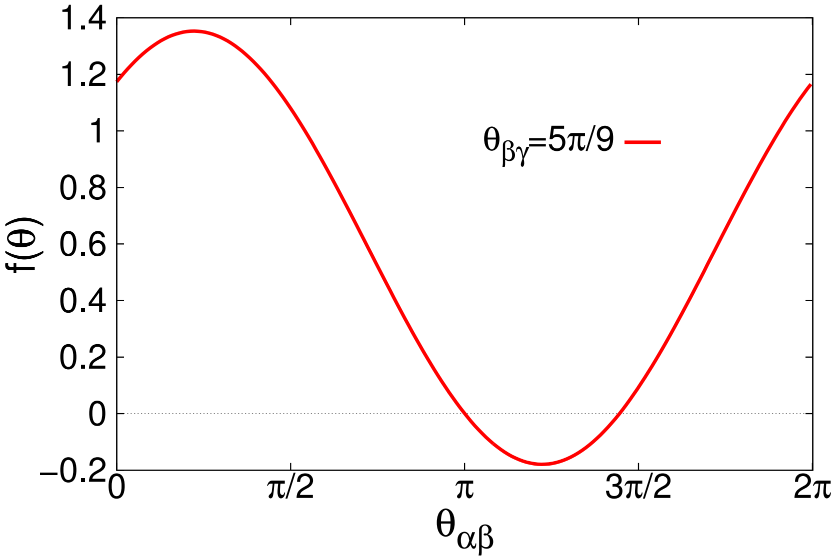

FIGURE 2.3: Bell's Inequality in Eq. 2.13 with the LHS labeled $f(\theta)$ and the angle $\theta_{\beta\gamma} = \frac{5}{9}\pi$. Any value of the function less than zero breaks the inequality and is considered entangled.

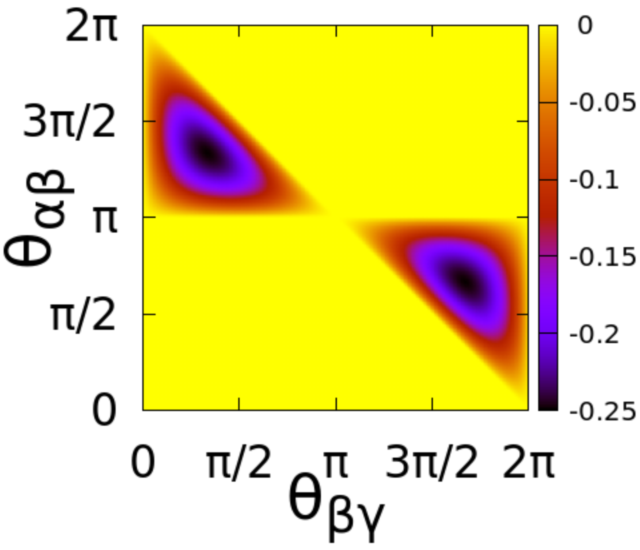

FIGURE 2.4: Bell's Inequality in Eq. 2.13 with the LHS plotted as a surface dependent on the two angles $\theta_{\alpha\beta}$ and $\theta_{\beta\gamma}$. For legibility, any part of the function that obeys the inequality, i.e. is ≥ 0 is capped and plotted in yellow. The two dark triangular regions show the parameters for the angles that give a negative results and break the inequality, thus show and experimental arrangement to detect entanglement.

As an example, let $\theta_{\alpha\beta} = 200°$ and $\theta_{\beta\gamma} = 100°$ then the function gives the value -0.133 to [3 s.f]. This is in clear violation of Bell's Inequality and indicates a non-classical and therefore entangled system.

There are many ways to develop a Bell-type inequality in order to test for entangled pairs, Clauser and Horne worked on a variant called the Clauser-Horne-Shimony-Holt (CHSH) inequality [22] [23] [15]. In 1981 Lo and Shimony derived a new Bell-type inequality with a specific experimental arrangement in mind that would take into account the efficiency of the detection process [1]. In short, they proposed an experiment that used Na atom pairs forced into an electronic singlet state, which once suitably separated were sent through Stern-Gerlach fields to send up-spin particles to one detector and down-spin to another for each pair.

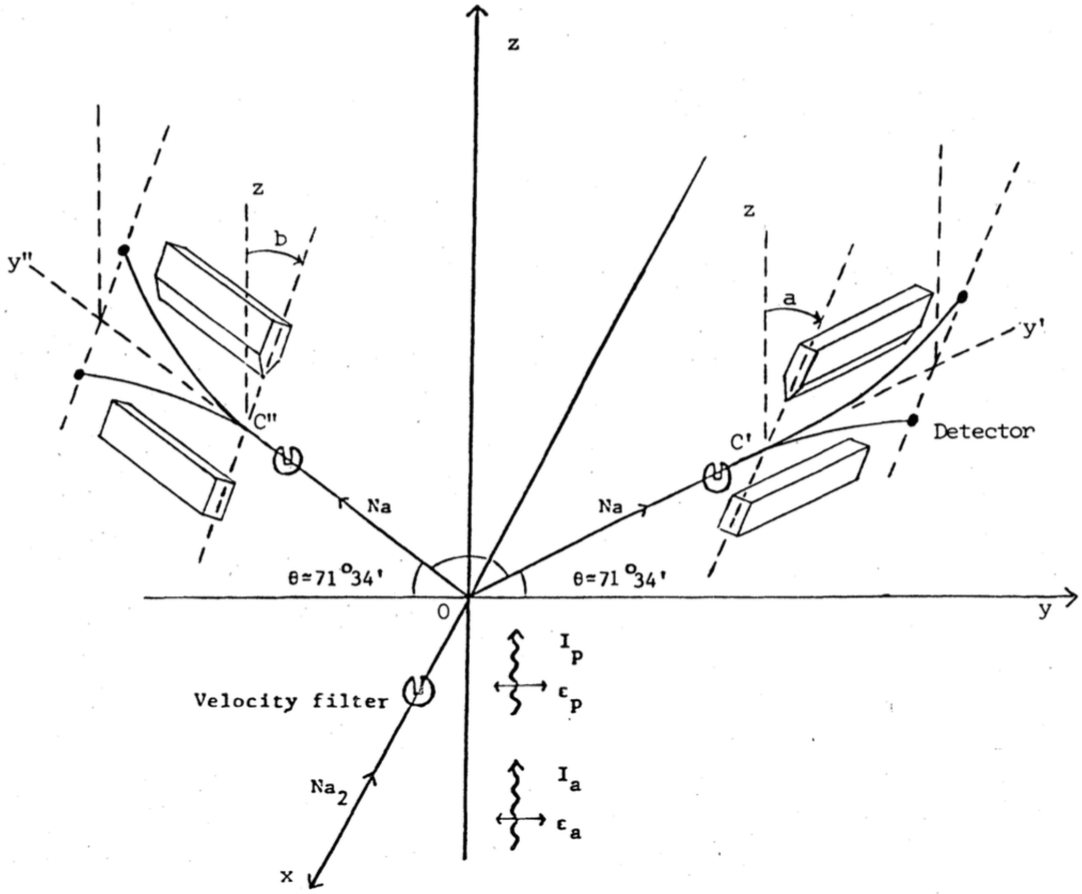

FIGURE 2.5: Experiment arrangement from Lo and Shimony 1981. The sodium atoms travel along the x axis to a point where a laser pump excites them into a known entangled state. They are then separated far enough away to ensure that they out outside of each others local environments. Their respective spins are determined by Stern-Gerlach set-ups which can be rotated to different orientations given by ‘a’ and ‘b’ to measure the spins in different directions. There are detectors after the Stern-Gerlach sections to measure that the spins are ‘up’ or ‘down’ in that particular direction. A statistical picture of the entangled states can be built up to determine whether they break Bell’s Inequalities. [1]

Figure.2.1.2 shows the proposed experiment from their 1981 paper. The Stern-Gerlach sections rotate on their own y axis denoted by y' and y'' with an angle respect to the z axis labeled a and b, allowing for a flexible measurements in different directions. This experiment type using atomic cascades and others with polarisers where explored in the 1980s by such groups as Shimony's, Selleri and Zeilinger, and Alain Aspect [38] [39] [40]. Alain Aspect and collaborators ran a series of high accuracy experiments using calcium cascade sources and published in 1981 and 1982 in agreement with the quantum mechanical predictions of entanglement over any local theory, even giving the optimal angles used to break the CHSH inequity [38] [39]. Aspect *et al.* experiments are considered the definitive experiments that support the quantum mechanic interpretation of these types of systems. It is widely accepted through the development of Bell's Inequalities and the experiments that followed that entanglement and its unusual implications are real and can not be explained using LHVM, and that the Copenhagen interpretation of quantum mechanics does the best job of explaining quantum phenomena.

2.2 Measures of Entanglement

Quantum information (QI) is a young discipline whose development provides an exciting platform to explore uses for quantum phenomena such as using entanglement as a commodity or a resource. Quantum mechanics is a theory based on probability and ensembles, QI is a natural progression of the theory by taking the link between probability and entropy. Quantifying entanglement is akin to quantifying entropy and entropy is used to describe the amount of information in a system [15]. This section explains some of the basics behind quantifying entanglement using the approach of quantum information theory and starts with von Neumann entropy [22] [23] [41] [42].

2.2.1 von Neumann Entropy

A pure state that describes a pair of spins, for example, antiferromagnetically aligned as $|\uparrow\downarrow\rangle$, does not need to be written using probabilities and contains only one piece of information. An entangled singlet as written in eq. 2.4 has an equal probability of being in $|\uparrow\downarrow\rangle$ or in $|\downarrow\uparrow\rangle$. The entangled state contains more possibilities and thus has a higher entropy than a pure state and contains more capacity for information. The entropy used to probe entangled systems is called the von Neumann entropy and is given below:

$$S(\hat{\rho}) = -Tr(\hat{\rho}\log_2 \hat{\rho}). \tag{2.14}$$

The argument of the von Neumann entropy is the density operator $\hat{\rho}$. The density operator in terms of the density matrix is written as:

$$\hat{\rho} = \sum_{nm} |u_m\rangle \, \rho_{mn} \, \langle u_n| \tag{2.15}$$

where the orthonormal basis states are described by $|u\rangle$ and ρ_{mn} are the matrix elements of the density matrix for positions m and n. These elements are calculated from the all the eigen states of the system $|\psi_i\rangle$ (in the $|u_n\rangle$ basis). It is scaled by the probability p_i of the system being in any particular state (an example of this being a Boltmann distribution across the states dependent on temperature):

$$\rho_{mn} = \sum_i \langle u_m|\psi_i\rangle \, \langle\psi_i|u_n\rangle \, p_i. \tag{2.16}$$

For a quantum mechanical system the probability of the system being in state $|\psi_i\rangle$ is p_i such that all probabilities of possible states is unity: $\sum_i p_i = 1$. This means that all the probabilistic information about the state of a quantum system is contained in the density matrix and the density operator. If the system is in one state $|\psi\rangle$, such that the probability of being in that state is exactly 1 and the probability of being in any other state is zero, that state could be a pure state or an entangled state but not a superposition of multiple states. In this case the density matrix is made from a single state that contains all the information about the system. The density operator is analogous to the number of microstates or multiplicity in classical entropy. The von Neumann entropy is usually given in log base 2 to describe the entropy as an expression or expectation value of 'bits' of information.

This definition of entropy in a quantum mechanical system and the density matrix provide the foundation for most of the difference methods used in quantifying entanglement. With the recent developments in QI there have arisen many different but similar parameters used to quantify the amount of entanglement in a system all of which give zero for a pure state as one limit to the scale and 1 for a maximally entangled state. These methods differ with the quantity of entanglement present in a system, as they are sensitive to it in different ways [19] [43] [44] [45] [46]. A popular measure of entanglement, and the one predominantly used in this project is Concurrence.

2.2.2 Concurrence

In the late 90's and early 2000's William Wootters wrote several papers on entanglement as a quantifiable resource focusing on different ways to theoretically quantify entanglement and in the potential quantum technologies fields that were opening up to make use of entanglement as a resource [19] [20] [21]. This section will briefly describe Wootters process in developing concurrence as a measure of entanglement. Chapter 4 uses concurrence to quantify entanglement in a dimer and Chapter 5 does the same for larger finite-sized systems.

One mathematical way to test how entangled a given state is, would be to test how 'separable' it is by seeing how much it overlaps with an orthogonal state. The spin-flip transformation takes a state and transforms its components into a state orthogonal to the original. The central concept of concurrence is to project the spin-flipped state onto its original state and see how much they overlap. A pure state would have no overlap and an maximally entangled state i.e a Bell state would have maximal overlap [47]. For example for the Bell state given by equation 2.4 the spin-flipped state is simply $|\tilde{\psi}\rangle = -|\psi\rangle$, thus when projected $|\langle\psi|\tilde{\psi}\rangle|$ gives the maximum overlap of 1 [47]. This is the definition of concurrence for a 2-qubit state as seen in Wootter's original paper in 1997 and the definition is expanded to apply to more complex systems between more particles in Coffman, Kundu and Wooters paper on 'Distributed Entanglement' in 2000 [21]. Here the density matrix is used to describe the system so that ρ_{AB} is the density matrix that describes a qubit represented by A and B. The spin-flipped density matrix (between two spins) is defined as:

$$\tilde{\rho} = (\sigma_y \otimes \sigma_y)\, \rho^* \,(\sigma_y \otimes \sigma_y)\,, \tag{2.17}$$

where σ_y is the Pauli matrix for y and where the matrix basis is $(|\uparrow\uparrow\rangle, |\uparrow\downarrow\rangle, |\downarrow\uparrow\rangle, |\downarrow\downarrow\rangle)$. [2] The spin-flipped density matrix is then projected as a matrix product $\rho_{AB}\tilde{\rho}_{AB}$ and the eigenvalue of this 4×4 matrix are taken and are all real and positive. The positive

---

[2] The multiple qubit spin-flip operation is $\tilde{\rho} = \sigma_y^{\otimes N} \rho^* \sigma_y^{\otimes N}$

roots of these eigenvalues are λ_i for $i = 1, 2, 3$ and 4 from the highest eigenvalue to the lowest. The concurrence is then quantified as: [21]

$$\mathcal{C}_{AB} = \max\left\{\lambda_1 - \lambda_2 - \lambda_3 - \lambda_4, 0\right\}. \tag{2.18}$$

This is the concurrence for any pair of qubits in a system of particles. For larger systems the concurrence is a local measurement and can be taken from a 2-qubit subsystem that represents the behaviour of the whole system [48]. This is achieved using the reduced density matrix and is shown explicitly in Chapter 5. This means that the above equation for concurrence can be used for any system that can be reduced to a 4×4 matrix with only 4 eigenvalues λ.

The above definition for concurrence is for the ground state concurrence, i.e. when the qubit system is at $T = 0$. For finite temperatures, thermal concurrence or concurrence mixing is a non-trivial approach in comparison. The range of eigenstates of the system can be weighted in different ways with interesting results for different low temperature ranges [26]. Thermal concurrence is not calculated in this project but would have been one of the first calculations to explore in further work connected to this project.

There are many ways that have been developed that can quantify entanglement in the past decade [49] [44] [50]. A lot of them adopt similar methods to von Neumann entropy and the concept of information as a resource, or mutual information between systems [51][52][53]. Many other use similar concepts to concurrence or start with concurrence and modify it [54] [55] [56]. In this thesis, to specifically quantify entanglement, only concurrence is used as a suitable local measure for the systems and models explored. We emphasise that the main criterion for the project is to calculate results of experiments that do not necessarily quantify entanglement directly but may show phenomena associated with changes in entanglement. Concurrence, in this respect has been our guide as a theoretical measure to gather more about the systems studied in this project.

2.3 Quantum Critical Points

A phase transition marks a quantitative and qualitative change in the behaviour of a system. Common phase transitions are encountered in normal environmental thresholds, for example water freezing into ice. Like with ice, temperature is a common parameter used to explore phase transitions, but depending on the type of transition, pressure and external magnetic fields are also common. Water turning into ice is a good example of a first order phase transition, which means that the transition is discontinuous. In this case a sudden structural change takes place that reorganizes the water molecules into an ordered crystal structure. A water to gas transition can be second order around a critical point where pressure and temperature parameters can be controlled to achieve a continuous transition from liquid to vapor or vice versa [13] [57].

A critical point indicates some very interesting behaviour, often called criticality that has a region of influence from that point. Near the critical point, thermodynamical quantities of the system demonstrate power law distributions describing the distance from the critical point. These power law properties and parameters are characterised by a set of critical exponents that annotate the specific power law. These critical exponents describe the power law change in specific heat, isothermal compressability, or the difference in density between the gas and liquid phases as the critical point is approached [14] [13]. The correlation length of a system diverges at a critical point and in a magnetic transition the spin-spin correlation functions are often used to explore a measurable changes in the system.

A quantum phase transition [QPT] is a transition that has been suppressed to zero and is driven by quantum fluctuations instead of thermal fluctuations. At a quantum critical point the transition becomes second order and the correlation length still diverges but correlations in the system should be of an entirely quantum nature. The difference between a system that is classically correlated and one that is dominated by quantum correlations is that the quantum correlations are inherently entangled. A well studied system that has interesting entangled ground state properties are 1D antiferromagnetic systems which are the core systems considered in this project. The models used to describe them are documented in Chapter 3 [57].

The purpose of the project was to explore a specific kind of transition at a QCP that indicates a change of the type of entanglement in a system as opposed to a change in its phase. The recent resurgence of interest in entangled systems and how to quantify entanglement has lead some scientists to reevaluate the QPT phenomenon particularly in 1D-antiferromagnetic chains. This has brought to the fare the phenomena of factorisation [18] and the entanglement transition which are closely related, but distinct from the QPT.

2.4 The Entanglement Transition

The entanglement transition, though not a phase transition, is a quantum transition that occurs in the ground state of certain entangled systems [9] [56] [12]. These types of systems that are explored in this project are outlined in Chapter 3 and are chosen because of a factorisation phenomena that they possess in an applied field. It is demonstrated that the factorisation point of our model are distinct from the QCP that occurs as a phase transition in antiferromagnetic chains when they become ferromagnetically aligned with the external field. Factorisation is pivotal to the entanglement transition as it destroys entanglement, making the system a semi-classical anti-ferromagnetic chain at the factorisation field only [58] [59]. Above and below this point the system is entangled and is so in such a way the the entanglement present is entirely different after the transition. In the thermodynamic limit the entanglement goes from anti-parallel entanglement to parallel entanglement, entirely in the antiferromagnetically ordered phase before experiencing the QPT at the critical field.

The next chapter introduces the systems used in this project to identify the entanglement transition and explains factorisation in these chains and its relationship with the entanglement transition. Chapter 4 shows the processes used to identify the entanglement transition in a 2-site dimer model, using the small system size as an advantage to explore the entangled states directly. Here we show the required change of entanglement; from anti-parallel to parallel, with the entanglement being completely broken at the factorisation field. These requirements for an entanglement transition are tested in compliance to small finite-sized models in Chapter 5. We then start to explore the implications of the transition with respect to measurable quantities by gaining more understand by using the real space correlation functions. The real space correlation functions show quantum correlations in the ordered phases, which are destroyed at the factorisation field. This can be seen by a complete 'flatness' in the absolute value of the real space correlation functions. Lastly, Chapter 6 explores the experimental implications further by calculating the neutron scattering cross-section for small quantum spin clusters showing a robustness to low temperatures of the signatures of the entanglement transition.

Chapter 3

Quantum Magnets

Identifying the entanglement transition using neutron scattering experiments is a complicated task. The approach requires a balance between theoretical models as a foundation and potential real materials that are comparable. The theory portion of the collaboration builds upwards, using finite-sized calculations that are exactly solvable for a range of spin chain based models. These models can represent different arrangements, such as; 1D chains, doped chains or small ring shaped magnets. With this flexibility, they may be easily adjusted by using the correct parameters to predict real crystal behaviour. Presently, the experimental side of the collaboration has focused on 1D crystal experiments using Cs_2CoCl_4 that relates to the anisotropic 1D XY-model [5] [60]. Further models and potential materials are discussed in this chapter to demonstrate the breadth of systems that could provide an experimental insight into the entanglement transition.

The previous chapter outlined the key qualities and features of entanglement and the difficulties involved in study entanglement both theoretically and experimentally. With the concepts behind detecting entanglement and theoretically quantifying entanglement, the entanglement transition was introduced in relation to the quantum critical point as a separate phenomenon [16]. It was also shown that recent theoretical studies have managed to find signatures of the entanglement transition in the anisotropic XY-model [9] [12]. Though with similar intentions, this projects aims to identify the entanglement transition using neutron scattering experiments at achievable temperatures. To realise this, it is vital to understand the models involved and how they can relate to certain real materials. This chapter contains a discussion of the suitability of various models that may be used find an appropriate material for use in a neutron scattering experiment. The theoretical models used are presented here with their Hamiltonians as a guide to be referred back to in the remainder of the thesis.

3.1 Model Hamiltonians

Spin chain systems are well-established within the condensed matter community and have been a prime candidate for re-examination using more recent quantum information theory (QIT) concepts [17] [22] [23] [24]. This approach has exposed an untapped resource of entangled systems that can be used to identify the entanglement transition. The majority of the work conducted in this project and the relevant literature [61] [56] [58] [59] [62] [63] [64] [65] [66] [67] [68] [69] [70] have used variations of the anisotropic XY-model for a 1D spin system. The core reason for this is that the doubly degenerate ground state of the anisotropic XY-model is highly entangled and exactly solvable. For the thermodynamic limit, the model is solved using analytical methods that are well documented and commonly used [10]. These methods were introduced by Lieb, Shultz and Mattis in 1961 [71], applied to the anisotropic XY-model in the ground state with no additional external field. The Hamiltonian for the anisotropic XY-model is;

$$\hat{H} = -J\sum_{j=1}^{N}(1+\gamma)\hat{S}_j^x\hat{S}_{j+1}^x + (1-\gamma)\hat{S}_j^y\hat{S}_{j+1}^y. \tag{3.1}$$

It describes a Heisenberg spin chain of spin 1/2 moments confined to lay on the xy plane. The sign of the interaction energy, J, determines whether the system is antiferromagnetic or ferromagnetic, with nearest neighbour interactions only. The anisotropy between x and y interactions is given by γ, and for $0 < \gamma \leq 1$ the model is in the Ising universality class. The Ising model for interactions only allowed in the x direction is returned for $\gamma = 1$;

$$\hat{H} = -2J\sum_{j=1}^{N}\hat{S}_j^x\hat{S}_{j+1}^x. \tag{3.2}$$

With no interaction terms in the y direction the Ising model acts as the classical limit to the XY-model. The other limit on the anisotropy parameter is $\gamma = 0$, which recovers the isotropic XY-model where the interactions in x and y are equal;

$$\hat{H} = -J \sum_{j=1}^{N} \hat{S}_j^x \hat{S}_{j+1}^x + \hat{S}_j^y \hat{S}_{j+1}^y. \tag{3.3}$$

Where the model is in the XY universality class. For a more generalised spin-$\frac{1}{2}$ chain that allows for interactions in any direction the XYZ-model is introduced;

$$\hat{H} = -J \sum_{j=1}^{N} (1+\gamma) \hat{S}_j^x \hat{S}_{j+1}^x + (1-\gamma) \hat{S}_j^y \hat{S}_{j+1}^y + \Delta \hat{S}_j^z \hat{S}_{j+1}^z. \tag{3.4}$$

A new anisotropy parameter is added for the interaction in the z direction called Δ. For all the models and their respective Hamiltonians listed above for 1D chains of various interactions they can be applied to finite sized systems or 1D chains in the thermodynamic limit where the chain length $N \to \infty$ to replicate the behaviour of a crystal made of 1D chains.

To guide these models towards an entanglement transition or critical behaviour, such as described in Chapter 2, the tuning parameter is an applied external field. Therefore the most generalised version of the Hamiltonian for a 1D chain with an external field is given;

$$\hat{H} = -J \sum_{j=1}^{N} (1+\gamma) \hat{S}_j^x \hat{S}_{j+1}^x + (1-\gamma) \hat{S}_j^y \hat{S}_{j+1}^y + \Delta \hat{S}_j^z \hat{S}_{j+1}^z - h_z \sum_{j=1}^{n} \hat{S}_j^z. \tag{3.5}$$

In this instance the direction of the field, though given in the z direction is still completely general as in relation to the interactions in different directions any model can be resolved. By setting the z direction interactions to zero, i.e $\Delta = 0$, then the anisotropic XY-model with an applied transverse field is formed. In this case the direction of the field is very important and will be kept in the transverse z direction as shown below;

$$\hat{H} = -J \sum_{j=1}^{N} (1+\gamma) \hat{S}_j^x \hat{S}_{j+1}^x + (1-\gamma) \hat{S}_j^y \hat{S}_{j+1}^y - h_z \sum_{j=1}^{n} \hat{S}_j^z. \tag{3.6}$$

The anisotropy in a 1D system originates from the difference between the interaction strengths in the xy plane, instead of relating to the crystallographic directions of the chain. Fig. 3.1 depicts a single site where the xy plane is shown in cyan. This interaction plane is called the easy plane, and the transverse field is perpendicular to this in the z

axis. With the xyz axes set up as the interaction axes, the notation abc is used for the crystallographic axes. The Hamiltonian dictates the physics involved in the model and it will only describe observables in terms of the interaction xyz axis. The crystallographic axes become relevant when real materials are introduced and knowledge of the crystal parameters are needed.

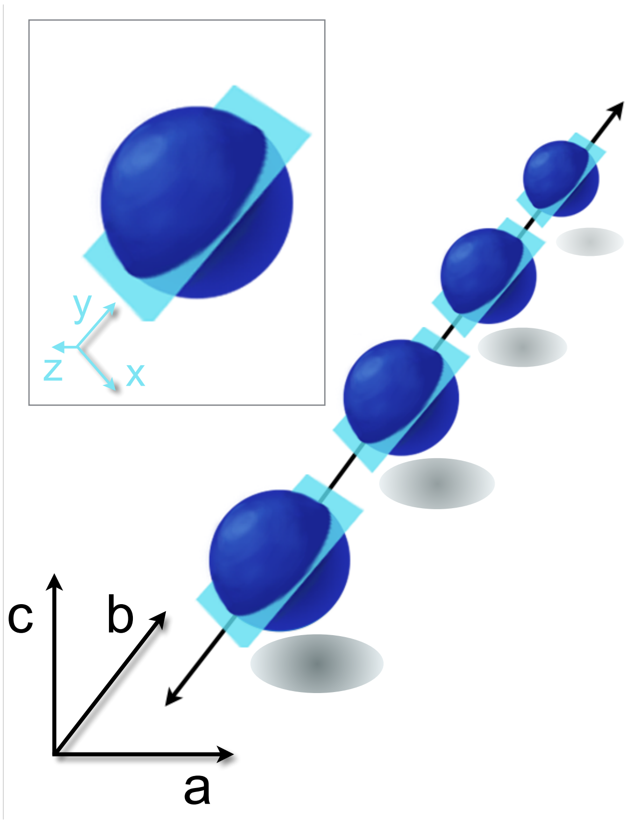

FIGURE 3.1: The direction of the chain is arbitrary and is chosen to be along the b-axis in relation to the crystallographic basis. The interaction xyz-axes can be oriented in any way in relation to the chain direction. In practice there would be a crystal field that links the orientation of the two bases by a rotation matrix. The inset maps out the interaction axes in cyan, where the 2D plane through the ion represents the easy-plane for the XY-model as the xy-plane. The application of an applied transverse field would be transverse to the easy-plane i.e. the z direction and not necessarily perpendicular to the orientation of the chain.

In a general sense, the above means that the direction of the chain is dependent on the material and could be coupled to the interaction axes in any way. This is discussed in more detail in section 3.4, with Cs_2CoCl_4 as an example. Fig. 3.1 fixes the chain direction along the b axis as an example. The figure demonstrates the relationship between the axes and how this can potentially relate to a range of variations on the XY-model and a range of possible candidate materials.

The anisotropic XY-model is the core Hamiltonian (Eq. 3.6) used in this thesis for reasons that are documented in this chapter, in regards to its properties and the promise of different materials that it can be applied to. The 1D anisotropic XY-model with a transverse field is inherently entangled. This has recently reignited interest in 1D spin chains, making them accessible models to identify and quantify entanglement. This forms the basis of the research conducted in this project.

3.1.1 The Factorisation Field

Quantum spin chains have have a very unusual ground state feature, called factorisation, as described by Kurmann, Thomas and Muller in 1982 in their paper 'Antiferromagnetic Long-Range Order in the Anisotropic Quantum Spin Chain' [18]. The spin chains with a non-zero applied field have two phases; an antiferromagnetically ordered phase with long-range order (LRO); and after some critical field value a ferromagnetic phase aligned with the field. LRO means that the correlations between any pairs of spins proliferate the whole sample, with any pair of spins regardless of distance apart, having a non-zero correlation (this is described in more detail in Chapter 5). Within the ground state of the ordered phase the correlation functions are effected by quantum fluctuations only except at one particular value of the field that forcing the system into a semi-classical state and effectively neutralising all quantum fluctuations. At this point, at the factorisation field, the system is a 'classically' ordered antiferromagnetic chain with the signature of a completely flat correlation function for its absolute value.

The ground state for the thermodynamic limit of the spin chains is known to be doubly degenerate [71] [72] [10] for the ordered phase, up to the critical field. Below the factorisation field the system is anti-parallel entangled and above it, parallel entangled. Exactly at factorisation the system has zero entanglement and the degenerate states become separable.

The factorisation field is dependent on the anisotropy of the system, for the XYZ-model given by Eq. 3.5 it is dependent on the three directions and their different strength of interactions; where the interaction in the x direction is $J_x = J(1+\gamma)$; the interaction in the y direction is $J_y = J(1-\gamma)$; and the interaction in the z direction is $J_z = J\Delta$.

The general formula for the factorisation field to obey is, from Kurmann *et al.* [18];

$$\frac{h_x^2}{(J_x+J_y)(J_x+J_z)}+\frac{h_y^2}{(J_x+J_y)(J_y+J_z)}+\frac{h_z^2}{(J_x+J_z)(J_y+J_z)}=1. \tag{3.7}$$

This describes an ellipsoidal surface for the factorisation field that can be easily simplified for the different Hamiltonians used in this thesis. For both the anisotropic XY-model and XYZ-model there is only a field in the z direction thus $h_x = 0$ and $h_y = 0$. For the anisotropic XY-model there is also no interaction in the z direction, thus $J_z = 0$, therefor the factorisation field h_f for the anisotropic XY-model is;

$$h_f = \sqrt{1-\gamma^2}, \tag{3.8}$$

and for the XYZ-model is;

$$h_f = \sqrt{(1+\Delta)^2-\gamma^2}, \tag{3.9}$$

using the notation for the anisotropy parameters used in the Hamiltonians, and where the field is in units of J.

The factorisation field always occurs in the ordered phase, thus it is always less than or equal to the critical field: $h_f \leq h_c$. For the anisotropic XY-model the critical field is $h_c = 1$, for the isotropic model where $\gamma = 0$ then $h_f = h_c = 1$ the two field values over lap and there is no entanglement transition, as there is no entanglement recovered in the ferromagnetic phase for $h > 1$ [2]. By choosing a material that coincides with suitable value of the anisotropy γ then the entanglement transition can be tuned away from the critical field and any region of criticality that might interfere with the entanglement transition.

The factorisation field is described in more detail in subsequent chapters in regards to finite-sized systems and how to detect its effects. Chapter 4 solves for a dimer the requirements for a factorised state, where for the anisotropic XY-model it is shown to be the same as Eq. 3.8 and further details the phenomenon in terms on the energy spectra of the model and the eigen states involved [16] [17] [58] [59] [56]. Chapter 5 expands on this for larger finite-sized calculations; commenting on the effects of system size; discussing the importance of degeneracy in the ground state; proving the conditions for factorisation in an $N = 4$ system; and using the correlation functions to detect the effects of factorisation on larger finite-sized systems.

3.2 Theory

The previous section introduced the models and variants used in this thesis, focusing on the anisotropic XY-model for antiferromagnetic spin chains. This section discusses the methods used to solve them.

The majority of the literature study some variation of the XY-model in the thermodynamic limit [61] [56] [58] [59] [62] [63] [64] [65] [66] [67] [68] [69], with some using finite-sized system calculations with periodic boundary conditions [9] [12]. These finite-sized models open up a wider range of materials to examine, all with different benefits and difficulties. This project explores a variety of the finite-sized systems, by exact diagonalisation of the Hamiltonian with the addition of the XYZ-model, which can not be solved exactly in the thermodynamic limit. The model is flexible enough to explore open and periodic boundary condition effects for a range of small systems that can provide insight into the thermodynamic limit. An appealing benefit of using finite-sized calculations with periodic boundary conditions is that it may be used to solve a selection of generalised molecular magnets [73] [74] [75] [29].

Using exact diagonalisation to solve for finite-sized systems has a lot of benefits; the solutions are exact and provide the full breadth of eigen vectors and associated eigen values; with these it is possible to accurately calculate thermal properties using the Boltzmann distribution; and for very small systems it is possible to study the relevant states directly, which is put to great use in Chapters 4 and 5. The only disadvantage is that the Hilbert space of the Hamiltonians scales with 2^N meaning that the computational limit for exact diagonalsation is met for systems around $N = 12$. This thesis explores system sizes up to $N = 10$ consistently, with $N = 12$ calculations used sparingly to emphasis an argument, or feature tending towards the thermodynamic limit.

This project focuses on finite-sized calculations with some commentary on the thermodynamic limit. There are a few key papers that document the anisotropic XY-model in the thermodynamic limit using complex analytical methods to solve it exactly. Lieb, Shultz and Mattis focused on the anisotropic model, stating that the isotropic model has no long range order (LRO) [71]. They use the correlation functions to probe the ordered phase. The correlation functions are;

$$\rho^{\alpha\beta}_{j,j'} = \langle\psi_0|\hat{S}^{\alpha}_{j}\hat{S}^{\beta}_{j'}|\psi_0\rangle. \tag{3.10}$$

The correlation operator gives the expectation value of the correlation between any two components $\alpha, \beta = x, y, z$ of the spins at two sites (j and j') separated by any distance in a known state $|\psi_0\rangle$. For a system in the thermodynamic limit, Leib 1961 uses Wicks Theorem from quantum field theory to form the following results, which are quoted here without proof. This process was then developed further by Pfeuty 1971 [72] and Barouch and McCoy 1971 [10] separately, with variation to the model. Pfeuty 1970 takes the 1D Ising Model with an additional term in the Hamiltonian for a transverse external field. Barouch and McCoy also use an external transverse field but keep the model more general by allowing for in-plane anisotropic interactions. Thus the Barouch McCoy paper studies the Hamiltonian given by Eq.3.6, which is the bench mark for the collaboration .The two point correlation functions developed in these papers are given below for correlations in xx, yy and zz respectively;

$$\rho_{xx}(R) = \frac{1}{4}\begin{vmatrix} G_{-1} & G_{-2} & \cdots & G_{-R} \\ G_0 & G_{-1} & \cdots & G_{-R+1} \\ \vdots & \vdots & \ddots & \vdots \\ G_{R-2} & G_{R-3} & \cdots & G_{-1} \end{vmatrix}, \tag{3.11}$$

$$\rho_{yy}(R) = \frac{1}{4}\begin{vmatrix} G_{1} & G_{0} & \cdots & G_{-R+2} \\ G_2 & G_{1} & \cdots & G_{-R+3} \\ \vdots & \vdots & \ddots & \vdots \\ G_{R} & G_{R-1} & \cdots & G_{1} \end{vmatrix}, \tag{3.12}$$

$$\rho_{zz}(R) = h_z^2 - \frac{1}{4}G_R G_{-R}. \tag{3.13}$$

The parameter R is the distance between any pair of spins at two sites j and j' so that $R = |j - j'|$. The function G_R is defined as;

$$G_R = \int_0^{\pi} d\phi \frac{\tanh\left(\beta\omega_\phi\right)}{2\pi\omega_\phi}\left[\cos\left(R\phi\right)(1 + h_z\cos\phi) - h_z\gamma\sin\left(R\phi\right)\sin\phi\right], \tag{3.14}$$

where $\beta = 1/T$ is the inverse temperature and the function ω_ϕ defined as;

$$\omega_\phi = \frac{1}{2}\sqrt{(h_z\gamma\sin\phi)^2 + (1 + h_z\cos\phi)^2}. \tag{3.15}$$

Any results presented in this thesis regarding the anisotropic XY-model in the thermodynamic limit were obtained using the above formulae [71] [72] [10], with codes written within the collaboration by Jorge Quintanilla with assistance from Luigi Amico, with careful consideration taken to ensure all results converge.

3.3 Materials

This section provides a literature review on the different types of materials that relate to the Hamiltonians from section 3.1 and their theoretical results. Attention is given to the energy spectra of these models and and level crossings observed in finite-sized systems and and theoretical measures of entanglement. The link between level crossings degeneracy and the requirement for factorisation is found in Chapter 4 for the dimer and discussed in more detail in Chapter 5 for other finite-sized systems.

The dimer model ($N = 2$) on its own, even when used as a toy model, has been instrumental in unlocking the core mechanisms behind the entanglement transition [76] [77] [78] [79] [2]. It is a great indicator that investigation of finite-sized systems may aid in identifying the entanglement transition in molecular magnets using neutron scattering experiments. In addition, the dimer model is well-represented by two linked molecules representing a spin-$\frac{1}{2}$ each.

More recent reports demonstrate that exploitation of these molecular spin clusters may be used as a resource for exploring quantum magnetic phenomena like entanglement [2]. The benefit of small molecular systems is that they allow for tailored coupling in a collection of synthesised materials. In particular, antiferromagnetic rings have proven useful in quantum information processes [74] [80]. Candini (2010) *et al.* explore an effective dimer system synthesised as two connected rings of Cr_7Ni. Each ring is approximated as a $S = 1/2$ molecule. The two molecules are antiferromagnetically interacting with one another through a superexchange in the joining ligand as shown in Fig. 3.2.

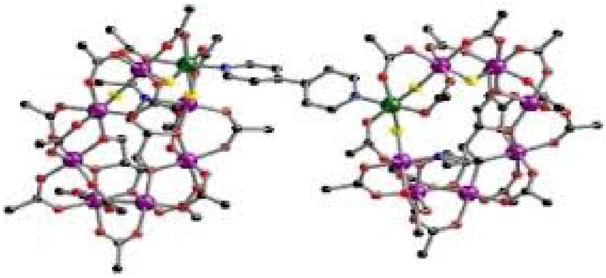

FIGURE 3.2: The bipy-dimer structure from two Cr_7Ni rings. Cr ions are in purple and Ni ions are in green. The remaining colours are non magnetic particles that do not contribute to the overall spin From Candini (2010) [2].

The system behaves like a dimer and undergoes a ground state crossing by a lowering of one of the triplet states crossing the singlet state. The energy levels and state structures for a dimer are discussed in greater detail in chapter 4. They are integral in explaining underlying magnetic behaviour in quantum spin clusters using quantum entangled states [81] and are commonly used as a starting point for analysing entangled states in spin systems [64] [82].

Entanglement can be theoretically detected using concurrence to quantify entanglement on a scale between 1 (for maximally entangled states) and 0 (for a completely separable state) see Chapter 2 section 2.2 and for a calculated example for the dimer see Chapter 4 section 4.4. Candini (2010) *et al.*. predict this in an experimentally accessible range as an effect detectable at 50mK. It can be observed from Fig. 3.3 that as the temperature tends to zero, the change in concurrence becomes a transition between a maximally entangled state from the singlet ground state, to a factorisable state with zero concurrence.

Concurrence is applied to finite-sized chain systems with periodic boundary condition by Rossignoli (2008,2009) using spin-$\frac{1}{2}$ anisotropic XYZ Heisenberg chains in a applied field for different types of interactions [83] [3]. They explore systems of $N = 10$ and 50 qubits in their ground state, and describe a transition in parity between entangled anti-parallel and parallel states that occurs over the factorisation field. The concurrence is not sensitive to the type of entanglement and it is through an analysis of the parity that the difference in the states above and below transition can be ascertained.

A key conclusion of the above paper is that at sufficiently low temperatures $kT = 5 \times 10^{-4} J_x$, where the thermal concurrence goes to zero. Fig. 3.4 from Rossignoli *et*

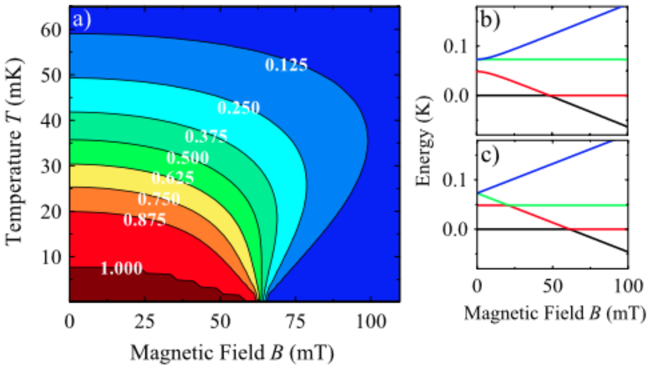

FIGURE 3.3: a) is the thermal Concurrence calculated for the (Cr$_7$Ni)$_2$-dimer model for a range of temperatures and external magnetic field in the z-direction **B**. The dark red region describes a state that is maximally entangled (in this example it is the maximally entangled singlet state) and the dark blue region represents a pure state with zero concurrence. b) shows the molecular dimer energy spectrum and a level crossing for field parallel to x and c) parallel to z. The level crossing coincides with the change from an entangled state to a pure one. From Candini *et al.* (2010-Figure 4). [2]

al.. shows the concurrence for a cyclic chain of 50 sites for $T = 0$ (dotted lines) and $kT = 5 \times 10^{4-} J_x$ (filled lines). At zero temperature there is a break in the concurrence at the factorisation field as the amount of entanglement from one state is given below the transition, and amount of entanglement for another state is taken past the transition.

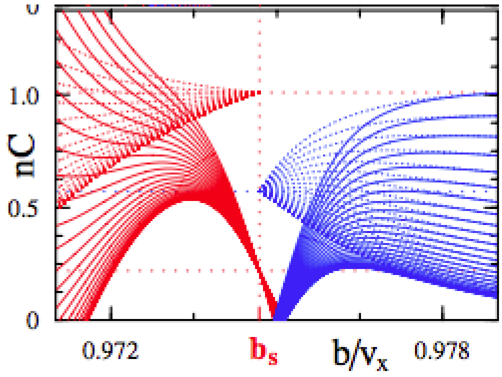

FIGURE 3.4: The concurrence and thermal concurrence (nC for a scaled concurrence)for the periodic XYZ-model for 50 spins. The red lines represent the antiparallel entangled state and the blue lines are parallel entangled states. The dashed lines are for the zero temperature calculations and the filled lines are for $kT = 5 \times 10^{-4} J_x$, where in this paper $V_x = J_x$ the interaction energy in x . The factorisation field for this model (h_f) in this paper is called b_s. The ground state concurrence shows a break in concurrence at the factorisation field, where the entanglement is quantified for the antiparallel state and then suddenly for the parallel state. At low finite temperature, a mixing in the states allows for the entanglement to go to zero, though there is a slight shift away from the exact factorisation field. From Rossignoli *et al.*. (2014-Figure 4) [3].

This measure is more physical when the thermal concurrence is calculated and the concurrence at the factorisation field goes to zero at sufficiently low temperatures. Concurrence is a suitable tool for a range of models both infinite and finite-sized to quantify entanglement. To fully understand the nature of entanglement, a more in depth analysis in conjunction with concurrence is recommended.

For other finite-sized systems, we explore more complex configurations, like ring structures and can identify any entangled states and interesting ground state features in the energy spectrum. Lorusso *et al.* explore three CrCu based ring configurations where they focus on the effect the copper ions have as a magnetic defect in the rings. The copper has a different spin value than the chromium and gives an additional inhomogeneity favouring ferromagnetic coupling. The paper looks at how these concepts affect the entanglement in the different ring systems. The ring structures and energy spectra are shown in Fig. 3.5a and 3.5b.

The energy spectra of two of the molecules, Cr_8Cu and $Cr_{12}Cu_2$, are shown for an externally applied field ranging from 0T to 7T, which was suitable for their purposes. In relation to the entanglement transition, to select these molecules as viable candidates we would need to go to higher fields to observe a level crossing between the two lowest states as discuses in Chapters 4 and 5. The spectra diagrams do not show a crossing, though it is easily deduced that the energy of one of the excited states is rapidly lowered with the external field and would cross the previous ground state at a higher value of the field.

The field value required for a crossing, though comparatively high, is not unobtainable for these materials. With or without the additional copper ions, the chromium rings are well studied and various different sizes of rings would give an interesting family of compounds to explore entanglement, and the entanglement transition. An array of possible models that exhibit a factorisation field form a sensible beginning for the project's exploration for a detectable entanglement transition. They give, in turn, a range of potential materials that would give real experimental impact to the field.

In recent years, Siloi and Troiani have thoroughly explored the entanglement in a family of Cr_8 molecular nanomagnets [29] [30] [4], and the flexibility that these structures bring to the task of detecting entanglement. They use an entanglement witness that, like concurrence, originates from the reduced density matrix called Negativity. They

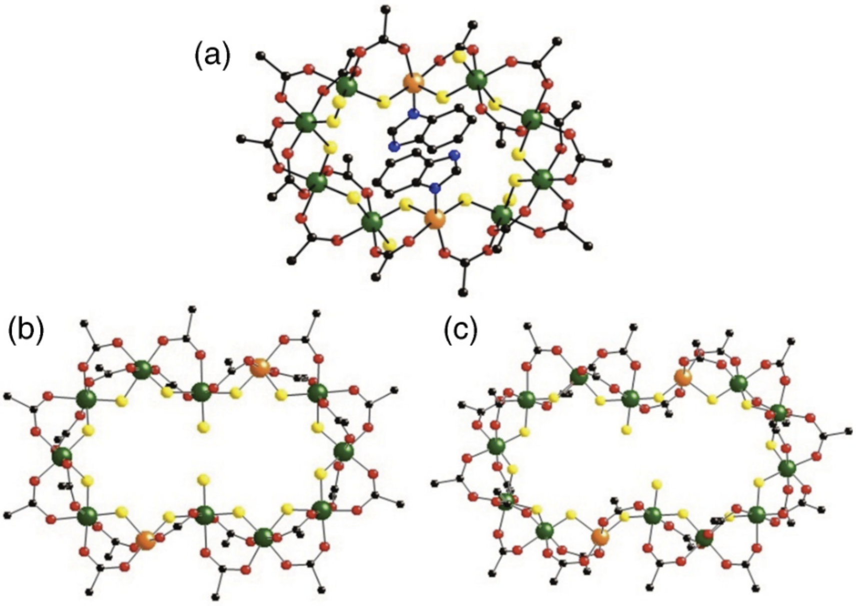

(A) From Lorusso *et al.*. Figure 1 and 4. left) is a selection of structures for the three CrCu ring configurations that Lorusso explore. Green: Cr and Orange: Cu. right) The low level energy spectra for Cr_8Cu_2 and $Cr_{12}Cu_2$ [28].

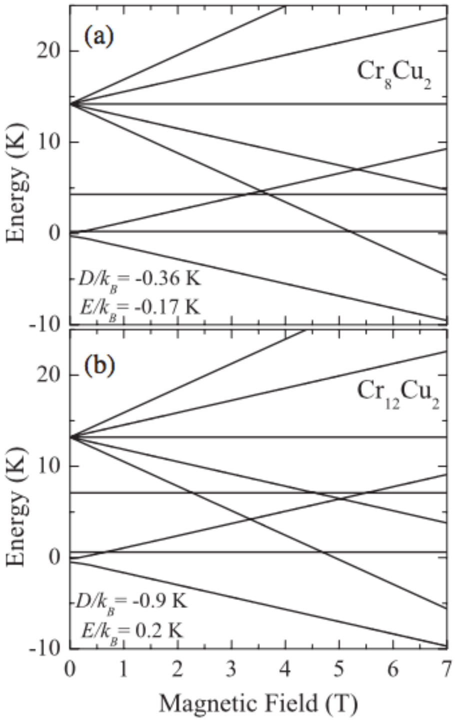

(B) For the range of applied field given there is no level crossing in the ground state for either molecule. If the field was increased further it would be expected that one of the excited states would cross the ground state [28].

use Negativity as a method of theoretically quantifying entanglement and they give a threshold temperature range in which the quantity can be detected.

For a pure Cr_8 ring the energy gap is given as $\Delta = 0.559J$. That in turn gives a threshold temperature of $T = 1.58J$. Silio *et al.* addresses two main variants of the Cr_8 rings; firstly they take the ring in reference to their individual spins whilst exchanging the eighth ion for a range of different ions with varying spin vales; secondly they take the molecule as a whole and link two together as a dimer through a super exchange as also seen in Candini *et al.* [29] [30] [4] [2]. By exchanging a chromium ion with various other magnetic ions they are able to change the entanglement in the system in a way that would be chemically tunable. What they find is that the neighbouring ions to the magnetic defect acquire a stronger entangled state as an entangled pair with the defect. If the defect has a larger spin value than the chromium i.e $S_{Cr} = 3/2$ then the entanglement is increased. If the spin of the defect ion was less than 3/2 then the opposite would occur and the neighbouring pairs would become less entangled. This principle is demonstrated in Fig. 3.6.

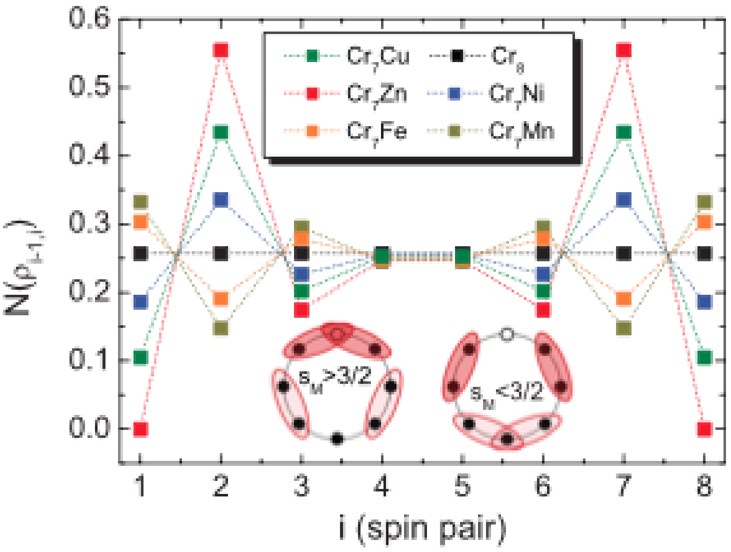

Figure 3.6: Using Negativity to quantify entanglement, Silio *et al.* show the amount of entanglement experienced by nearest neighbour pairs in a family of 8-spin chromium rings doped by different metals with different spin values. If the dopant ion has a spin value greater than chromium i.e 3/2, then the entanglement around that ion increases. If it is less than $S = 3/2$ then the amount of entanglement around the ion decreases, as indicated diagrammatically. From Siloi *et al.* Figure 2 [4].

The figure describes the amount of entanglement in each neighbouring pair of spins in the family of chromium rings. The eighth ion is replaced by a different magnetic ion with a different spin that affects the entanglement of its neighbouring interacting spins. The black boxes provide a reference as the pure chromium ring and the plots show that with a higher spin value i.e zinc, the entanglement between the zinc and the chromium is increased and for an ion like manganese the opposite is observed. The effect of this on the entangled pairs is shown diagrammatically in the figure inset. This reflects the tunability and flexibility of these molecules when studying entanglement with the additional advantages of a large energy gap and temperature spectrum.

The last part of the paper describes the rings as whole spin clusters acting together as a dimer. The advantages of a maximally entangled state composed of the ring dimer can show factorisation, with an entanglement witness like Negativity going to zero. It is not a concept that is fully elaborated upon but strengthens the idea that these clustered materials would be ideal to physically detect the entanglement transition through neutron scattering experiments.

3.4 Experiments

The previous section detailed some of the underlying theoretical concepts that help to identify a suitable candidate system to explore further to predict experimental results. In this section we look at the effects of some of these concepts and models have in experiments documented in the literature, outlining a range of different types of materials. Such as, the effect of level crossing in the measured magnetisation [7], or the neutron scattering cross section for chromium rings. Firstly, we discuss experiments on a material that closely matches the anisotropic XY-model for Eq. 3.6, looking at 1D crystals for the infinite system model. Then discussing a selection or interesting dimer materials and some clustered quantum nano-magnets. Where possible, we remark on temperature scales, applied field ranges of factorisation and other relevant factors or complications that the theoretical models do not consider, as to provide a commentary on their respective suitability for experimentation.

3.4.1 1D Crystals

A material of interest for our collaboration was Cs_2CoCl_4 as a good candidate for preliminary experiments. The material is an approximation of the anisotropic XY-model with the anisotropy equated to $\gamma = 0.2$. Algra *et al.* describe its complex structure and how it relates to the 1D XY-model [5]. The study investigates the specific heat capacity of Cs_2CoCl_4 under 1K experimentally, and compares it to predictions using the XY-model while discussing the applicability of the theory under specific parameters. The crystal structure is orthorhombic K_2SO_4 with the lattice parameters $a_0 = 9.74\text{Å}$,$b_0 = 7.39\text{Å}$ and $c_0 = 12.97\text{Å}$.

The cobalt ions provide the basis to understanding the magnetic structure and are surrounded by tetrahedra of chlorine ions. These tetrahedra are slightly distorted, which leads to a splitting of the $S = 3/2$ orbital. This leaves the system occupying $S = 1/2$ states with a sufficient energy gap of 1.3(1)eV that allows the model to be a good approximation. It is not clear from the physical structure alone where the 1D magnetic structure forms; the magnetic chains are represented by a superexchange between Co ions through neighbouring Cl ions.

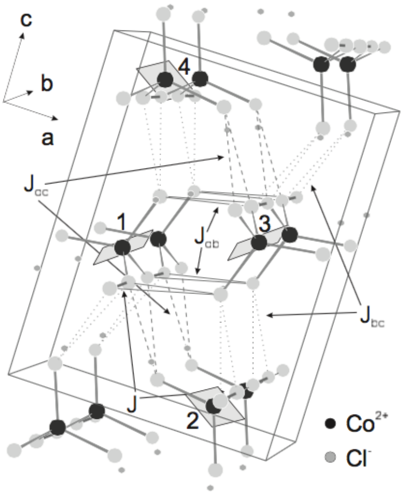

(A) The crystal structure of Cs_2CoCl_4. The black ions represent the Co^{2+} spheres and the grey spheres show the structure of the distorted Cl tetrahedra. The chains formed by the magnetic interactions are directed along the *b*-axis. On four of the Co^{2+} ions are shaded angular planes showing the orientations of the *xy* easy plane. The inter-chain interactions are depicted with different dashed lines. From Kenzelmann *et al.*. (2002-Figure 2) [60].

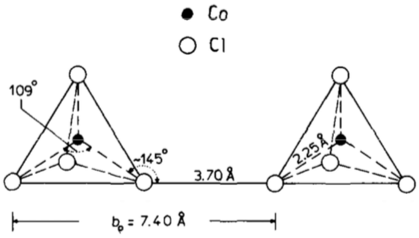

(B) The superexchange path between two Co^{2+} through their Cl tetrahedra forming an interaction along the *b*-axis. From Algra (1976- Figure 2).

FIGURE 3.7: The crystallographic structure and the 1D magnetic structure of Cs_2CoCl_4 [5].

The 1D magnetism arises from a superexchange interaction between the cobalt ions along the *b*-axis as depicted in Fig.3.7b from Algra *et al.*; the resulting exchange leads to antiferromagnetic 1D chains. Fig. 3.7a shows a selection of these chains within the crystal lattice, where angular grey planes indicate the orientations of the easy xy plane. The chains couple weakly with each other, drawn as dashed lines for J_{ab} and J_{ac}. In a certain temperature range these interactions are negligible until the system passes below 222mK and transitions into a 3D ordered phase. Below this temperature the energy scale of the inter-chain interactions is comparable to the temperature scale, and the 1D XY-model is no longer an option for describing the system.

The chains cant with respect to each other with two different easy plane orientations, the consequences being some small frustration is added to the system and an added difficulty in applying a transverse field to both xy planes. Kenzelmann (2002) *et al.*. did not apply a transverse field to both sets of chains, instead having to compromise between them.

The crystal Cs_2CoCl_4 represents the anisotropic 1D XY-model sufficiently for temperature states above 222mK, where the energy scale and gap allow for a $S = 1/2$ spin regime. The magnetic chains form along the b-axis, and in relation to the Hamiltonian the anisotropy of the crystal is equivalent to $\gamma = 0.2$. The anisotropy in the system tunes the entanglement transition away from the critical field, i.e. for $\gamma = 0.2$ the factorisation field is approximately $h_f = 0.98h_c$.

The material has shown that the model is very sensitive towards perturbations that take it out of the 1D regime and the temperature scale to find this quantum phenomenon is very important. Kenzelmann *et al* gives the exchange coupling $J = 0.23 \pm 0.01$ meV which gives a maximum temperature scale of 2.7K, the transition at 222mK, would thus equate to approximately 8% of the exchange coupling. In terms of relating this to the theory, where the temperature scale is set dependent to the exchange coupling J, then a calculation done for $T = 0.1J$ would be a real temperature of 260 ± 15mK in an experiment. These experimental conditions are taken under consideration with all temperature calculations. Theory and experiment agree that this is not a sufficient balance of external parameters to find the entanglement transition.

3.4.2 Dimer Materials

The dimer model is an extremely useful origin for understanding theoretical concepts as it is easy to solve and break down to its component states [77] [76]. It is more than just a toy model and can be applied to more complex models and systems including structures made of dimers [41] [78] [79], cluster systems that approximate a dimer [2] [77] and a dimerised 1D chain of spins [84] [85].

Section 3.3 introduced one of the models that uses concurrence to quantify entanglement Candini (2010), which approximates a spin 1/2 dimer made up of two connected Cr_7Ni rings. This molecular dimer magnet is called a $(Cr_7Ni)_2$-bipy dimer and is shown in Fig.3.2.

The bipy-dimer would be a good candidate in terms of the entanglement as a dimer model exhibits a maximally entangled anti-parallel state and results are calculated for concurrence at 50mK and 55mT for the transition which could be achieved experimentally. To fully assess a bipy-dimer, as to its suitability to detect the entanglement transition in an experiment further work would be needed to construct some theoretical neutron scattering data. For our definition of the entanglement transition (see section 2.4) the states above and below the factorisation field need to be entangled and for the isotropic XY-model, represented by the bipy-dimer, this is not the case. If it is possible to adjust or dope the molecular rings that make up the dimer to exhibit some anisotropy in the xy plane then I believe it would be feasible to detect the entanglement transition using this basis, as explored in Chapter 4.

Dimers can turn up in a range of materials. Belik *et al.* 2007 discuss magnetic susceptibility in copper based materials that have many possible structures [77]. They describe a $Cu_2O_6(OH)_2$ crystal that is made up of edge sharing dimers and form a chain structure. The spin gap of this system is given as 139K, which would allow the entangled singlet of the dimer to dominate behaviour. Although they measure magnetisation for a wide range of fields $(0 - 30\text{T})$, there is not enough information to assess any change of spin state that would support an entanglement transition. However, these type of complex dimer materials that contain additional structures could warrant further study with respect to entanglement measures and their possible detection by measuring neutron scattering cross sections [79].

3.4.3 Molecular Magnets

Clustered quantum materials offer an exciting platform for many research areas. Recently some groups have emerged that are looking at the entanglement present in these molecules [73] [28] [29] [30] [4]. There are also many publications on magnetic molecules that discuss their energy spectrum and step features in their magnetisation that could be indicative of a change in entanglement [86] [8] [87] [6] [88] [7] [89] [75]. Any of these materials could become the ideal candidate to physically detect the entanglement transition in a real material with additional analysis of the theoretical models .

A review article in the Chemical Society Review by Timco, McInnes and Winpenny in 2013 provides information on the process of synthesising and studying heterometallic rings [6]. They outline the synthesis of Chromium based rings with the flexibility of replacing chromium ions with other magnetic impurities. The current methods allow for an impressive range of possible ring structures, constructing large single crystals of rings using 8, 10 or 12 magnetic ions per ring.

The review discusses a few of the different compounds that switch one chromium ion with other magnetic ions, with the reasoning that the Cr rings "give rich well-resolved EPR (electron paramagnetic resonance) spectra" [6]. They use this with other techniques, including inelastic neutron scattering (INS) and magnetic susceptibility experiments to identify the energies of the spin states involved in this family of materials.

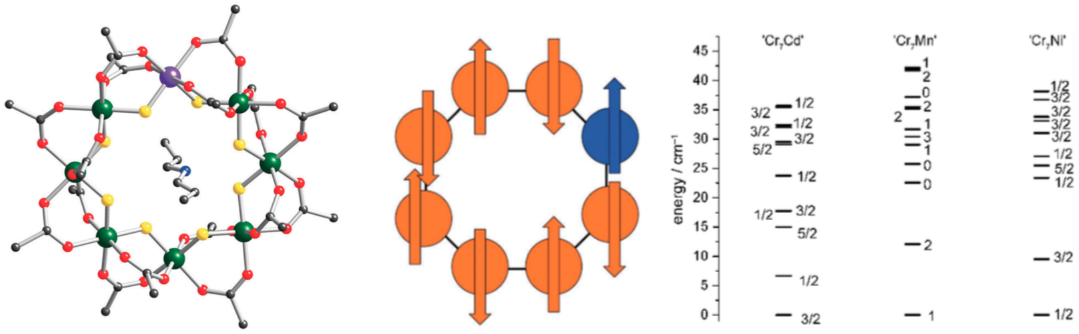

FIGURE 3.8: a) The structure of a 8 spin chromium ring with an ion swapped. Green: Cr, Purple: dopant, Red: O, Yellow: F, Blue: N and Black: C. b) shows the antiferromagnetic scheme of the ring in the case where the exchanged ion also supports antiferromagnetic interactions. c) The spin ladders for Cr_7Cd, Cr_7Mn and Cr_7Ni; the spin values for the ground states and the available excited states are labelled. This is generated using two J_{CrCu} exchange interactions; one anti-ferromagnetic (-12 cm^{-1}); and one ferromagnetic ($+6.5$cm^{-1}) From Timco *et al.*. Figure 1 and 2. [6].

The coloured molecule in Fig. 3.8 shows a general schematic for the family of rings studied. The green balls represent the chromium ions and the purple ball shows the replaced ion, which were Ni, Co, Mn, Zn, Cd and Mg. The pure chromium ring consists of antiferromagnetically-interacting spins in an octagon arrangement; the additional atoms do not contribute to the magnetic structure. The listed magnetic ions that the purple ball represents are also in favour of antiferromagnetic interactions, as indicated by the schematic in Fig. 3.8. It is also possible to dope the rings with an ion that favours ferromagnetic interactions such as copper [7]..

Using a variety of techniques including INS they are able to take the molecule as a whole macroscopic system and determine the spin and energy of the ground state and lowest excited states. These are shown as a 'spin ladder' in Fig. 3.8 for Cr_7Cd, Cr_7Mn and Cr_7Ni respectively. This is a fairly simple approach and for some of the dopants it is not effective to consider the system as a whole but instead to use a microscopic Hamiltonian, which considers the individual spins, as in the XY-model. This has its computational restrictions that puts a cap on the size of molecule that can be solved using exact diagonalisation based on our full spectrum diagonalisation studies. This makes an 8-spin system viable, a 12-spin system extremely time consuming and anything greater impractical or impossible on a work station.

Engelhardt *et al.* use quantum Monte Carlo (QMC) methods applied to a 12-spin chromium ring with two chromium ions replaced with copper on sites 6 and 12 [7]. They use a microscopic isotropic Heisenberg Hamiltonian that considers the nearest neighbour interactions with cross term interactions. They compare QMC results with experimental methods looking at magnetic susceptibility and magnetisation, using them to probe the existence of state level crossings with the energy spectrum.

The peaks observed in the magnetic susceptibility that are labelled in the green inset as 2.35T, 5.31T and 13.32T match up with the calculated level crossings in the ground state indicated by black blocked in arrows in Fig. 3.9. Other level crossings within the low level excited states are indicated with empty arrows. These crossings are visible experimentally at low temperatures, which gives a good thermal occupation of the states involved in the crossings only. For finite-sized molecules, using magnetic susceptibility and observing 'steps' in the magnetisation is a viable option for experimentally measuring level crossing features in the energy spectrum.

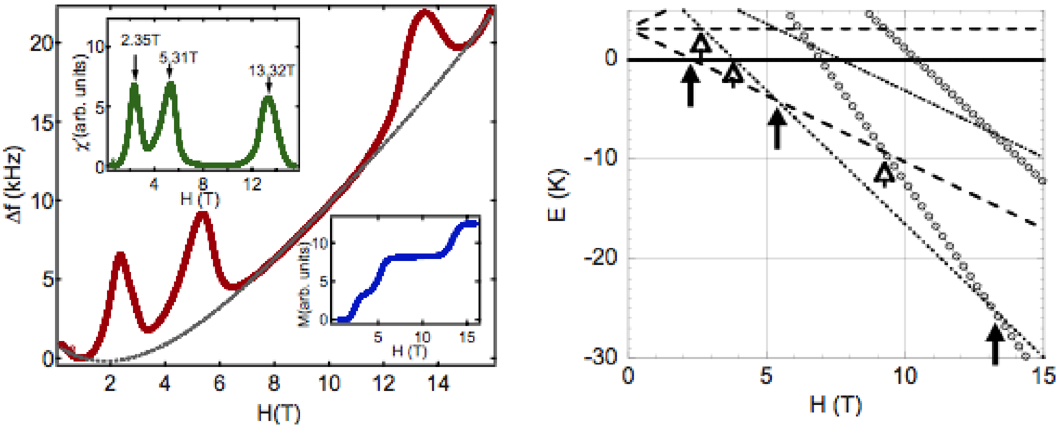

FIGURE 3.9: Figure 4 and 6. a) Data from magnetic susceptibility experiments showing peaks at 2.35T, 5.31T and 13.32T for $Cr_{10}Cu_2$. The insert in blue shows these peaks as steps in the magnetisation. b) these peaks are a result of level crossings in the ground state indicated by the black arrows. The empty arrows point to level crossings in the excited states that would be detectable at higher temperatures.From Engelhardt *et al.* [7].

If we were to apply a microscopic Hamiltonian (e.g. the anisotropic XY-model) to one of these chromium ring systems, be it a pure ring of any ion or mixed/ doped ring, it is vital to understand how the geometry effects the interactions in the molecule. Some of the systems could be well represented by a 1D chain Hamiltonian with periodic boundary conditions. This allows for a single orientation local axis with anisotropic interaction axes. Other models may have a complex orbital structure where the interaction axes require a different local axes per site. This would require a more complex Hamiltonian that accounts for cross terms in the interactions depending on the angles between axes. Neutron scattering data are calculated for these options are in Chapter 6 with the orientation of the model fully described.

Timco *et al.* considers this option for the case of Cr_7Ni and they look at the energy gap of the system for a range of external fields up to 12T at a low temperature of 66mK. They observe a minimum where the system avoids a level crossing in the ground state at 10.5T, which they describe as what would have been the critical field in this finite system. In Chapter 5 we discuss such level crossings in detail, showing that, rather than corresponding with the critical field they correspond to the factorisation field. They do observe a level crossing within the excited state that affects the size of the gap as shown in Fig. 3.10.

It is clear that this family of chromium ring structures offer a promising opportunity

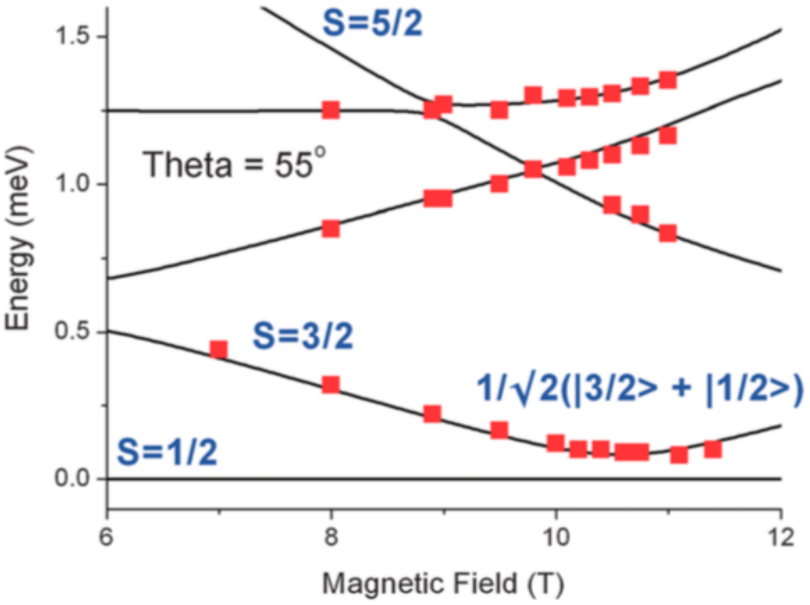

FIGURE 3.10: Part of the energy spectrum for Cr_7Ni ring between 6T and 12T data collected at 66mK using INS transitions, indicating occupation in the low energy levels. From Timco *et al.* [6].

to study the energy spectra and states of small nanomagnets. Consequently this gives insight to the entanglement within these states. These materials are diverse and exciting; the synthesis is well documented, allowing for single crystal samples of many different combinations of ions. They offer an energy gap that would support low temperature experiments. Careful analysis could find materials where experiments would scan over a range of external fields that would feature a level crossing between different spin states. It is also very clear that a careful study of interactions and orbitals would be required to identify what kind of microscopic Hamiltonian would be an acceptable model for the molecule, specifically whether the anisotropic 1D XY-model would be suitable or a more complex Hamiltonian that considers cross term interactions. With this in mind, the validity of the theory connected to modelling small nanomagnets using Eq. 3.6 with periodic boundary is confirmed but the path to finding a suitable physical candidate to match is a task that requires further study into molecular magnets.

INS techniques are vital in probing the entangled low-lying states of these molecular nanomagnets. Using Cr_8 rings as a benchmark for a whole family of suitable ring materials, Baker *et al.* [8] provide the ground work for INS experiments. The techniques require high quality single crystals to be able to identify the unique structure of the rings. Fortunately many of the papers discussed here describe the ring systems' synthesis as extremely tunable and diverse, producing high quality samples [86] [8] [87] [28] [4].

A pure chromium ring is described by the following Hamiltonian [8]

$$\hat{H} = -J\sum_{j=1}^{8}\hat{S}_j\hat{S}_{j+1} + D\sum_{j=i}^{8}\hat{S^z}_j^2. \tag{3.16}$$

With periodic boundary conditions to link site 8 to site 1, $J = 1.46$meV and $D = -0.038$meV with the anisotropy D in the z-axis being perpendicular to the plane of the molecule. Baker *et al.* explore the ground state and higher energy states using INS and compare with a simulation built from the neutron scattering cross section, which projects the correlations between sites into reciprocal space. These results are presented in Fig. 3.11.

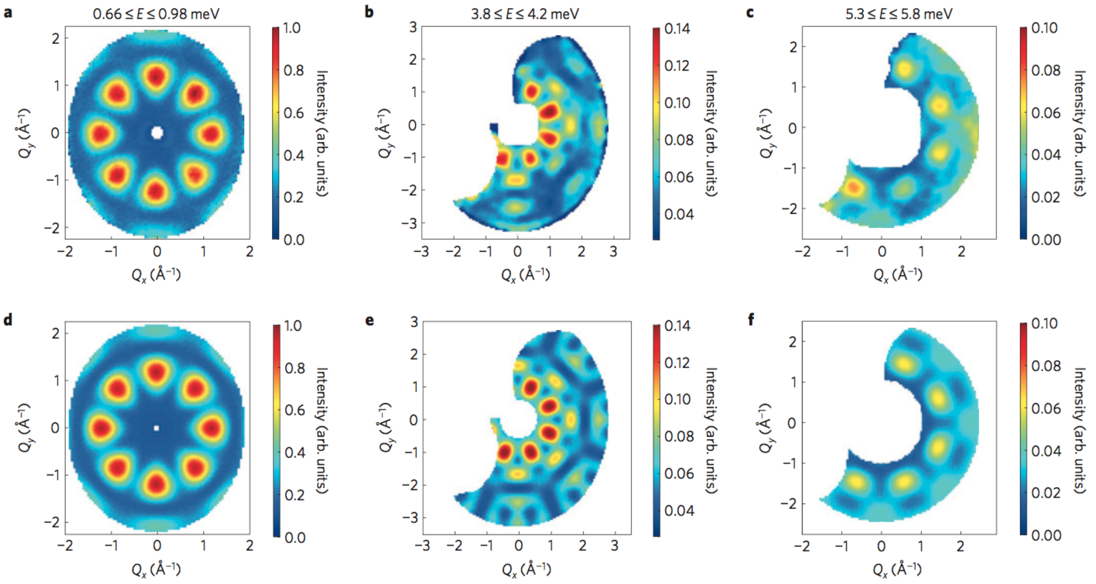

FIGURE 3.11: (a)-(c) INS data for a Cr_8 ring for a range of energies showing different magnetic structure. (d)-(f) simulated data matching the above using the equation for scattering cross section.From Baker *et al.*. Figure 3 [8].

The model and scattering cross section function recreate the data effectively. This validates our intentions to use a simple 1D model with periodic boundary conditions to predict INS data in an experiment that probes the entangled low-energy states in these types of ring configurations. Baker *et al.* do not search for entanglement in the Cr_8, but the entanglement transition signature could be detectable using the scattering function applied to the Hamiltonian shown in eq 3.16. This would be a strong basis on which to put forward a suitable material for experimental purposes.

The chromium rings are a precursor to an abundance of exotic nanomagnets that intrinsically hold interesting entangled states. It is speculated that a compound within this family could be synthesised to have some kind of anisotropy within the xy-plane. It would then be feasible to more directly model a system using the parameters for a specific molecular magnet i.e. the anisotropy value, and the value exchange interaction J, to determine a suitable range of fields and temperatures to experiment with. It would be valuable to see if a similar process could be done with smaller nanomagnets of 4 or 6 spins, in particular with the special case of an $N = 4$ plaquette, where a detailed analysis of the wavefunctions is possible and would greatly enrich the understanding towards an experiment (calculated and documented in Chapter 5 with INS data in Chapter 6).

The above small, clustered materials are the main focus of this thesis, where they have been modelled thoroughly using exact diagonalisation of the Hamiltonian. The systems are small enough to allow for exact diagonalisation despite the large Hilbert space that is involved. The models show promising neutron scattering cross section data, but as of date there are no experimental results to compare with.

It is believed that these nanomagnets or dimer-based materials would be the ideal candidates to experimentally detect the entanglement transition for the first time. This will be applied theoretically over the following chapters

Chapter 4

The Entanglement Transition in a Spin Dimer

The previous chapter outlined the theoretical models explored in this project and their physical counter parts. It is understood that the entanglement transition is found in 1D spin chain systems where the size of the chain is not a factor. It is logical to initiate a study of the entanglement and the entanglement transition with the well-known spin dimer. The spin dimer is much more than a toy model; as discussed in chapter 3, it can directly relate to real materials [2] [28] and is inherently strongly entangled and easily solved. It offers the unique opportunity to understand the mechanism behind the entanglement transition by being able to look directly at the exact entangled states involved.

In this chapter, both analytical and numerical methods are used to solve the dimer model for a factorised state. The XY-model is an ideal simplification of the general spin chain model to start with, as it is well documented in the thermodynamic limit [71] [72] [10] [18] and it is useful to consider this comparison. In addition, the study expands into the XYZ-model to demonstrate the similarities in the models whilst taking advantage of the flexibility of the dimer.

4.1 Wavefunction Derivation of a Factorised Dimer

Chapter 3 introduced the factorisation field in section 3.1.1 as the key to understanding the entanglement transition. It was identified that the factorisation field in 1D spin chains is the driving mechanism underlying the entanglement transition [16]. In the thermodynamic limit this accounts for a certain field value that causes the two-fold degenerate ground state to become semi-classical and exhibit a 'flatness' in the correlation functions in the ordered phase. At this point the system is no longer quantum mechanical and can not be entangled in any way; above and below this point the system is entangled and the act of passing through the factorisation field changes the type of the entanglement [3]. Kurmann et al. assumes a factorised wavefunction for a general 1D anitferromagnetic spin chain and derives an ellipsoidal function of a general field that describes the factorisation field [18].

The Hamiltonian for a general 1D spin chain with an applied field is given in Eq. 3.5 with the anisotropy parameters given as γ and Δ. The Hamiltonian is general and allows for the applied field to point in any direction in a basis that is related to the interaction axis. The factorisation field h_f is addressed as a ground state property that turns the degenerate ground state in the thermodynamic limit into a separable state that can not be entangled, but is classically antiferromagnetically ordered. More explicitly, Kurmann says "it [the ground state] factorises into single-site states exhibiting the same expectation values $\langle S_i^\alpha \rangle$ as the classical two-sublattice Neel-type state with the spins of the two sublattices being in a spin-flop configuration within the XY plane."[18]. Both above and below this field value the system shows correlator effects from quantum fluctuations. The formula for the factorisation field is given in the previous chapter in Eq. 3.7. Where the anisotropy parameters are as follows; $J_x = J(1+\gamma)$, $J_y = J(1-\gamma)$ and $J_z = J\Delta$. The factorisation field for the anisotropic XY-model is given in Eq. 3.8 and the XYZ-model given in Eq. 3.9, where h_f is in terms of the interaction energy J for both cases.

It is possible to explicitly derive Eq. 3.8 for the anisotropic XY-model using the same methods as Kurmann *et al.* for the two site model, showing no N-dependence for the factorisation field in finite-sized systems. We start by writing the general Hamiltonian from Eq. 3.5 for a 2-site model with periodic boundary conditions [18];

$$H = \sum_{\alpha=x,y,z} J_\alpha \hat{S}_1^\alpha \hat{S}_2^\alpha + J_\alpha \hat{S}_2^\alpha \hat{S}_1^\alpha - h_\alpha \hat{S}_1^\alpha - h_\alpha \hat{S}_2^\alpha . \tag{4.1}$$

This has the basis as $\{|\uparrow\uparrow\rangle\ , |\uparrow\downarrow\rangle\ , |\downarrow\uparrow\rangle\ , |\downarrow\downarrow\rangle\}$ for the dimer. In this basis we write a known separable antiferromagnetic state for two sites in the form;

$$|\Psi\rangle = |\psi_1\rangle |\psi_2\rangle = (a_1 |\uparrow\rangle + b_1 |\downarrow\rangle) \otimes (a_2 |\uparrow\rangle + b_2 |\downarrow\rangle). \tag{4.2}$$

This can then be applied to the Schrodinger equation such that it is an eigenstate of the Hamiltonian:

$$H |\Psi\rangle = E |\Psi\rangle . \tag{4.3}$$

By substituting the spin operators for their Pauli matrices counterparts; $\hat{S}^\alpha = \frac{\hbar}{2}\sigma^\alpha$; and allowing the Eq. 4.2 act on the appropriate site, the following $H|\Psi\rangle \equiv H|\psi_1\rangle|\psi_2\rangle$ becomes;

$$H |\psi_1\rangle |\psi_2\rangle = \frac{J_\alpha \hbar^2}{4} \sum_{\alpha=x,y,z} (\sigma^\alpha \otimes \mathbb{I}) |\psi_1\rangle (\mathbb{I} \otimes \sigma^\alpha) |\psi_2\rangle - \frac{h_\alpha \hbar}{2} \sum_{\alpha=x,y,z} (\sigma^\alpha \otimes \mathbb{I}) |\psi_1\rangle + (\mathbb{I} \otimes \sigma^\alpha) |\psi_2\rangle , \tag{4.4}$$

where $\mathbb{I}$ is the unity matrix $\left(\begin{smallmatrix} 1 & 0 \\ 0 & 1 \end{smallmatrix}\right)$. By writing Eq. 4.2 in its separate states in vector form, such that;

$$\begin{aligned} |\psi_1\rangle &= a_1 |\uparrow\rangle + b_1 |\downarrow\rangle = \begin{pmatrix} a_1 \\ b_1 \end{pmatrix} \\ |\psi_2\rangle &= a_2 |\uparrow\rangle + b_2 |\downarrow\rangle = \begin{pmatrix} a_2 \\ b_2 \end{pmatrix} , \end{aligned} \tag{4.5}$$

it is possible to expand Eq. 4.4 fully and determine the requirements for each component of the basis ($\{|\uparrow\uparrow\rangle\ , |\uparrow\downarrow\rangle\ , |\downarrow\uparrow\rangle\ , |\downarrow\downarrow\rangle\}$) for a real eigenstate that would factorise the system and find the field, in which that state would occur. These components for the basis can be found when expanding Eq. 4.2 for its more general form $|\Psi\rangle$ and applied to Eq. 4.3;

$$E |\Psi\rangle = E a_1 a_2 |\uparrow\uparrow\rangle + E a_1 b_2 |\uparrow\downarrow\rangle + E b_1 a_2 |\downarrow\uparrow\rangle + E b_1 b_2 |\downarrow\downarrow\rangle . \tag{4.6}$$

Using this and comparing it to the expanded form of Eq. 4.4 then the following equation for each basis component are found;

$$\begin{aligned}
Ea_1a_2\left|\uparrow\uparrow\right\rangle &= \Bigg(\frac{\hbar^2}{2}[(J_x-J_y)b_1b_2+J_za_1a_2]-\frac{\hbar}{2}[(h_1^x-ih_1^y)b_1a_2 \\
&+ (h_2^x-ih_2^y)a_1b_2+(h_1^z+h_2^z)a_1a_2]\Bigg)\left|\uparrow\uparrow\right\rangle, \\
Ea_1b_2\left|\uparrow\downarrow\right\rangle &= \Bigg(\frac{\hbar^2}{2}[(J_x+J_y)b_1a_2-J_za_1b_2]-\frac{\hbar}{2}[(h_1^x-ih_1^y)b_1b_2 \\
&+ (h_2^x+ih_2^y)a_1a_2+(h_1^z-h_2^z)a_1b_2]\Bigg)\left|\uparrow\downarrow\right\rangle, \\
Eb_1a_2\left|\downarrow\uparrow\right\rangle &= \Bigg(\frac{\hbar^2}{2}[(J_x+J_y)a_1b_2-J_zb_1a_2]-\frac{\hbar}{2}[(h_1^x+ih_1^y)a_1a_2 \\
&+ (h_2^x-ih_2^y)b_1b_2-(h_1^z-h_2^z)b_1a_2]\Bigg)\left|\downarrow\uparrow\right\rangle, \\
Eb_1b_2\left|\downarrow\downarrow\right\rangle &= \Bigg(\frac{\hbar^2}{2}[(J_x-J_y)a_1a_2+J_zb_1b_2]-\frac{\hbar}{2}[(h_1^x+ih_1^y)a_1b_2 \\
&+ (h_2^x+ih_2^y)b_1a_2-(h_1^z+h_2^z)b_1b_2]\Bigg)\left|\downarrow\downarrow\right\rangle. \qquad (4.7)
\end{aligned}$$

From here small simplifications can be applied to the system. For the anisotropic XY-model model the field is not staggered and applied in the transverse z so $h_1 = h_2 = h_z$ and $h_x = h_y = 0$. The interactions are simplified too: $J_z = 0$, and as stated above $J_x = J(1+\gamma)$ and $J_y = J(1-\gamma)$. So that the Eqs. 4.7 become;

$$\begin{aligned}
Ea_1a_2 &= \hbar^2\gamma Jb_1b_2-\hbar h_za_1a_2 \\
Ea_1b_2 &= \hbar^2Jb_1a_2 \\
Eb_1a_2 &= \hbar^2Ja_1b_2 \\
Eb_1b_2 &= \hbar^2\gamma Ja_1a_2+\hbar h_zb_1b_2. \qquad (4.8)
\end{aligned}$$

By substituting the J and $\hbar$ terms for $\mathcal{E} = \frac{E}{J\hbar^2}$ and $h_f = \frac{h_z}{J\hbar}$ the four equations become;

$$\begin{aligned}
(\mathcal{E}+h_f)a_1a_2 &= \gamma b_1b_2 \\
\mathcal{E}a_1b_2 &= b_1a_2 \\
\mathcal{E}b_1a_2 &= a_1b_2 \\
(\mathcal{E}-h_f)b_1b_2 &= \gamma a_1a_2. \qquad (4.9)
\end{aligned}$$

These are then solved simultaneously to find that for the anisotropic XY-model the result for the factorisation field is $h_f = \sqrt{1-\gamma^2}$ as shown by Kurmann *et al.* and given in Eq. 3.8 [18]. It has been demonstrated that the factorisation field present in the dimer is quite independent of the size of the system. It is now logical to explore the energy spectra of the dimer models and to explicitly show a factorised state taking advantage of the small Hilbert space of the dimer.

4.2 Energy Spectrum

The energy spectra of the dimer is well known and can be obtained directly by solving the Hamiltonian for two interacting spins [90]. It is useful to explore using different parameters affecting the system, such as the anisotropy and for a transverse field. As previously stated, the Hamiltonian for the general XYZ-model with an applied field is provided in Chapter 3 Eq.3.5, this section details the results for the energy spectra of this Hamiltonian and its anisotropic XY-model counterpart, for $N = 2$.

4.2.1 Anisotropic XY-Model

For the anisotropic XY-model dimer we form the Hamiltonian matrix from Eq. 3.6 by letting $N = 2$. As before, γ is the anisotropy in the easy-plane and Δ is the interaction strength in the z direction, when $\Delta = 0$ we recover the XY-model. The Hamiltonian matrix follows:

$$H_{XY} = \begin{pmatrix} -h_z & 0 & 0 & \gamma \\ 0 & 0 & 1 & 0 \\ 0 & 1 & 0 & 0 \\ \gamma & 0 & 0 & h_z \end{pmatrix} \tag{4.10}$$

This can be solved analytically or numerically for the parameters h_z for the applied field and the anisotropy γ. Solving the eigen value problem Eq. 4.10, the eigenvalues are given analytically as:

$$E_0 = -1 \quad , \quad E_1 = -\sqrt{\gamma^2 + h_z^2} \quad , \quad E_2 = \sqrt{\gamma^2 + h_z^2} \quad \text{and} \quad E_3 = 1. \tag{4.11}$$

These values are plotted in Fig. 4.1 as the whole energy spectra of the anisotropic XY-model dimer for several value of γ.

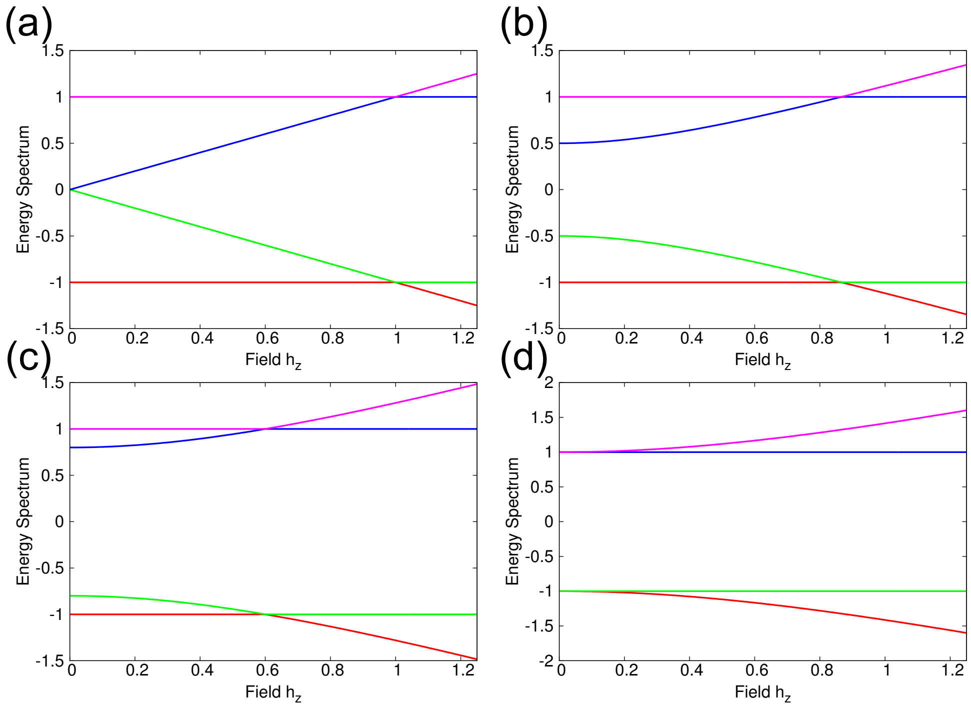

FIGURE 4.1: The energy spectra for the anisotropic XY-model dimer. (a) Isotropic XY-model where $\gamma = 0$. (b) Anisotropic XY-model where $\gamma = 0.5$. (c) Anisotropic XY-model where $\gamma = 0.8$. (d) Ising Model returned when $\gamma = 1$. The data for these plots was calculated numerically.

With the exception of the Ising model, the energy spectrum plots in Fig. 4.1 shows the two lowest energy levels and their associated eigenstates cross over. For the Ising case, the states form two doublets at zero field Fig. 4.1 (d), the red line represents the spins in favourable alignment with the field, thus it lowers the energy required to be in that state. For the anisotropic case the two levels that cross each other are entangled with the initial ground state having antiparallel entanglement and the second ground state having parallel entanglement. For the isotropic model (Fig. 4.1 (a)) the state that crosses is a pure ferromagnetic state in the direction of the applied field as also seen in Candini *et al* reproduced in Fig. 3.3. These level crossings are where the entanglement changes and provides the first insight into what is driving the entanglement transition [2].

The field value where the states cross is dependent on γ. Fig. 4.2 (left) shows the level crossing for a range of anisotropy for $0 \leq \gamma \leq 1$. The antiferromagnetically entangled ground state singlet is neither dependent on γ nor the applied field and is plotted as the straight black line. As the anisotropy increases the level crossing tends to zero field

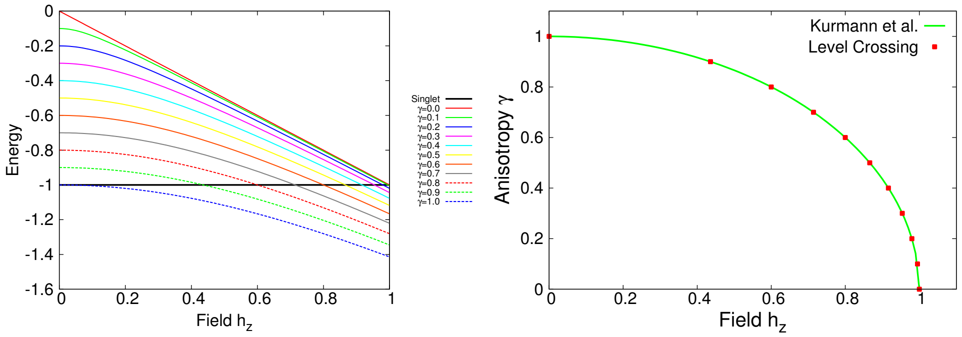

FIGURE 4.2: (a) The two lowest energy states for a range of anisotropy γ for the XY-model calculated numerically. The singlet ground state is independent of field and anisotropy. As the transverse field increases it lowers the energy of the first excited state until the gap is closed and the states cross over. (b) the points where the two levels cross is compared to the factorisation field obtained analytically by Eq. 3.8.

until it becomes the Ising model. These points are then taken and compared to the factorisation field from Eq. 3.8 and plotted in Fig. 4.2 (right). It is clear that the level crossing takes place at the factorisation field and it is this degeneracy between differently entangled states that enables factorisation.

To be exact, using the two lowest eigenvalues from Eq. 4.11 (found analytically), and equating them as $-1 = -\sqrt{\gamma^2 + h_z^2}$, this is a simple rearrangement to return the factorisation field from Eq. 3.8.

4.2.2 XYZ-Model

The Hamiltonian matrix for the XYZ-model dimer calculated from Eq. 3.5 is given as:

$$H_{XYZ} = \begin{pmatrix} -h_z + \frac{\Delta}{2} & 0 & 0 & \gamma \\ 0 & \frac{-\Delta}{2} & 1 & 0 \\ 0 & 1 & \frac{-\Delta}{2} & 0 \\ \gamma & 0 & 0 & h_z + \frac{\Delta}{2} \end{pmatrix} \tag{4.12}$$

For comparison, it is necessary to explore the energy spectra of the XYZ-model. Figs. 4.3 and 4.4 are results for different values of the out-of-plane anisotropy as Δ, each demonstrating the in-plane anisotropy for $\gamma = 0.0, 0.4, 0.8$ and 1.0. It can be seen how Δ affects the energy spectra.

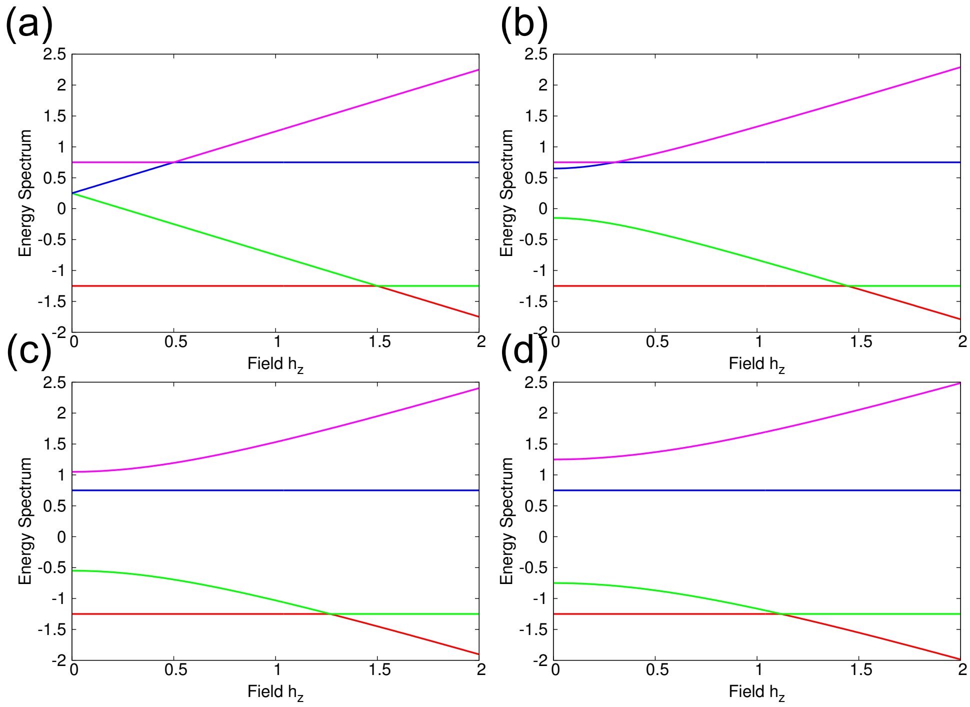

Figure 4.3: The energy spectra for the XYZ-model dimer for a selection of in-plane anisotropy γ. For the out-of-plane anisotropy are $\Delta = 0.5$. (a) $\gamma = 0.0$. (b) $\gamma = 0.4$. (c) $\gamma = 0.8$. and (d) $\gamma = 1.0$.

As expected, the energy diagrams are similar to the anisotropic XY-model and with inspection of the eigenstates they are essentially the same. Like with the XY-model, the in-plane anisotropy parameter γ takes the two ferromagnetically entangled states (plotted in pink and green) and separates them in energy. As a result, as γ increases, the value of h_z, at which the energy levels cross, decreases. The addition of a finite Δ lowers the energy of the antiferromagnetically entangled states. By controlling γ and Δ, one could effectively position the entanglement transition at a desirable applied field strength. One would also have control over the size of the gap and therefore the temperature where a transition could still be detected.

For the XYZ-model the factorisation field is dependent on two parameters, γ and Δ and is shown as a region in Fig. 4.5. The data is taken from the level crossings and matches values when Eq. 3.9 is used. Like before, the analytical solution for the energy levels for the XYZ-model dimer is given as:

$$E_0 = \frac{\Delta - 2}{2}, \quad E_1 = \frac{-2\sqrt{\gamma^2 + h_z^2} - \Delta}{2}, \quad E_2 = \frac{2\sqrt{\gamma^2 + h_z^2} + \Delta}{2}, \quad \text{and} \quad E_3 = \frac{\Delta + 2}{2} \tag{4.13}$$

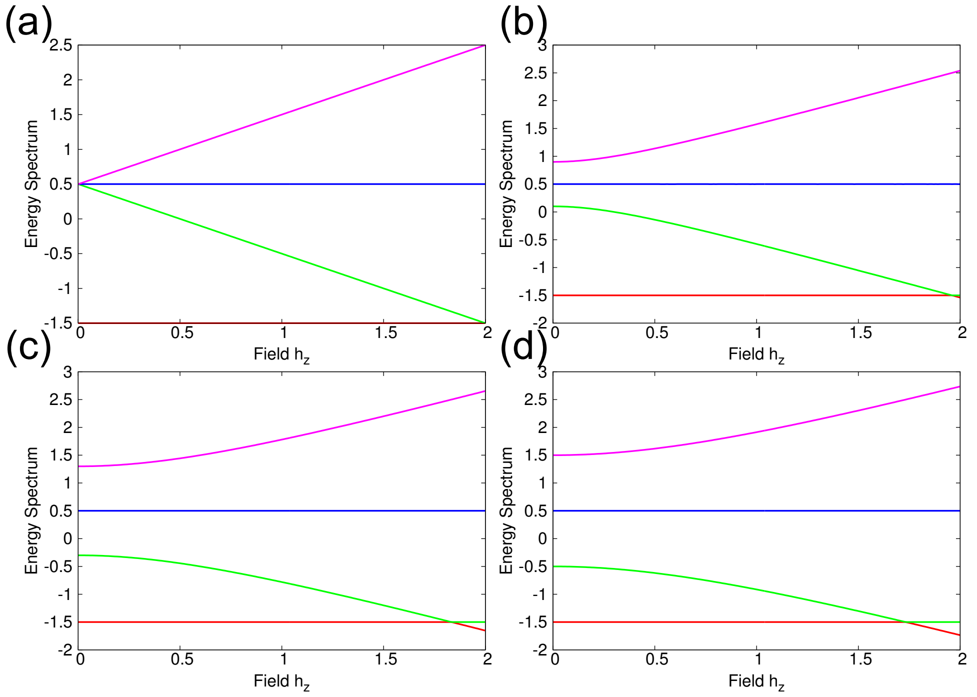

FIGURE 4.4: The energy spectra for the XYZ-model dimer for a selection of in-plane anisotropy γ. For the out-of-plane anisotropy are $\Delta = 1.0$. (a) $\gamma = 0.0$. (b) $\gamma = 0.4$. (c) $\gamma = 0.8$. and (d) $\gamma = 1.0$.

By using the two lowest energy eigenvalues and equating them: $\frac{\Delta-2}{2} = \frac{-2\sqrt{\gamma^2+h_z^2}-\Delta}{2}$ then this is also easily rearrange to show the factorisation field for the XYZ-model as a function of Δ and γ.

With this level of flexibility within the anisotropy planes, that only seem to move the entanglement transition, it is plausible that some anisotropic molecular dimer could be the key material to detect it experimentally.

4.3 Entangled and Factorised States

The energy spectra plots have pin pointed the factorisation field and have related it to the crossing of the two lowest eigenstates. In this section these states will be specifically probed to analyse their structure and to relate their degeneracy to a factorised state. At the level crossing where the two states become degenerate, any linear combination of these states is also a valid eigenstate, but it is a particular combination of the states that will factorise.

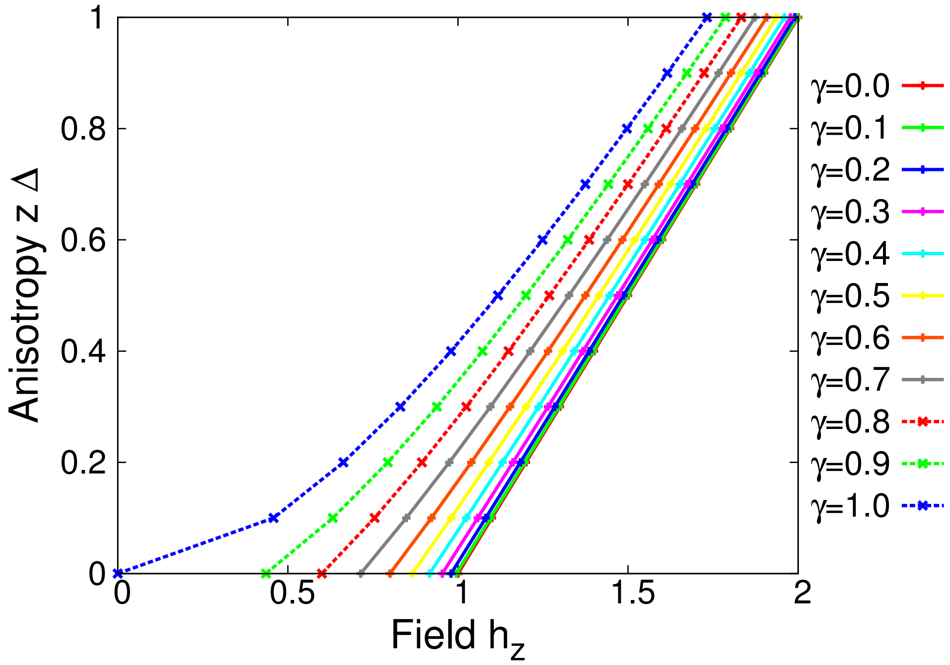

Figure 4.5: The factorisation field for the XYZ-model is given by Eq. 3.9. The figure shows the factorisation field as a region covered by the anisotropy $0 < \gamma < 1$ and $0 < \Delta < 1$ where the values are taken from the level crossings in the energy spectra that represent the factorisation field. These resu;ts were obtained numerically and checked against Eq. 3.9.

Factorisation is vital to the entanglement transition as it explicitly demonstrates that the entanglement in the system is exactly zero at the transition. It is also advantageous to analyse the separate state as it will show the type of entanglement that each state has, thus a complete change in entanglement across the transition is observed. This is key as operators that quantify entanglement, like concurrence, can not differentiate between types of entanglement.

A general factorised state for a spin dimer is represented by the following equation:

$$|\psi\rangle = (\alpha_1 |\uparrow\rangle + \beta_1 |\downarrow\rangle) \otimes (\alpha_2 |\uparrow\rangle + \beta_2 |\downarrow\rangle), \tag{4.14}$$

this is expanded and can be written in terms of a vector in the same basis ($\{|\uparrow\uparrow\rangle$, $|\uparrow\downarrow\rangle$, $|\downarrow\uparrow\rangle$, $|\downarrow\downarrow\rangle\}$) as the eigenstates in order to compare them directly.

$$|\psi\rangle = \begin{pmatrix} \alpha_1\alpha_2 \\ \alpha_1\beta_2 \\ \beta_1\alpha_2 \\ \beta_1\beta_2 \end{pmatrix}. \tag{4.15}$$

This is used in the next two sections to prove factorisation in the anisotropic XY-model and XYZ-model.

4.3.1 Anisotropic XY-Model

One of the two lowest eigenstates for the XY-model is given analytically by:

$$|\psi_A\rangle = \begin{pmatrix} \frac{1}{\sqrt{1+\Lambda^2}} \\ 0 \\ 0 \\ -\frac{\Lambda}{\sqrt{1+\Lambda^2}} \end{pmatrix}, \tag{4.16}$$

where for simplicity

$$\Lambda = \frac{\sqrt{\gamma^2 + h_z^2} - h_z}{\gamma}, \tag{4.17}$$

which at the factorisation field becomes:

$$\Lambda = \frac{1 - \sqrt{1-\gamma^2}}{\gamma}. \tag{4.18}$$

The other lowest state is antiferromagnetic and remains constant, displayed:

$$|\psi_B\rangle = \frac{1}{\sqrt{2}} \begin{pmatrix} 0 \\ 1 \\ -1 \\ 0 \end{pmatrix}. \tag{4.19}$$

For this dimer model any linear combination of the two lowest ground states that would be valid at the factorisation field can be written as:

$$A\left|\psi_A\right\rangle + B\left|\psi_B\right\rangle = A\begin{pmatrix} a_1 \\ 0 \\ 0 \\ a_2 \end{pmatrix} + B\begin{pmatrix} 0 \\ b_1 \\ b_2 \\ 0 \end{pmatrix}, \tag{4.20}$$

from knowing their general structure from Eqs. 4.16 and 4.19. These can then be compared to the factorised state:

$$\begin{pmatrix} Aa_1 \\ Bb_1 \\ Bb_2 \\ Aa_2 \end{pmatrix} = \begin{pmatrix} \alpha_1\alpha_2 \\ \alpha_1\beta_2 \\ \beta_1\alpha_2 \\ \beta_1\beta_2 \end{pmatrix}. \tag{4.21}$$

These form four simultaneous equations for an under determined system, with the additional requirement of A and B being probabalistically normalised, i.e $|A|^2 + |B|^2 = 1$, additionally $|\alpha_1|^2 + |\beta_1|^2 = 1$ and $|\alpha_2|^2 + |\beta_2|^2 = 1$. A solution to these simultaneous equations proves that they are able to factorise. Examples for both the XY-model and XYZ-model are provided to demonstrate that a linear combination of the states can be found to obey the requirements to factorise.

Example: For $\gamma = 0.80$ then from Eq. 4.18 $\Lambda = \frac{1}{2}$ at the factorisation field. Putting this value for Λ into the linear combination written in Eq. 4.20;

$$A\left|\psi_A\right\rangle + B\left|\psi_B\right\rangle = A\begin{pmatrix} \frac{2\sqrt{5}}{5} \\ 0 \\ 0 \\ \frac{\sqrt{5}}{5} \end{pmatrix} + \frac{B}{\sqrt{2}}\begin{pmatrix} 0 \\ 1 \\ -1 \\ 0 \end{pmatrix} = \begin{pmatrix} \alpha_1\alpha_2 \\ \alpha_1\beta_2 \\ \beta_1\alpha_2 \\ \beta_1\beta_2 \end{pmatrix}. \tag{4.22}$$

This gives the following set of simultaneous equations:

$$\begin{aligned} A &= \frac{\sqrt{5}}{2}\alpha_1\alpha_2 \\ B &= \alpha_1\beta_2\sqrt{2} \\ B &= -\beta_1\alpha_2\sqrt{2} \\ A &= \beta_1\beta_2\sqrt{5}. \end{aligned} \tag{4.23}$$

Solving these gives, and using the normalisation rules states above, the linear combination of $|\psi_A\rangle$ and $|\psi_B\rangle$ that give a factorised state for $\gamma = \frac{4}{5}$ is:

$$B = \frac{2}{3} \quad \text{and} \quad A = \frac{\sqrt{5}}{3}. \tag{4.24}$$

Having established that, when degenerate at the factorisation field, the ground state becomes factorisable, there is some last additional information that can be learned from looking at the occupied ground state and its basis components. This will be useful as a comparison to larger finite-size systems for N=4 where the basis is more complicated. As said before and is clear by looking at Eq. 4.16 and 4.19 one of the two lowest-lying states is a ferromagnetically entangled state and the other is the maximally antiferromagnetically entangled state. Both are impossible to factorise on their own and it can be said that they are entangled in completely different ways.

Fig.4.6 shows the amplitudes of the ground state in the basis $\{|\uparrow\uparrow\rangle\ , |\uparrow\downarrow\rangle\ , |\downarrow\uparrow\rangle\ , |\downarrow\downarrow\rangle\}$. It is seen that the antiferromagnetically entangled state has equal occupation in the two antiferromagnetic bases $|\uparrow\downarrow\rangle$ and $|\downarrow\uparrow\rangle$ as is normal. But now the occupation can be visualised for the ferromagnetically entangled state, where the majority of the state is in $|\uparrow\uparrow\rangle$ with the alignment of the applied field. There is little occupation left in $|\downarrow\downarrow\rangle$. As the field increases, the two spins will slowly saturate to fully occupy the pure state $|\uparrow\uparrow\rangle$ and lose all entanglement. The amount of entanglement quantified by concurrence for both models is calculated in section 4.4.

4.3.2 XYZ-Model

With the anisotropic XY-model and XYZ-model being of the same universality class, the similarities in the XYZ-model spectra is also seen in their states, with Fig.4.7 showing

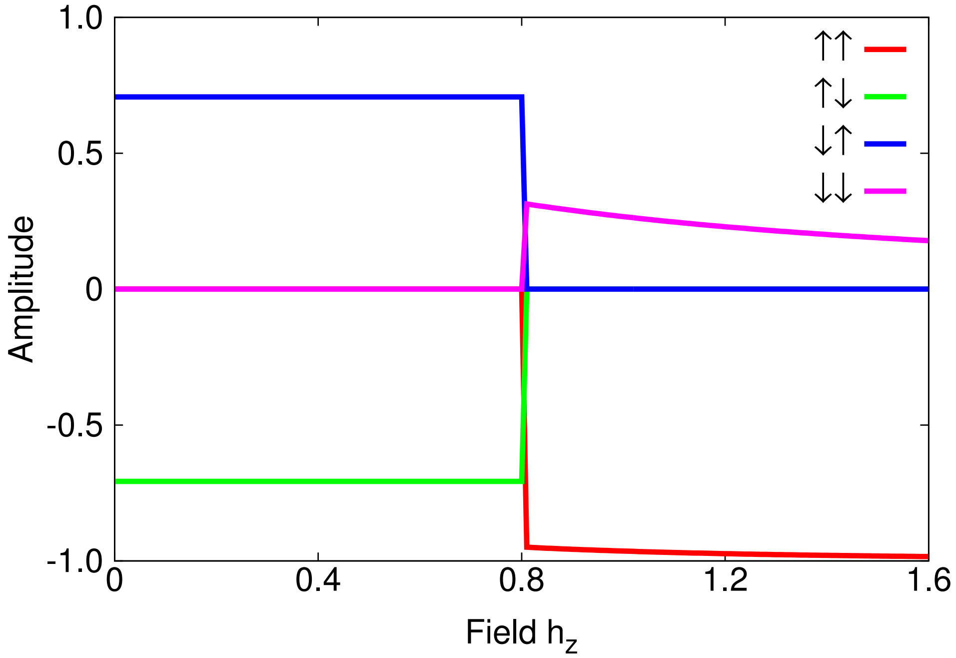

FIGURE 4.6: Using the parameter $\gamma = 0.6$ for the XY-model that gives $h_f = 0.80$, the basis components of the ground state are shown as a function of the transverse field. The amplitude is taken over the probability density of the wavefunction so that it is easier to distinguish between the constituent plots. This becomes more vital when looking at larger states where there is a lot of overlap in the probability density.

the amplitudes of the basis of the XYZ-model and Fig. 4.6 being essentially the same. The first lowest-lying energy state for the XYZ-model is the same as the XY-model show as $|\psi_B\rangle$ in Eq. 4.19 and the other lowest-lying state $|\psi_A\rangle$ has the same structure as Eq. 4.16 but with a new definition of Λ given below;

$$\Lambda = \frac{\sqrt{\gamma^2 + h_z^2} - h_z}{\gamma}, \tag{4.25}$$

which at h_f for the XYZ-model (from Eq. 3.9) becomes;

$$\Lambda = \frac{1 + \Delta - \sqrt{(1+\Delta)^2 - \gamma^2}}{\gamma}. \tag{4.26}$$

Example: For the parameters shown in Fig. 4.7 the anisotropies are $\gamma = 0.5$ and $\Delta = 0.5$, which gives the following ferromagnetically entangled state to [4dp] (calculated analytically and verified numerically):

$$|\psi_A\rangle = \begin{pmatrix} 0.9856 \\ 0 \\ 0 \\ -0.1691 \end{pmatrix}. \tag{4.27}$$

Using the same method that was demonstrated for the anisotropic XY-model shown by following in Eqs. 4.20 and 4.21 and solving for a new set of simultaneous equations,the linear combination that factorises when these states are degenerate is $A = 0.9988$ and $B = 0.0495$ to [4dp].

The amplitudes of the ground state wavefunction in the basis $\{|\uparrow\uparrow\rangle, |\uparrow\downarrow\rangle, |\downarrow\uparrow\rangle, |\downarrow\downarrow\rangle\}$, for the same parameters are given in Fig. 4.7. It is clear that the XYZ-model has the same state behaviour as the XY-model with the difference being only where the states cross.

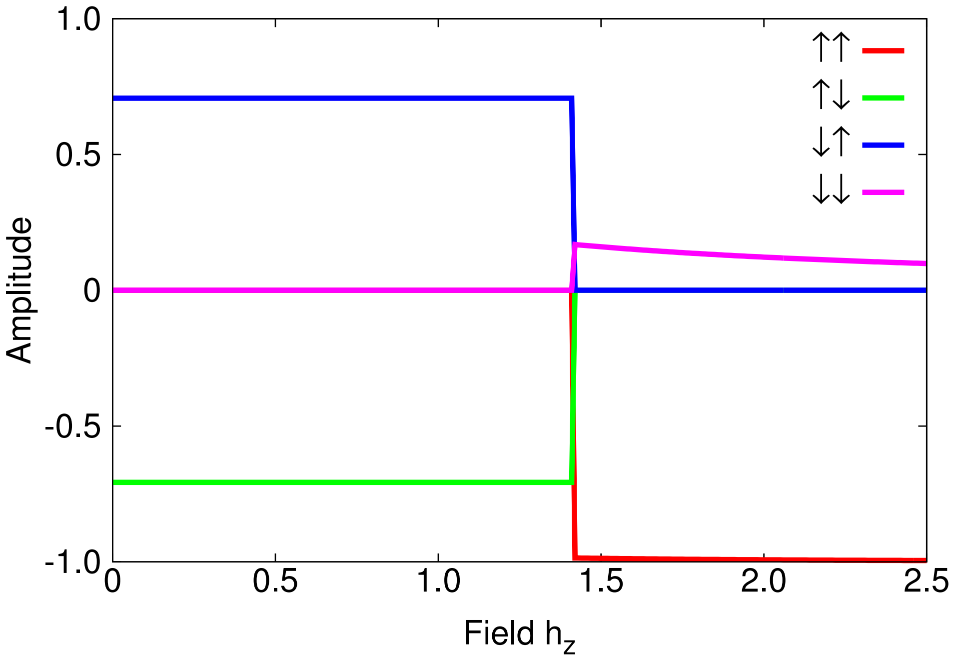

FIGURE 4.7: Using the parameters $\gamma = 0.5$ and $\Delta = 0.5$ for the XYZ-model that gives $h_f = \sqrt{(}2)$. Unsurprisingly Δ does not appear to change the structure or amplitudes of the ground state, in comparison to the ground state in the anisotropic XY-model. The only apparent affect of Δ is to change where the states factorise and cross.

It is important to demonstrate the similarities in the XY-model and the XYZ-model by using the dimer which is solvable for both, because in the thermodynamic limit the XYZ-model is not exactly solvable (analytically and numerically), but the mechanisms are the same and real materials should not be excluded for experimentation. It is speculated that finite-sized systems could be used to predict the factorisation field value in materials that can be modeled by the XYZ-model in the thermodynamic limit, and further assist in verifying new materials for experimentation.

4.4 Concurrence

In Chapter 2 we discuss the theoretical measures of entanglement and introduce concurrence in section 2.2.2. In short, concurrence describes the overlap between a state and its orthogonal spin-flipped self, the concept being that an entangled state will have some overlap and a pure state will not [15].

The dimer is a special model when considering entanglement and has been prevalent in the studies around quantum information [15] and using entanglement as a resource. The spin dimer can occupy a maximally entangled state with any additional sites reducing the amount of entanglement as the complexity of the Hilbert space grows. This is discussed in [21] paper on "Distributed Entanglement", when using three entangled qubits: A, B and C. They use concurrence to "show that the squared concurrence between A and B, plus the squared concurrence between A and C, cannot be greater than the squared concurrence between A and the pair BC." That is to say, for three sites interacting equally, no pair of sites can be maximally entangled and still be entangled with the third site as the entanglement is distributed between them.

In this section, the concurrence for the maximally entangled state from Eq.2.4 that applies to both models for the dimer will be explicitly calculated. The density matrix for a dimer in the singlet state (from Eq. 4.19) can be written as follows:

$$\hat{\rho} = \frac{1}{2}\begin{pmatrix} 0 & 0 & 0 & 0 \\ 0 & 1 & -1 & 0 \\ 0 & -1 & 1 & 0 \\ 0 & 0 & 0 & 0 \end{pmatrix}. \tag{4.28}$$

The spin-flip matrix $\tilde{\rho}$ is calculated using Eq. 2.17 and as $\hat{\rho}$ is real and Hermitian then the complex conjugate of $\hat{\rho}$ is also $\hat{\rho}$. When $\tilde{\rho}$ is calculated it is also the same as $\hat{\rho}$:

$$\tilde{\rho} = \frac{1}{2}\begin{pmatrix} 0 & 0 & 0 & 0 \\ 0 & 1 & -1 & 0 \\ 0 & -1 & 1 & 0 \\ 0 & 0 & 0 & 0 \end{pmatrix}. \tag{4.29}$$

So for this example the product $\hat{\rho}\tilde{\rho}$ is also just $\hat{\rho}$. It is this product matrix whose eigenvalues (λ_i in descending order) are used to define concurrence, shown in Eq. 2.18. The eigenvalues of $\hat{\rho}\tilde{\rho}$ are $\lambda_1 = 1, \lambda_2 = 0, \lambda_3 = 0$ and $\lambda_4 = 0$, therefore the square roots are the same, making the concurrence $\mathcal{C} = \max\{1, 0\}$ and thus the concurrence for the maximally entangled state is 1 as expected. When a state is maximally entangled then it has a complete overlap with its spin-flipped version, hence the maximum value for concurrence is 1.

The same method is used for the other lowest-lying state but has been calculated numerically for a range of anisotropy γ and Δ and as a function of the applied field. The results for these are plotted for the XY-model in Fig. 4.8 and the XYZ-model in Fig. 4.9.

Fig. 4.8 shows the numerically calculated concurrence for the anisotropic XY-model for a range of in-plane anisotropy values including $\gamma = 0$ for the isotropic model and $\gamma = 1.0$ for the Ising model. At the factorisation field, where the energy levels cross, the two lowest-lying eigenstates become degenerate and thus any linear combination of them is a valid eigenstate of the system. The calculation uses state $|\psi_B\rangle$ from Eq. 4.19 in the field-steps in the calculation up until the factorisation field, and then $|\psi_A\rangle$ from Eq. 4.16 after the crossing. At the exact point of factorisation it was checked analytically using the results for the in-plane anisotropy $\gamma = 0.8$ at $h_f = 0.6$ for the linear combination found in Eq. 4.22 that the concurrence is indeed zero for a factorisable state. Rossignoli *et al.* experience a break in the concurrence for the ground state concurrence as seen in Fig. 3.4 for their finite-sized calculations [3].

Fig. 4.8 gives the concurrence for the isotropic XY-model (for $\gamma = 0$) and produces the same results for concurrence in the ground state as Candini *et al.* reproduced in Fig.3.3. The system has maximum entanglement for $\mathcal{C} = 1$ before the level crossing and

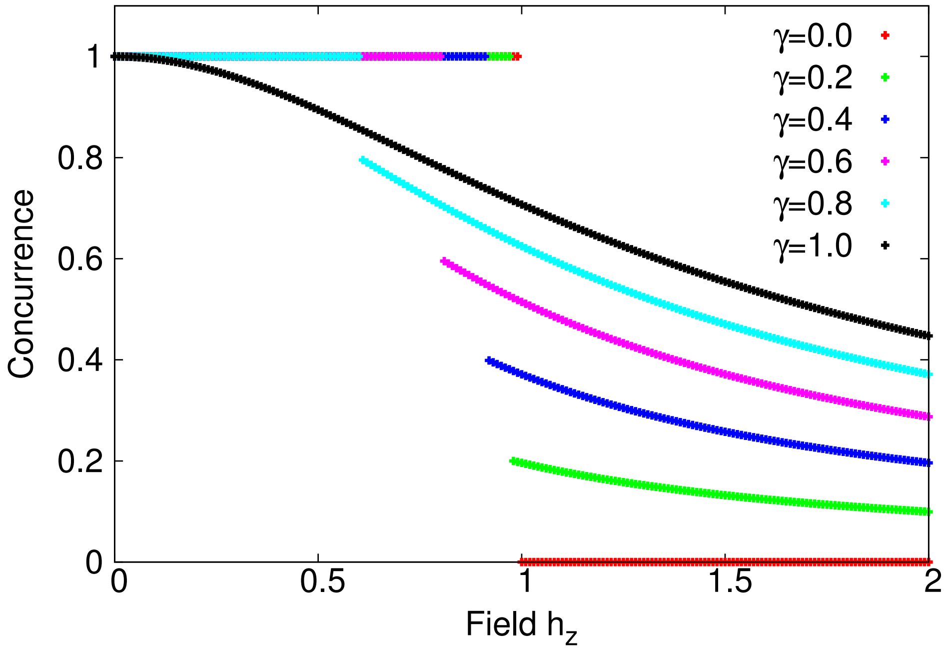

FIGURE 4.8: Concurrence for the XY-model for a selection of in-plane anisotropy γ. The concurrence quantifies the amount of entanglement in a single ground state. It does not consider the level crossing as a degenerate state i.e any linear combination of the two lowest-lying eigenstates would be valid and could give a different value for the concurrence, it is only the linear combination of states that give a factorised state that would give a zero value for concurrence. Instead the calculation uses the singlet state up to the crossing value and the lowered ground state after the crossing, this is represented as a sudden break in the concurrence and is why at the factorisation field the concurrence is not given as zero.

zero entanglement for the pure state $|\uparrow\uparrow\rangle$ with $\mathcal{C} = 0$. For higher γ it is observed that although the system is not maximally entangled for the state in Eq. 4.16, and despite the small occupation in $|\downarrow\downarrow\rangle$ component, as seen in Fig.4.6, there is still a substantial amount of entanglement in this region. This slowly decreases as the system saturates.

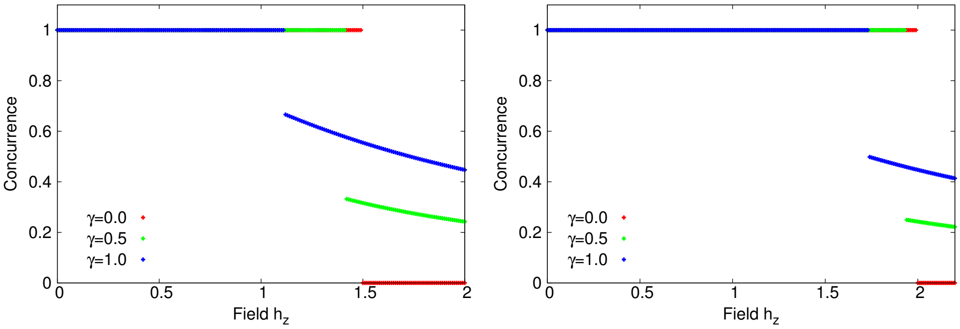

FIGURE 4.9: Concurrence for the XYZ-model for (a) $\Delta = 0.5$ and (b) $\Delta = 1.0$.

Lastly, the concurrence for the XYZ-model is plotted for $\Delta = 0.5$ and $\Delta = 1.0$ for a few values of γ. Again the entangled singlet is clearly depicted as having $\mathcal{C} = 1$ and the ferromagnetic state having decreasing concurrence with applied field.

The spin dimer has been successful in helping to define the underlying mechanism behind the entanglement transition within finite sized systems. In its own right it can be directly related to magnetic dimer molecules. By breaking down the states and energy spectra it is seen that the factorisation field coincided with a level crossing between the two lowest states. At this point a linear combination of these states can be found for both the anisotropic XY and XYZ-model that shows the state to factorise, and therefore become separable. It is this mechanism of an antiparallel entangled state changing into a parallel entangled state whilst having zero entanglement at the point that they cross that defines the entanglement transition. As it has been discussed the factorisation field has no size dependence on the system. In subsequent chapters it is shown how these ideas evolve for larger finite-sized systems.

Chapter 5

The Entanglement Transition in 1D Spin Chains

This chapter extends on the principles discussed in the previous chapter with regards to the dimer model. As the model evolves into more complex finite-sized systems, the work is split into two variants: one for open boundary conditions (OBC) and one for periodic boundary conditions (PBC). The calculations are small enough to use exact diagonalisation methods to obtain the eigenstates and eigenvalues of the Hamiltonian, but can be used together to provide insight into the thermodynamic limit. The entanglement transition is examined with regards to the system size. It is found that factorisation within the ground state plays the crucial role in both the finite-sized systems and the thermodynamic limit.

It is important to develop a technique for detecting the entanglement transition in these systems when it is impractical to look at just the energy spectra. This is achieved by studying the correlation functions in the ordered phase (i.e the antiferromagnetically ordered phase with long range order (LRO)) that would indicate a semi-classical/ factorised state by exhibiting a complete flatness in the absolute value of the correlation functions [25]. The correlation functions form the main ingredient towards predicting neutron scattering data, so if, in real space, they can show a signature of the entanglement transition it is practical to suggest that a signal could be detected in the neutron scattering function [8]. The neutron scattering cross-section is modeled in Chapter 6 on the foundations made in this chapter by studying closely the real space correlation functions. Although concurrence has been discussed in Chapters 2, 3, 4 and at the end of this chapter, it is a theoretical measure for quantifying entanglement and the ultimate purpose of the project is to form a theory of the entanglement transition that can be experimentally tested.

The main focus in this chapter is to understand the mechanism driving the entanglement transition in finite-sized systems whilst identifying their advantages over the thermodynamic dynamical limit. This is then applied to identify more real finite-sized models to simulate neutron scattering experiments in the next chapter.

5.1 Energy Spectrum and the Energy Gap

In the thermodynamic limit the two lowest states are completely degenerate until the critical field is reached [10]. The factorisation field does not correspond to a crossing between the energy levels of these states as there is never a difference in their respective energies until the critical field. Instead, there is an apparent change in the type of entanglement dominating the behaviour of the system. Rossignoli *et al.* describes factorisation in the anisotropic XYZ Heisenberg model as exhibiting a "degenerate symmetry-breaking separable ground state", meaning at the point in which the system factorises the ground state, spontaneously becomes unentangled and the type of entanglement present switches [3]. For the finite-sized systems, discussed in this chapter, the two differently entangled states cross multiple times, also switching the type of entanglement but without factorising. The entanglement transition in these finite-sized must have a stricter definition than the dimer model explored in Chapter 4. The dimer model exhibits just one level crossing that meets the requirement for factorisation, but the finite-sized systems have multiple points of degeneracy, thus the definition of the entanglement transition in these systems must match the implications shown in the thermodynamic limit (i.e must prove factorisation in the ground state). The absolute definition of the entanglement transition is that it is not enough for the system to change the type of entanglement present but at the point of the transition, for the entanglement to be completely broken.

For the dimer, the structure of the entanglement of the two states was simple, with one being antiferromagnetically entangled and the other being completely ferromagnetically entangled as seen in Figs. 4.6 and 4.7. In the thermodynamic limit the states are described as anti-parallel and parallel entangled and having an additional phase transition at the critical field that indicates a ferromagnetic phase at high fields. Small systems in between these have more complicated entangled states. In this chapter, to better understand the entanglement in finite-sized system we are able to look at the two lowest-lying energy states for the $N = 4$ system taking advantage of its still relatively small Hilbert space (that grows 2^N).

For all these finite-sized systems it is possible to observe the energy spectrum and the energy gap between the two switching ground states. To be clear, the gap in the thermodynamic limit is between the degenerate ground state and the next excited state. It is one of the main differences that contributes to the adequateness of finite-sized systems for detecting the entanglement transition above zero temperature, compared to those in the thermodynamic limit.

5.1.1 Finite Chains

This section is split in two parts to deal with open boundary conditions (OBC) and periodic boundary conditions (PBC) separately to explore the energy spectrum and to identify the main difference that shows that PBC are vital for a factorised state to occur.

Open Boundary Conditions: Single Chains

Open boundary conditions describe single unattached chains of varying length. This could be achieved by doping a quasi-1D system leading to a Poisson distribution of chain lengths. The chains would be formed from doping the quasi-1D material with a non-magnetic impurity, with the doping percentage dictating the distribution of chain length. A simulation of up to a million sites was performed for different doping percentages and confirmed that a Poisson distribution of chain lengths is indeed obtained. Fig. 5.1 is a diagram representation of a doped chain system.

With appropriate levels of doping, this system can be easily approximated by a relatively small range of chain lengths that can be solved using exact diagonalisation. This means that chain lengths longer than N=10 are so improbable that they can be neglected. The distribution of the chain length requires that any change of entanglement to be

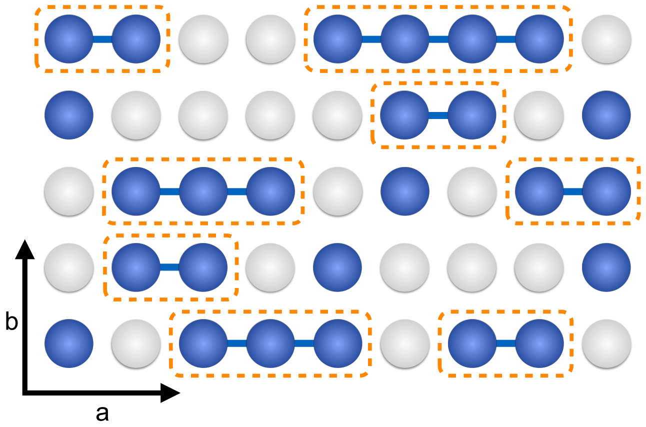

Figure 5.1: A diagram of an example of a doped system with a distribution of chain sizes. The blue balls are the magnetic ions and the grey balls are the non-magnetic dopants. Small finite-sized chains are formed along the a axis in this example

detected needs to be consistent regardless of chain length. Having a level crossing at the factorisation field would support this idea.

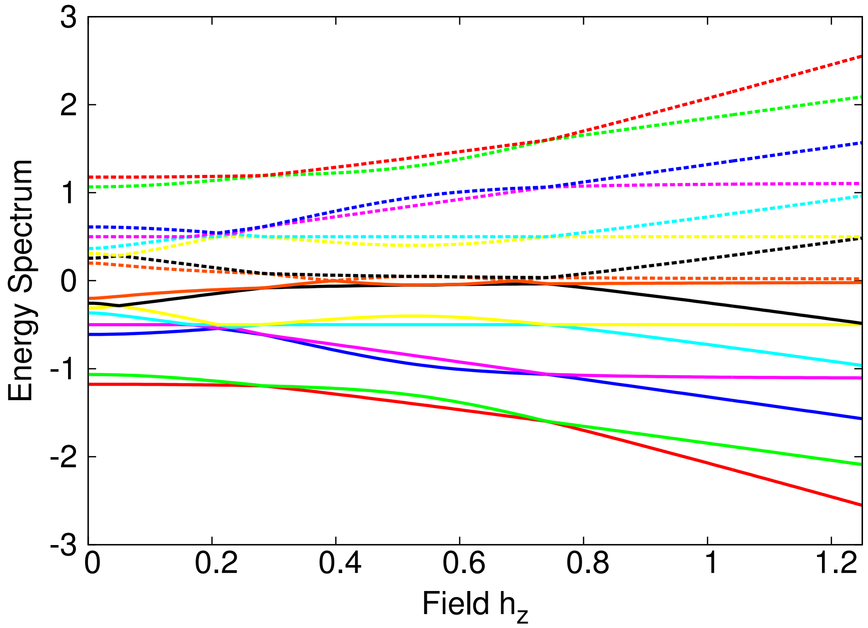

Figure 5.2: The energy spectrum of the anisotropic XY-model with $\gamma = 0.4$ for a $N = 4$ chain with open boundary conditions.

Fig. 5.2 and 5.3 show the complete energy spectra for an N=4 chain described by the anisotropic XY-model for the anisotropy parameter $\gamma = 0.4$ and 0.8, respectively. The two lowest energy levels cross twice in both cases without any higher energy levels crossing with them. For $\gamma = 0.8$ it becomes difficult to see the level crossings in this way,

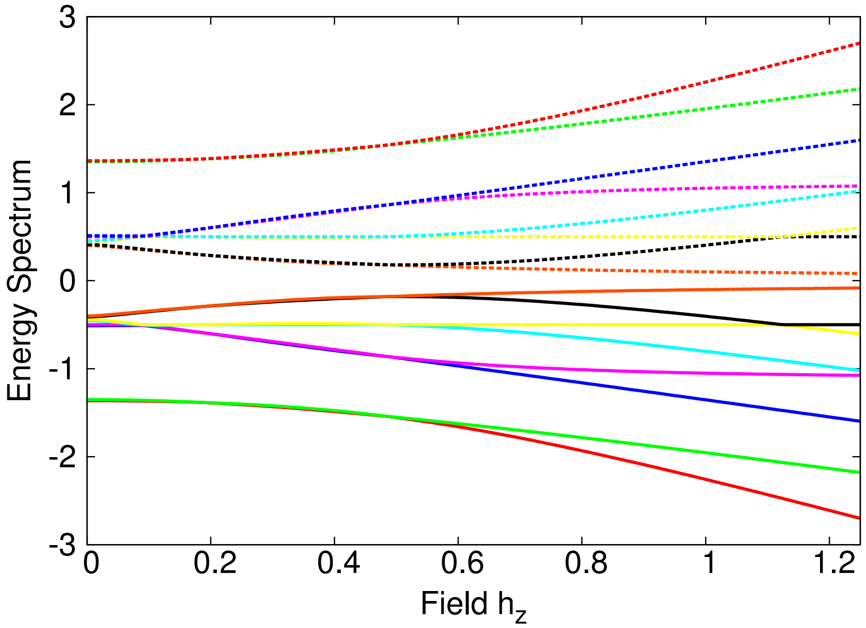

FIGURE 5.3: The energy spectrum of the anisotropic XY-model with $\gamma = 0.8$ for a $N = 4$ chain with open boundary conditions.

so to display it more clearly Fig. 5.4 plots the energy gap between the two lowest energy levels. This is for a range of even chain lengths from $N = 2$ to $N = 10$ for $\gamma = 0.2$ [1].

For different chain lengths the two lowest energy levels cross a number of times equal to $\frac{N}{2}$, as seen in the literature for the anisotropic XY-model [31]. None of the crossings for the different chain lengths occur at a common point. None of them cross at the factorisation field, which for $\gamma = 0.2$ is $h_f = 0.980$. This is discouraging for the OBC model as without a common trend independent of chain lengths, no common trend can be detected in a doped system. Also without a crossing at the factorisation field, the states can not factorise (this is addressed more explicitly in the following section 5.3. In contrast, for periodic boundary conditions, the results are more promising [9] [12].

An alternative option, OBC could be realised by synthesizing molecular magnets with one doped non-magnetic impurity per ring. This would allow for a consistent chain length within a single material, instead of a distribution of chain length. The is conceptualised in Fig. 5.5, which gives a diagrammatic example of the type of system that would be applicable to a model with OBC.

---

[1] this is to compare values with PBC in later sections.

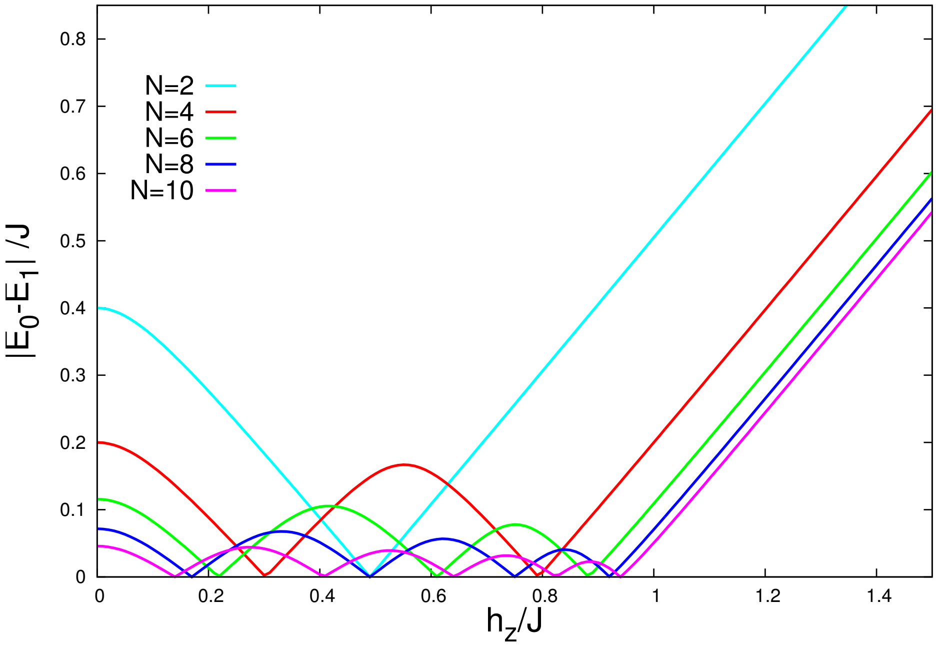

FIGURE 5.4: The absolute value of the gap between the two lowest energy states $|E_0 - E1|$ for the anisotropic XY-model where $\gamma = 0.2$ for a range of chain lengths with open boundary condition for $N = 2, 4, 6, 8, 10$

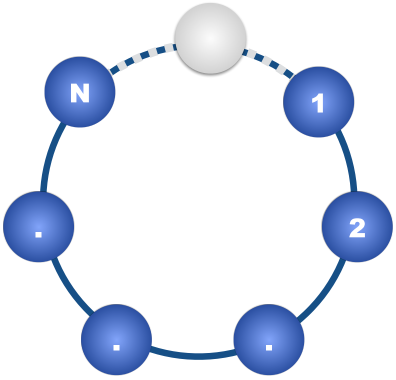

FIGURE 5.5: A diagram of an example of a doped ring system with chain size N. The blue balls are the magnetic ions and the grey ball is a non-magnetic dopants. The ring has open boundary conditions due to the non-magnetic impurity indicated by the dashed line and dopant breaking the interaction between sites 1 and N.

For any interesting features that occur in OBC systems but are not consistent with chain length then it could still be possible to study them in suitable molecular magnets that have been doped to break the interaction between the first and last sites. Silio *et al.* doped molecular magnets with single ion that interacted differently to the Cr ions that made up the rest of the ring, it seems plausible to dope with a non-magnetic ion [29] [30] [4].

Periodic Boundary Conditions: Bulk Properties and Clusters

Periodic boundary conditions let the last spin in the chain interact with the first spin as if they were nearest neighbours, giving a symmetry to the system that the OBC single chains do not have. This can be used to simulate the bulk of a material to give information about the thermodynamic limit or can be used to describe small molecular spin clusters. In this chapter the discussion is valid for both, and in the next chapter molecular magnets and their neutron scattering cross section is calculated where the geometry of the model effects the results.

When looking at the $N = 4$ energy spectra for the same parameters as before but now with PBC, the structure of the ground state appears similar with $\frac{N}{2}$ level crossings, but unlike the case of OBC, the last level crossing coincides with the factorisation field for the different anisotropy values. This is shown in Figs. 5.6 and 5.7.

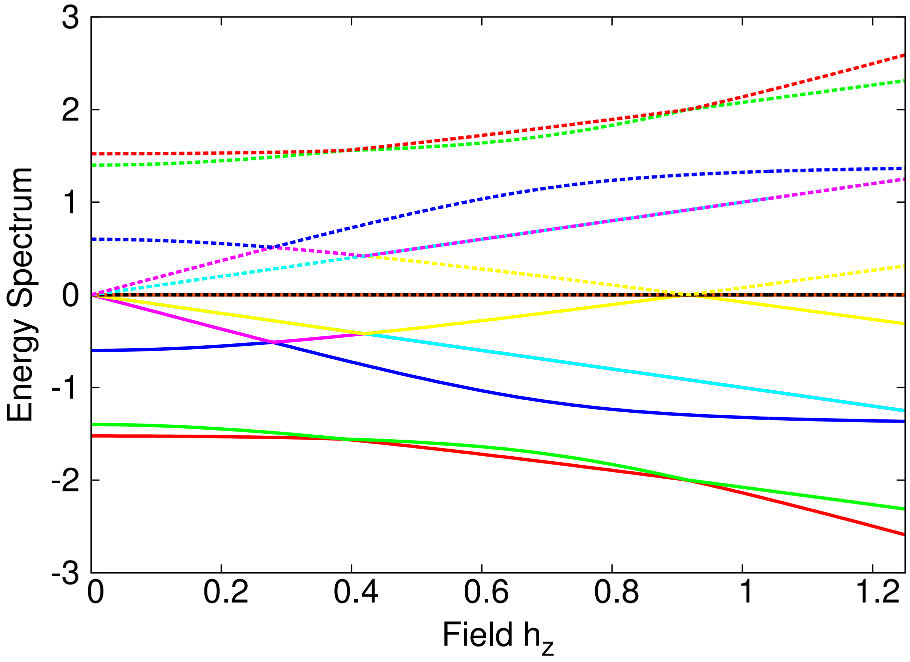

FIGURE 5.6: The energy spectrum of the anisotropic XY-model with $\gamma = 0.4$ for a $N = 4$ system with periodic boundary conditions.

Again it is the two lowest energy levels that form a switching ground state and the other excited states to do not cross the ground state. For $N = 6$ and 8, the two lowest energy levels are plotted in Fig. 5.8 and this behaviour can be confirmed for these larger

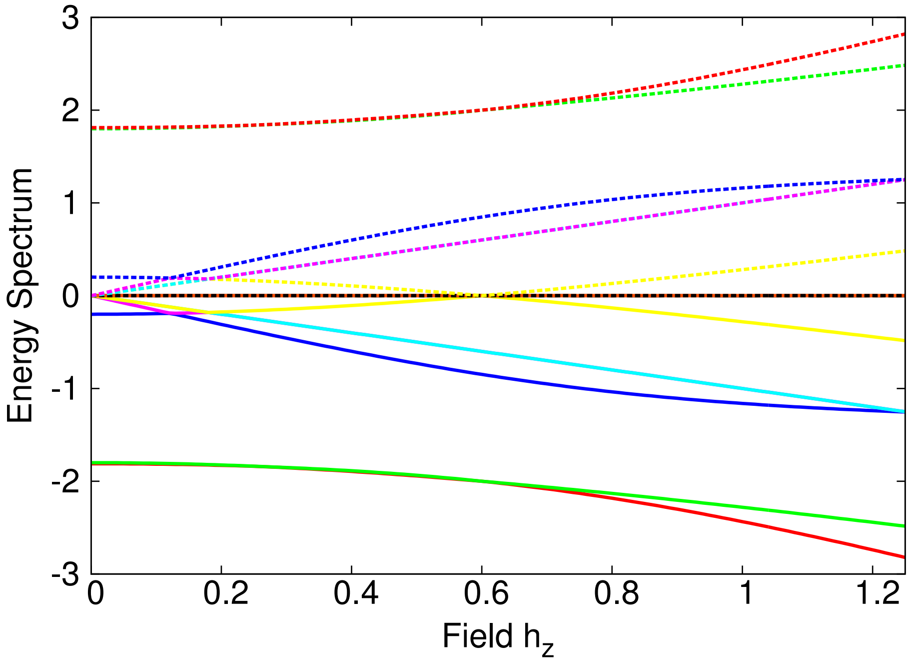

FIGURE 5.7: The energy spectrum of the anisotropic XY-model with $\gamma = 0.8$ for a $N = 4$ chain with periodic boundary conditions.

systems. They also support the trend that the states cross a number $\frac{N}{2}$ times, with the last level crossing always positioned at the factorisation field.

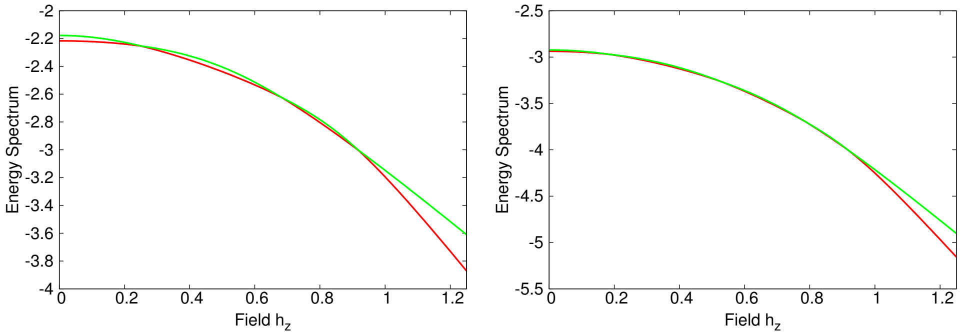

FIGURE 5.8: The two lowest energy level for the anisotropic XY-model with $\gamma = 0.4$ and PBC for $N = 6$ (left) and a $N = 8$ (right). The levels cross $\frac{N}{2}$ times. No other, higher energy levels cross the ground state energy.

For clarity in exploring larger system sizes, the value of the gap between the two ground state energies is taken and plotted for the anisotropic XY-model and XYZ-model to comment on the thermodynamic limit.

5.1.2 Thermodynamic Limit

The bulk properties using finite-sized calculations with PBC can offer an insight into the properties in the thermodynamic limit. It is known that as $N \to \infty$ the two states become degenerate up to the critical field [10] [71] [72]. This trend is observed using the finite-sized system calculations up to $N = 10$ and the features from the energy spectra are used to developed a method to find the critical field in this section. This section seeks to show the differences and similarites in the system between finite-sized calculations and the thermodynamic limit, in particular, focusing on the factorisation field and criticality.

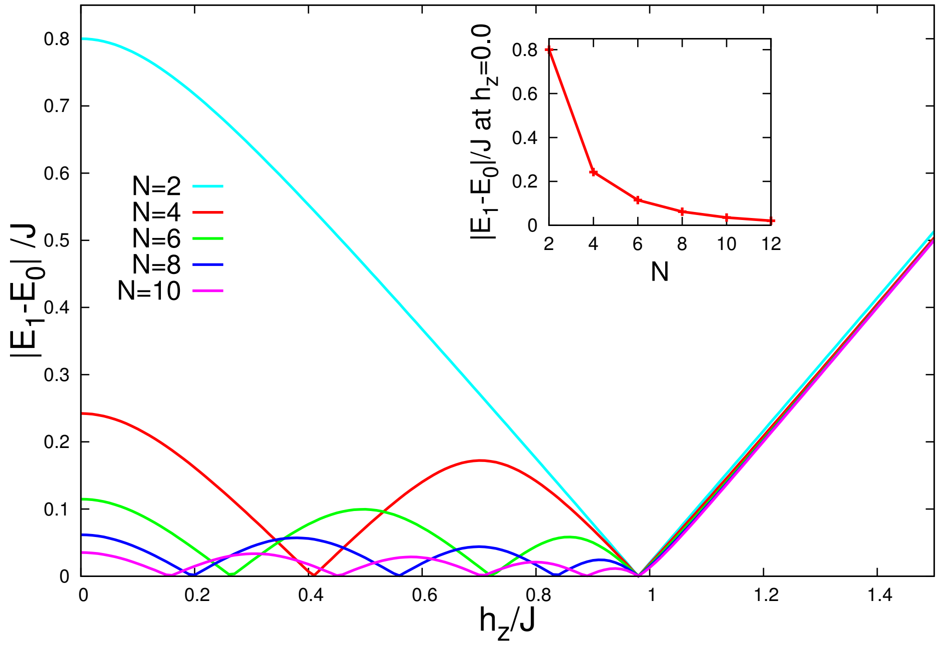

FIGURE 5.9: The absolute value of the gap between the two lowest energy states for the anisotropic XY-model, where $\gamma = 0.2$ for a range of system sizes with periodic boundary condition for $N = 2, 4, 6, 8, 10$. The figure inset illustrates the fate of the degeneracy found as the thermodynamic limit is approached: as the system sizes increase the gap at zero field tends towards zero.

Fig. 5.9 shows the gap for a range of even N (to avoid magnetic frustration [2]. Frustration can seriously effect the physical properties of a system and is an interesting field to study in its own right [91] [92]) for $N = 2$ to 10 for anisotropy $\gamma = 0.2$. As expected, the two ground states cross $\frac{N}{2}$ times like the OBC case before it, but with each systems' final

---

[2] Magnetic frustration is a conflict in magnetic interactions. In this case, if a an antiferromagnetically interacting chain of an odd number of spins were connected with periodic boundary conditions then the two edge spins would be of the same spin orientation and would not be able to interact antiferromagnetically towards each other [90]

level crossing always occurring at the factorisation field $h_f = 0.980$ for the example in Fig. 5.9 . As the system size increases, the number of ground state level crossings also increases, therefore, with the last crossing always being at h_f, the distances between crossings get smaller as the gap begins to completely close. This is supported by the insert in Fig. 5.9 that shows the largest value of the gap, which we find to be always at $h = 0$, tending towards zero. To fully explore the degeneracy of these two states, it is the region between the factorisation field and the critical field that needs to be closely examined.

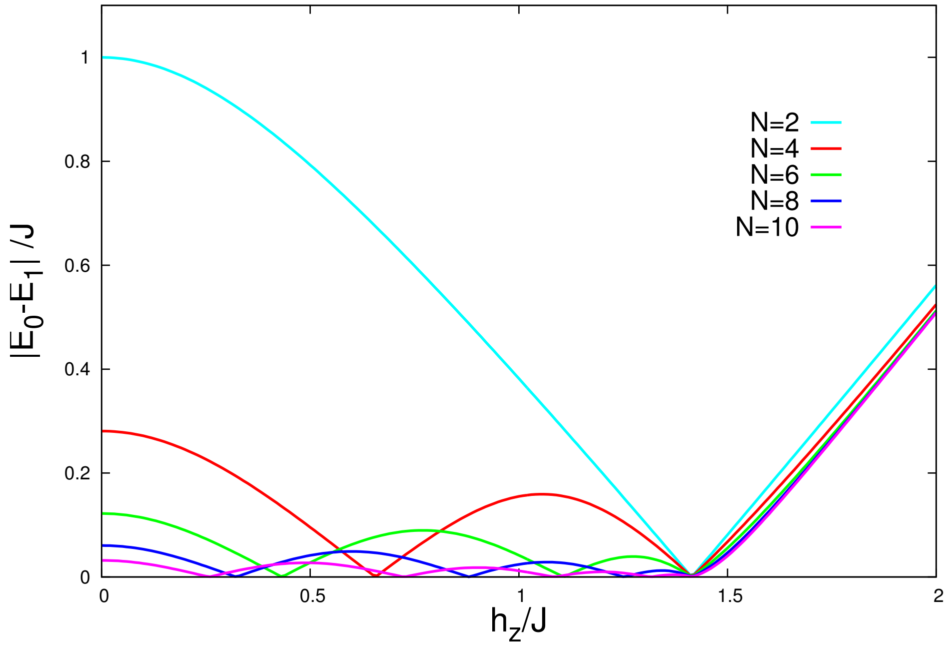

Figure 5.10: The absolute value of the gap between the two lowest energy states for the anisotropic XYZ-model where $\gamma = 0.5$ and $\Delta = 0.5$ for $N = 2, 4, 6, 8, 10$ with periodic boundary conditions.

For the XYZ-model the same trends are observed for the parameters $\gamma = 0.5$ and $\Delta = 0.5$ with the factorisation field $h_f = 1.414$ [3dp]. The difference for the XYZ-model is that the critical field is unknown, but an analysis of the degeneracy could open up an easy way in which finite-sized calculations could approximate the critical field for the XYZ-model in the thermodynamic limit. We will now discuss this.

Criticality

Although finite-sized systems do not exhibit a critical field, these calculations can be used to pinpoint where the degeneracy of the ground state would split in the thermodynamic limit. As a proof of concept this is done for the anisotropic XY-model to show the critical field with reasonable errors at $h = 1.00$, by analysis of the gradient of the gap past the factorisation field.

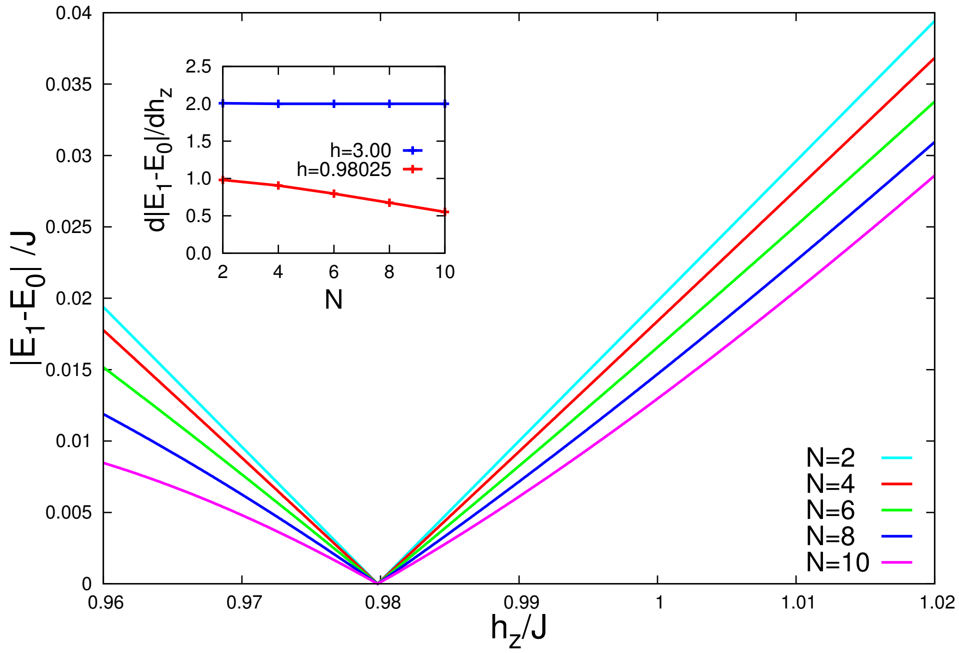

Figure 5.11: This takes a higher resolution of data points from Fig.5.9 in the region before the factorisation field at $h_f = 0.9798$ to a reasonable higher field value. As the system size increases and the two lowest states become complete degenerate in the thermodynamic limit, this degeneracy is kept until the critical field, and not the factorisation field. This is examined by assessing the gradient of the energy gap as shown in the inset. At high fields the gradient is a constant and after the factorisation field but before the critical field it tends towards zero, this indicates that the gap is tending towards zero in this region.

Fig. 5.11 shows a section of Fig. 5.4 from $h = 0.96$ to $h = 1.02$ that is recalculated at higher resolution and plotted to focus on the region between the factorisation field and the critical field. As the system size increases, there is a difference in the behaviour of the gap in this small section. Just after the factorisation field, as N increases, the slope of the gap vs h_z curve decreases. This then inflects so at higher fields the curves for different system sizes become parallel. This is depicted in the figure inset, where the gradient of the gap for the field value $h = 0.98025$, which is slightly above h_f, tend towards zero in the thermodynamic limit. this is attributed to the gap closing and the two lowest-lying energy levels closing and the ground state becoming slowly degenerate. For much higher values of the field where the spins are likely to be saturated, $h = 3.00$, the gradient is independent of system size and above zero. This means that past the factorisation field the states remain degenerate in the thermodynamic limit where at some point (the critical field) they diverge.

Using Ansatz methods it is possible to further confirm this critical behaviour as the system tends to the thermodynamic limit by achieving larger system sizes [93]. The XY-Hamiltonian is rewritten using second quantisation and is used to explore the two different parity ground states. The formula for the energy dispersion is calculated from this; Barouch *et al.* and Leib *et al.* both use the Jordan-Wigner Transformations (JWT) to describe the Hamiltonian in the mathematical context of spinless fermions [10] [71] Here we follow the more accessible proof from lecture notes by Fabio Franchini.

Using the raising and lowering operators it is possible to rewrite the XY-Hamiltonian given by Eq.3.6 using second quantisation;

$$\begin{aligned} \sigma^{+} &= (\sigma^{x} + i\sigma^{y})/2 \\ \sigma^{-} &= (\sigma^{x} - i\sigma^{y})/2, \end{aligned} \tag{5.1}$$

The anisotropic XY-Hamiltonian becomes:

$$\begin{aligned} H &= -\frac{J}{2}\sum_{j}^{N}\left(\frac{1+\gamma}{8}\right)\left[\sigma_j^{+}\sigma_{j+1}^{+} + \sigma_j^{+}\sigma_{j+1}^{-} + \sigma_j^{-}\sigma_{j+1}^{+} + \sigma_j^{-}\sigma_{j+1}^{-}\right] \\ &\quad -\left(\frac{1-\gamma}{8}\right)\left[\sigma_j^{+}\sigma_{j+1}^{+} - \sigma_j^{+}\sigma_{j+1}^{-} - \sigma_j^{-}\sigma_{j+1}^{+} + \sigma_j^{-}\sigma_{j+1}^{-}\right] - h\sum_{j}^{N}\sigma_j^{z} \\ &= -\frac{J}{2}\sum_{j}^{N}\frac{1}{4}\left[\gamma\sigma_j^{+}\sigma_{j+1}^{+} + \sigma_j^{+}\sigma_{j+1}^{-} + \sigma_j^{-}\sigma_{j+1}^{+} + \gamma\sigma_j^{-}\sigma_{j+1}^{-}\right] - h\sum_{j}^{N}\sigma_j^{z}. \end{aligned} \tag{5.2}$$

This Hamiltonian cannot be diagonalised as different sites obey different commutation and anticommutation relations. The JWT are applied to the Hamiltonian in this form, where the JWT are given for each operator as:

$$\begin{aligned}
\sigma_j^+ &= \mathrm{e}^{i\pi\sum_{l<j}\psi_l^\dagger\psi_l}\psi_j \\
\sigma_j^- &= \psi_j^\dagger\mathrm{e}^{-i\pi\sum_{l<j}\psi_l^\dagger\psi_l} \\
\sigma_j^z &= 1-2\psi_j^\dagger\psi_j. \qquad (5.3)
\end{aligned}$$

The JWT give an additional phase factor $\mathrm{e}^{\pm i\pi}$. In Eq.5.3, ψ represents the fermionic operators and $\psi_j^\dagger\psi_j$ can be described as a number operator $\hat{n}_i$. The number operator counts up to site j but does not include it, as it commutes with the string to the left of site j. A new dummy indexing variable l is being used that has to be on the commuting side of j and for $j+1$ includes j. The fermion operators obey the following relations:

$$\left\{\psi_i,\psi_j^\dagger\right\}=\delta_{ij},\quad \{\psi_i,\psi_j\}=0,\quad \left\{\psi_i^\dagger,\psi_j^\dagger\right\}=0, \qquad (5.4)$$

this means that the number operator can only equal zero for sites where it can create, and 1 for sites where it can annihilate: $\hat{n}_l=\begin{cases}0\\ \\ 1\end{cases}$. Using this principle and changing the sum of the exponentials to a product as $\mathrm{e}^{i\pi(\hat{n}_1+\hat{n}_2+\ldots+\hat{n}_{j-1})}\equiv\mathrm{e}^{i\pi\hat{n}_1}\cdot\mathrm{e}^{i\pi\hat{n}_2}\ldots\mathrm{e}^{i\pi\hat{n}_{j-1}}$ then an alternative way to write the JWT becomes:

$$\begin{aligned}
\sigma_j^+ &= \prod_{l=1}^{j-1}\mathrm{e}^{i\pi\hat{n}_l}\psi_j=\prod_{l=1}^{j-1}(1-2\hat{n}_l)\psi_j \\
\sigma_j^- &= \psi_j^\dagger\prod_{l=1}^{j-1}\mathrm{e}^{-i\pi\hat{n}_l}=\prod_{l=1}^{j-1}(1-2\hat{n}_l)\psi_j^\dagger \\
\sigma_j^z &= 1-2\hat{n}_j. \qquad (5.5)
\end{aligned}$$

By writing the JWT in this way it takes away the exponential terms, making it easier to manage. Looking at these and reviewing the anticommutation relations gives $\{1-2\hat{n}_l,\psi_l\}=\left\{1-2\hat{n}_l,\psi_l^\dagger\right\}=0$. Taking the Hamiltonian in the form from Eq.5.2, the individual terms can be transformed and simplified in the following way:

$$\begin{aligned}
\sigma_j^+\sigma_{j+1}^+ &= \psi_{j+1}\psi_j \\
\sigma_j^+\sigma_{j+1}^- &= \psi_{j+1}^\dagger\psi_j \\
\sigma_j^-\sigma_{j+1}^+ &= \psi_j^\dagger\psi_{j+1} \\
\sigma_j^-\sigma_{j+1}^- &= \psi_j^\dagger\psi_{j+1}^\dagger, \qquad (5.6)
\end{aligned}$$

where at the boundary for $j = N$, the transformation terms cannot pair to left of the Jordan-Wigner string and $j+1$ becomes $j+1 = 1$ for periodic boundary conditions in the new basis. For the separate boundary conditions of the string we let μ^x_N a dual lattice operator;

$$\mu^x_N \equiv \prod_{j=1}^{N} (1 - 2\hat{n}_j)\,, \tag{5.7}$$

such that the boundary terms are;

$$\begin{aligned}
\sigma^+_N \sigma^+_1 &= \mu^x_N \psi_1 \psi_N \\
\sigma^+_N \sigma^-_1 &= \mu^x_N \psi^\dagger_1 \psi_N \\
\sigma^-_N \sigma^+_1 &= \mu^x_N \psi^\dagger_N \psi_1 \\
\sigma^-_N \sigma^-_1 &= \mu^x_N \psi^\dagger_N \psi^\dagger_1,
\end{aligned} \tag{5.8}$$

Thus the transformed Hamiltonian becomes:

$$\begin{aligned}
H &= -\frac{J}{2}\sum_{j=1}^{N-1}\left[\frac{1}{4}\left(\psi^\dagger_{j+1}\psi^\dagger_j + \psi^\dagger_j\psi_{j+1} + \gamma\psi^\dagger_j\psi^\dagger_{j+1} + \gamma\psi_{j+1}\psi_j\right)\right] \\
&\quad -\frac{J\mu^x_N}{8}\left(\psi^\dagger_N\psi^\dagger_1 + \psi^\dagger_1\psi_N + \gamma\psi^\dagger_1\psi^\dagger_N + \gamma\psi_N\psi_1\right) \\
&\quad -h\sum_{j=1}^{N}(1 - 2\hat{n}_j).
\end{aligned} \tag{5.9}$$

The anisotropic XY-model in this form does not commute with σ^z, this means that it does not conserve the number of fermions, however since they are only created or destroyed in pairs then whether the system is even or odd remains consistent. [93]. By separating the Hamiltonian into even and odd parity, it can be managed using periodic and anti-periodic boundary conditions, incorporated into Eq. 5.9 by $\mu^x_N = +1$ for PBC and $\mu^x_N = -1$ for anti-PBC. These separate conditions describe the two differently entangled ground states of this system. The Hamiltonian can be separated as:

$$H = H^+ + H^-. \tag{5.10}$$

These separate parts of the Hamiltonian take different boundary conditions, where the even term H^+ takes PBC where $\psi_{j+N} = \psi_j$, and the odd term H^- take anti-PBC where $\psi_{j+N} = -\psi_j$. The even and odd Hamiltonians can be solved separately using the same methods giving the same dispersion relation. This is done by using their different boundary conditions to give formulae for the two lowest energy levels up to the critical field, which in the thermodynamic limit becomes the same level. This process will not be described in full, with the method outlined in more detail in Fabio Franchini's lecture notes [93]. The Hamiltonians are Fourier transformed into k-space and then for the Hamiltonian to be diagonalised the Bogoliubov transformation is used to define a new basis of operators. This new basis allows the Hamiltonian to be diagonalised [94]. The Bogoliubov transformation rewrites the Hamiltonian and finds its energy spectrum. The dispersion is given;

$$\mathcal{E}_k = \sqrt{(\cos k - h)^2 + \gamma^2 \sin^2 k}, \tag{5.11}$$

where in k-space the different periodic boundary conditions for the JW string can be rewritten as:

$$k = \begin{cases} \frac{2\pi}{N} n & \text{for PBC} \\ \frac{2\pi}{N}(n + 1/2) & \text{for anti-PBC} \end{cases} \tag{5.12}$$

where $n = 0, 1, \cdots, N-1$ the two energy levels are then calculated for each condition where:

$$E = \frac{1}{2} \sum_{k}^{N-1} \mathcal{E}_k. \tag{5.13}$$

Using Eq.5.11 and 5.13 with the two conditions on k from Eq. 5.12, then it is possible to further explore the behaviour of the energy spectrum of the anisotropic XY-model. We emphasize that the different boundary conditions that give the separate parity states are for the transformed Hamiltonian in Eq. 5.9 both applied to the original Hamiltonian for the anisotropic XY-model with PBC. The above derivation for the dispersion and energy levels was provided by Sam Carr. These equations for the energy levels are used in this section to calculate results for finite-sized calculations that tend towards the thermodynamic limit for field values up to the critical field $h_c = 1$. This is used for system sizes that can not be reached using exact diagonalisation. Fig.5.12 shows how the gap changes for systems up to $N = 16$. The figure inset zooms in near the critical field and shows how the two states become completely degenerate in the thermodynamic limit, using $N = 200$ and two anisotropy values for $\gamma = 0.2$ (red line) and $\gamma = 0.6$ (blue dashed line).

The purpose of the above derivation is to demonstrate that in the thermodynamic limit the states are truly degenerate past the factorisation field and up to the critical field.

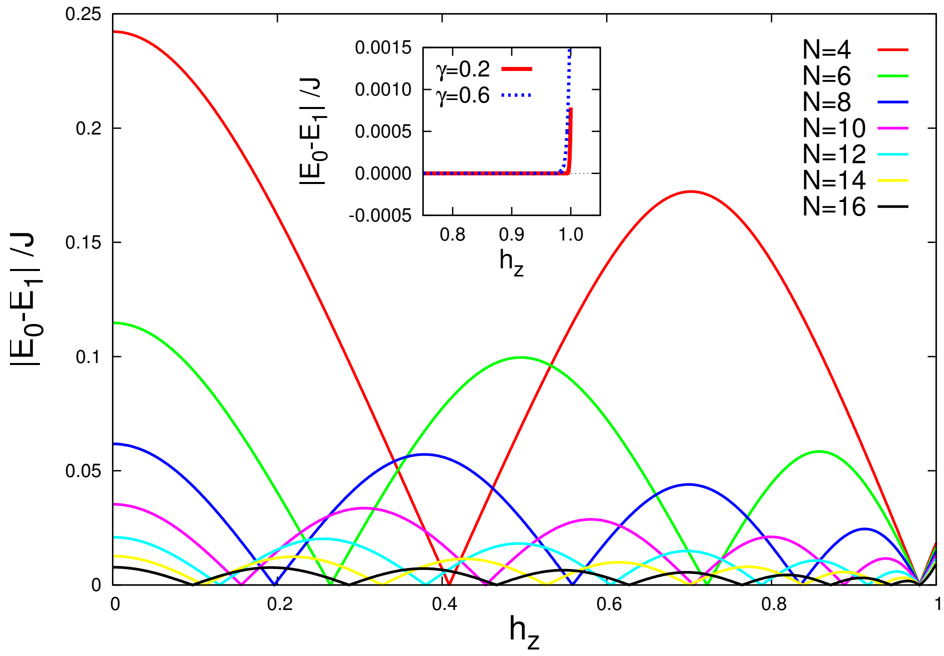

FIGURE 5.12: The gap function plotted from the absolute difference from Eq 5.11 given the two parameters in Eq. 5.12 provide by Sam Carr. This is for system sized up to $N = 16$ and the figure inset zooms in around the critical field for system size $N = 200$ for the anisotropy $\gamma = 0.2$ and 0.6.

This is important because it stresses the real difference for the entanglement transition whether it is in the thermodynamic limit or for finite-sized systems. In finite-sized systems the entanglement transition is a very clear switching of ground states at a level crossing. The gap is defined slightly differently in the thermodynamic limit as it is the gap between the two ground states and the first excited state. This difference from the gap could support the reasoning why finite-sized systems are so promising for the experimental detection of the entanglement transition at finite temperature.

Exploring the thermodynamic limit and understanding how the system become degenerate in the ground state, it is possible to use this to probe where the critical field of a system is, by using finite-sized calculations that best represent the behaviour of thermodynamic limit around criticality.

It seems evident that the system size up to $N = 10$ is enough to be able to predict thermodynamic limit behaviour, in particular with identifying the critical point. Figure. 5.13 is the gradient analysis of Figure. 5.11 for the different system sizes. Small intervals in the field are taken and their slope recorded. Just after the factorisation field, as the system grows, the gradient tends to zero. At higher fields it tends towards some finite

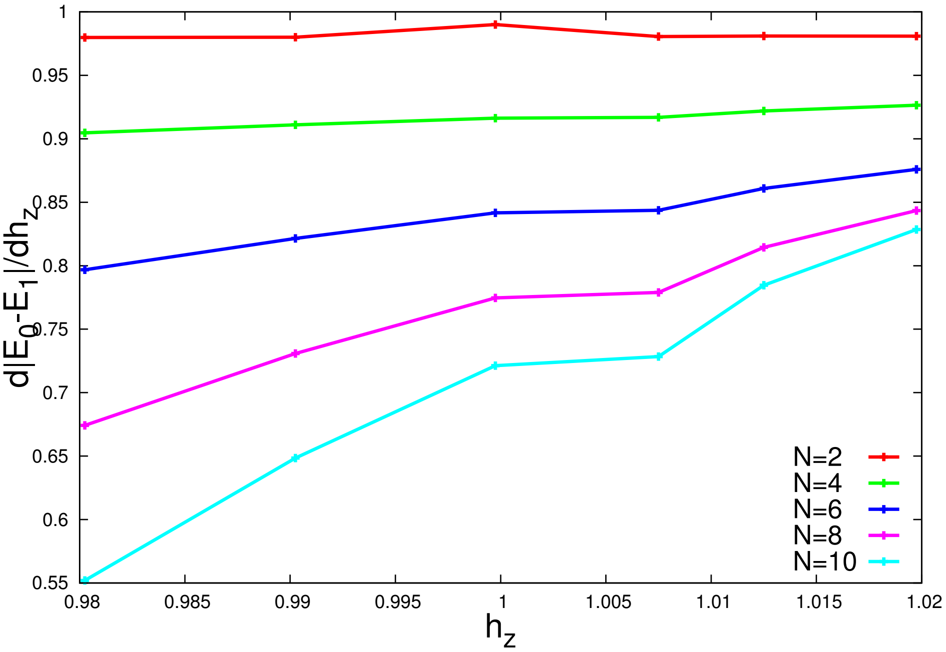

FIGURE 5.13: The gradient analysis of the energy is fully explored in this figure where for the values of the field between the factorisation field and $h = 1.00$ the gradient lowers as the system size N increases. Past this it tends towards a constant. The kink in the gradient suggest that in the thermodynamic limit the two lowest energy states peel away from each other between $0.99975 \leq h \leq 1.0075$, this indicate the critical field.

value. What is encouraging is that there is a very noticeable kink in the graph for $N = 8$ and $N = 10$, that indicates a critical field where the degeneracy splits. This 'kink' is situated with the accuracy of $0.99975 \leq h_c \leq 1.0075$. It can also be noted that for systems $N = 2, 4$ and 6 the critical field can not be seen in this way.

A similar analysis was undertaken for the XYZ-model to identify the critical field for the anisotropy parameters $\gamma = 0.5$ and $\Delta = 0.5$. The gap for this model is shown in Fig. 5.10. Similar to the XY-model, it can be seen that after the factorisation field $h_f = 1.414$ [3dp] the gap is closing again. At higher fields, the different system sizes converge on one slope. Within that region there is a critical field for the thermodynamic limit and a gradient analysis was able to approximate a value for the critical field as $h_f < h_c < 1.5$. An accuracy greater than this was not be observed. In an experimental situation even this approximation would be useful to material where the value for the critical field is unknown [95].

5.2 Additional Discussion

Within the duration of this project, some literature on the Entanglement Transition emerged, with two particular papers being very relevant to this collaboration. The first of the two papers is discussed in brief in this section to the extent that their goals overlap with the work presented in this thesis. The second paper uses neutron scattering predictions and is discussed in Chapter 6.

Campbell *et al.* 2014 thoroughly explore the long-range quantum correlations in 1D spin chains [9]. They use the anisotropic XY-model which is introduced in Chapter 3, in brief the interactions between spins are within the xy plane and the strength of the interaction in the x direction differs to the strength of the interaction in the y direction. The paper studies the version of the model with ferromagnetic interactions with an applied transverse field. The model has a ferromagnetic ordered phase and goes through a QPT and becomes paramagnetic at the QCP where the driving parameter is the applied field, which at this point is called the critical field. They use finite sized calculations to show that at finite temperatures the model complies with scaling behaviour and information about the thermodynamic limit can be estimated. Using these finite sized systems and techniques that describe the thermodynamic limit they probe criticality and a second point of interest where the system factorises.

In the thermodynamic limit the ground state of the anisotropic XY-model is doubly degenerate and at factorisation they become separable. For smaller systems sizes the two lowest states cross and become factorisable at the factorisation field. This is shown by Campbell *et al.* in Figure. 5.14.

In Figure 5.14 the applied transverse field is given by λ and the anisotropy between the interaction strength is given by γ. The left hand side figure shows the difference between the lowest two energy states, the white lines are where they cross. The right hand side figure gives an example of the energy spectrum for $\gamma = 0.5$ where the two lowest energy levels cross at a particular value of the field. This is for a system size of 5 spins where the levels cross twice but only one of the crossings coincide with the factorisation field. The key point about factorisation is that when the states become separable but are degenerate their can be no entanglement in the system. However above and below this field they are entangled the the act of passing through the factorisation field changes the

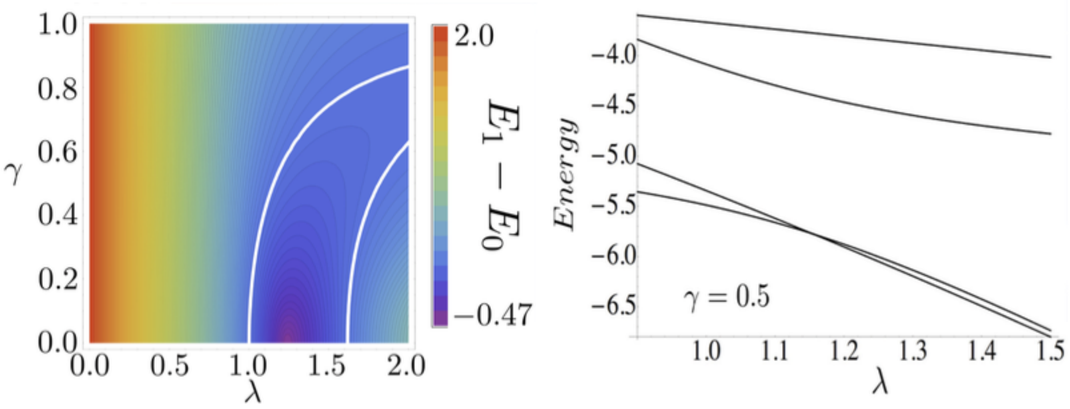

FIGURE 5.14: The energy spectrum information for the anisotropic XY-model from Campbell *et al.* (right) shows an example of the lowest energy level eigenvalues for an $N = 5$ spin chain with periodic boundary conditions. The two lowest eigenvalues cross twice, this is elaborated upon by the left figure which shows $E_1 - E_0$ for a range of the applied transverse field λ and the anisotropy parameter γ, the white lines indicate the two level crossings. [9].

type of entanglement present. This forms our definition of the entanglement transition that would predict a quantity of entanglement going to zero at the transitions and changing the type of entanglement after it.

Campbell *et al.* use two different measures of entanglement, these are Quantum Discord (QD) and Entanglement of Formation (EoF) [9]. QD uses the concept of information behind von Neumann Entropy as described in section 2.2.1. The EoF quantifies the minimum number of entangled qubits that would be needed to replicate the real state being measured and uses concurrence as described in section 2.2.2. They use these techniques to probe the correlations and thermal correlations in the system for both finite sized systems and in the thermodynamic limit. They conclude that the ground state factorisation that is observed in the finite sized calculations is an inherently different quantum transition from criticality.

5.3 Factorisation and Degeneracy

The key requirements for the entanglement transition in finite-sized systems are clear; firstly the two ground states with parallel and anti-parallel entanglement to become degenerate at a level crossing, and secondly the states need to factorise in order to break the entanglement at that point. For small systems larger than the dimer, the two ground states cross multiple times offering more than one field where the states are degenerate. It is at this stage where it needs to be shown that the degeneracy does not necessarily lead to factorisation. As it is seen in the thermodynamic limit where the states are completely degenerate, it is the factorisation field that separates the states as proven in Kurmann *et al.* [18].

Following from the process employed in Chapter 4 where we looked at the structure of the eigenstates that were the two ground states before and after the entanglement transition we found the wave functions of our model analytically for $N = 2$. To recap, for $h \leq h_f$, the ground state is the anti-ferromagnetic singlet $|\psi_A\rangle = \frac{1}{\sqrt{2}}\big(|\uparrow\downarrow\rangle - |\downarrow\uparrow\rangle\big)$. For $h \geq h_f$ the ground state is ferromagnetically entangled: $|\psi_B\rangle = \frac{1}{\sqrt{1+\delta^2}}\big(|\uparrow\uparrow\rangle - \delta\,|\downarrow\downarrow\rangle\big)$. The parameter δ controls the amount of parallel entanglement in this state. It has the form $\delta = \sqrt{1 + h_z^2/\gamma^2} - h_z/\gamma$ and evidently $\delta \to 0$ as $h_z \to \infty$. In Chapter 4, examples for the anisotropic XY-model and XYZ-model were taken to demonstrate factorisation at h_f. In this section, we will develop this further and apply it to the $N = 4$ systems for OBC and PBC and demonstrate that it is only at the level crossing that coincides with h_f where factorisation is possible. As the system sizes increase, so does the Hilbert space by a factor of 2^N making it considerably more difficult to examine the wavefunctions. For $N = 4$ there are 16 basis states that make up the Hilbert space and it is still reasonable to examine the states directly. The basis is $\{|\uparrow\uparrow\uparrow\uparrow\rangle, |\uparrow\uparrow\uparrow\downarrow\rangle, |\uparrow\uparrow\downarrow\uparrow\rangle, |\uparrow\uparrow\downarrow\downarrow\rangle, |\uparrow\downarrow\uparrow\uparrow\rangle, |\uparrow\downarrow\uparrow\downarrow\rangle, |\uparrow\downarrow\downarrow\uparrow\rangle, |\uparrow\downarrow\downarrow\downarrow\rangle, |\downarrow\uparrow\uparrow\uparrow\rangle, |\downarrow\uparrow\uparrow\downarrow\rangle, |\downarrow\uparrow\downarrow\uparrow\rangle, |\downarrow\uparrow\downarrow\downarrow\rangle, |\downarrow\downarrow\uparrow\uparrow\rangle, |\downarrow\downarrow\uparrow\downarrow\rangle, |\downarrow\downarrow\downarrow\uparrow\rangle, |\downarrow\downarrow\downarrow\downarrow\rangle\}$ for sites labeled $|1234\rangle$.

The $N = 4$ systems for both open and periodic boundary conditions have two level crossings, but only with periodic boundary conditions does one of these level crossings coincide with the factorisation field. With the dimer it was seen that the degeneracy at a level crossing, allowed for a linear combination of these states to become factorisable. For systems with more than one level crossing it is important to assess whether the level crossing at the factorisation field offers factorisation and verify that the others do not. The linear combination of the ground state at a level crossing is, for any system:

$$|\Psi\rangle = A\,|\psi_A\rangle + B\,|\psi_B\rangle\,. \tag{5.14}$$

For all values of N we investigated, the last crossing between the two ground states is at h_f. The ground state is $|\psi_A\rangle$ for $h_z \leq h_f$ and $|\psi_B\rangle$ for any $h_z > h_f$. At h_f the coefficients A and B in the linear combination (Eq. 5.14) can be chosen to produce an unentangled state, i.e. one of the form:

$$\begin{aligned} |\Psi\rangle &= (a_1 |\uparrow\rangle + b_1 |\downarrow\rangle) \otimes (a_2 |\uparrow\rangle + b_2 |\downarrow\rangle) \otimes \\ &\quad \ldots \otimes (a_{N-1} |\uparrow\rangle + b_{N-1} |\downarrow\rangle) \otimes (a_N |\uparrow\rangle + b_N |\downarrow\rangle) . \end{aligned} \tag{5.15}$$

Indeed Kurmann, Thomas and Muller proved that the particular factorised state obtained by choosing $a_{2n+1} = a_1, b_{2n+1} = b_1, a_{2n} = a_2, b_{2n} = b_2$ for all $n = 1, 2, \ldots$ is realised at h_f but not at any other value of the field (we note that the proof in Kurmann *et al.* is N-independent)[18]. In particular, the Kurmann-Thomas-Muller state is not realised at the other crossings occurring at lower values of h_z. One could ask, however, whether the more general factorised state in Eq.5.15 could be achieved by an appropriate choice of the coefficients A and B at other values of the field. We have checked this explicitly in the $N = 4$ case by examining the numerically-determined wave functions.

Factorisation cannot be achieved unless there is degeneracy between $|\psi_A\rangle$ and $|\psi_B\rangle$. This still leaves open the possibility of factorisation at the field $h_1 < h_f$ where the first gap closing occurs. To examine this possibility, we equate the linear superposition (Eq. 5.14) to the factorised state given in Eq. 5.15. For N spins, this leads to 2^N equations (one for each spin) in $2N + 2$ unknowns (A, B and the a and b coefficients). The variables are therefore over-determined for $N \geq 4$. we observe a common structure to the two ground states, such that the component parts of the basis used in ψ_A are not used in

ψ_B and vice versa, as shown in the below representation of the states:

$$A\left|\psi_A\right\rangle = A\begin{pmatrix} 0 \\ \alpha_1 \\ -\alpha_1 \\ 0 \\ \alpha_1 \\ 0 \\ 0 \\ -\alpha_2 \\ -\alpha_1 \\ 0 \\ 0 \\ \alpha_2 \\ 0 \\ -\alpha_2 \\ \alpha_2 \\ 0 \end{pmatrix}, \quad B\left|\psi_B\right\rangle = B\begin{pmatrix} -\beta_1 \\ 0 \\ 0 \\ \beta_2 \\ 0 \\ -\beta_3 \\ \beta_2 \\ 0 \\ 0 \\ \beta_2 \\ -\beta_3 \\ 0 \\ \beta_2 \\ 0 \\ 0 \\ -\beta_4 \end{pmatrix}, \tag{5.16}$$

thus the system reduces to 2^{N-1} equations involving the A coefficient and another 2^{N-1} equations involving the B coefficient for $N = 4$ with periodic boundary conditions. Any linear combination of the two lowest states when they are degenerate are in turn valid eigenstates. Using α and β we show the vector configuration of the states for $N = 4$ that when compared to the factorised state given by Eq. 5.15, the 16 simultaneous equations that are formed are decoupled into two subsets each dependent on one of the single-spin states:

$$\begin{aligned}
A\alpha_1 &= a_1a_2a_3b_4 \quad , \quad -B\beta_1 = a_1a_2a_3a_4,\\
-A\alpha_1 &= a_1a_2b_3a_4 \quad , \quad B\beta_2 = a_1a_2b_3b_4,\\
A\alpha_1 &= a_1b_2a_3a_4 \quad , \quad -B\beta_3 = a_1b_2a_3b_4,\\
-A\alpha_2 &= a_1b_2b_3b_4 \quad , \quad B\beta_2 = a_1b_2b_3a_4,\\
-A\alpha_1 &= b_1a_2a_3a_4 \quad , \quad B\beta_2 = b_1a_2a_3b_4,\\
A\alpha_2 &= b_1a_2b_3b_4 \quad , \quad -B\beta_3 = b_1a_2b_3a_4,\\
-A\alpha_2 &= b_1b_2a_3b_4 \quad , \quad B\beta_2 = b_1b_2a_3a_4,\\
A\alpha_2 &= b_1b_2b_3a_4 \quad , \quad -B\beta_4 = b_1b_2b_3b_4.
\end{aligned} \tag{5.17}$$

Due to the few parameters that characterise the amplitudes it can be deduced that all 'a' coefficients are the same magnitude as are all 'b' coefficients.

$$\begin{aligned}
|a_1| &= |a_2| = |a_3| = |a_4| \text{ where } -a_1 = a_2 = a_3 = a_4;\\
|b_1| &= |b_2| = |b_3| = |b_4| \text{ where } -b_3 = b_1 = b_2 = b_4.
\end{aligned} \tag{5.18}$$

This reduces the complexity of the problem and allows us to find equivalent ratios from both states that must be equally satisfied, if the states are to be completely separable:

$$\frac{\beta_1}{\beta_4} = \frac{a^4}{b^4} \quad ; \quad \frac{\alpha_1^2}{\alpha_2^2} = \frac{a^4}{b^4}. \tag{5.19}$$

The two degenerate states are factorisable only if the following ratio is true:

$$\frac{\alpha_1^2}{\alpha_2^2} \equiv \frac{\beta_1}{\beta_4}. \tag{5.20}$$

This equality was tested for both level crossings for the $N = 4$ system and was found true for the values at the factorisation field. The ratio is not satisfied at the first level crossing where the states, though degenerate, are unable to factorise. The results for both level crossing are summarised in table 5.1. The table gives results for level crossings for the anisotropy parameter $\gamma = 0.6$ which leads to the first level crossing at $h_{LC1} = 0.345$ (found numerically) and the second level crossing at the factorisation field $h_{LC2} = 0.800$ (found numerically and verified by Eq. 3.8). Here, it is shown that the results for the first level crossing do not obey Eq. 5.20 and does not factorise; whereas, the results for the second level crossing, at the factorisation field does obey Eq. 5.20 and therefore, can fully factorise.

Field h	$\alpha_1 =$	$\alpha_2 =$	Ratio $\alpha =$	Result:
$h_{LC1} = 0.345$	0.43279197427683	0.250381927198709	2.9878 [4 d.p]	
	$\beta_1 =$	$\beta_2 =$	Ratio $\beta =$	
	0.4111456380398136	0.1729715591278917	2.3770 [4 d.p]	×
Field h	$\alpha_1 =$	$\alpha_2 =$	Ratio $\alpha =$	Result:
$h_{LC2} = 0.800$	0.474341649025257	0.15811388300842	9.0 [8 d.p]	
	$\beta_1 =$	$\beta_2 =$	Ratio $\beta =$	
	0.7717436331412898	0.0.08574929257125442	9.0 [8 d.p]	✓

TABLE 5.1: The table documents the results on whether a level crossing in the $N = 4$ spin system with PBC can factorise or not. Using the values obtained numerically for $N = 4$ with in plane anisotropy $\gamma = 0.6$ at the levels crossings; $h_{LC1} = 0.345$ and $h_{LC2} = 0.800$. For the first level crossing, at h_{LC1}, the parameters for α_1, α_2, β_1 and β do not obey the ratio derived in Eq.5.20 and are unable to factorise. For the second level crossing, at the factorisation field: $h_{LC2} = 0.800$, the parameters for α_1, α_2, β_1 and β not obey the ratio derived in Eq.5.20 and therefore can factorise.

For larger systems it becomes impractical to directly examine the coefficients of the ground state wavefunctions. In these instances it is possible to observe the real space correlation functions. At factorisation, as the states become separable the system becomes semi-classical. This is reflected in the correlation functions in the LRO phase where the correlation functions, in essence go ‘flat’ and ground state fluctuations disappear [25]. By scanning over the multiple level crossings for larger systems we observe true factorisation only for the level crossings that coincide with the factorisation field, the results for the correlation functions are given in section 5.5.

5.4 Wavefunctions

By taking advantage of the $N = 4$ system and the manageable size of the states, it is possible to probe the states exactly. This allows us to explore this complex arrangement of entanglement within the different ground states, and visually show the difference in the states between OBC and PBC.

The differences between the open boundary conditions and the periodic boundary conditions become vividly apparent when viewed visually. By looking at the energy levels alone, it is the similarities that are obvious; most prevalently it can be seen that the two energy levels cross the same number of times. The periodic boundary conditions add a symmetry to the system, which is reflected in the wavefunction and is best discussed by plotting the amplitude of the probability of our chosen basis states for the ground state wavefunction. The basis is given in the above section 5.3. These are given in Fig. 5.15, 5.16 and 5.17 for OBC, PBC and the XYZ-model with PBC respectively.

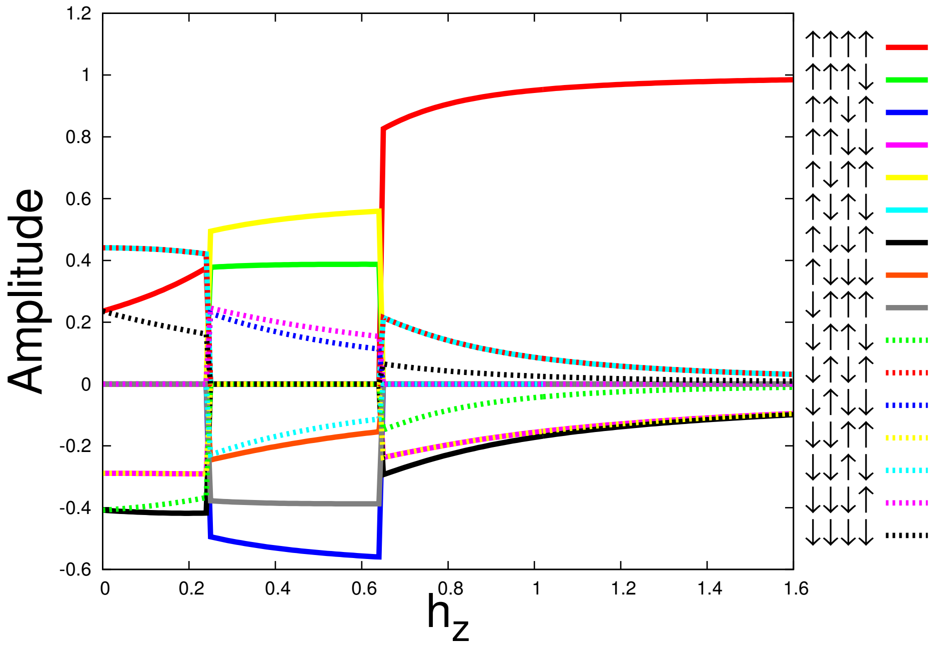

FIGURE 5.15: The wavefunction amplitude for the anisotropic XY-model spin chain for $N = 4$ and $\gamma = 0.6$. The spin basis for a $N = 4$ system is more complicated than for the dimer and without PBC the occupied states lack symmetry. Only the fully antiferromagnetic states pair up ($|\uparrow\downarrow\uparrow\downarrow\rangle + |\downarrow\uparrow\downarrow\uparrow\rangle$) and the two ferromagnetic anti aligned pairs ($|\uparrow\uparrow\downarrow\downarrow\rangle + |\downarrow\downarrow\uparrow\uparrow\rangle$)

The wavefunction for the ground state of the $N = 4$ chain (OBC) is similar to the structure for PBC, but lacking in symmetry which means that the amplitudes do not group like they did for PBC. The amplitude of the individual basis states rarely repeat with only the fully antiferromagnetic states ($|\uparrow\downarrow\uparrow\downarrow\rangle + |\downarrow\uparrow\downarrow\uparrow\rangle$) matching interactions and amplitudes, and the two ferromagnetic anti aligned pairs ($|\uparrow\uparrow\downarrow\downarrow\rangle + |\downarrow\downarrow\uparrow\uparrow\rangle$) as indicated in Fig. 5.15.

The states swap over at the level crossing and switch from one set of eight basis states with non-zero amplitudes to the other set of eight, which would be a step towards making the states separable at the level crossings. As neither of the level crossings occur at the factorisation field for OBC and the differences in the amplitudes, it is not possible to acquire a linear combination of these states that leads to factorisation.

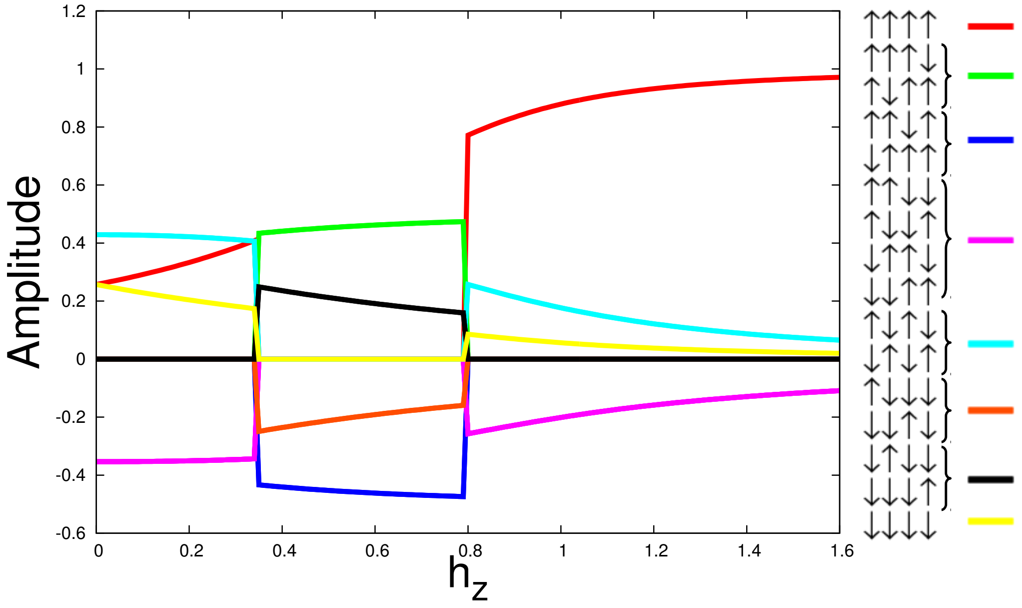

FIGURE 5.16: The wavefunction amplitude for the anisotropic XY-model for a $N = 4$ system with period boundary conditions for $\gamma = 0.6$. With the periodic boundary conditions all spins in the system experience the same interactions. This four-fold symmetry is reflected in the occupied ground state, where orientation with the same interactions can now double up as indicated in the legend.

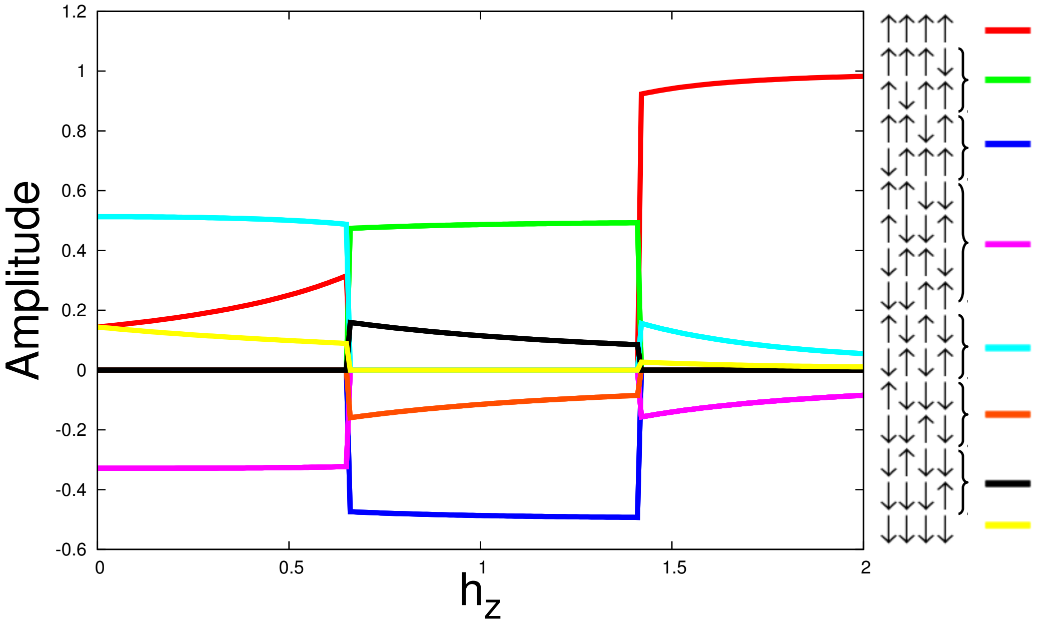

FIGURE 5.17: The wavefunction amplitude for the anisotropic XYZ-model for a $N = 4$ system with period boundary conditions for $\gamma = 0.6$. As supported by the dimer results and the energy spectrum there is no real difference in the XYZ-model where the same basis states are occupied in the ground state as found in the XY-model.

When periodic boundary conditions are applied, all the conditions for a factorised ground state come together. The amplitudes of the wavefunction for the anisotropic XY-model with $\gamma = 0.6$ are given in Fig.5.16 and in comparison to OBC the wavefunction becomes much clearer to understand. To aid this, the two states can be rewritten in kets representing a plaquette $N = 4$ arrangement:

$$
\begin{aligned}
|\psi_A\rangle &= |\alpha_1| \left| \begin{array}{c} \boxed{} \\ \uparrow\ \uparrow \end{array} \right\rangle + \left| \begin{array}{cc} \begin{matrix}\uparrow\\ \uparrow\end{matrix} & \boxed{\begin{matrix}\\ \end{matrix}} \end{array} \right\rangle + \left| \begin{array}{c} \uparrow\ \uparrow \\ \boxed{} \end{array} \right\rangle + \left| \begin{array}{cc} \boxed{\begin{matrix}\\ \end{matrix}} & \begin{matrix}\uparrow\\ \uparrow\end{matrix} \end{array} \right\rangle \\
&\quad + |\alpha_2| \left(\left| \begin{array}{c} \boxed{} \\ \downarrow\ \downarrow \end{array} \right\rangle + \left| \begin{array}{cc} \begin{matrix}\downarrow\\ \downarrow\end{matrix} & \boxed{\begin{matrix}\\ \end{matrix}} \end{array} \right\rangle + \left| \begin{array}{c} \downarrow\ \downarrow \\ \boxed{} \end{array} \right\rangle + \left| \begin{array}{cc} \boxed{\begin{matrix}\\ \end{matrix}} & \begin{matrix}\downarrow\\ \downarrow\end{matrix} \end{array} \right\rangle \right) \qquad (5.21)
\end{aligned}
$$

$$
\begin{aligned}
|\psi_B\rangle &= |\beta_1| \left| \begin{array}{cc} \uparrow & \uparrow \\ \uparrow & \uparrow \end{array} \right\rangle + |\beta_4| \left| \begin{array}{cc} \downarrow & \downarrow \\ \downarrow & \downarrow \end{array} \right\rangle \\
&\quad + |\beta_2| \left(\left| \begin{array}{cc} \uparrow & \downarrow \\ \downarrow & \uparrow \end{array} \right\rangle + \left| \begin{array}{cc} \downarrow & \uparrow \\ \uparrow & \downarrow \end{array} \right\rangle \right) \\
&\quad + |\beta_3| \left(\left| \begin{array}{cc} \downarrow & \uparrow \\ \downarrow & \uparrow \end{array} \right\rangle + \left| \begin{array}{cc} \uparrow & \downarrow \\ \uparrow & \downarrow \end{array} \right\rangle + \left| \begin{array}{cc} \downarrow & \downarrow \\ \uparrow & \uparrow \end{array} \right\rangle + \left| \begin{array}{cc} \uparrow & \uparrow \\ \downarrow & \downarrow \end{array} \right\rangle \right) \qquad (5.22)
\end{aligned}
$$

Where we have used the standard shorthand $\boxed{}$ for singlets. Here, we write the ket notation for the $N = 4$ system in a square clockwise arrangement to be able to demonstrate a singlet state between sites four and one, i.e. $\left|\begin{smallmatrix}1&2\\4&3\end{smallmatrix}\right\rangle$. The parameters α's and β's are functions of h_z and are from Eq.5.16. The field-evolution of these wavefunctions is plotted in Fig.5.16 alongside the $N = 2$ case. Note that both ground states feature both parallel and anti-parallel entanglement.

In continuation from conclusions drawn from the dimer, the XYZ-model $N = 4$ system is consistent with the anisotropic XY-model. The same states are occupied at similar proportions and the same conditions for factorisation are satisfied at the second level crossing.

The size of the states quickly become unmanageable for systems above $N = 4$ where $N = 6$ states are made up of 64 bases, even visually it is impractical. Fortunately there are other ways that indicate a factorised state in a spin chain. In the thermodynamic limit the correlation functions are used to find a 'flatness' that would indicate a semi-classical state where the spins classically snap into antiferromagnetic long-range order.

5.5 Correlation Functions

The correlation functions are an effective measurement that visually represent the spin behaviour in a chain. In the thermodynamic limit the real space correlators take any spin in the chain and compare it to all others as a function of their displacement. This can show the order and give information about the correlation length of the system. Directly, the correlation functions can not quantify the entanglement in the system and even a very strongly correlated system does not equal an entangled system.

For all directions for $\alpha\beta = x, y, z$ the correlation functions for displacement R where $R = |i - j|$ are given as:

$$\rho_{\alpha\beta}(R) = \left\langle \hat{S}_i^\alpha \hat{S}_{i+R}^\beta \right\rangle . \tag{5.23}$$

For antiferromagnetic interactions, the correlation function zigzags between anti-correlated and correlated as the spins form a general anti-ferromagnetic order. The maximum value the correlation functions can take is $\rho_{\alpha\beta}(R) = \frac{1}{4}$, an example of this being at $R = 0$ when the calculation is for a spin correlated with itself. It should be noted that to have LRO, the correlators do not have to be all maximally correlated. LRO is demonstrated by a non-zero correlator at long distances, where it can be shown that the correlator tends to some finite value as $R \to \infty$. The behaviour of the correlation functions is carefully considered in the numerical results depending on the computational limit and requirement on R, meaning that when discussing the thermodynamic limit it is important to verify that all calculations computationally converge.

Quantum fluctuations in the ground state of the anisotropic XY-model effect the correlation functions but do not destroy LRO in the antiferromagnetically ordered phase. Thermal fluctuation can destroy LRO and their effects can mask the behaviour of quantum fluctuations. Above zero temperature there are additional thermal fluctuations and for the system to still exhibit an entanglement transition it needs to be in a regime that is dominated by the ground state. This means that the temperature of the system needs to be comparable to the gap of the system, where in the thermodynamic limit this gap is between the doubly degenerate ground state and the excited states. Fig.

5.18 shows diagrammatically an antiferromagnetic chain with LRO in the ordered phase with quantum fluctuations; a classical antiferromagnetic correlation with LRO, such that would be seen at the factorisation field; and an antiferromagnetic correlations with very strong fluctuation that could be thermal fluctuations, with the full length of decay of the correlators shown demonstrating a finite correlation length [25] [56] [96] [48].

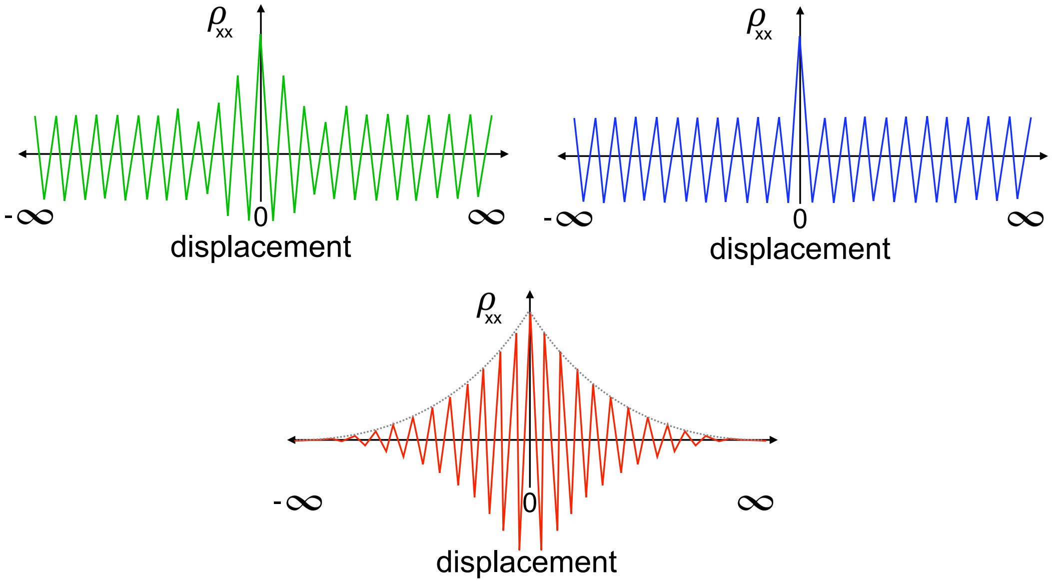

FIGURE 5.18: The green plot shows an example of an antiferromagnetic chain with LRO and quantum fluctuations. The blue plot shows an example of an antiferromagnetic chain with LRO and no fluctuations. The red plot shows an example of an antiferromagnetic chain with no LRO with a finite correlation length, where the fluctuations that caused the decay could be thermal fluctuations.

Ideally, in the correct temperature regime, the effect of the factorisation field would be enough to overcome any thermal and quantum fluctuations and produce classical looking ‘flat’ correlation function . This temperature needs to be comparable to the gap in the system. This is a very low temperature, which has implications on the numerical methods used to compute the results in the thermodynamic limit. The computations need to go to larger and larger system sizes the lower the temperature is, in order to capture the full behaviour of the system. This is related to the correlation length and becomes incredibly important at these low temperatures, where the decay in correlations span large distances. If the full correlation length is not taken, then the system when Fourier transformed can lead to false results [3].

---

[3] Imagine an extremely long correlation length that decays over many sites but only the portion of the middle of the correlation function was taken and Fourier Transformed. The middle section would appear ‘flat’ and it’s Fourier transform would tend towards a delta peak.

Computationally, the lowest temperature that was achieved with full convergence of results was at $T = 0.1J$. This was not low enough to find the entanglement transition in the thermodynamic limit and was in agreement with unpublished experimental results from within the collaboration.

5.5.1 Thermodynamic Limit

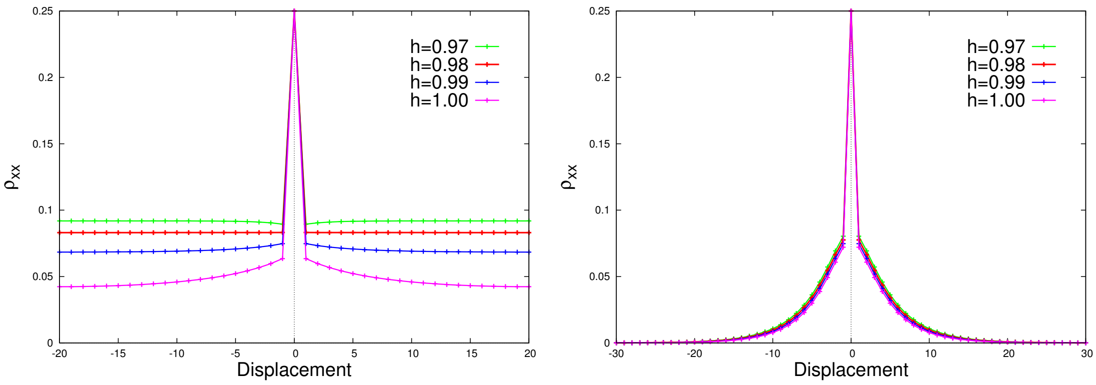

FIGURE 5.19: The absolute value for the correlation function for the xx interactions for the thermodynamic limit. (a) is the ground state correlations across the factorisation field $h_f = 0.98$ [3 sf] for $\gamma = 0.2$. The red line shows a flat correlation function at the factorisation field and it can be clearly seen that above and below this value the corrrelators buckle around the red line demonstrating the quantum fluctuations. (b) shows the same results for above zero temperature for $T = 0.1J$ the correlations in the system decay monotonically, no LRO is recovered at the factorisation field or around it, and definitely no LRO flat correlations. These results were calculated using the equations given in Chapter. 3 section 3.2 for the method developed by Barouch and McCoy [10]

Fig. 5.19 shows results calculated for the thermodynamic limit in the ground state and at $T = 0.1J$, across the factorisation field for $\gamma = 0.2$ at $h_f = 0.980$. The absolute value for the correlator is taken as it is already known that the system is antiferromagnetic for the xx correlation function. This makes it is easier to identify true 'flatness' in the ordered phase. The red line shows a flat correlation function at $h_f = 0.980$ exactly and just above and below it there is a 'buckling' around that flat line indicating quantum fluctuations. At above zero temperature the decay of the correlation length is severe at $T = 0.1J$ and there is no LRO an no identifiable quantum fluctuations.

The correlation functions, and as a progression the neutron scattering cross section, are global measurements, which is another reason why it is vital to capture the entire correlation behaviour of the system. It is important to be able to quantify and identify entanglement using a global measurement. Entanglement is typically quantified by a local theoretical measures, like concurrence. When using finite-sized systems, the difference between a global measurement and a local measurement becomes less distinct, and it is more relevant to discuss the finite-sized systems with PBC as molecular magnets instead of using them to describe bulk properties of the thermodynamic limit. The correlations are strengthened by periodic boundary conditions, making them ideal candidates to resist fluctuations in the correlation functions as is demonstrated in the section below.

5.5.2 Finite Chains

In this section, the correlation functions are used to explore the region across the level crossings in the finite-sized systems for both the OBC and PBC and for low temperature calculations.

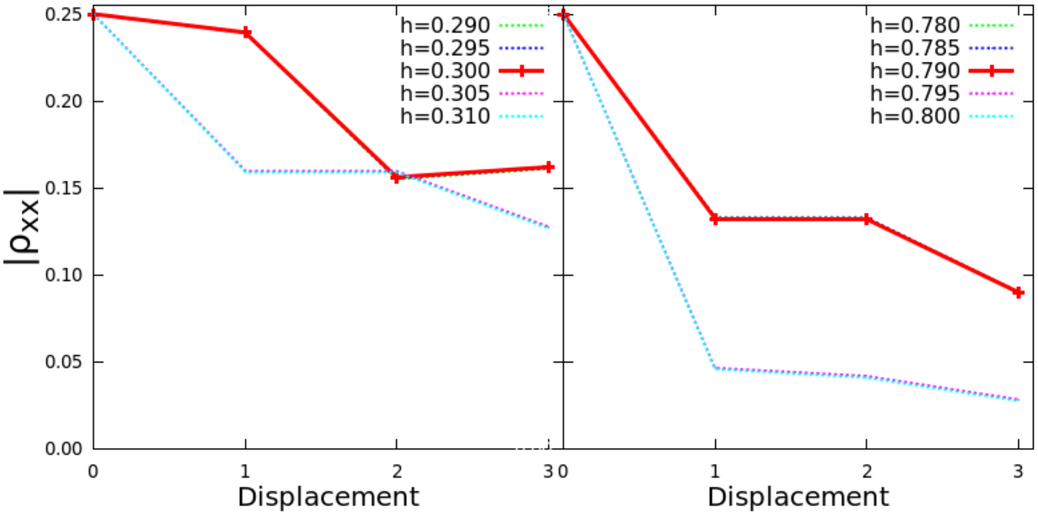

Figure 5.20: The absolute value for the correlation function for the xx interactions for the $N = 4$ chain with open boundary conditions for the interactions from one edge of the chain to the other, where the pairs of correlations ($\rho_{i,j}$) start at site $i = 1$ and the comparison site j runs from $j = 1, 2, 3, 4$ to the other edge of the chain. Field values are taken across the two level crossing for (a) LC1 and (b) LC2. The degeneracy at these points do not offer a flatness in the correlation function, however the presence of a level crossing is indicated by a general 'step' down in the correlation function. For both the plots the correlation functions just before the levels crossings do not noticeably change and are behind the red lines

Fig. 5.20 shows the absolute value for the real space correlator ρ_{xx} . For a better comparison to the periodic boundary conditions the displacement of the correlator is taken for pairs of spins from one end of the chain to the other where the pairs of

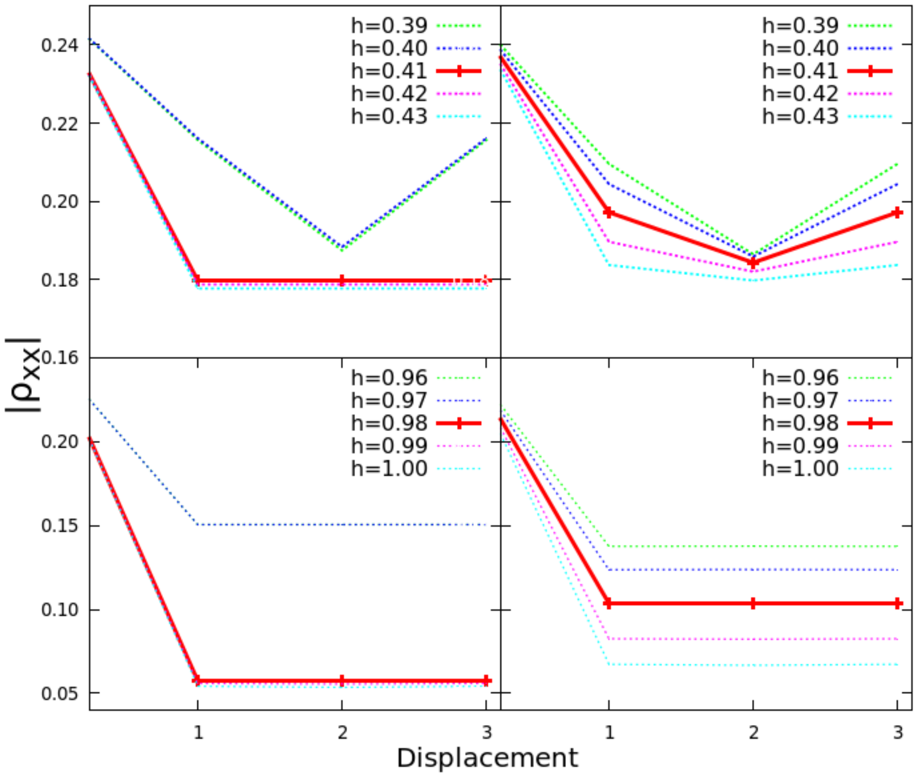

FIGURE 5.21: The absolute value for the correlation function for the xx interactions for the $N = 4$ chain with periodic boundary conditions where because of the symmetry for the PBC case the displacement is $R = |i - j|$. The first column are results for the zero temperature ground state and the second is for above zero temperature at $T = 0.1J$. The interactions are the same for any site at the displace on the x axis due to the symmetry of the system. As with the open boundary conditions, results across both the level crossings are shown in the rows. The $N = 4$ system is quite unique and with the system being so small, a flat correlation function is achieved at the first level crossing in the ground state despite the system not completely factorising. The correlator remains flat and the second level crossing at the factorisation field is indicated by a large 'jump' in the correlations. At $T = 0.1J$ it is seen that the temperature fluctuations destroy LRO at LC1 but it is recovered at the factorisation field $h_f = 0.980$.

correlations ($\rho_{xx}(i,j)$) start at site $i = 1$ and the comparison site j runs from $j = 1, 2, 3, 4$ to the other edge of the chain. This way the furthest displacement is possible to analyse the full 'length' of the correlation function. Measurements are taken that span both level crossings for this system at $h_{LC1} = 0.300$ and $h_{LC2} = 0.790$, neither of which coincide with the potential factorisation field for $\gamma = 0.2$ at $h_f = 0.980$. Without the feature of a level crossing there is no chance to break the entanglement. It has already been shown in previous sections that these states do not factorise. As a test to the correlation functions it is also observed that no 'flatness' is achieved. Despite this, the states still cross over and a 'jump down' in the correlators is seen, thus the correlators are sensitive to the level crossings.

The $N = 4$ system with PBC in Fig. 5.21 shows the correlators (left column) for the ground state and (right column) for the temperature $T = 0.1J$. With PBC, the $N = 4$ correlators become quite compact with the furthest distance two spins can be apart being two sites. Therefore any flatness in the correlations are reliant on the correlation between sites 1 and 3 (or 2 and 4). This isn't ideal, so it is fortunate that an analysis of the states was directly possible. At zero temperature, the systems' xx-correlation function goes flat at the first level crossing and remains so until it passes through the second level crossing at the factorisation field. By looking at the $T = 0.1J$ correlator it is seen that the correlator only goes flat at the factorisation field $h_f = 0.980$. This is robust at these temperatures. This is very promising and could indicate a temperature range for possible experimentation.

For the slightly larger systems for $N = 6$ with OBC and PBC assessing the correlation functions gives a wider distance of sites to confirm a flat behaviour for the whole system. It is the best option to look for factorisation where we can no longer study the states on their own. Results are plotted for measurements that span each level crossing for the parameter $\gamma = 0.2$ for OBC and PBC at zero and finite temperatures.

The $N = 6$ open chain correlation functions plotted in Fig. 5.22 holds no surprises. Across all three of the level crossings there is no evidence for a factorised state. Again, the level crossings do not coincide with the factorisation field but they are detectable as jumps in the correlators.

The same system with PBC becomes instantly more interesting. At each level crossing, as the field increases to the final level crossing at the factorisation field, the correlators detect the crossing but experience an overall reduction. As Fig.5.23 shows, at the first level crossing exactly, there is some flattening in the 'middle' of the system. This flattening spreads a little on the second level crossing and at the factorisation field the system goes completely flat.

Above zero temperature for $T = 0.1J$ it can be seen in Fig.5.24 that the flatness in the correlators at the factorisation field is robust at this temperature. This stands as an encouraging result for finite-sized systems and a more thorough temperature analysis takes place in the next chapter when discussing neutron scattering data.

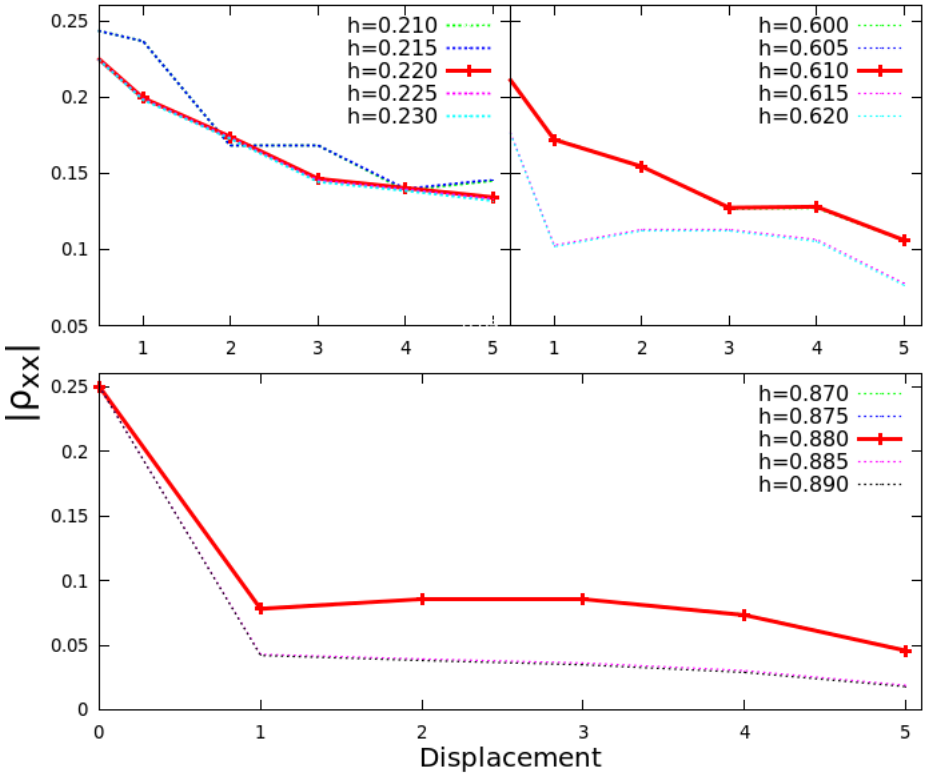

FIGURE 5.22: The absolute value for the correlation function for the xx interactions for the $N = 6$ chain with open boundary conditions for the interactions from one edge of the chain to the other, where the pairs of correlations ($\rho_{i,j}$) start at site $i = 1$ and the comparison site j runs from $j = 1, 2, 3, 4, 5, 6$ to the other edge of the chain. Again, without periodic boundary condition edge effects prevent any LRO or 'flatness' in the correlation functions in the single chains.

The $N = 8$ systems are the last system size where correlators will be plotted for the same parameters and temperatures given from the $N = 6$ example. The trends and advantages of these systems are clear and there are more techniques to consider in conjunction with the correlations functions. Fig.5.25 shows the correlation function for a $N = 8$ single chain spanning its four level crossings. No indication to a factorised state is found across any of the level crossings. Interestingly, at the last level crossing, the correlator does level out in comparison, but can not maintain a flat behaviour towards the the edge of the chain.

The correlations for the $N = 8$ system with PBC at zero temperature is shown in Fig.5.26 with its temperature counterpart at $T = 0.01J$ given in Fig.5.27 spanning its four level crossings. Like the $N = 6$ model, with each level crossing as the field increases the correlators increasingly flatten at the that degenerate point. The states switch until at the factorisation field the correlators become truly flat indicating a classical correlation.

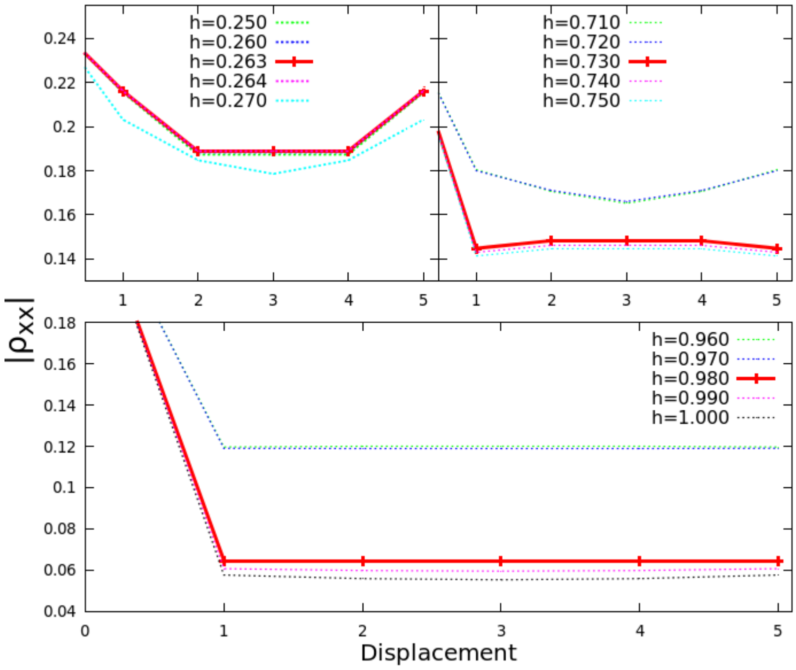

FIGURE 5.23: The absolute value for the correlation function for the xx interactions for the $N = 6$ system with periodic boundary conditions taking field values across all three level crossings.

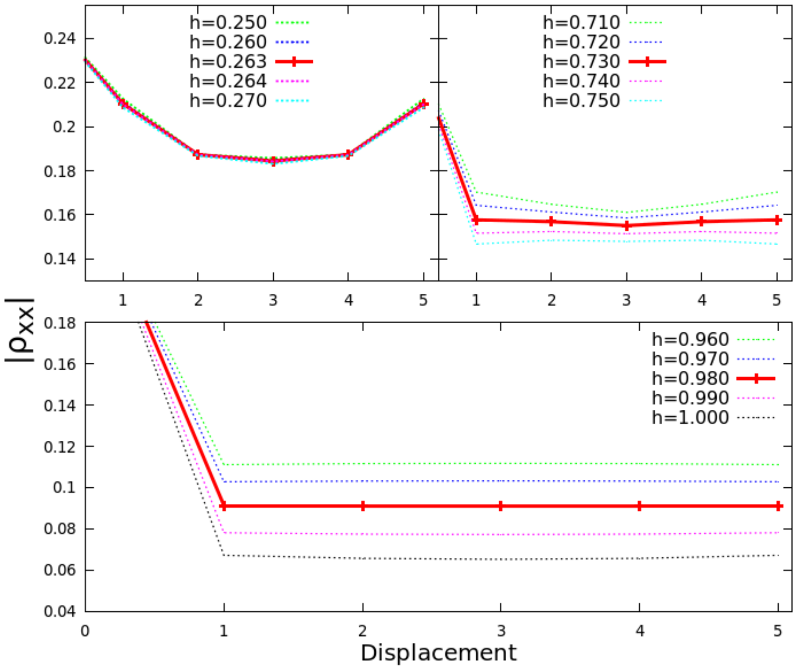

FIGURE 5.24: The absolute value for the correlation function for the xx interactions for the $N = 6$ system with periodic boundary conditions taking field values across all three level crossings for $T = 0.1J$.

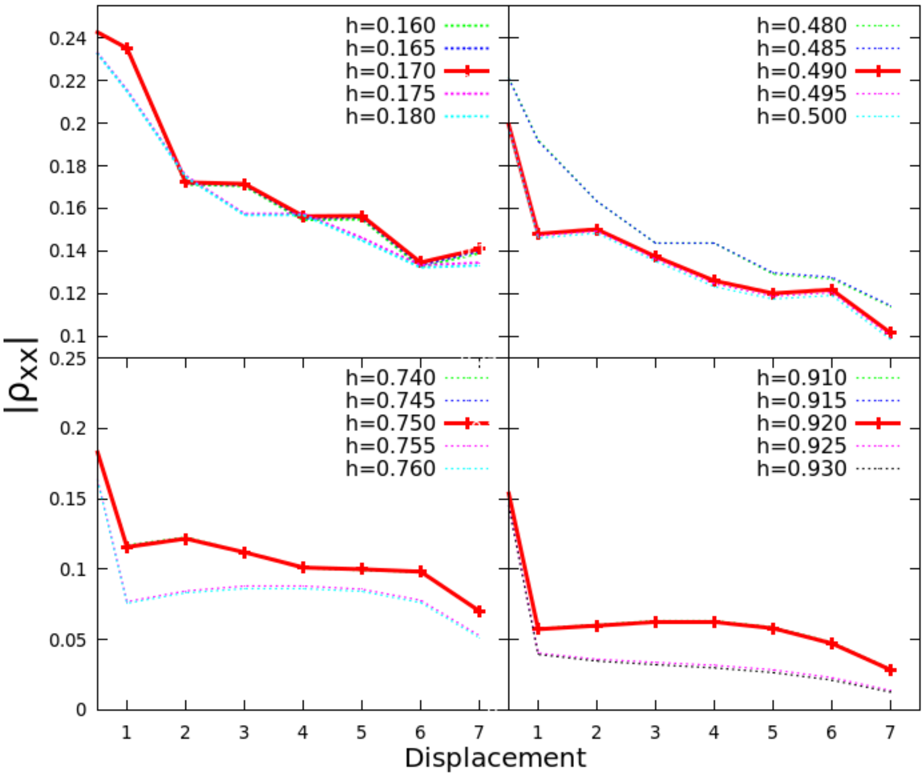

FIGURE 5.25: The absolute value for the correlation function for the xx interactions for the $N = 8$ chain with open boundary conditions for the interactions from one edge of the chain to the other, where the pairs of correlations ($\rho_{i,j}$) start at site $i = 1$ and the comparison site j runs from $j = 1, 2, 3, 4, 5, 6, 7, 8$ to the other edge of the chain, taking field values across all the level crossings. The chain system does not tend towards the behaviour of the thermodynamic limit and finds no flat behaviour in the correlators across any field range.

At finite temperature, for $T = 0.01J$, these features are still seen but the jumps in the correlators seems to vanish and it is the factorisation field features that remain robust at low temperatures.

The next chapter explores these small periodic boundary condition systems as small magnetic rings. It is ascertained whether these features shown in the correlators are detectable using neutron scattering techniques and tests their evolution within a low temperature scale.

5.5.3 Reciprocal Space Correlations Function

A step towards studying the neutron scattering cross section, which has its complications for small geometric shaped molecules, is to look at the reciprocal space correlation

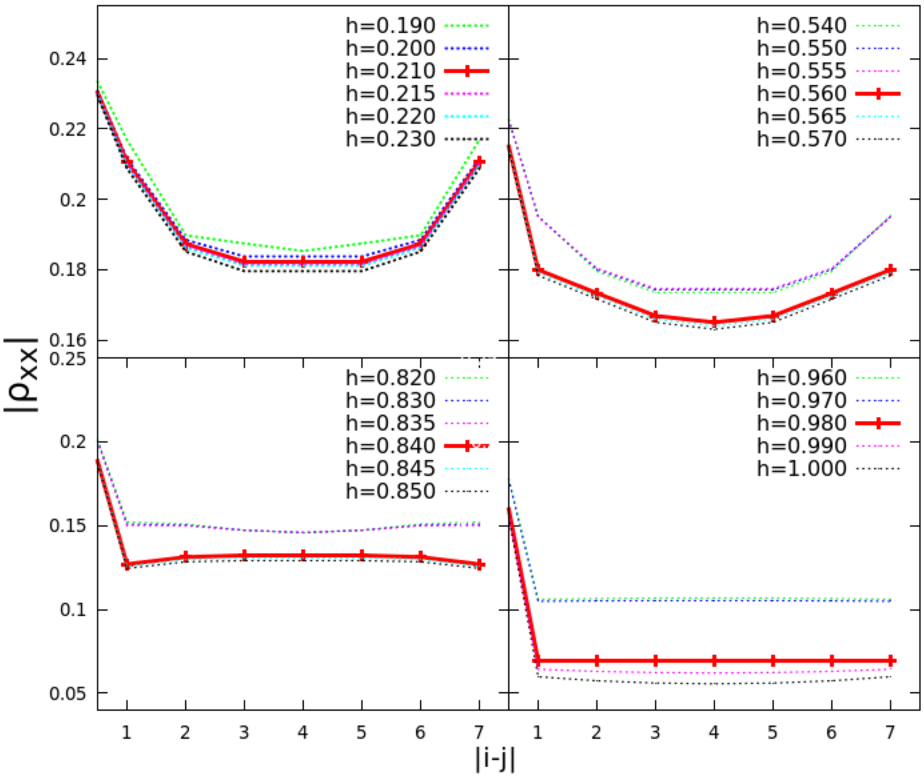

FIGURE 5.26: The absolute value for the correlation function for the xx interactions for the $N = 8$ system with periodic boundary conditions taking field values across all the level crossings. Across the first three level crossings there is a little flattening of the correlation function but it doesn't reach the whole system. Only at the factorisation field $h_f = 0.98$ does the system become completely flat

function in the thermodynamic limit. Simply transforming the correlation functions into reciprocal space would not consider the geometry for a small clustered system that the neutron would experience. When discussing bulk properties using finite-sized systems with PBC, the systems are so small that numerical resolution in creating the step sizes in reciprocal space would add fluctuations around the peak. In this section, to relate better to more realistic neutron scattering data, only the thermodynamic limit will be discussed as a preface to principles behind neutron scattering.

As mentioned previously, neutron scattering information is global information; the neutrons can not limit themselves to only interact with pairs of sites within the sample. The data produced is in reciprocal space. This highlights how important it is when considering the correlation function to capture the whole length of behaviour of the system, whether it is LRO or a full correlation decay.

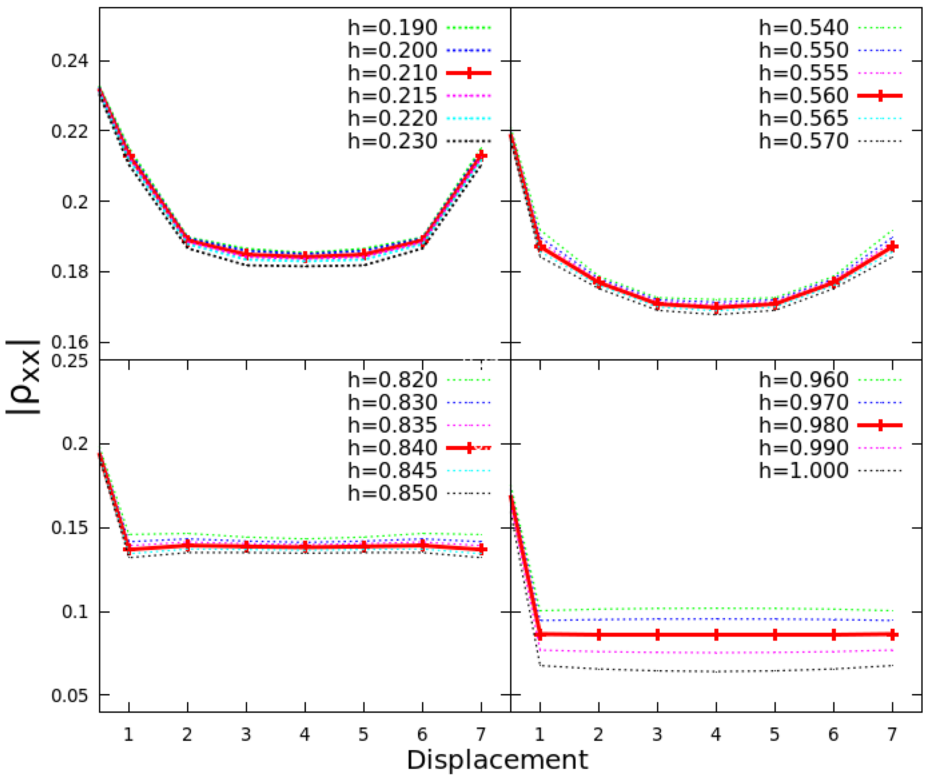

FIGURE 5.27: The absolute value for the correlation function for the xx interactions for the $N = 8$ system with periodic boundary conditions taking field values across all three level crossings for $T = 0.01J$. This temperature does not affect the flat behaviour at the factorisation field.

By understanding the real-space correlation functions it is possible to split $\rho_{xx}(R)$ into two terms that describe different parts of its behaviour, such that;

$$\rho_{xx}(R) = (-1)^R \left[\rho_{xx}^{short}(R) + \left|\rho_{xx}^{bulk}\right|\right]; \tag{5.24}$$

where $(-1)^R$ shows the underlying antiferromagnetic behaviour in the correlators; ρ_{xx}^{short} represents the effect of the quantum fluctuations on the correlators, thus at h_f then $\rho_{xx}^{short} = 0$; and $\left|\rho_{xx}^{bulk}\right|$ represents the bulk behaviour of the correlators. $\left|\rho_{xx}^{bulk}\right|$ is a positive constant in the ordered phase and zero when disordered. The system is disordered in xx at $h \geq h_c$ and for finite temperatures $T \geq 0$. In simplistic terms, the reciprocal space correlation functions are just the Fourier transform of the real space correlation functions, as written below [97];

$$\mathcal{F}[\rho_{xx}](k) = \frac{1}{2\pi} \sum_{R=-\infty}^{\infty} \exp^{-ikR} \rho_{xx}(R), \tag{5.25}$$

For our purposes, for a theoretical view of the entanglement transition at zero temperature the Fourier transform of $\mathcal{F}[\rho_{xx}^{short}](k)$ is a suitable tool. In the ground state we look for the behavior of $\mathcal{F}[\rho_{xx}^{short}](k)$ to equal a flat line of finite value at exactly h_f [4]. The flat line corresponds to the anti-ferromagnetic classical chain that ρ_{xx}^{bulk} represents, $\mathcal{F}[rho_{xx}^{bulk}]$ would give a delta peak if the limits of $R \pm \infty$ could be taken. By eliminating the FT of the bulk takes the delta peak away, leaving any FT peak a result of quantum fluctuations. Above and below the transformed peak has different behaviour giving the peak a non-monotonic trend as h passes over the entanglement transition [97] [25].

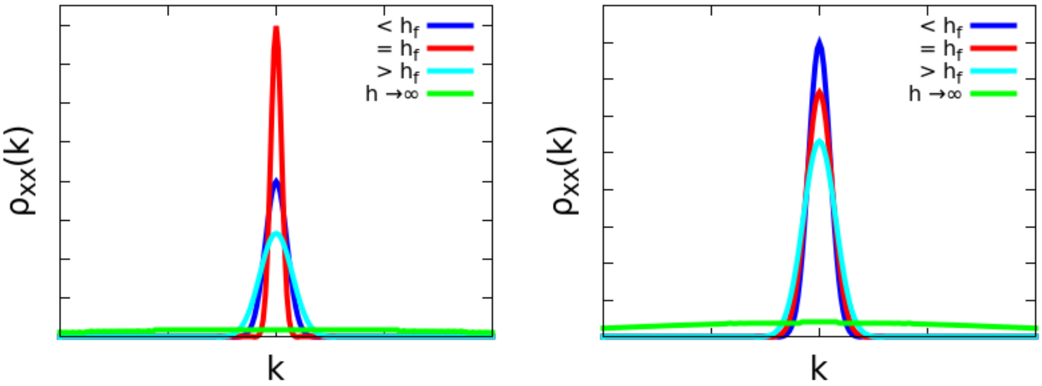

FIGURE 5.28: These show diagrammatically the FT behaviour of the model in the thermodynamic limit above zero temperature for an example of (a) non monotonic behaviour of the k-space correlator indicating a collapse of quantum fluctuations and the entanglement transition and (b) monotonic behaviour that indicates that no transition has taken place as the FT peak steadily decays.

Above zero temperature, a more realistic behaviour of the FT peak is from all of Eq.5.25 including the bulk behaviour, which because of thermal fluctuations is no longer a delta peak and needs to be considered. As h increases the area under the FT peak must stay the same so the width of the peak is an indicator for our purpose. To elaborate, without the entanglement transition the correlators would show an antiferromagnetic ordered phase become a ferromagnetic one as h increased, with the FT peak steadily decreasing to a flat line as the spins saturated in the z direction. If there was an entanglement transition and its signature was able to dominate over the thermal fluctuations then at that point the system would become a classical-like antiferromagnetic chain and the FT peak would tend towards a delta peak depending on the computational limits on R. This would be represented by a non-monotonic behaviour in the FT peak as h passed over h_f. These two scenarios are represented diagrammatically by Fig.5.18.

---

[4] $\mathcal{F}[\rho_{xx}^{short}](k)$ also equals a flat line at high fields as the system has classically saturated and there are no quantum fluctuations as $h \to \infty$.

For the finite-sized calculation for small quantum clustered materials, a signature of the entanglement transition is identified directly using the neutron scattering cross section in chapter 6.

5.6 Concurrence

Concurrence was introduced in Chapter 2 as a commonly employed theoretical measure of entanglement and in Chapter 4 it was shown explicitly how to calculate concurrence for a dimer model. Concurrence is a local measure between two spins. For systems larger than $N = 2$ the concurrence of any two spins within that system is sensitive to the entanglement of the whole the system. This means that two spins can be labeled as a 'subsystem' with the remainder of the whole system being its effective 'environment'. The concurrence calculated for the subsystem contains information about the environment too, and for our ring models with PBC any two spin subsystem will give the concurrence for the whole system. To separate the subsystem the reduced density matrix RDM is used to describe the behaviour of the whole system [56]. To prove its effectiveness to the system as a whole entity we will give an example using a two-spin system, where the first spin is called the subsystem and the second spin is called the environment. This arrangement is diagrammatically shown in Fig. 5.29.

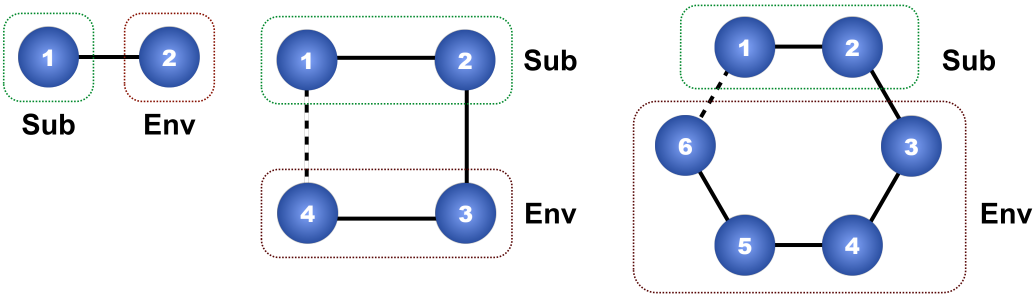

FIGURE 5.29: These are diagrams showing how to separate a whole system into a subsystem and the environment that acts on for a few different system sizes that go towards constructing the reduced density matrix. The dashed lines indicate the different options for periodic or open boundary conditions.

In practice there is very little reason to perform the RDM on a two spin system as exact operations are simple to do on such a small system. Here, we will use the example to demonstrate that a measurement performed on the subsystem of the two-spin system only, i.e. on spin 1, can detect whether the system as a whole is in an entangled or pure state. We recall from Chapter 4 the density matrix for the ground state singlet $|\psi\rangle$ for a dimer is:

$$\hat{\rho} = |\psi\rangle \langle\psi| = \frac{1}{2}\begin{pmatrix} 0 & 0 & 0 & 0 \\ 0 & 1 & -1 & 0 \\ 0 & -1 & 1 & 0 \\ 0 & 0 & 0 & 0 \end{pmatrix}. \tag{5.26}$$

The RDM is;

$$\hat{\rho}_{RDM} = \sum_{\chi=\uparrow,\downarrow} \left(\mathbb{I} \otimes \langle\chi|_e\right) \hat{\rho} \left(\mathbb{I} \otimes |\chi\rangle_e\right), \tag{5.27}$$

here, χ represents the spin of the environment of the system that is discarded i.e $\uparrow$ and $\downarrow$ for the dimer, and the unity matrix $\mathbb{I}$ ensures that the operation is performed on the correct spins such that: $|\chi\rangle_s \equiv |\chi\rangle \otimes \mathbb{I}$ and $|\chi\rangle_e \equiv \mathbb{I} \otimes |\chi\rangle$. The operation pulls out everything attached to the environment and its spin basis and the RDM of the subsystem is left behind.

$$\begin{aligned} \hat{\rho}_s \;\; = \;\; & \sum_{\chi=\uparrow,\downarrow} \langle\chi|_e \frac{1}{2}\Big(|\uparrow\rangle_s |\downarrow\rangle_e \langle\uparrow|_s \langle\downarrow|_e - |\downarrow\rangle_s |\uparrow\rangle_e \langle\uparrow|_s \langle\downarrow|_e \\ & - |\uparrow\rangle_s |\downarrow\rangle_e \langle\downarrow|_s \langle\uparrow|_e + |\downarrow\rangle_s |\uparrow\rangle_e \langle\downarrow|_s \langle\uparrow|_e \Big) |\chi\rangle_e ; \end{aligned} \tag{5.28}$$

extracting out the environment:

$$\begin{aligned} \hat{\rho}_s \;\; = \;\; & \sum_{\chi=\uparrow,\downarrow} \Big[\frac{1}{2} \langle\chi|\downarrow\rangle_e \langle\chi|\downarrow\rangle_e^* |\uparrow\rangle_s \langle\uparrow|_s - \frac{1}{2} \langle\chi|\uparrow\rangle_e \langle\chi|\downarrow\rangle_e^* |\downarrow\rangle_s \langle\uparrow|_s \\ & -\frac{1}{2} \langle\chi|\downarrow\rangle_e \langle\chi|\uparrow\rangle_e^* |\uparrow\rangle_s \langle\downarrow|_s + \frac{1}{2} \langle\chi|\uparrow\rangle_e \langle\chi|\uparrow\rangle_e^* |\downarrow\rangle_s \langle\downarrow|_s \Big] \\ = \;\; & \frac{1}{2} |\downarrow\rangle_s \langle\downarrow|_s + \frac{1}{2} |\uparrow\rangle_s \langle\uparrow|_s . \end{aligned} \tag{5.29}$$

Therefore the RDM of the system is:

$$\hat{\rho}_{RDM} = \frac{1}{2}\begin{pmatrix} 1 & 0 \\ 0 & 1 \end{pmatrix}. \tag{5.30}$$

This reduced density matrix, though only containing data from the subsystem, can tell us that the system as a whole is not pure and contains entanglement. For comparison, let the system be in an available pure state $|\uparrow\uparrow\rangle$ and produce the reduced density matrix in the same way:

$$\begin{aligned}
\hat{\rho}_s &= \sum_{\chi=\uparrow,\downarrow} \langle\chi|_e\, \hat{\rho}\, |\chi\rangle_e \\
&= \sum_{\chi=\uparrow,\downarrow} \langle\chi|_e \left(|\uparrow\rangle_s |\uparrow\rangle_e \right)\left(\langle\uparrow|_s \langle\uparrow|_e \right) |\chi\rangle_e \\
&= \sum_{\chi=\uparrow,\downarrow} \langle\chi|\uparrow\rangle_e \langle\uparrow|\chi\rangle_e^* |\uparrow\rangle_s \langle\uparrow|_s \\
&= |\uparrow\rangle_s \langle\uparrow|_s \,,
\end{aligned} \tag{5.31}$$

this gives the following reduced density matrix;

$$\hat{\rho}_{RDM} = \begin{pmatrix} 1 & 0 \\ 0 & 0 \end{pmatrix}. \tag{5.32}$$

In contrast to entangled singlet state, Eq. 5.32 tells us the the whole system is in a pure state.

We return to Fig 5.29 but regard the two diagrams larger than two spins, we show that for the calculations in this section the subsystem taken from the finite-sized systems contains spin 1 and 2 only as N increases. The dashed lines in the diagrams indicate that both PBC or OBC can be used. For PBC the system is symmetric and any pair of neighbouring spins would give the RDM. It should be noted that different pairs of spins, that are not nearest neighbours, would yield different results. For OBC the implications of the RDM are more complex, as the calculation is heavily dependent on which sites make up the subsystem, i.e. a subsystem for sites 1 and 2 would give different results than a subsystem containing sites 2 and 3 despite also being nearest neighbours. It is speculated that the edge sites contain very different effects than bulk sites. In this section, results for concurrence for OBC are given with a subsystem of sites 1 and 2 only. The following derivation for the RDM for our model is not generalised enough to calculate for any pair of spins, but the preliminary results are interesting and thus included.

For all the finite-sized systems used in this work we are able to take the exact ground state as calculated numerically and use it form the RDM for a system that completely occupies the ground state at $T = 0$. This also means that the calculation does not consider the degeneracy at different level crossings, and can only take a single state at a time instead of being able to take any linear combination of degenerate states. For the finite-sized systems we will derive the RDM matrix for the $N = 4$ system outlining the process that is consequently the same for the $N = 6$ and above models. A general state $|\psi\rangle$ in the basis for a $N = 4$ system in terms of its wavefunction amplitudes is:

$$|\psi\rangle = \begin{pmatrix} C_1 \\ C_2 \\ C_3 \\ \vdots \\ C_{16} \end{pmatrix} \tag{5.33}$$

For this state the subsystem will consist of spin 1 and spin 2 and the environment that is extracted will be spin 3 and 4. The extraction basis for χ comes from spins 3 and 4 and is $\uparrow\uparrow$, $\uparrow\downarrow$, $\downarrow\uparrow$ and $\downarrow\downarrow$. The reduced density matrix can be written in general:

$$\hat{\rho}_s = \sum_{\chi=\uparrow\uparrow,\uparrow\downarrow,\downarrow\uparrow,\downarrow\downarrow} \langle\chi|_e \big(|\psi\rangle \langle\psi| \big) |\chi\rangle_e \,. \tag{5.34}$$

As the sum is processed through $\chi =\uparrow\uparrow, \uparrow\downarrow, \downarrow\uparrow, \downarrow\downarrow$ it pulls out the environment and leaves the subsystem behind. This can be considerably slimmed down since only the parts of the extracted basis that match up will give a non-zero term for the subsystem. For example, let χ^e be any part of the extracted basis and χ^s be what is left over from the subsystem (with i representing which amplitude C from $|\psi\rangle$ from $i = 1, 2, 3...16$ and j from $\langle\psi|^*$):

$$C_j^* C_i \langle\chi|\chi_i^e\rangle \langle\chi_j^e|\chi\rangle |\chi_i^s\rangle \langle\chi_j^s| \,, \tag{5.35}$$

this will only give a non-zero term if $\chi_i^e = \chi_j^e$ for when the sum takes the terms for $\chi = \chi^e$. For example, when $\chi =\uparrow\uparrow$ and $\chi^e =\uparrow\uparrow$:

$$C_j^* C_i \langle\uparrow\uparrow | \uparrow\uparrow\rangle \langle\uparrow\uparrow | \uparrow\uparrow\rangle |\chi_i^s\rangle \langle\chi_j^s| \Rightarrow C_j^* C_i |\chi_i^s\rangle \langle\chi_j^s| \,. \tag{5.36}$$

This is repeated for all the extracted basis $\uparrow\uparrow$, $\uparrow\downarrow$, $\downarrow\uparrow$ and $\downarrow\downarrow$ of the environment. The RDM is made up of a sum of the coefficients $C_j^* C_i$ and the subsystem basis $|\chi_i^s\rangle \left\langle\chi_j^s\right|$ essentially describes the position in the 4×4 RDM that the sequences of coefficients are placed. As shown:

$$\hat{\rho_s} = \begin{pmatrix} \sum_i^4 C_i^* C_i & \sum_i^4 C_{i+4}^* C_i & \sum_i^4 C_{i+8}^* C_i & \sum_i^4 C_{i+12}^* C_i \\ \sum_i^4 C_i^* C_{i+4} & \sum_i^4 C_{i+4}^* C_{i+4} & \sum_i^4 C_{i+8}^* C_{i+4} & \sum_i^4 C_{i+12}^* C_{i+4} \\ \sum_i^4 C_i^* C_{i+8} & \sum_i^4 C_{i+4}^* C_{i+8} & \sum_i^4 C_{i+8}^* C_{i+8} & \sum_i^4 C_{i+12}^* C_{i+8} \\ \sum_i^4 C_i^* C_{i+12} & \sum_i^4 C_{i+4}^* C_{i+12} & \sum_i^4 C_{i+8}^* C_{i+12} & \sum_i^4 C_{i+12}^* C_{i+12} \end{pmatrix}. \tag{5.37}$$

This process was repeated for the $N = 6$ system where the subsystem for spins 1 and 2 were retained, and the environment of spins 3 to 6 was extracted. The coefficients C_i of the state $|\psi\rangle$ and the coefficients C_j^* of $\langle\psi|$ were for $i, j = 1, 2, 3...64$ and for larger systems $i, j = 1, 2, 3...2^N$ for system size N. A pattern was quickly apparent and though extrapolation a RDM was constructed for any finite-sized system where the state is known. The pattern can be summerised as follows:

$$\hat{\rho_s} = \begin{pmatrix} \sum_l^m C_l^* C_l & \sum_l^m C_{l+m}^* C_l & \sum_l^m C_{l+2m}^* C_l & \sum_l^m C_{l+3m}^* C_l \\ \sum_l^m C_l^* C_{l+m} & \sum_l^m C_{l+m}^* C_{l+m} & \sum_l^m C_{l+2m}^* C_{l+m} & \sum_l^m C_{l+3m}^* C_{l+m} \\ \sum_l^m C_l^* C_{l+2m} & \sum_l^m C_{l+m}^* C_{l+2m} & \sum_l^m C_{l+2m}^* C_{l+2m} & \sum_l^m C_{l+3m}^* C_{l+2m} \\ \sum_l^m C_l^* C_{l+3m} & \sum_l^m C_{l+m}^* C_{l+3m} & \sum_l^m C_{l+2m}^* C_{l+3m} & \sum_l^m C_{l+3m}^* C_{l+3m} \end{pmatrix}. \tag{5.38}$$

Where $m = \frac{2^N}{4}$ for finite-sized systems of size N. It should be reiterated here that this general form for the RDM is for our finite-sized model where the subsystem taken is always sites 1 and 2. This (4×4) RDM for Eq.5.38 is used to calculate the ground state concurrence of any of the finite-sized systems discussed in this chapter from the subsystem containing sites 1 and 2. In the same method that was demonstrated in the previous chapter for the dimer model.

The matrix $\hat{\rho}\tilde{\rho}$ is solved for the eigenvalues (λ_i) in descending order, and are used to define concurrence from Eqs. 2.17 and 2.18.

Fig.5.30 uses this derivation to calculate the ground state nearest neighbour concurrence for a range of finite-sized systems up to $N = 12$ for PBC for $\gamma = 0.5$ and $h_f = 0.866$. As concurrence can not distinguish between types of entanglement, it can only comment on a scaled amount of entanglement. It is observed that despite switching states multiple times, the finite-sized system evolves quickly towards thermodynamic limit behaviour, leaving an apparently smooth curve (within the plots precision) for $N = 12$. As with the dimer calculations, in the ground state, the calculation does not consider degeneracy, so it can not give zero entanglement based on this constraint, see section 4.4. For N=4 it was possible to find the correct linear combination of ground states that lead to a factorised state, then use the calculated linear combination to calculate concurrence. For the in-plane anisotropy $\gamma = 0.6$ and out-of-plane anisotropy $\Delta = 0$ the factorisation field is $h_f = 0.8$ exactly; the linear combination for $A\,|\psi_A\rangle + B\,|\psi_B\rangle$ is $A = 0.729$ and $B = -0.685$ [3d.p] gives the concurrence tending towards zero 8.70×10^{-5}.

In the apparent thermodynamic limit ($N = 12$) both alternating states are tending towards zero entanglement at the factorisation field. This supports that the thermodynamic limit does not require a switching of states for an entanglement transition to take place, suggesting that in the thermodynamic limit, concurrence is a continuous function.

In contrast, for very small systems, having proved that entanglement is zero at the factorisation field it can be deduced that the entanglement transition happens suddenly as the states become degenerate and switch. This occurs with relatively strong entanglement on each side of the factorisation field, which facilitates the detection of the transition compared to the thermodynamic limit.

The same calculation was run again for the exact same parameters for $\gamma = 0.5$ and $h_f = 0.866$ but for OBC. Fig.5.31 plots the results. Without the same symmetry that the periodic boundary conditions system has, this plot only shows the amount of entanglement at the edge of the chains; for sites 1 and 2 only. It is likely that the concurrence in the centre of the respective chain lengths is quite different. Unfortunately, this avenue was not explored and it can only be speculated that the results would give further interesting insights in the chain models and their edge effects.

By studying Fig.5.31 alone there are some interesting features to discuss. Despite the system not factorising and the correlators producing showing no indication of a classical state, as N increases, the thermodynamic limit evolves towards a common behaviour that looks very much like an entanglement transition. This has not been fully understood in this project. It seems that for both $N = 10$ and $N = 12$ they find a common behaviour and tend towards zero at around the same field value. This field value is not the factorisation field for the parameters plotted, and if it does coincide with a level crossing we do not know if it is the last level crossing or if there is any significance if it is. Perhaps more interestingly, would be to see if the concurrence calculated from the central spins of the chain (i.e. for sites $\frac{N}{2}$ and $\frac{N}{2} \pm 1$) would also have a point where the concurrence tended to zero as the system size increased towards the thermodynamic limit and whether it was at the same point as Fig. 5.31, somewhere new, or even tending towards the same behaviour as the PBC plots in Fig. 5.30. This would ask the question whether there was some finite-sized system size where the behaviour PBC and OBC tend towards each other and if so, then that particular limit could still be exactly solvable using exact diagonalisation. Alternatively, if both OBC and PBC tend towards different outcomes then this comments on the very strong effects the edges of chains can have on the overall behaviour of the system. As said, this particular avenue for OBC was not pursued as was conducted late into the project. Further work into this area and, in general, by exploring the behaviour of thermal concurrence would offer further information into the entanglement transition in these 1D antiferromagnetic systems.

The following chapter solely looks at the finite-sized models with periodic boundary conditions and examines molecular magnets of different sizes. The chapter focuses on the experimental implications of the entanglement transition and explores the neutron scattering cross section of these small nanomagnets. We show their suitability for detecting the entanglement transition above zero temperatures.

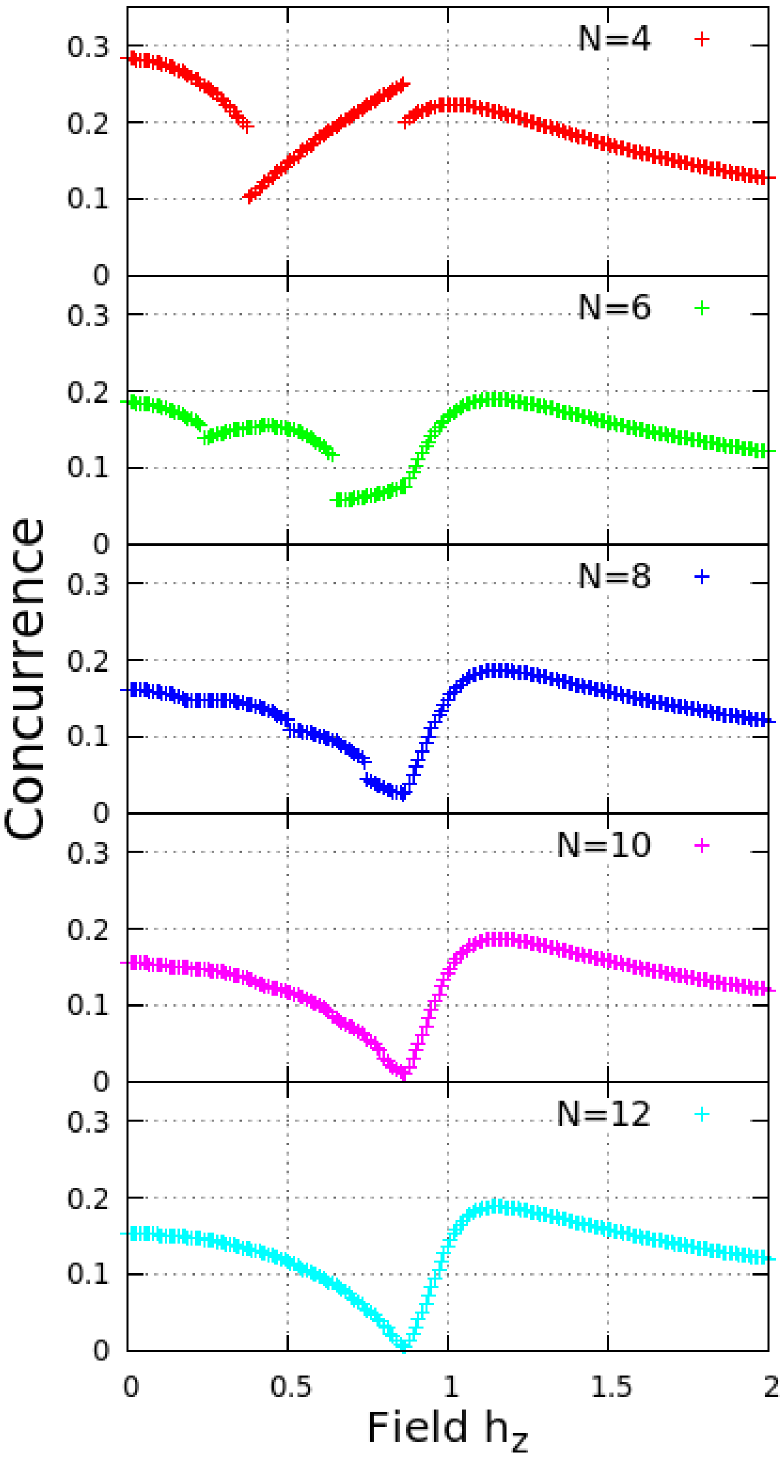

Figure 5.30: The concurrence between two neighbouring spins as calculated from the reduced density matrix for a range of system sizes $N = 4, 6, 8, 10$ and 12 for the anisotropic XY-model with $\gamma = 0.5$ at the ground state. As the system evolves towards the thermodynamic limit, the concurrence tends to zero at the factorisation field only. For smaller systems, breaks can be seen that indicate the level crossings and the states switching over. The calculation does not take the states as degenerate at these crossings and thus the vanishing of concurrence exactly at the factorisation field exactly can not be shown.

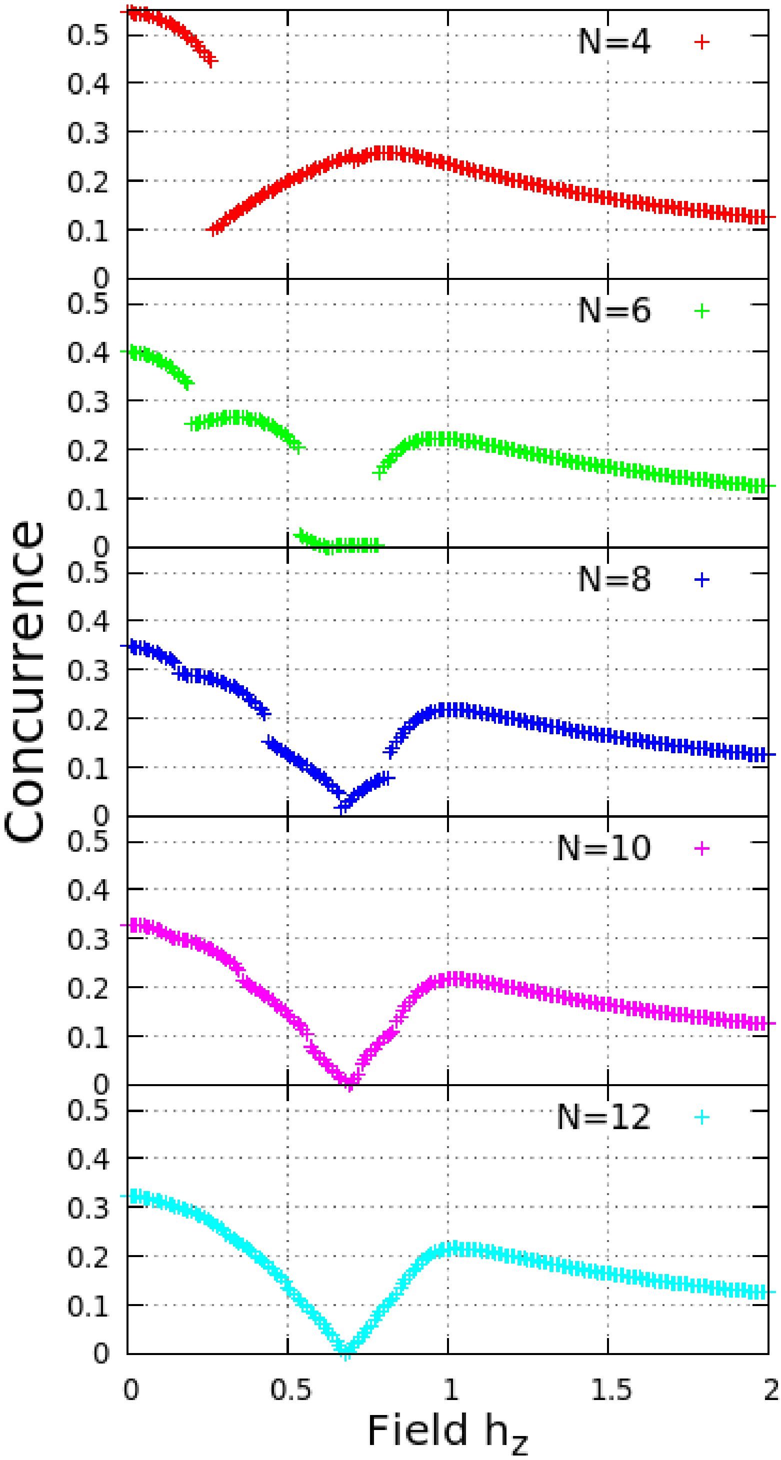

FIGURE 5.31: The nearest neighbour concurrence as calculated from the reduced density matrix from sites 1 and 2 for a range of system sizes $N = 4, 6, 8, 10$ and 12 for the anisotropic XY-model with $\gamma = 0.5$ at the ground state for OBC.

Chapter 6

Experimental Implications for Molecular Magnets

The theoretical foundations that describe the mechanism of the entanglement transition have been fully described in previous chapters. Chapter 4 identifies the connection between the entanglement transition and a level crossing between the two lowest-lying energy levels at the factorisation field. Chapter 5 expands on this by exploring the energy spectra of larger finite-sized systems and finds that the number of level crossing is dependent on system size $\frac{2}{N}$ as supported by Giorgi *et al* [31]. We go on to prove that it is only the last level crossing in the systems with periodic boundary conditions that coincides with the factorisation field that actually factorises. It is clear that for the entanglement transition in finite-sized systems to occur the two lowest eigenstates need to cross, at that point they become degenerate. Degeneracy in the ground states doesn't automatically mean that they would be able to completely factorise and it is this factorisation that breaks the entanglement in the system. The requirement is so; the system must undergo a change in the type of entanglement, and at the transition, the entanglement must be broken letting the system become separable. The particular type of entanglement in the finite-sized systems is not straight forward, and is not a simple case of antiferromagnetic entanglement switching over to ferromagnetic entanglement. An observation of the amplitudes of the states involved show a complex arrangement of entanglement in both states, but what is clear is that these states are orthogonal to each other. In this chapter we are able to plot the neutron scattering cross-sections and to better understand what the measurable effects of these two ground states would be.

Chapter 5 also calculated the real space correlation functions, which contribute to the neutron scattering function. A clear indication of the entanglement transition was seen in the real space correlation functions when the absolute value of $|\rho_{xx}(R)|$ became 'flat' across the displacement in the system for all $R \neq 0$ where $R = |i - j|$. These effects translate well into reciprocal space and their neutron scattering cross-section that relates directly to real experiments, give a clear signature of the entanglement transition in this chapter.

Chapter 6 explores the experimental implications of these finite-sized systems by using a more physical interpretation of their PBC by studying them as small magnetic molecules. We present neutron scattering predictions for a range of system sizes, whilst focusing on the plaquette and hexagon model in great detail. Neutron scattering experiments offer a wide range of techniques to probe the inner magnetic structure of materials. Albeit based on simplified models, the theoretical predictions in this chapter are produced in a way that are easily comparable to real experimental results. As a preface to the calculated scattering functions for clustered quantum molecules, a brief outline of the basics behind various neutron scattering methods is also provided.

6.1 Magnetic Signature

It is well-known that the level crossings described in the previous chapter coincide with jumps in total magnetisation [89]. Fig.6.1 shows the magnetisation of the anisotropic XY-model as a function of the applied field for $N = 4$ open and closed clusters (the parameter values are given in the caption). $N/2$ jumps are seen, corresponding to each of the gap closings. For the closed rings, the last jump coincides with the entanglement transition.

In previous chapter we have shown that the key feature of the state at h_f in our model is that it is devoid of quantum entanglement [18] [62] [63] [58] [59] [16]. One consequence of this is that, as in any classical state, but unlike the states at higher and lower values of h_z, all phase coherence between the wave functions of individual spins is lost at h_f. Meaning that the individual quantum components, i.e the spins, can be described using their wave functions and when the system is entangled all the wavefunctions are in phase. At the factorisation field, when the entanglement is broken, the phase of the

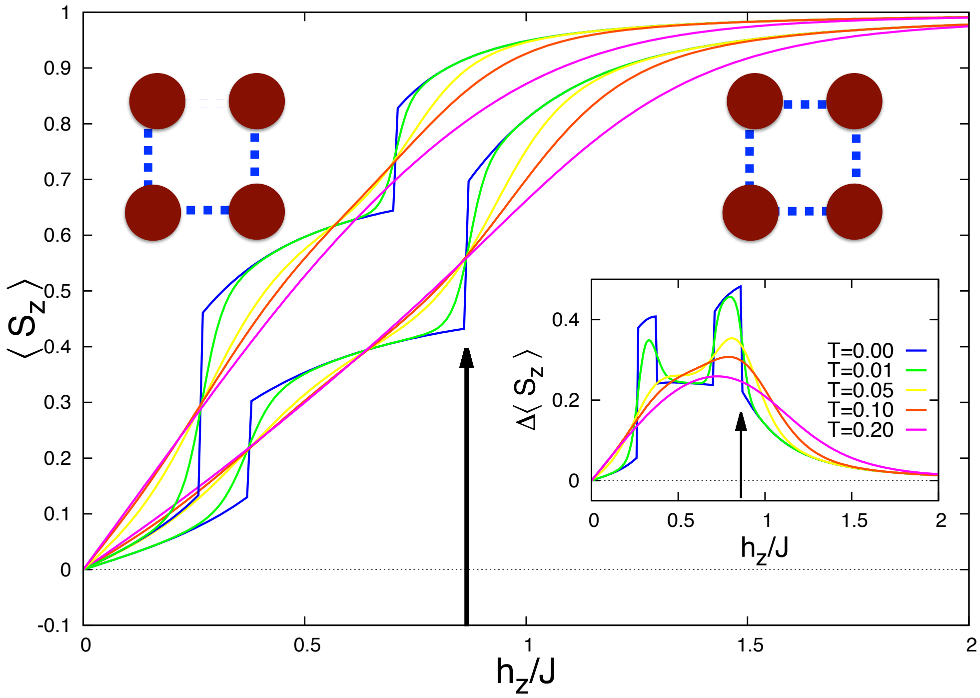

FIGURE 6.1: Total z-axis magnetisation per site $\langle S_z \rangle$ as a function of applied field for a cluster with $N = 4$ magnetic sites described by the anisotropic XY-model. The temperatures are as indicated (in units T/J), with the bottom set of curves corresponding to a closed ring, or plaquette, and the top set of curves to a small chain segment or, equivalently, a broken ring, as depicted. The anisotropy parameter is $\gamma = 0.5$ in all cases. The inset shows the difference between the chain and the ring. The arrow indicates the field at which the ground state of the ring factorises exactly, where the largest jump in magnetisation takes place and also where the difference between the chain and ring magnetisation is largest.

wave function of each individual spin can fluctuate independently of the others. The individual spin phases can be considered as a new, delocalised degree of freedom that emerges at $h_z = h_f$.

Experimentally, this could be accessed through measurements of magnetisation of samples with different concentrations of open and closed rings. The inset to Fig. 6.1 shows the prediction for such a measurement in the simplest, limiting case, when one sample is made up exclusively of open rings, while the others are all closed. Clearly, in the ground state, the maximum difference in magnetisation $\langle \Delta S_z \rangle$ occurs quite precisely at the factorisation field. The effect is smoothed by temperature, but it is clearly visible for $T \sim 10\%$ of J. Two sample values of J/k_B for real cluster magnets are 17 K for Cr_8 [8] and 138 K for Cu_2PO_4OH [77] . A smaller peak is seen at the field at which there is another level crossing. This is what one would expect in view of the approximate factorisation at that field which we noted above. The enhanced value of $\langle \Delta S_z \rangle$ is due to the fact that the jump in magnetisation occurs at a different value of the field for an open ring, where the exactly factorised state is never realised.

6.2 Neutron Scattering Techniques

Neutron scattering techniques offer a wide and versatile approach to exploring condensed matter with many advantages over other methods. Thermal neutrons (300K) have the ideal wavelength ($\lambda \simeq 1.6$ Å) for probing solids and excitations [98]. Neutrons interact with matter in two ways; they can scatter directly off the nuclei to provide information about the structure; and they can interact with the electron orbitals. Neutrons have an intrinsic spin. This means that the neutron can scatter off the spin orbitals and give data about the magnetic structure of the system through a dipole-dipole interaction. This is a sweeping generalisation, as the processes involved in neutron scattering are very complicated. The data that is theoretically predicted for neutron scattering experiments rely on the advanced methods in magnetic neutron scattering [99]. This section will outline the basics of different types of neutron scattering as a progression towards constructing the scattering function that was used to produce results for a simplified model of a small family of magnetic molecules.

6.2.1 Neutron Scattering for Magnetic Molecules

This chapter is connecting the theory of the entanglement transition with quantities that can be measured and are easily comparable to real neutron scattering experiments. The models used with PBC are now fully recognised as small molecular rings and magnetic structures instead of representing any bulk properties of the larger system size limit. Here, we take the anisotropic XY-model 1D Hamiltonian as first given by Eq. 3.6 with PBC and use this to model a 1D antiferromagnetic chain that has been shaped into a ring based molecule. Fig. 6.2 shows the formation of our rings diagrammatically for the $N = 4$ system to make a plaquette and the $N = 6$ system that forms a hexagon. In Chapter 5 when discussing our models with PBC the results for the energy spectra and correlation functions did not depend on the geometry of the system. When calculating

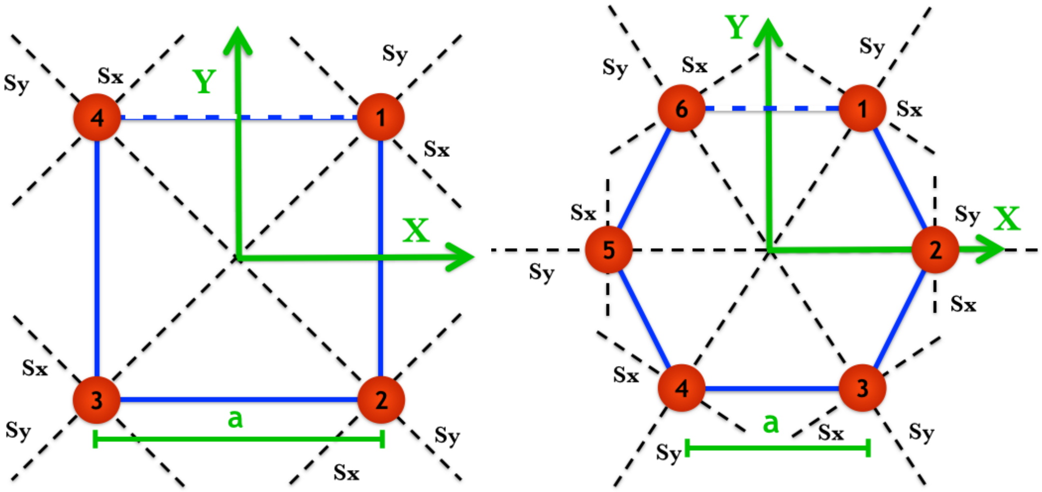

FIGURE 6.2: A simple model of a magnetic cluster with $N = 4$ (left) and $N = 6$ (right) magnetic sites. The green arrows represent the global X, Y axes. The dashed lines represent the local S^x and S^y easy axes (tangentially and radially, respectively; by convention the positive orientations correspond to the clockwise and outward directions, respectively). The Z and S^z axes point out of the page. The blue lines represent bonds along which magnetic interactions occur. We assume the interactions between the spins are diagonal in the local axes and given by the anisotropic XY-model in Eq. 3.6. If one of the bonds is missing between site N and site 1 we obtain open boundary conditions, indicated by the blue dashed lines. The distance "a" indicated on each plot is used as the unit of length and is set to 1 for any calculations.

the neutron scattering cross-section the geometry of the molecules does matter with regards to the incoming neutrons that interact with the molecules.

This section gives the formula used to calculate the neutron scattering cross-section predictions that are plotted in this chapter. Here, we also provide enough of the theoretical background to the neutron scattering cross-section to be able to understand it and demonstrate how we use it with respects to our magnetic molecules. In the model defined by Fig. 6.2 and Eq. 3.6, $\hat{S}_i^x$ and $\hat{S}_i^y$ are the first two components of the spin at site i, measured along axes contained in the xy plane but forming an angle ϕ_i with the x and y axes, respectively. Let $\hat{\sigma}^{\alpha}_{\mathbf{R}_i}$ be the $\alpha^{\underline{\text{th}}}$ component of the spin at site i with respect to the global axes x, y depicted in Fig. 6.2, which are site-independent. These are global axes fixed to the orientation of the crystal. In the case of a neutron scattering experiment, they could equivalently be taken to be the axes of the instrument. The neutron scattering cross-section is given by Lovesey [100], and its component parts are explain in turn in the following text:

$$\frac{\partial^2\sigma}{\partial\Omega\partial E'} = \frac{k_s}{k_i}\left(\gamma r_e\right)^2\left|\frac{g}{2}F\left(\mathbf{q}\right)\right|^2 e^{-2W(\mathbf{q})}S\left(\mathbf{q},\omega\right), \tag{6.1}$$

Here the function $F(\mathbf{q})$ is the magnetic form factor, which depends on the shape in momentum space of the magnetic moment of the ions, which can not be considered point particles in an experiment. The Debye-Waller factor is $e^{-2W(\mathbf{q})}$, which reduces the intensity of the scattered peaks and is caused by the motion of the atoms from their equilibrium positions. the g-factor and γ refer to effects of the neutron and are also not considered in our theoretical calculations, as we only plot the scattering function. Before describing the scattering part of Eq. 6.1 represented by the function $S(\mathbf{q}, \omega)$ we will take a couple of paragraphs to describe some of the basics of neutron scattering with the purpose of explaining the cross-section, and where $\mathbf{q}$ and ω originate from.

In Chapter 5 we discussed briefly the reciprocal-space correlation functions that are often described as being in k-space. These were obtained using simple Fourier transforms for our model in the thermodynamic limit. K-space relates to the change of momentum that the neutrons experience as they interfere with the sample. The simplest version of neutron scattering is elastic scattering. The incoming, or incident, neutrons interact with the nuclei of the sample and scatter without exchanging energy, i.e. without gaining or losing energy from the sample. Therefore the interaction can be described by the change of momentum that the neutrons experience;

$$\mathbf{P} = \hbar\mathbf{k_i} - \hbar\mathbf{k_s} = \hbar\mathbf{q}. \tag{6.2}$$

The transfer of momentum is described using vectors where $\mathbf{k_i}$ is the wave vector for any incident neutron and $\mathbf{k_s}$ is its scattered wave vector. The notation $\mathbf{q}$ is introduced as the projection between them: $\mathbf{q} = \mathbf{k_i} - \mathbf{k_s}$. As this is elastic scattering, there is no energy transfer, so the energy can be given as $E = \hbar(\omega_i - \omega_s) = 0$, where the frequency is $\omega = 2\pi\nu$ and does not change.

Inelastic Scattering is a more generalised approach to neutron scattering experiments, as it allows for an exchange of energy to occur, in addition to a transfer of momentum. This allows the neutrons to probe excitations such as spin waves by interacting with the spin orbitals in the sample. The first difference comes from redefining the scattering vector $\mathbf{q}$ from Eq. 6.2 as the scattered neutrons can now take on a different wave vector and wavelength. This is shown in Fig. 6.3 that shows diagrammatically energy loss or gain when the neutrons interfere with the sample.

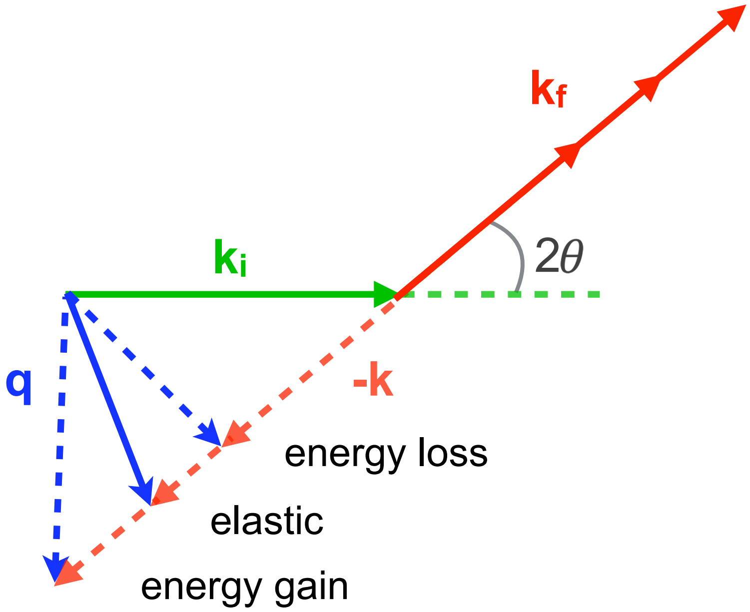

FIGURE 6.3: The scattering vector **q** is the difference of the momentum between the initial k_i and scattered neutrons k_s for inelastic scattering. Here the scattered neutron can either gain or loss energy during their interaction with the sample, this is reflected in the scattering vector.

The scattering vector **q** for inelastic neutron scattering is given by [99]

$$q^2 = k_i^2 + k_s^2 - 2k_i k_s \cos 2\theta. \tag{6.3}$$

The transfer of energy can be written as $E = E_i - E_s = \hbar(\omega_i - \omega_s)$. This convention means that if the scattered neutron loses energy to the sample then $E > 0$ and vice versa.

The detectors in a neutron scattering experiment count the number of neutrons in a small area dependent on a scattering angle, the energy of the scattered neutrons and a unit of times for that the detectors collect ‘counts’, this is incorporated into the neutron scattering cross-section. The incident neutrons are described as a collimated beam of monochromatic neutrons; they interact with a sample and are scattered. The differential cross-section counts the scattered neutrons in given directions defined by polar co-ordinates: 2θ given in Fig. 6.3 and ϕ as elevation from that plane. These angles create a solid angle to a detector, where the flux of scattered neutrons Φ is counted.

The solid angle defined by polar co-ordinates is given by the symbol Ω, where $\delta\Omega = \frac{\delta A}{r^2}$.

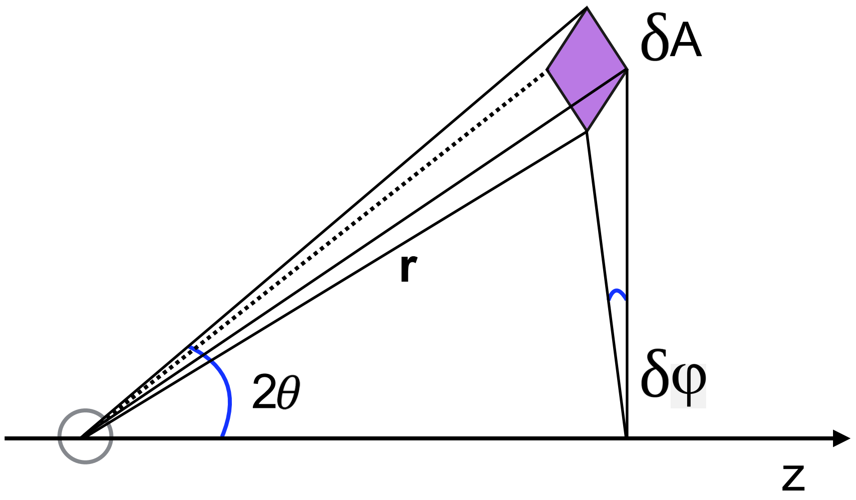

Figure 6.4: The solid angle is mapped out using the polar co-ordinates θ and ϕ. This is shown as the volume that projects δA at a radius r. The cross-section is a differential with respect to the solid angle $\partial\Omega$ with the idea of setting the resolution at the detectors.

The area at the detector δA and the polar angles involved are drawn diagrammatically in Fig.6.4. The total cross-section σ is the ratio of scattered neutrons per unit time, integrated for the total solid angle of a sphere $\sigma = 4\pi r^2$. To gather information about the flux of neutrons in a given direction, the differential cross-section $\frac{\delta\sigma}{\delta\Omega}$ is used in respect to the solid angle, so that $\delta\Omega$ is very small. This differential function is defined in different ways depending on the purpose of the measurement and the type of scattering. As a general definition it is the solid angle density of neutrons scattered at a specific direction per unit time over the incident flux.

For inelastic neutron scattering, the change of energy $E = E_i - E_s = \hbar(\omega_i - \omega_s)$ is brought into the cross-section, turning it into a double differential over the scattering angle $\delta\Omega$ and also with respect to the energy transfer δE. In a broad interpretation this is described as [99]:

$$\frac{\partial^2\sigma}{\partial\Omega\delta E} = \frac{\text{number or neutrons scattered per unit time into } \partial\Omega \text{ and } \delta E}{\text{incident flux } \cdot \partial\Omega\partial E}. \tag{6.4}$$

The partial differential cross-section is represented differently depending on the experiment and implications. This can be for experiments that are a mixture of elastic and inelastic scattering, or could be time varying samples and 'time of flight' experiments. As the need of this project requires magnetic scattering over information about the structure of the material, it is fortunate that the neutrons can be used to assess the space-time correlation function between magnetic components. For the predicted data calculated in this chapter, it is assumed that the system is in equilibrium and the time dependence is neglected. It is the scattering function in terms of the correlation functions that will form the backbone of our neutron scattering predictions.

Returning to Eq. 6.1, the most important term is the total scattering function, which can be broken down as follows:

$$S\left(\mathbf{q},\omega\right)=\sum_{\alpha,\beta}\left(\delta_{\alpha,\beta}-\hat{\mathbf{q}}_{\alpha}\hat{\mathbf{q}}_{\beta}\right)S_{\alpha\beta}\left(\mathbf{k},\omega\right). \tag{6.5}$$

The term $\left(\delta_{\alpha,\beta}-\hat{\mathbf{q}}_{\alpha}\hat{\mathbf{q}}_{\beta}\right)$ describes that the neutrons give information about the component of the magnetic moment of the ions perpendicular to $\mathbf{q}$, where $\hat{\mathbf{q}}_{\alpha}$ and $\hat{\mathbf{q}}_{\beta}$ are the unit vectors for the components of $\mathbf{q}$ for $\alpha,\beta=x,y$ and z, though in our calculation we constrain the neutrons to the xy plane so that $\hat{\mathbf{q}}_z=0$. The spin-resolved scattering function is given by

$$S_{\alpha\beta}\left(\mathbf{k},\omega\right)=\frac{1}{2\pi\hbar}\int dte^{-i\omega t}\left\langle\hat{\sigma}^{\alpha}_{\mathbf{k}}\left(0\right)\hat{\sigma}^{\beta}_{-\mathbf{k}}\left(t\right)\right\rangle. \tag{6.6}$$

Here

$$\hat{\boldsymbol{\sigma}}_{\mathbf{k}}=\frac{1}{\sqrt{N}}\sum_{\mathbf{R}_j}e^{i\mathbf{k}.\mathbf{R}_j}\hat{\boldsymbol{\sigma}}_j \tag{6.7}$$

is the Fourier transform of the spin operator expressed in terms of the global axes. Assuming we know the magnetic form factor, Debye-Waller factor, etc. and that we detect all neutrons regardless of the energy exchanged with the sample, $\hbar\omega$, the experiment gives the integral $S\left(\mathbf{q}\right)\equiv\int d\omega S\left(\mathbf{q},\omega\right)$, which can be straight-forwardly related *via* Eq. 6.5 to the energy-integrated scattering function,

$$S_{\alpha\beta}\left(\mathbf{q}\right)=\int d\omega S_{\alpha\beta}\left(\mathbf{q},\omega\right). \tag{6.8}$$

Inserting Eq. 6.7 into Eq. 6.6 and integrating w.r.t. ω we obtain

$$S_{\alpha\beta}\left(\mathbf{q}\right)=\frac{1}{N\hbar}\sum_{i,j}e^{i\mathbf{q}\cdot\left(\mathbf{R}_i-\mathbf{R}_j\right)}\left\langle\hat{\sigma}^{\alpha}_{i}\hat{\sigma}^{\beta}_{j}\right\rangle. \tag{6.9}$$

Here $\mathbf{R}_i$ denotes the position vector of the $i^{\underline{\text{th}}}$magnetic site in the cluster. The scattering function is now represented in real space where the information about the spins in the system comes from the real space correlation functions, which were discussed and plotted in the previous chapter. The problem of predicting the neutron scattering experiment therefore reduces to expressing the correlators $\left\langle \hat{\sigma}_i^{\alpha} \hat{\sigma}_j^{\beta} \right\rangle$ in terms of those in terms of the local axes, $\left\langle \hat{S}_i^{\alpha} \hat{S}_j^{\beta} \right\rangle$. We do this using the rotations

$$\begin{aligned}
\hat{\sigma}_i^x &= \cos\phi_i \hat{S}_i^x && -\sin\phi_i \hat{S}_i^y && ; \\
\hat{\sigma}_i^y &= \sin\phi_i \hat{S}_i^x && +\cos\phi_i \hat{S}_i^y && ; \\
\hat{\sigma}_i^z &= && \hat{S}_i^z && .
\end{aligned} \tag{6.10}$$

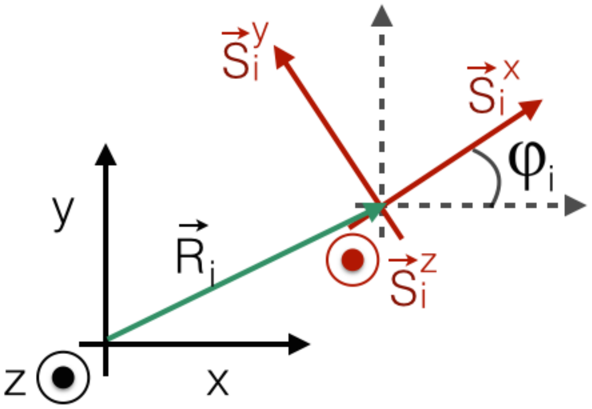

FIGURE 6.5: The local axis maps onto the global axis per site as a function of the rotations dependent on site and for angle ϕ. This is a rotation in spin space, which translates as the rotated Pauli matrices being written in terms of both σ_x and σ_y. As the rotation is within the easy plane the z components remain unchanged.

This is shown visually by Fig.6.5, where the global axes in black share their origin with the centre of a given molecule. The red local axis has its rotation dependent on site and the vector $\mathbf{R}_i$ shows the site position as relates directly to Eq. 6.9.

Thus σ can be generalised

$$\hat{\sigma}_i^{\alpha} = \sum_{\mu} \Lambda_{\alpha,\mu}\left(\phi_i\right) \hat{S}_i^{\mu}, \tag{6.11}$$

where the matrix

$$\left[\Lambda_{\alpha,\mu}\left(\phi\right)\right]_{\substack{\alpha \;=\; x,y,z \\ \mu \;=\; x,y,z}} = \begin{pmatrix} \cos\phi & -\sin\phi & 0 \\ \sin\phi & \cos\phi & 0 \\ 0 & 0 & 1 \end{pmatrix} \tag{6.12}$$

and the real space correlators are

$$\left\langle \hat{\sigma}_i^{\alpha} \hat{\sigma}_j^{\beta} \right\rangle = \sum_{\mu} \sum_{\gamma} \Lambda_{\alpha,\mu}\left(\phi_i\right) \Lambda_{\beta,\gamma}\left(\phi_j\right) \left\langle \hat{S}_i^{\mu} \hat{S}_j^{\gamma} \right\rangle , \tag{6.13}$$

which reduces the problem of calculating the correlators between components of the spins defined with respect to the instrument's axes $\left\langle \hat{\sigma}_i^{\alpha} \hat{\sigma}_j^{\beta} \right\rangle$ to the correlators with respect to the local crystal axes $\left\langle \hat{S}_i^{\mu} \hat{S}_j^{\gamma} \right\rangle$. This can be inserted into Eq. 6.9 to calculate $S_{\alpha\beta}\left(\mathbf{q}\right)$. Once $S_{\alpha\beta}\left(\mathbf{q}\right)$ are obtained, it is easy to get $S\left(\mathbf{q}\right)$.

For the results in this chapter, it is this scattering function that will be used to display the information about the chosen magnetic molecules as they are all that are needed to properly encapsulate the physics behind the ET and the experimental signatures that could be taken from a real experiment.

6.3 Plaquette

As experienced from previous chapters, from a theoretical point of view, the most salient feature of our model at the factorisation field h_f is the transition between different types of quantum entanglement [16]. It was shown from the amplitudes of the wavefunctions that the two ground states that switch over at the transition are completely orthogonal to each other. This suggests a strong effect on the correlation functions, as seen from a flattening in the real-space correlation function for PBC seen in section 5.5. In this section, focusing on the plaquette the possibility of measuring, using neutrons, ET is demonstrated by calculating the neutron scattering function.

Specifically, neutron scattering can be used to discriminate between antiferromagnetic and ferromagnetic correlations and therefore a significant change in the magnetic neutron scattering cross-section at h_f is expected.

6.3.1 Anisotropic XY-model

Fig. 6.6 shows the frequency-integrated neutron scattering function $S\left(\mathbf{q}\right)$ as a function of q_x and q_y for the anisotropic XY-model pictured in Fig. 6.2 for the $N = 4$ plaquette, each time a ground state degeneracy is encountered there is a re-organisation of spectral

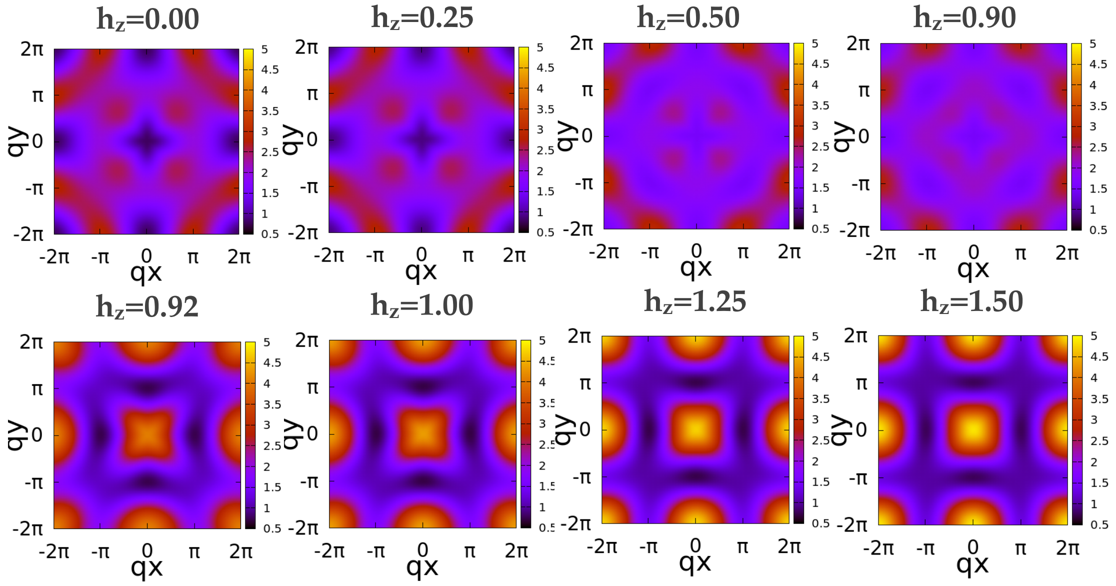

Figure 6.6: Frequency-integrated neutron scattering function $S(\mathbf{q})$ as a function of q_x and q_y for the anisotropic XY-model pictured in Fig. 6.2 for the $N = 4$ plaquette. Each panel corresponds to a magnetic field h_z, as indicated for the Hamiltonian parameters; $\gamma = 0.4$ and $\Delta = 0$. Note the values of h_z are regularly-spaced except for two additional panels, chosen to emphasise the sudden changes near the entanglement transition at $h_f \approx 0.917$.

weight. For this set of parameters for N=4 and $\gamma = 0.4$ the first level crossing occurs between the plots at $h_z = 0.25$ and $h_z = 0.50$. At the last degeneracy, i.e. at the factorisation field $h_f = 0.916$, there is a large transfer of weight to ferromagnetic peaks that are not present in the zero-field state: one at $\mathbf{q} = 0$ and N more at $|\mathbf{q}| = \frac{2\pi}{a}\cos(\frac{\pi}{N})^{-1}$, $\phi = \frac{2\pi}{N}n$ with $n = 0, 1, 2, N-1$. The peaks corresponding to anti-ferromagnetic correlations between the spins get much weaker, as their spectral weight is transferred to the new, purely ferromagnetic ones. Thus the gap-closing fields between the two lowest lying energy states (and especially the last one, corresponding in our model to exact factorisation) have clear signatures in the neutron scattering cross-section, indicating the re-organisations of correlations at such field values are crossed.

It is illuminating to plot the individual correlation functions $S_{\alpha\beta}(\mathbf{q})$, between different components of the spins, which contribute to the scattering function $S(\mathbf{q})$. Such spin-resolved correlators can be accessed experimentally *via* polarisation analysis. Alternatively, they can be obtained by observing, in a crystal, different regions of reciprocal space and exploiting the dipole-selection rules. Our predictions are shown in Fig. 6.7 (a) for the ground state of the $N = 4$ model with $\gamma = 0.4$. From the previous chapter, it is known that the system after h_f, though dominated by ferromagnetic interactions, there

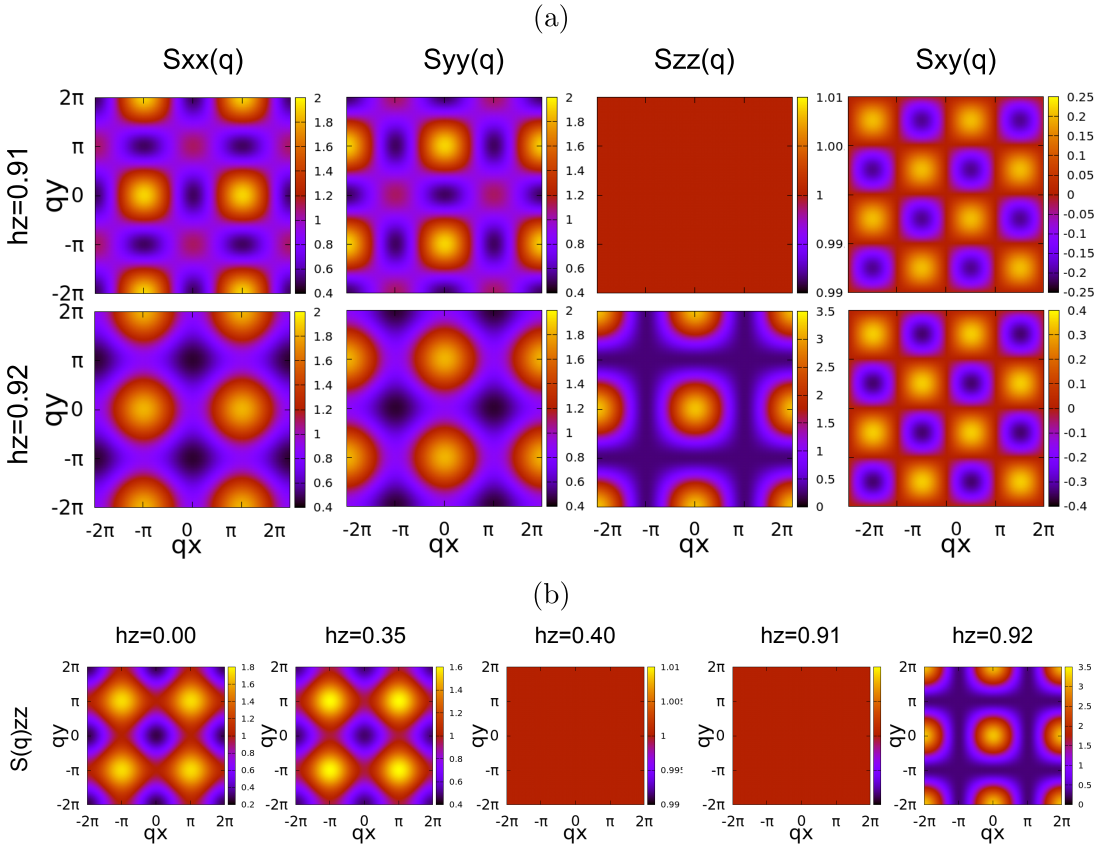

FIGURE 6.7: Top panels: field dependence of the spin-resolved correlators across the entanglement transition for a cluster with $N = 4$ spins and anisotropy parameter $\gamma = 0.4$. The top panels show the correlators $S_{xx}(\mathbf{q})$, $S_{yy}(\mathbf{q})$, $S_{zz}(\mathbf{q})$, and $S_{xy}(\mathbf{q})$ under the indicated applied magnetic field, which is just below the factorisation field $h_f \approx 0.916$. The bottom panels show the same correlators at a slightly higher field, also indicated, which is just above h_f. Bottom panels: the $S_{zz}(\mathbf{q})$ correlator over a broader range of fields, as indicated. The two leftmost panels correspond to fields below the first gap closing, the third and fourth panels are between the first gap closing and the factorisation field, and the last panel is above the factorisation field.

is additional entanglement with other components of the state with antiferromagnetic interaction. These are apparent as small antiferromagnetic peaks that lessen as the applied field continues to increase. This is made evident by Fig.6.7 that splits up the scattering function into its component parts before and after the entanglement transition.

The top panel shows how $S_{xx}(\mathbf{q})$, $S_{yy}(\mathbf{q})$, $S_{zz}(\mathbf{q})$, and $S_{xy}(\mathbf{q})$ change as the factorisation field h_f is spanned. The latter is essentially unchanged by the entanglement transition. The xx and yy correlators have two sets of anti-ferromagnetic peaks: some are very intense and are unaffected by crossing the entanglement transition; others are much weaker and get suppressed as h_z goes from just below to just above h_f. It is these latter peaks whose disappearance is noticed in Fig. 6.6. Their persistence indicates that anti-ferromagnetic correlations overall change very little at the entanglement transition. Clearly, the suppression of anti-ferromagnetic correlations is *not* the dominant phenomenon at h_f. This sets a clear distinction between the entanglement transition and the quantum critical point known to exist in the bulk ($N \to \infty$) phase diagram of these models. In contrast, the zz correlator changes dramatically at h_f: it goes from being featureless just below h_f to showing very strong ferromagnetic peaks. This is consistent with the jump in magnetisation discussed above section.

Fig. 6.7 (b) shows the zz correlator over a broader range of fields. At low fields the z components of the spins are anti-ferromagnetically correlated. At the first closing of the gap the system goes into the state where there are no correlations between the z components of different spins, before emerging into the ferromagnetically-correlated state above h_f. Interestingly the first state is an adiabatic continuation of the third one (supported by Fig. 5.16), the only difference being the relative amplitudes of ferro- and antiferromagnetic configurations. Although the $S_{zz}(\mathbf{q})$ function of $\mathbf{q}$ has the highest spectral weight after the ET, the addition interactions from the remaining functions can not be ignored as their contribution to the ferromagnetic peaks require that the new overall state is entangled. This entanglement is lost at very high fields. When the field saturates the spins to a state $|\uparrow\uparrow\uparrow\uparrow\rangle$ then the neutron scattering peaks become circular in the $2D$ $q_x q_y$ plane.

At finite temperatures, the neutron scattering functions look similar to those in the ground state, as Fig. 6.7 also shows. The broadening of the entanglement transition with temperature is further discussed below as seen in Fig. 6.8.

This shows the scattering function plots for a range of increasing field values for the same anisotropic XY-model at $T = 0.1J$, which as a comparison to the thermodynamic limit was unable to find any indication of the entanglement transition at the same finite temperature. The graphs show that the same states are occupied compared to the zero temperature plots and that a change to the ferromagnetically entangled state occurs, however, the transition is more gradual. This is acceptable and the different entangled states are still detectable using these neutron techniques.

It is clear from the above results that a diffuse neutron scattering experiment on such finite-size magnets can be used to determine a "phase diagram" of the entanglement

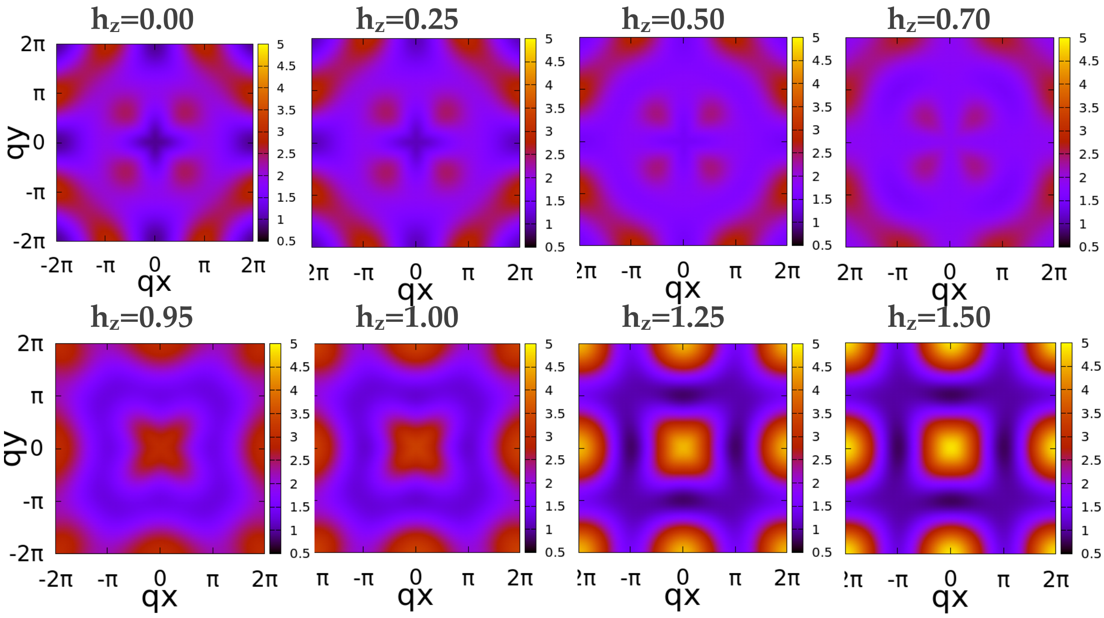

FIGURE 6.8: Frequency-integrated neutron scattering function $S(\mathbf{q})$ as a function of q_x and q_y for the anisotropic XY-model pictured in Fig. **??** for the plaquette at $T = 0.1J$. Each panel corresponds to a magnetic field h_z, as indicated for the Hamiltonian parameters; $\gamma = 0.4$ and $\Delta = 0$. The transition becomes spread through a larger range of field values at this temperature, though the changes in spectral weight are consistent for the ET.

transition. Specifically, a sudden jump in $S(\mathbf{q} = 0)$ reflects the sudden change of correlations occurring at $h_z = h_f$.

Interestingly, the sharp transition occurs at a value of the field that is $N-$independent and given by the Kurmann *et al.*. 3.8 (the cyan line in Fig.6.9). Note in particular that the transition identified does *not* correspond with the quantum critical point (QCP) known to occur at $h_c = 1$ in the thermodynamic limit $N \to \infty$ (the black line in the same figure).

The sharpness of the entanglement transition is in clear contrast to a quantum-critical point, which is expected to be very broad in such small systems, even at zero temperature. Indeed the critical field is evident as a much broader feature at another field h_c^*, which is independent of γ but depends strongly on N, being closer to h_c for the larger N value. This is what finite-size scaling would suggest for a critical point and is in marked contrast to the signatures of the entanglement transition and other level crossings that has been discussed above. The latter are thus clearly not long-wavelength phenomena. Indeed as shown in Fig.6.9 the smoothed QCP is only apparent outside

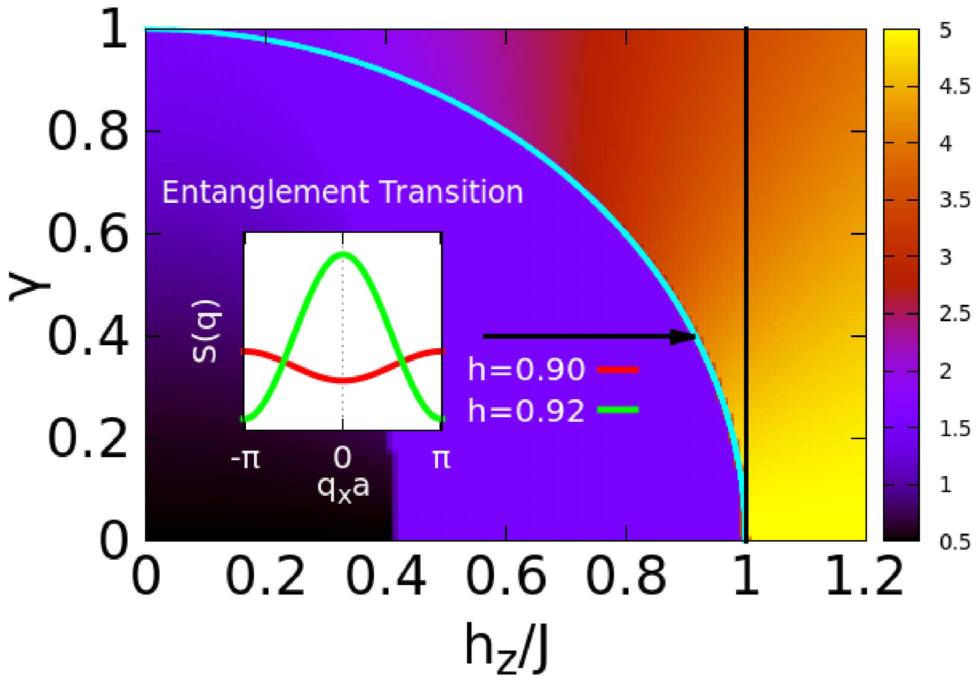

FIGURE 6.9: Ground-state value at $\mathbf{q} = 0$ of the magnetic neutron scattering function, $S(\mathbf{q})$, as a function of the anisotropy parameter γ and the applied field h_z for $N = 4$. The curved cyan and vertical black lines indicate, respectively, the factorisation field h_f ($h_f = \sqrt{(1-\gamma^2)}$) and the quantum critical field in the limit $N \to \infty$, $h_c = 1$. [10] [11] Insets: dependence of $S(\mathbf{q})$ on wave vector $\mathbf{q}$ for $h = 0.90$ and 0.92, respectively. These two values are just below and just above the entanglement transition.

the dome defined by the factorisation field, indicating that factorisation, not criticality, dominates the phase diagram for clustered magnets.

6.3.2 XYZ-model

In this section we employ the same approach as above and discuss the calculated neutron scattering cross-section plots for the XYZ-model, whose Hamiltonian is given in Eq. 3.5.

Fig. 6.10 is the scattering function for the ground state of the XYZ-model for the following in plane anisotropy parameter $\gamma = 0.5$ and out-of-plane anisotropy parameter $\Delta = 0.5$ as explored in the previous chapter for its energy spectra etc. A more detailed selection of field values are provided, but it can be seen that the spectral weight only changes at two field points. These correspond to the two degenerate points at the first level crossing and the factorisation field at $hf = 1.41$. As expected, the plots are directly comparable to the anisotropic XY-model from Fig. 6.6 as the distribution of the spectral

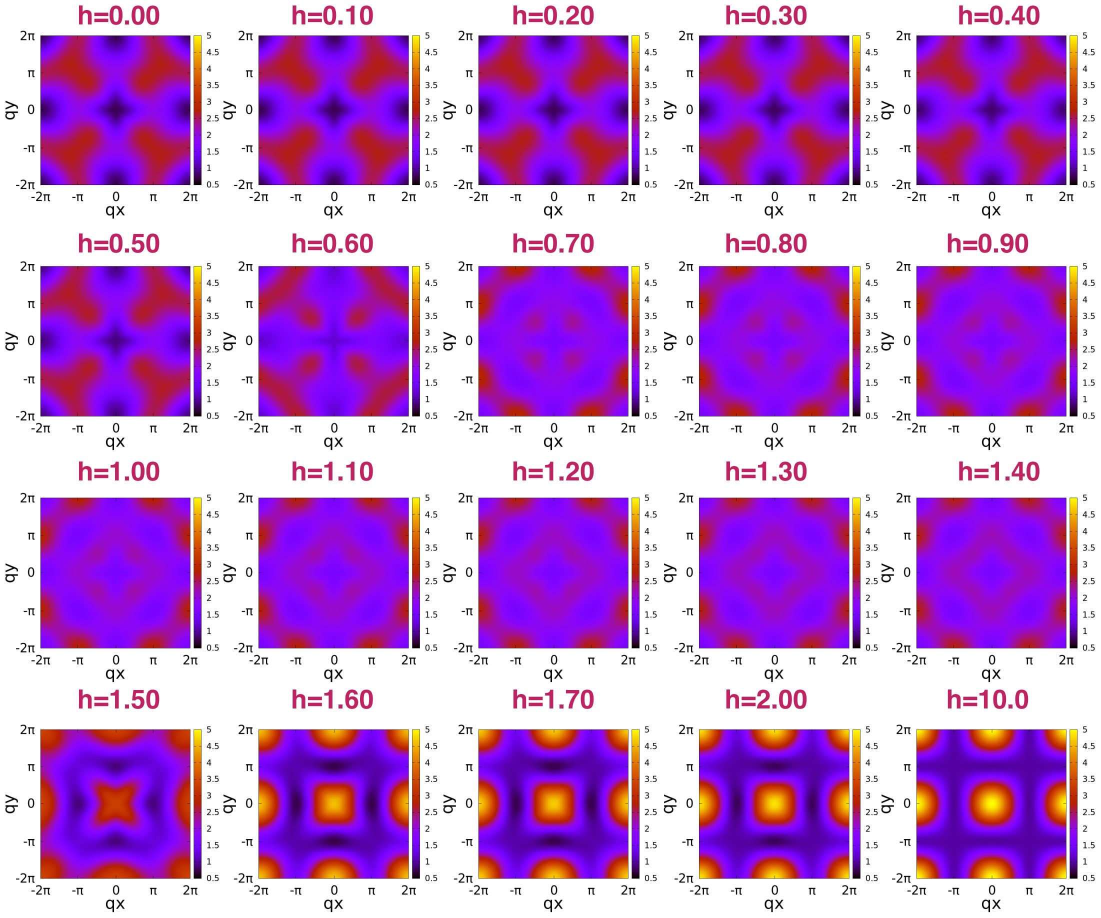

Figure 6.10: Frequency-integrated neutron scattering function $S\left(\mathbf{q}\right)$ as a function of q_x and q_y for the XYZ-model pictured in Fig. 6.2 for the plaquette. Each panel corresponds to a magnetic field h_z, as indicated for the Hamiltonian parameters; $\gamma = 0.5$ and $\Delta = 0.5$. An additional panel for a saturated field of $h_z = 10$ is given at the end to show how the ferromagnetic peaks become more rounded as the system become pure

weight for different phases are basically the same and it is only the position of the level crossings that change.

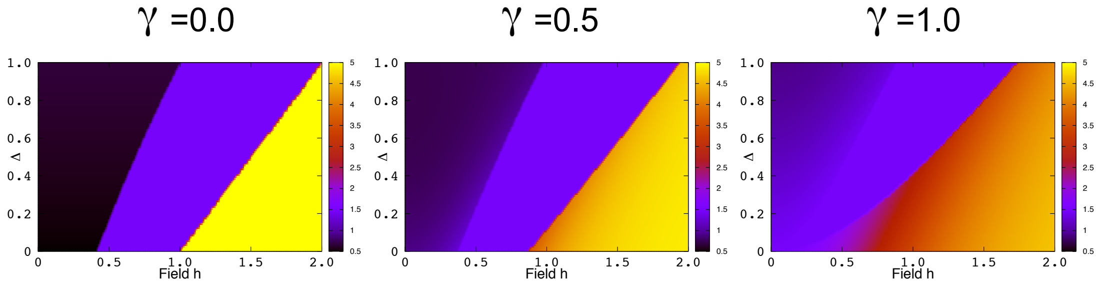

Figure 6.11: Ground-state value at $\mathbf{q} = 0$ of the magnetic neutron scattering function, $S(\mathbf{q})$, as a function of the applied field h_z and anisotropy parameters Δ for $\gamma = 0.0, 0.5$ and 1.0 respectively, for the XYZ-model $N = 4$ plaquette.

The same approach is taken to construct phase diagrams for the XYZ-model for a selection of in plane anisotropy values for $\gamma = 0.0, 0.5$ and 1.0 for $0.0 \leq \Delta \leq 1.0$ as given in Fig. 6.11. The factorisation field follows the second level crossing from Eq. 3.9 and there is a very distinct change from the predominantly antiferromagnetically entangled ground state to the predominantly ferromagnetically entangled ground state, where the ferromagnetic peak from $S(0)$ very suddenly appears as indicated by the bright yellow sections. Again, there is no indication of any QCP for systems of this small size and it is thought that by being about to solve the XYZ-model exactly, that it provides insight into further materials in which, to detect the entanglement transition using neutron scattering.

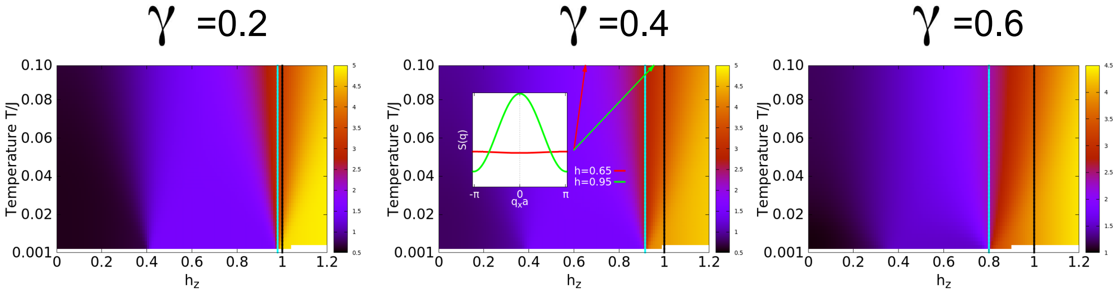

FIGURE 6.12: Temperature-dependence of the quantity plotted in Fig.6.9 for the plaquette. The in-plane anisotropy is $\gamma = 0.2, 0.4$ and 0.6 (left to right) as indicated. The factorisation field h_f is indicated in each case by the vertical cyan line. Inset: dependence of $S(\mathbf{q})$ on wave vector $\mathbf{q}$ for $T = 0.1J$ and the perpendicular values of field indicated, this corresponds to the inset of the ground state value in Fig.6.10.

At finite temperatures, the signature of the entanglement transition is less sharp, but still clearly visible for temperatures $\sim 10\%$ of the exchange constant J. This is clear from the finite-temperature plots in Fig.6.8. In addition, Fig.6.12 shows the same quantity depicted in Fig.6.9 as a function of field and temperature for three particular values of the anisotropy parameter, $\gamma = 0.2, 0.4$ and 0.6. Clearly, the rapid change of $S(\mathbf{q} = 0)$ with h_z near h_f persists. The insets to the $\gamma = 0.4$ panels also show very similar rearrangements of the $\mathbf{q}$-dependence of the scattering function to those shown in Fig.6.9, albeit they occur over a wider field range.

For completeness, Fig. 6.13 gives the finite temperature signature of the entanglement transition for the XYZ-model for the anisotropy values $\Delta = 0.5$ and $\gamma = 0.0, 0.5$ and 1.0 respectively. The dashed lines show the factorisation field for these values of the anisotropy. As with the anisotropic XY-model the transition is still apparent though

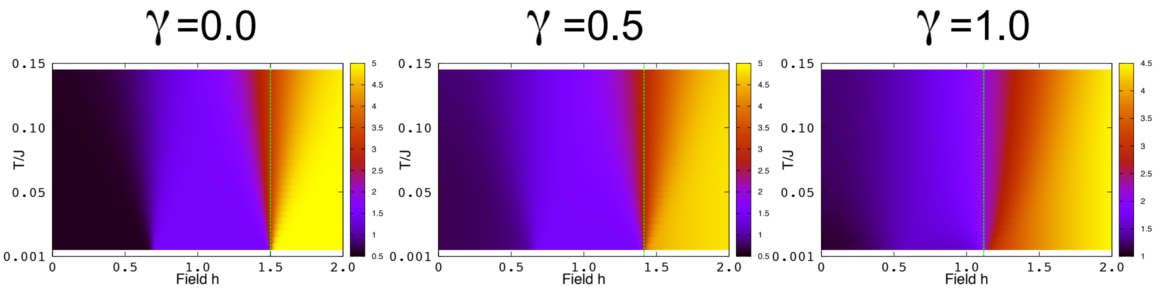

FIGURE 6.13: Temperature-dependence of the quantity plotted in Figure.6.11 for the plaquette in the XYZ-model. The in-plane anisotropy values are for $\Delta = 0.5\ \gamma = 0.0, 0.5$ and 1.0 (left to right) as indicated. The factorisation field h_f is indicated in each case by the vertical green dashed line.

over a broader range in the field as the temperature increases. It is arguable that the XYZ-model could even be used to detect the ET at temperatures up to 15% of the interaction energy.

The plaquette model provides a very strong case for a neutron scattering experiment that would easily detect the entanglement transition in an achievable environment.

6.4 Hexagon

The same approach is used in studying the hexagon model using Figure.6.2 as the method to calculate the global properties of the Hexagon. From the previous chapter, it is known that the $N = 6$ model with periodic boundary conditions has distinct behaviour in the correlation functions when the system experiences an external field that matches a level crossing in the energy spectrum. This $N = 6$ system size has three level crossings with the last level crossing at the factorisation field, where the correlation functions ‘flatten’ and the hexagon undergoes the ET. The neutron scattering function is plotted in Fig. 6.14 for the hexagon ground state for the same field steps as the plaquette and the same parameters for $\gamma = 0.4$ and $h_f = 0.916$.

The states are antiferromagnetically entangled at zero field and at high fields after the factorisation field level crossing become predominantly ferromagnetically entangled, though in between this there are some more complicated types of entanglement. There is little difference at the first level crossing but at the second level crossing there is some shift in the spectral weight to allow for some ferromagnetic peaks to join the

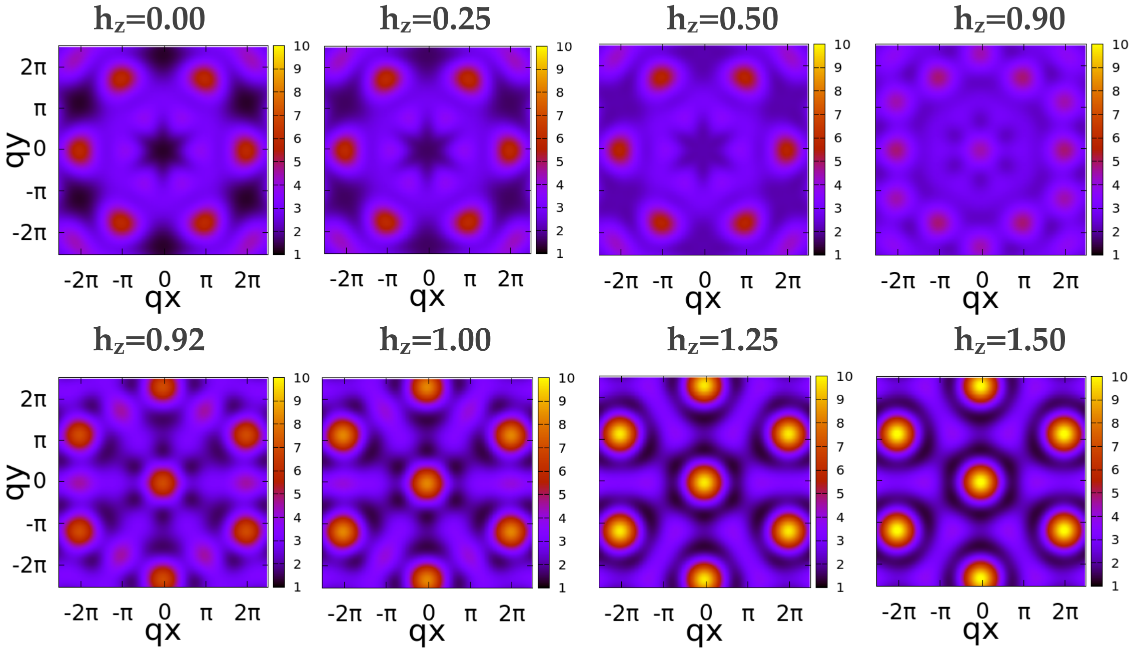

FIGURE 6.14: Frequency-integrated neutron scattering function $S(\mathbf{q})$ as a function of q_x and q_y for the XY-model pictured in Fig. 6.2 for the hexagon. Each panel corresponds to a magnetic field h_z, as indicated for the Hamiltonian parameters; $\gamma = 0.4$ and $\Delta = 0$. Note the values of h_z are regularly-spaced except for two additional panels, chosen to emphasise the sudden changes near the entanglement transition at $h_f \approx 0.916$.

antiferrormagnetic peaks. It is at the last level crossing that the antiferromagnetic peaks are reduced and the ferromagnetic peaks take an increase in intensity. As the field continues to increase there is a gradual decrease in the antiferromagnetic peaks until the state completely saturates and becomes ferromagnetic aligned with the field.

It was not possible to analyses directly the separate ground states for the system sizes larger than the plaquette. For the hexagon there are 64 basis states where each ground state has 32 non-zero amplitude components to assess, where again, the two ground states are orthogonal to each other. It is possible to break the scattering function into parts, as was done with the plaquette, in order to gain further information about the origins of the different complex arrangements of peaks. Fig 6.15 shows the individual contributions to the total scattering function. This break down reveals some complicated structures in the different global planes that come from the geometry of the hexagon. $S_{xx}(q)$ and $S_{yy}(q)$ have an antiferromagnetic contribution from particularly angled sites with potentially some magnetic frustration in these planes, indicated by a pinch point in the middle. However, when all summed the symmetry of the system is regained and the pinch point lost. The ferromagnetic peaks seem to only be from $S_{zz}(q)$ so are only

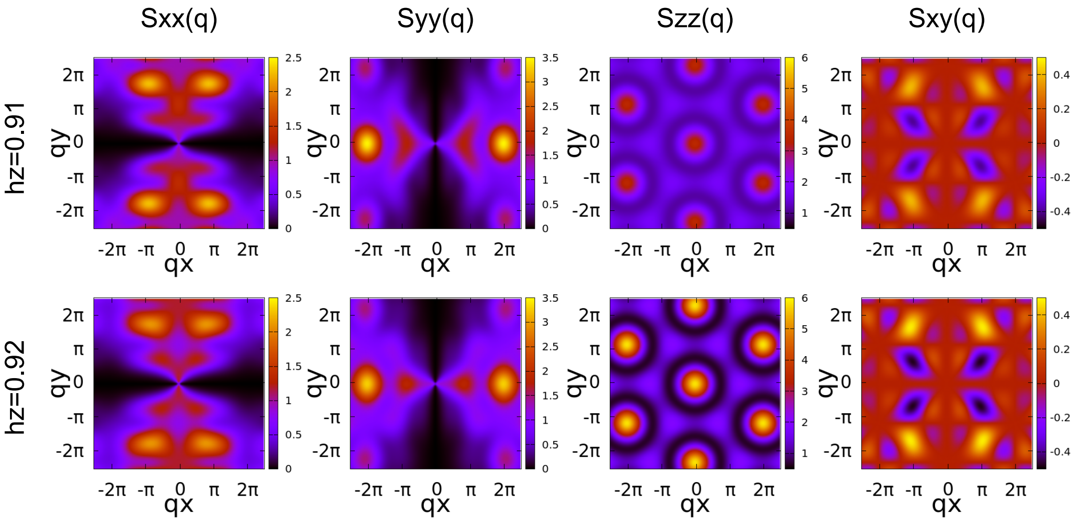

FIGURE 6.15: Field dependence of the spin-resolved correlators across the entanglement transition for a cluster with $N = 6$ spins and anisotropy parameter $\gamma = 0.4$. The panels show the correlators $S_{xx}(\mathbf{q})$, $S_{yy}(\mathbf{q})$, $S_{zz}(\mathbf{q})$, and $S_{xy}(\mathbf{q})$ under the indicated applied magnetic field, which are just below and above the factorisation field $h_f \approx 0.916$.

ferromagnetic aligned with the applied field. Across the factorisation field there is a little change in all the component parts, with the biggest visual change being the strength of the ferromagnetic interactions now dominating the scattering function. There is still a significant amount of antiferromagnetism left to add to the entanglement in the system. This is supported by the concurrence calculation in the previous chapter in Fig.5.30.

At finite temperatures, the shift in spectral weight for $S(q)$ as the field increases follows the same trends as the ground state from Fig. 6.14. The changes are, again, more gradual and over a broader range of fields as shown in Fig. 6.16 for a reasonable high finite temperature of $T = 0.1J$ but the intention is the same. To demonstrate this further the temperature scale is studied from a slice from the phase diagram, which like before was plotted from $S(0)$ for all anisotropy in Fig. 6.17.

Using Fig. 6.17, it is clearer to observe the changes over the level crossings, where for low anisotropy all three crossings can be seen. It is also seen that the ferromagnetic peak at $S(q)$ emerges at the second level crossing and significantly strengthens at the factorisation field. At high in plane anisotropy most of the features are lost and the growth of the ferromagnetism could be called monotonic. The inset shows a qualitative change in the scattering peaks for $\gamma = 0.4$ as the antiferromagnetic peaks are suppressed at the transition which can also be identified at temperatures up to $T = 0.1J$.

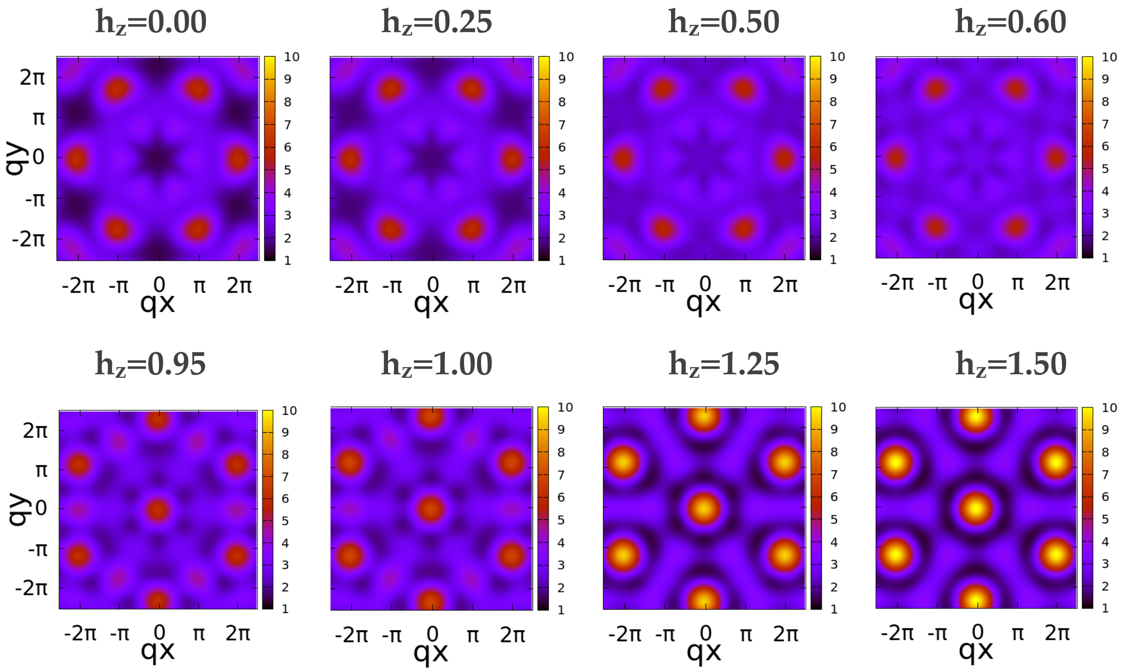

Figure 6.16: Frequency-integrated neutron scattering function $S(\mathbf{q})$ as a function of q_x and q_y for the anisotropic XY-model pictured in Fig. 6.2 for the hexagon at $T = 0.1J$. Each panel corresponds to a magnetic field h_z, as indicated for the Hamiltonian parameters; $\gamma = 0.4$ and $\Delta = 0$. The transition becomes spread through a larger range of field values at this temperature, though the changes in spectral weight are consistent for the ET.

The finite temperature effects broaden the transition, where the figure inset for $\gamma = 0.4$ in Fig.6.18 matches the qualitative change in behaviour as the one in Fig.6.17 but over a broader range of the field. Also for $\gamma = 0.4$ the distinction of the earlier level crossing is lost very quickly, leaving only the entanglement transition significantly changing the neutron scattering signature of the system at finite temperatures.

The XYZ-model gave encouraging results for the plaquette and results were obtained for the hexagon were equally promising. The scattering cross-section plots for $S(q)$ looked the same as the anisotropic XY-model and there is no need to provide them all here. Instead, in the same way as before, Fig. 6.19 shows a selection of phase diagrams for the anisotropy parameters for $\Delta = 0.5$ and $\gamma = 0.0, 0.5$ and 1.0 respectively.

For $\gamma = 0.0$ and 0.5 the distinction of all the level crossings are very apparent; the second crossing shows the appearance of the central ferromagnetic peak, which then jumps higher in intensity at the factorisation field in agreement with the plaquette from Fig. 6.11 . For the last panel, $\gamma = 1.0$ for low values of Δ the system tends towards the Ising model where, as was also seen, in Fig.6.17 that the clear boundary at the

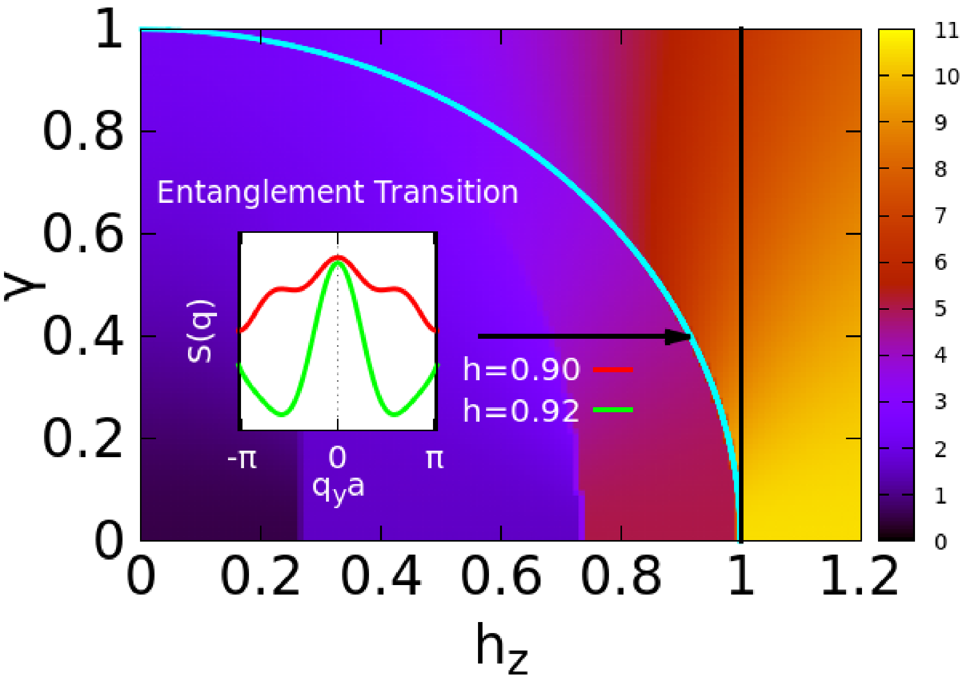

FIGURE 6.17: Ground-state value at $\mathbf{q} = 0$ of the magnetic neutron scattering function, $S(\mathbf{q})$, as a function of the anisotropy parameter γ and the applied field h_z for $N = 6$. The curved cyan and vertical black lines indicate, respectively, the factorisation field h_f ($h_f = \sqrt{(1-\gamma^2)}$) and the quantum critical field in the limit $N \to \infty$, $h_c = 1$. [10] Insets: dependence of $S(\mathbf{q})$ on wave vector $\mathbf{q}$ for $h = 0.90$ and 0.92, respectively. These two values are just below and just above the entanglement transition

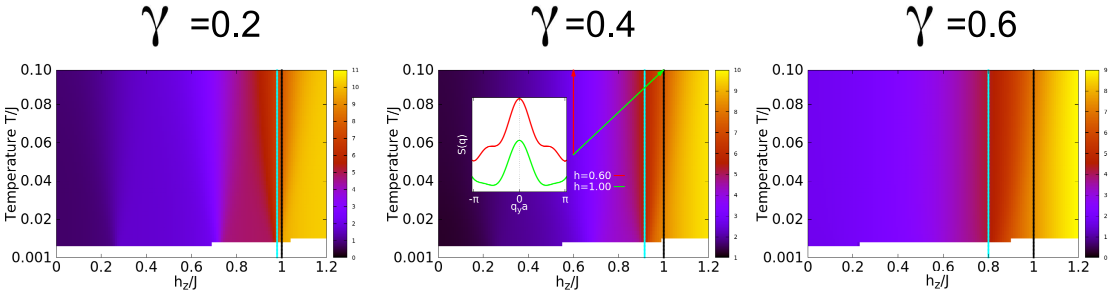

FIGURE 6.18: Temperature-dependence of the quantity plotted in Figure.6.17 for the hexagon. The in-plane anisotropy is $\gamma = 0.2, 0.4$ and 0.6 (left to right) as indicated. The factorisation field h_f is indicated in each case by the vertical cyan line. Inset: dependence of $S(\mathbf{q})$ on wave vector $\mathbf{q}$ for $T = 0.1J$ and the perpendicular values of field indicated, this corresponds to the inset of the ground state value in Figure.6.17

factorisation field is lost, we do not have a reason for this. The green line indicates the factorisation field for $\gamma = 1$ from Eq. 3.9, so it can be seen where the ferromagnetic peaks start to deviate away from it. Therefore, for the temperature analysis the values of $\gamma = 0.0$ and 0.5 are taken and expanded for a temperature scale both with anisotropy

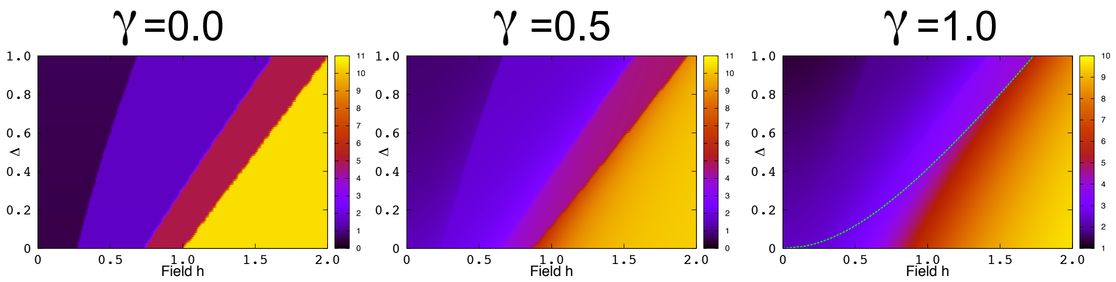

FIGURE 6.19: Ground-state value at $\mathbf{q} = 0$ of the magnetic neutron scattering function, $S(\mathbf{q})$, as a function of the applied field h_z and anisotropy parameter Δ for $\gamma = 0.0, 0.5$ and 1.0 respectively, for the XYZ-model hexagon. The dashed line on the last panel for $\gamma = 1.0$ shows the factorisation field h_z.

$\Delta = 0.5$ fixed in Figure.6.20.

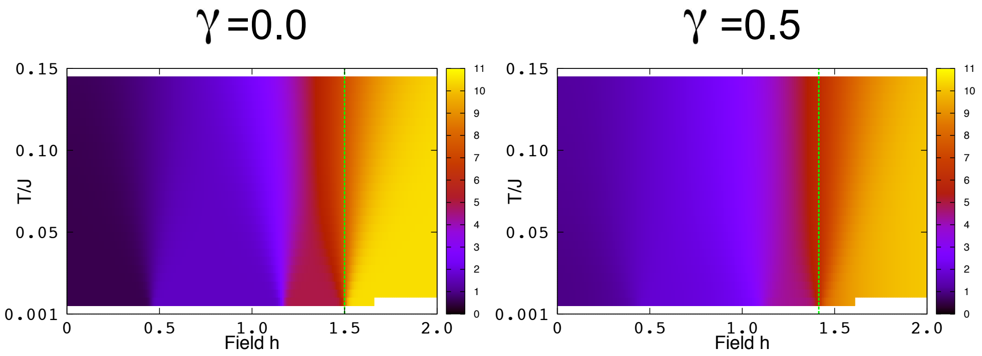

FIGURE 6.20: Temperature-dependence of the quantity plotted in Figure.6.19 for the hexagon in the XYZ-model. The in-plane anisotropy values are for $\Delta = 0.5$ $\gamma = 0.0$ (left) and 0.5 (right) as indicated. The factorisation field h_f is indicated in each case by the vertical green dashed line.

The temperature analysis remains promising, and just like the plaquette (Fig. 6.13), the XYZ-model shows a broadened entanglement transition up to a very respectable finite temperature of 15% of the interaction J. Despite the broadening in the transition there is still a very real qualitative change in behaviour of the system, that is more than change between antiferromagnetism to ferromagnetism. The analysis has shown that the states involved are complicatedly entangled and very differently entangled across the transition, with the two lowest-lying states being orthogonal. This is seen by the different contributions of the scattering function from Fig.6.15 in conjunction with the concurrence calculation in the previous chapter.

The hexagon model, though more complex that the plaquette in the states and arrangement of entanglement is also a viable candidate for experimentation on small clustered quantum materials.

6.5 Larger Rings

Having discussed very small spin clusters of $N = 4$ and $N = 6$ separately, this section will combine the discussion for slightly larger magnetic molecules as the behaviours exhibited by the rings follows similar trends.

The zero-field magnetic neutron scattering spectrum of a system with $N = 8$ has been investigated experimentally in detail by Baker *et al.* [8]. In their paper there is a deep minimum in scattering at the ferromagnetic wave vector $\mathbf{q} = 0$ and N sharp antiferromagnetic peaks with $|\mathbf{q}| = \frac{2\pi}{a}$ at angles $\phi = \frac{2\pi}{N}\left(\frac{1}{2} + n\right),\ n = 0, 1, 2, \ldots, N-1$ to the q_y axis. A similar calculation for $N = 8$ confirms this close resemblance in Fig. 6.21 for $\gamma = 0.0$ at zero field $h = 0.0$ (left) and at a saturated field $h = 10.0$ (right).

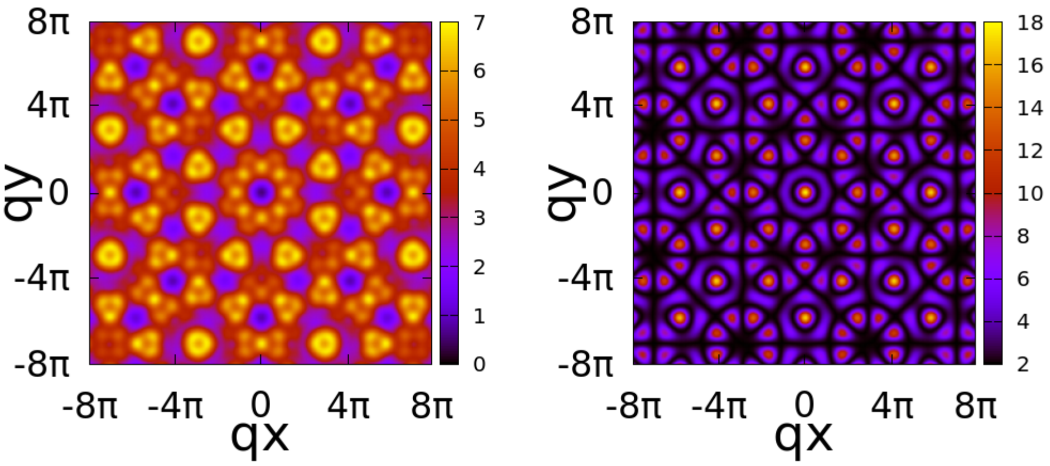

FIGURE 6.21: Frequency-integrated neutron scattering function $S(\mathbf{q})$ as a function of q_x and q_y for the anisotropic XY-model for the octagon. (left) is the zero field calculation for an isotropic ring of $N = 8$ dominated by antiferromagnetic entanglement. (right) is the saturated field calculation $h_z = 10$ for a classical ferromagnet aligned with the applied field.We take a larger range for q_x and q_y to visually determine that the whole range of the scattering function is captured and repeats.

The scattering function is calculated in much the same way as the smaller molecules shown in Fig. 6.2, a larger q range is used to ensure the whole signature is captured. When the systems get larger the analysis of the scattering function becomes more difficult and the number of level crossings appear to change the behaviour of the system more

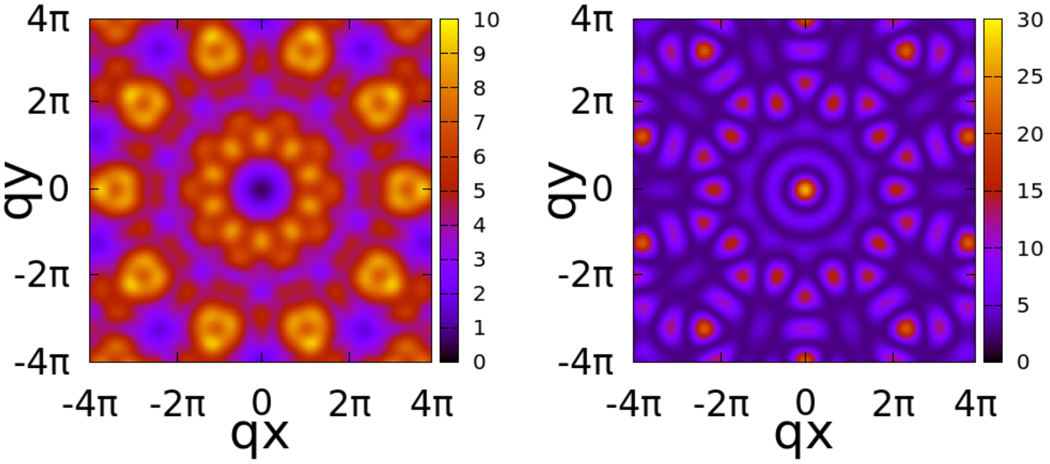

FIGURE 6.22: Frequency-integrated neutron scattering function $S(\mathbf{q})$ as a function of q_x and q_y for the XY-model for the decagon. (left) is the zero field calculation for an isotropic ring of $N = 10$ dominated by antiferromagnetic entanglement. (right) is the saturated field calculation $h_z = 10$ for a classical ferromagnet aligned with the applied field.

gradually making the last level crossing at the factorisation field more difficult to observe. From Figure.6.21 it is clear that at these simple limits for $h = 0$, $\gamma = 0$ the $N = 8$ system; and Fig.6.22 for the $N = 10$ system, are completely antiferromagnetic and at $h = 10.0$ for $\gamma = 0$ the ring systems are saturated ferromagnetically with the field.

These trends are seen in the hexagon and it was the signature of the transition that is observed most clearly in its phase diagram, as opposed to the lower level crossing features. Fig. 6.23 is the phase diagram for the octagon for values taken at $S(0)$, with additional information given by the break down of the neutron scattering function in Figs. 6.24 to 6.26.

The phase diagram does show some indication of all four level crossings for a $N = 8$ ring at low in-plane anisotropy, with the factorisation field being the most dominating feature. Ferromagnetism appears at the level crossing before the factorisation field as was observed with the hexagon model. The scattering function can be split up to better understand where the different features come from.

Starting with the zero field calculation for a ring with $\gamma = 0.4$ the system is mostly antiferromagnetically entangled. As plotted in Fig. 6.24 each panel contributes to some

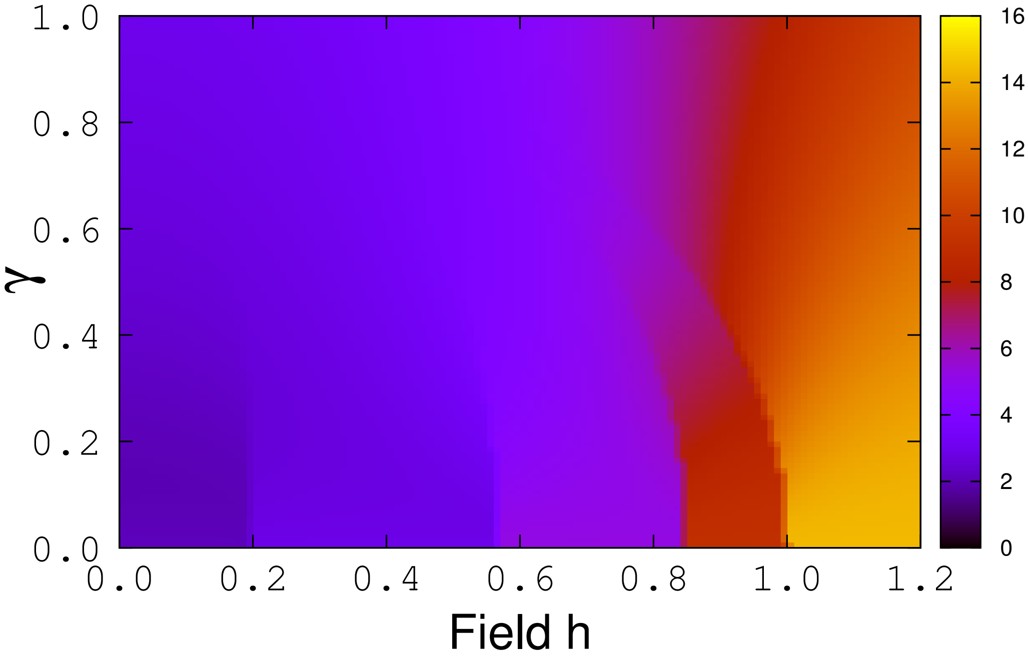

FIGURE 6.23: Ground-state value at $\mathbf{q} = 0$ of the magnetic neutron scattering function, $S(\mathbf{q})$, as a function of the anisotropy parameter γ and the applied field h_z for $N = 8$. There is some indication of all four level crossings at lower in-plane anisotropy range.

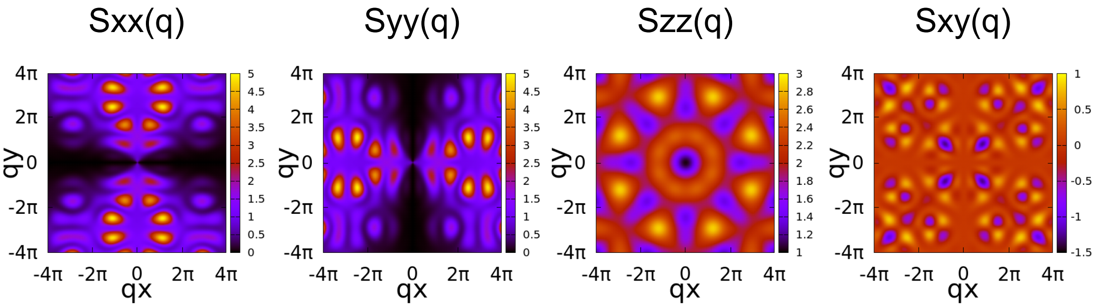

FIGURE 6.24: Field dependence of the spin-resolved correlators across the entanglement transition for a cluster with $N = 6$ spins and anisotropy parameter $\gamma = 0.4$. The panels show the correlators $S_{xx}(\mathbf{q})$, $S_{yy}(\mathbf{q})$, $S_{zz}(\mathbf{q})$, and $S_{xy}(\mathbf{q})$ at zero field.

complex arrangement of entanglement dominated by antiferromagnetic interactions. The next Fig. 6.25 shows before and after the entanglement transition.

The results are very similar to the hexagon; there is very little apparent shift in the spectral weight in its structure across the transition: the $S_{zz}(q)$ panel shows that the ferromagnetic peaks have already been established. The spectral weight is shifted though,

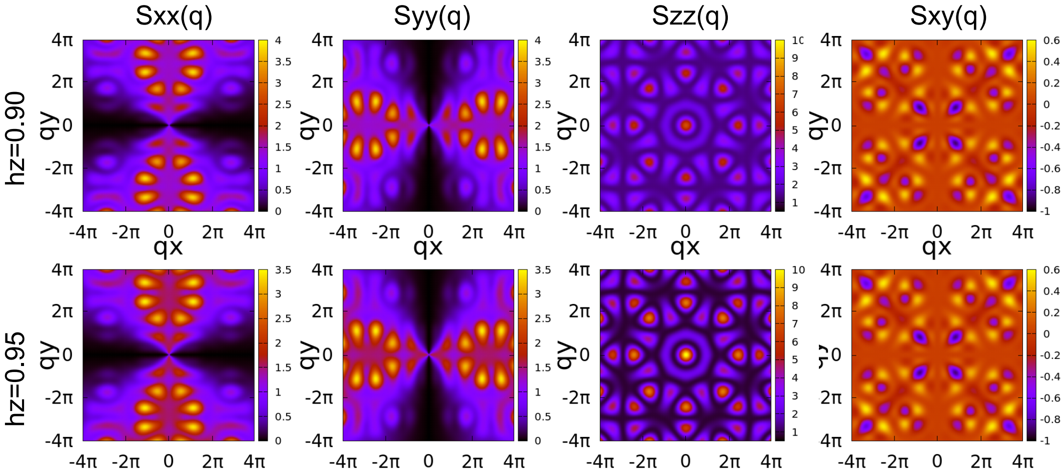

FIGURE 6.25: Field dependence of the spin-resolved correlators across the entanglement transition for a cluster with $N = 6$ spins and anisotropy parameter $\gamma = 0.4$. The panels show the correlators $S_{xx}(\mathbf{q})$, $S_{yy}(\mathbf{q})$, $S_{zz}(\mathbf{q})$, and $S_{xy}(\mathbf{q})$ at around the factorisation field.

as it is reduced from the antiferromagnetic peaks in $S_{xx}(q)$ and $S_{yy}(q)$ and there is a significant increase in $S_{zz}(q)$ ferromagnetic arrangement in favour of the applied field. The concurrence plots from the previous chapter indicate that the whole states are still quite strongly entangled and they also remind us that the behaviour of the thermodynamic limit can be mimicked by fairly small systems, even as small as $N = 10$. This is encouraging for these slightly larger systems as the amount of entanglement is reduced when distributed over more that one neighbour for an interacting site [21].

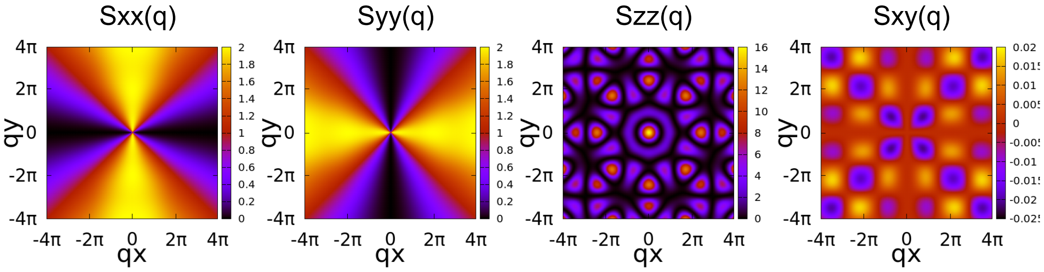

FIGURE 6.26: Field dependence of the spin-resolved correlators across the entanglement transition for a cluster with $N = 6$ spins and anisotropy parameter $\gamma = 0.4$. The panels show the correlators $S_{xx}(\mathbf{q})$, $S_{yy}(\mathbf{q})$, $S_{zz}(\mathbf{q})$, and $S_{xy}(\mathbf{q})$ at saturated field $h_z = 10$.

It is by saturating the field where Fig. 6.21 (right) can be recreated in a classical configuration of spins aligned with the field. Fig. 6.26 shows how $S_{xx}(q)$ and $S_{yy}(q)$ evolve in this limit, where their sum leads to a flat background scattering.

As these small clustered ring systems get larger, though there is evidence to suggest an entanglement transition, its experimental signature becomes more of a challenge to detect. There is an unusual balance between very small systems, where the complex arrangement of entangled states above and below the entanglement transition can be better understood, and a slightly larger ring systems. Their individual states are too large to fully study but they appear to tend towards some thermodynamic limit behaviour, which would suggest that the two ground states, as they slowly become degenerate average out to parallel and antiparallel entangled states [3]. As the level crossings get closer together it is only the effect of the factorisation field level crossing that remains as a detectable change of behaviour in the entanglement.

It is this balance of system size that finds a signature of the entanglement transition that can be picked up using the neutron scattering cross-section. Where the very small systems give a very clear change in scattering function that is robust to finite temperatures and the larger systems that mimic the thermodynamic limit which show a distinct feature in the concurrence but a better way of detecting it is needed.

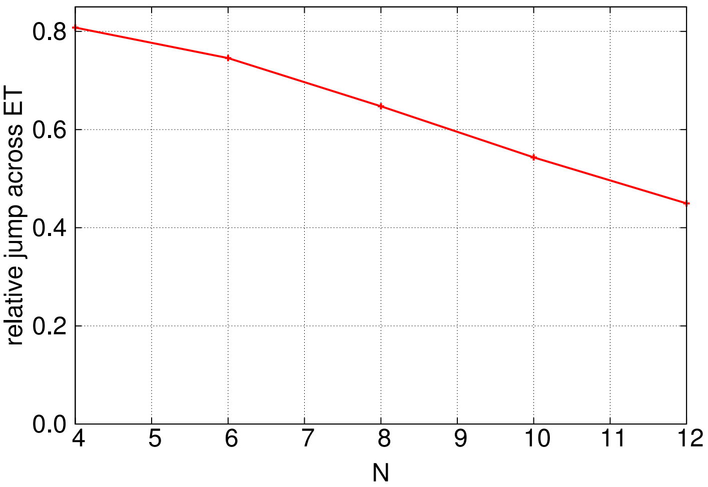

FIGURE 6.27: Dependence of an entanglement transition signature on cluster size, N. The plot shows the size of the jump in the quantity shown in the phase diagrams for the anisotropic XY-model for system sizes $N = 4, 6$ and 8 (and numerically calculated for larger systems) as the entanglement transition boundary is crossed, $\Delta S(\mathbf{q} = 0)$. The in-plane anisotropy is fixed at $\gamma = 0.4$.

Fig. 6.27 shows the relative size of the jump in $S(0)$ when compared to the value before and after the transition. The trend is that as the rings get larger their respective 'jump' at the transition gets smaller and harder to detect. For the smallest system $N = 4$ the jump is approximately 80% to the central peak where for the largest system calculated

$N = 12$ it was less than 50%. There are not enough data points to determine whether at the thermodynamic limit this signature tends to zero of some finite, albeit very low, temperature.

The best chances in experimentally detecting the entanglement transition using neutron scattering techniques would be to use either the plaquette or hexagon model where the signature of the transition is most clear and the temperatures potentially the most reasonable.

It is important to not completely discount the slightly larger systems as they clearly experience the entanglement transition as the thermodynamic limit does but may require a different technique to detect it clearly [97]. These rings would still hold an advantage over the real thermodynamic limit as it seems likely that they would have a more accessible temperature range than the infinite 1D chain systems, along with the flexibility of their synthesis as discussed in Chapter 3.

There is potential for this area to be expanded with specific materials in mind. The most natural progression of this work would be to directly model a real plaquette or hexagon based-material, but larger systems would benefit from an analysis of real anisotropic rings systems that can be modeled using the anisotropic XY-model or XYZ-model.

6.6 Additional Discussion

The previous chapter discussed a paper that was published by Campbell *et al* during the time spent working on this project [9]. Another pivotal paper was published during this time by Marty *et al.* with calculations towards neutron scattering experiments [12]. This paper is discussed in this section.

Marty *et al.* aim is to take the theoretical measures of entanglement in these types of systems and form some scattering based experimental predictions [12]. Their concept is to provide a lower bound estimation of entanglement of a general system using quantities found in the scattering function. They state that for a value of the scattering vector $\bar{q}$ (that relates to the change in momentum from a neutron scattered off the sample) then a Fourier Transform of the magnetic scattering cross section for $\bar{q}$ is a lower bound prediction on the amount of entanglement. This is a simplification of the process they have developed but outlines the key objective of the paper, which was to use experimentally measurable quantities to comment on the amount of entanglement in a general system.

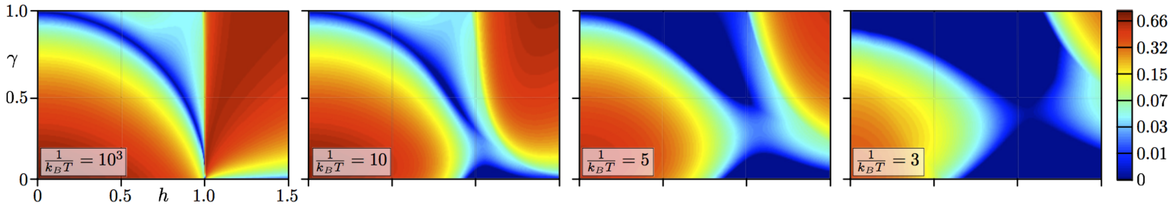

FIGURE 6.28: The lowest bound entanglement estimate for the anisotropic XY-model in the thermodynamic limit calculated with chain lengths $L = 200$ for a range of temperatures from lowest to highest from left to right. The lowest temperature plot shows the entanglement transition as the narrow dark blue region that indicates zero entanglement whilst above and below this value the entanglement in non-zero. This plot also indicates criticality at $h_c = 1.0$ for the thermodynamic limit for the applied transverse field. As the temperature increase the entanglement transition spreads out but would still be detectable at suitably low temperatures using this lower bound quantity [12].

Figure.6.6 shows the lower bound entanglement approximation for the anisotropic XY-model where h is the external transverse field and γ is the anisotropy parameter. From left to right the figures increase in temperature, starting effectively in the ground state and then a variety of low temperature states. The plots show that the amount of entanglement in the system is non-monotonic and that in the ground state there is an obvious blue trend dependent on h and γ where there is no entanglement. This non-entangled region spreads at higher temperature but the criteria for an entanglement transition is still apparent, i.e the system is entangled and using an applied field this can be tuned to zero at a particular point, after which it recovers. The point at which their entanglement measure goes to zero is the factorisation field and not the critical field, this is supported by Campbell *et al.* and our results [9]. Also in the finite temperature calculations, a feature indicating any criticaility for these system sizes does not appear in Fig.6.6.

This thesis explores many similar themes to Campbell *et al.* and Marty *et al.* but the work has found a unique niche in the literature by directly modeling the neutron scattering cross section for a range of magnetic molecules. With the very singular goal of finding a neutron signature of the entanglement transition at achievable temperatures it has lead the project through extensive study of finite-sized systems and the types of new and exciting spin clusters that could apply to them.

6.7 Axial Model

This entire project has been based around the use of 1D antiferromagnetic chains and their inherently entangled states. The focus of Chapter 6 has been to apply our 1D Hamiltonians to make 2D molecular magnets in the xy plane to explore the entanglement transition using neutron scattering predictions. This approach has been very successful. Using periodic boundary conditions in a 1D system to model small magnetic clusters, though a valid approach, is a simplistic method and avoids any cross term interactions that may arise in the geometry of the molecule. Another way of modeling the $N = 4$ plaquette and $N = 6$ hexagon is approached in this section that does consider cross-term interactions.[1]

The anisotropic XY-model and its continuation into the XYZ-model have been the foundation models for exploring the entanglement transition. One of the reasons being the well-understood nature of the factorisation field phenomena in these models. This has been discussed thoroughly in this thesis as the ET has been defined through this process. Adding periodic boundary conditions and forming a family of ring systems to model clustered quantum materials has allowed us to identify an ET signature using neutron scattering data to a relatively high temperature scale.

Taking the Hamiltonian for a 1D system and using it to predict the behaviour of a $2D$ molecule has been discussed as a valid method, however, it ignores any cross-term interactions in the xy-plane that the new geometry of the system might enforce. The cross-terms could be a result of some spin orbital overlap as the chain is 'bent' round a small circumference.

Some possible orientations of the orbitals is presented in Fig. 6.29 for a $N = 4$ system, starting with a simple chain then giving two speculative examples of a plaquette arrangement. Fig. 6.29 (b) has its interactions in the radial and tangential orientations for a molecule as would be fitting to our model in Fig. 6.2 for the plaquette, with the similar principle employed for the hexagon. Fig. 6.29 (c) is an equally valid approach to modeling a plaquette but with the additional contribution to the interactions from

---

[1] A third possible model to explore magnetic nano-structures would be to use Dzyaloshinskii-Moriya interactions to include cross terms is documented in relation to a factorising magnetic field for a trimer, seen in Florez *et al.* [101]

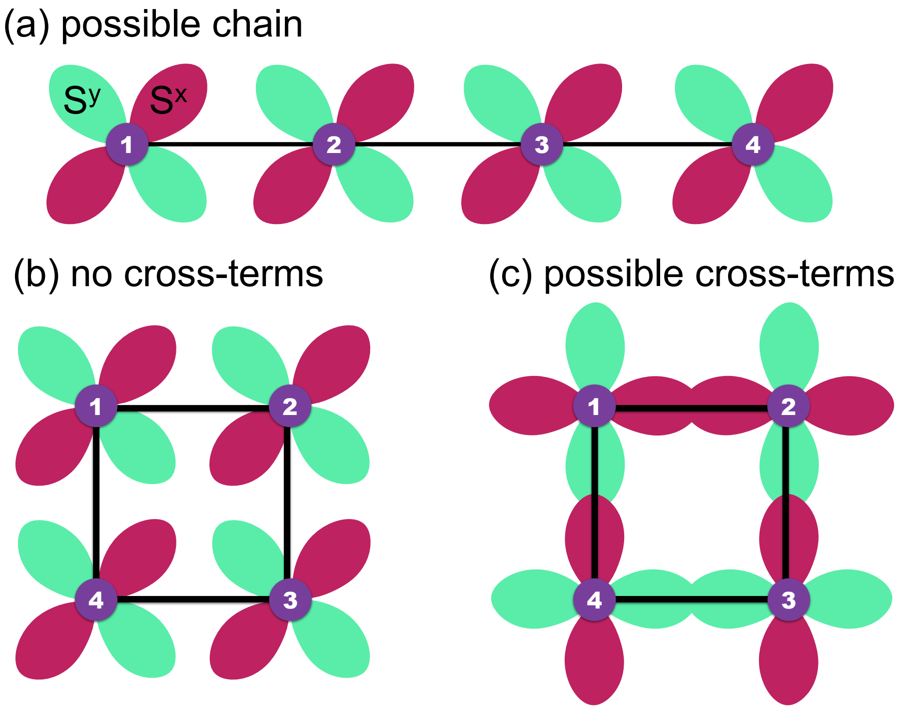

FIGURE 6.29: Our models when applied to real materials can form their interactions in many different ways. This figure is a collection of possible orientations of the spin interaction axis of our magnetic ions in a $N = 4$ system the green bubbles show an interaction orbital for the S_y spin interaction and the magenta bubbles indicate the interaction for the S_x spin direction. (a) shows a simple chain where arrangement of the spin orbitals are the same for every ion. This is a representation of the 1D spin Hamiltonians used throughout this project. (b) shows the possible arrangement of orbitals that have tangential and radial components with regards to the plaquette geometry as speculated for the results in the above sections for Chapter 6 and depicted in Fig. 6.2. (c) is an equally valid arrangement of the orbitals on a plaquette that contributes additional cross-terms to the interactions in the Hamiltonian, we will call his model the axial model. These allow for a scenario where the spin component S_x from one ion and interact with the S_y from its nearest neighbour, dependent on the angle between neighbouring pairs for larger rings

cross-terms between $\hat{S}^x$ and $\hat{s}^y$, we will refer to this model as the axial model as the interaction act along the axial bonds between ions.

These cross-terms would depend on the type of material and when included in the Hamiltonian, provide a different approach to modeling small nano-magnets. For the particularly small molecules, i.e $N = 4$ and 6 it is an interesting avenue to explore the effect that these additional interaction terms would give to the entanglement in the models. It is noted that the work presented in this section is not completed to the level that the previous anisotropic XY-model and XYZ-model work was. The analysis that was started shows this to be an interesting vein of work.

Unlike the XY-model it is not possible to write a new Hamiltonian that can be used for any small system size. Instead, the molecule, dependent on size, is considered as a whole mapped onto a Hamiltonian with all the interactions listed. The plaquette model becomes unique in this sense, that it can be entirely written in the global axis and include all possible interactions. Whereas for the hexagon and any molecule larger, each site has two axial arrangements for describing interactions: one for each neighbour as the direction of the bond between neighbours changes.

Fig. 6.30 describes how the plaquette is built in the global axis.

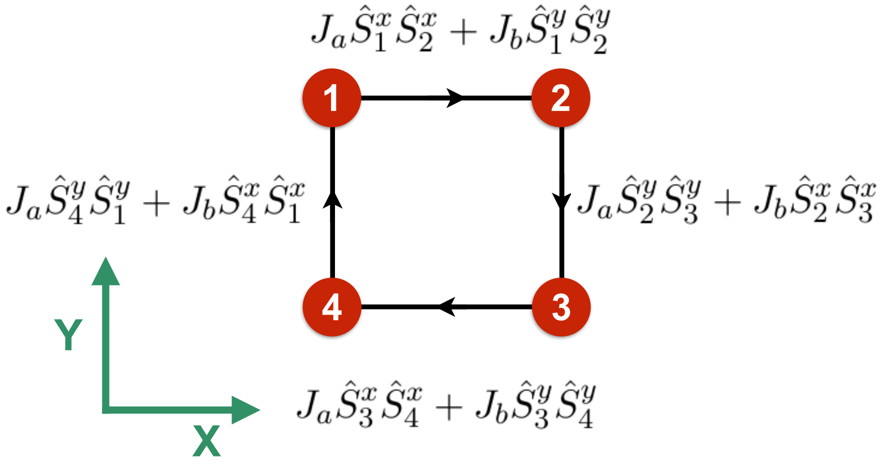

FIGURE 6.30: How to build the axial plaquette model for the global plane interactions.

The terms are taken and rotated into the local axes that matches the local axes from Fig.6.2 for the plaquette because the 4-fold symmetry of the plaquette allows for the each site to use the same interaction plane by rotating the axis on the site by $\frac{\pi}{4}$. The interactions on each site are defined as follows, where the prime notation indicates a common local axis:

$$\begin{array}{lcl}
\text{Site 1} & \longrightarrow & \hat{S}_1^x = \frac{1}{\sqrt{2}}\hat{S}_1^{x'} - \frac{1}{\sqrt{2}}\hat{S}_1^{y'} \\
 & & \hat{S}_1^y = \frac{1}{\sqrt{2}}\hat{S}_1^{x'} + \frac{1}{\sqrt{2}}\hat{S}_1^{y'} \\
\text{Site 2} & \longrightarrow & \hat{S}_2^x = \frac{1}{\sqrt{2}}\hat{S}_2^{x'} + \frac{1}{\sqrt{2}}\hat{S}_2^{y'} \\
 & & \hat{S}_2^y = -\frac{1}{\sqrt{2}}\hat{S}_2^{x'} + \frac{1}{\sqrt{2}}\hat{S}_2^{y'} \\
\text{Site 3} & \longrightarrow & \hat{S}_3^x = -\frac{1}{\sqrt{2}}\hat{S}_3^{x'} + \frac{1}{\sqrt{2}}\hat{S}_3^{y'} \\
 & & \hat{S}_3^y = -\frac{1}{\sqrt{2}}\hat{S}_3^{x'} - \frac{1}{\sqrt{2}}\hat{S}_3^{y'} \\
\text{Site 4} & \longrightarrow & \hat{S}_4^x = -\frac{1}{\sqrt{2}}\hat{S}_4^{x'} - \frac{1}{\sqrt{2}}\hat{S}_4^{y'} \\
 & & \hat{S}_4^y = \frac{1}{\sqrt{2}}\hat{S}_4^{x'} - \frac{1}{\sqrt{2}}\hat{S}_4^{y'} .
\end{array} \tag{6.14}$$

These terms for the local axes from Eq. 6.14 can then be substituted into the global definition from Fig. 6.30 and this is where the cross-terms for $S_i^\alpha S_{i+1}^\beta$ for $\alpha = x', y'$ and $\beta = y', x'$, come from. The terms are collected to form the following Hamiltonian for the plaquette:

$$\begin{aligned}
H_p \;=\; & \frac{J_a}{2}\left\{\sum_{i=1}^{N=4} \hat{S}_i^{x'}\hat{S}_{i+1}^{x'} - \hat{S}_i^{y'}\hat{S}_{i+1}^{y'} + \hat{S}_i^{x'}\hat{S}_{i+1}^{y'} - \hat{S}_i^{y'}\hat{S}_{i+1}^{x'}\right\} \\
& \frac{J_b}{2}\left\{\sum_{i=1}^{N=4} -\hat{S}_i^{x'}\hat{S}_{i+1}^{x'} + \hat{S}_i^{y'}\hat{S}_{i+1}^{y'} + \hat{S}_i^{x'}\hat{S}_{i+1}^{y'} - \hat{S}_i^{y'}\hat{S}_{i+1}^{x'}\right\} \\
& -h_z \sum_{i=1}^{N=4} \hat{S}_i^z .
\end{aligned} \tag{6.15}$$

Let the anisotropy for this model be called γ_g where:

$$\begin{aligned}
J_a &= J\left(1+\gamma_g\right) \\
J_b &= J\left(1-\gamma_g\right) .
\end{aligned} \tag{6.16}$$

The Hamiltonian can be written in its simplest form using the Pauli matrices:

$$H_p = \frac{J}{4}\sum_{i+1}^{N=4} \gamma_g\sigma_i^x\sigma_{i+1}^x - \gamma_g\sigma_i^y\sigma_{i+1}^y + \sigma_i^x\sigma_{i+1}^y - \sigma_i^y\sigma_{i+1}^x - \frac{h_z}{2}\sum_{i+1}^{N=4}\sigma_i^z . \tag{6.17}$$

The hexagon model can not be simplified in the same way as each site needs two axis along the interaction direction for each neighbour. These are written in full for each pair of interactions between sites where the xy are also the global plane:

$$\begin{aligned}
1 \longrightarrow 2 &= J_a\hat{S}_1^x\hat{S}_2^x + J_b\hat{S}_1^{y'}\hat{S}_2^y \\
2 \longrightarrow 3 &= J_a\left\{\frac{1}{4}\hat{S}_2^x\hat{S}_3^x + \frac{3}{4}\hat{S}_2^y\hat{S}_3^y - \frac{\sqrt{3}}{4}\hat{S}_2^x\hat{S}_3^y - \frac{\sqrt{3}}{4}\hat{S}_2^y\hat{S}_3^x\right\} \\
&+ J_b\left\{\frac{3}{4}\hat{S}_2^x\hat{S}_3^x + \frac{1}{4}\hat{S}_2^y\hat{S}_3^y + \frac{\sqrt{3}}{4}\hat{S}_2^x\hat{S}_3^y + \frac{\sqrt{3}}{4}\hat{S}_2^y\hat{S}_3^x\right\} \\
3 \longrightarrow 4 &= J_a\left\{\frac{3}{2}\hat{S}_3^x\hat{S}_4^x + \frac{1}{4}\hat{S}_3^y\hat{S}_4^y + \frac{\sqrt{3}}{4}\hat{S}_3^x\hat{S}_4^y + \frac{\sqrt{3}}{4}\hat{S}_3^y\hat{S}_4^x\right\} \\
&+ J_b\left\{\frac{3}{2}\hat{S}_3^x\hat{S}_4^x + \frac{3}{2}\hat{S}_3^y\hat{S}_4^y - \frac{3}{2}\hat{S}_3^x\hat{S}_4^y - \frac{3}{2}\hat{S}_3^y\hat{S}_4^x\right\} \\
4 \longrightarrow 5 &= J_a\hat{S}_4^x\hat{S}_5^x + J_b\hat{S}_4^y\hat{S}_5^y \\
5 \longrightarrow 6 &= J_a\left\{\frac{1}{4}\hat{S}_5^x\hat{S}_6^x + \frac{3}{4}\hat{S}_5^y\hat{S}_6^y - \frac{\sqrt{3}}{4}\hat{S}_5^x\hat{S}_6^y - \frac{\sqrt{3}}{4}\hat{S}_5^y\hat{S}_6^x\right\} \\
&+ J_b\left\{\frac{3}{4}\hat{S}_5^x\hat{S}_6^x + \frac{1}{4}\hat{S}_5^y\hat{S}_6^y + \frac{\sqrt{3}}{4}\hat{S}_5^x\hat{S}_6^y + \frac{\sqrt{3}}{4}\hat{S}_5^y\hat{S}_6^x\right\} \\
6 \longrightarrow 1 &= J_a\left\{\frac{3}{2}\hat{S}_6^x\hat{S}_1^x + \frac{1}{4}\hat{S}_6^y\hat{S}_1^y + \frac{\sqrt{3}}{4}\hat{S}_6^x\hat{S}_1^y + \frac{\sqrt{3}}{4}\hat{S}_6^y\hat{S}_1^x\right\} \\
&+ J_b\left\{\frac{3}{2}\hat{S}_6^x\hat{S}_1^x + \frac{3}{2}\hat{S}_6^y\hat{S}_1^y - \frac{3}{2}\hat{S}_6^x\hat{S}_1^y - \frac{3}{2}\hat{S}_6^y\hat{S}_1^x\right\}.
\end{aligned} \tag{6.18}$$

For the hexagon, the Hamiltonian will remain in the global plane as the cross-terms are already apparent. The interactions given in Eq. 6.18 can then be collected into the following Hamiltonian:

$$\begin{aligned}
H &= J_a\Big\{\hat{S}_1^x\hat{S}_2^x + \frac{1}{4}\hat{S}_2^x\hat{S}_3^x + \frac{3}{2}\hat{S}_3^x\hat{S}_4^x + \hat{S}_4^x\hat{S}_5^x + \frac{1}{4}\hat{S}_5^x\hat{S}_6^x + \frac{3}{2}\hat{S}_6^x\hat{S}_1^x + \frac{3}{4}\hat{S}_2^y\hat{S}_3^y + \frac{1}{4}\hat{S}_3^y\hat{S}_4^y \\
&+ \frac{3}{4}\hat{S}_5^y\hat{S}_6^y + \frac{1}{4}\hat{S}_6^y\hat{S}_1^y - \frac{\sqrt{3}}{4}\hat{S}_2^x\hat{S}_3^y + \frac{\sqrt{3}}{4}\hat{S}_3^x\hat{S}_4^y - \frac{\sqrt{3}}{4}\hat{S}_5^x\hat{S}_6^y + \frac{\sqrt{3}}{4}\hat{S}_6^x\hat{S}_1^y - \frac{\sqrt{3}}{4}\hat{S}_2^y\hat{S}_3^x \\
&+ \frac{\sqrt{3}}{4}\hat{S}_3^y\hat{S}_4^x - \frac{\sqrt{3}}{4}\hat{S}_5^y\hat{S}_6^x + \frac{\sqrt{3}}{4}\hat{S}_6^y\hat{S}_1^x\Big\} + J_b\Big\{\frac{3}{4}\hat{S}_2^x\hat{S}_3^x + \frac{3}{2}\hat{S}_3^x\hat{S}_4^x + \frac{3}{4}\hat{S}_5^x\hat{S}_6^x + \frac{3}{2}\hat{S}_6^x\hat{S}_1^x \\
&+ \hat{S}_1^y\hat{S}_2^y + \frac{1}{4}\hat{S}_2^y\hat{S}_3^y + \frac{3}{2}\hat{S}_3^y\hat{S}_4^y + \hat{S}_4^y\hat{S}_5^y + \frac{1}{4}\hat{S}_5^y\hat{S}_6^y + \frac{3}{2}\hat{S}_6^y\hat{S}_1^y + \frac{\sqrt{3}}{4}\hat{S}_2^x\hat{S}_3^y - \frac{3}{2}\hat{S}_3^x\hat{S}_4^y \\
&+ \frac{\sqrt{3}}{4}\hat{S}_5^x\hat{S}_6^y - \frac{3}{2}\hat{S}_6^x\hat{S}_1^y + \frac{\sqrt{3}}{4}\hat{S}_2^y\hat{S}_3^x - \frac{3}{2}\hat{S}_3^y\hat{S}_4^x + \frac{\sqrt{3}}{4}\hat{S}_5^y\hat{S}_6^x - \frac{3}{2}\hat{S}_6^y\hat{S}_1^x\Big\} - h_z\sum_{i+1}^{N=6}\hat{S}_i^z.
\end{aligned} \tag{6.19}$$

Unfortunately this does not simply further, though as before J_a and J_b can be substituted for γ_g using Eq. 6.16. It is the Hamiltonian for the axial model plaquette from Eq. 6.17 and the above Hamiltonian from Eq. 6.19 for the axial model Hexagon, that are solved for this section of results.

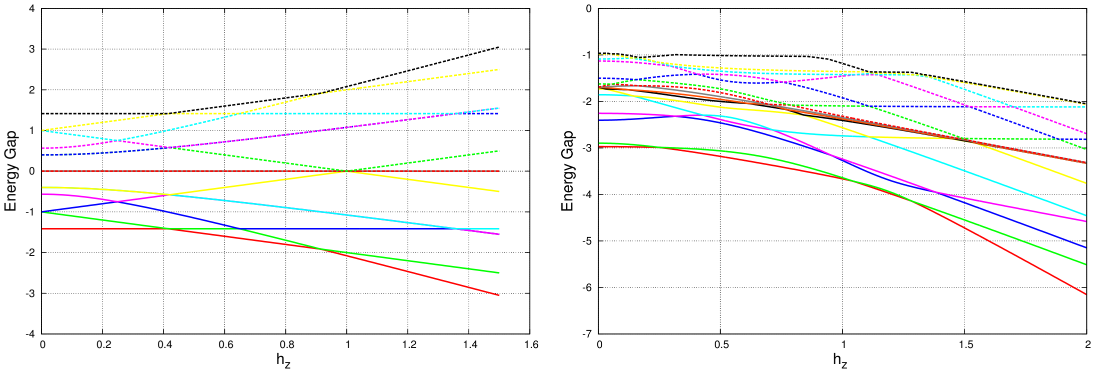

FIGURE 6.31: The energy spectra for the axial model plaquette (left) and the hexagon (right) for the fixed parameter $\gamma_g = 0.4$. For the hexagon we give the lowest 16 energy levels, as we are only interested in the behaviour of the lowest-lying energy states.

Using the same approach that was used with the anisotropic XY-model the initial step in understanding the new axial model is to look at the energy spectra for both the axial plaquette and the axial hexagon. These are shown in Fig. 6.31 for $\gamma_g = 0.4$. The whole spectrum is given for the plaquette (left) and the lowest 16 energy states for the hexagon (right) as it is only the lowest few states that are of interest.

The plaquette has two level crossings in the ground state between three different energy levels. If the states associated with these energy levels are numbered from $|1\rangle$ to $|16\rangle$ from lowest energy to highest energy from zero field then it is seen, that at the first level crossing state $|1\rangle$ is crossed by state $|2\rangle$, which, in turn at the second level crossing is crossed by state $|4\rangle$. Looking directly at these states, it quickly became obvious that any combination of these states at a degenerate crossing point would not make them factorisable. There are a few components of states that have zero amplitude for all three states involved, for example $|\downarrow\downarrow\downarrow\uparrow\rangle = 0$ for any field for $|1\rangle$, $|2\rangle$ and $|4\rangle$. Thus for any combination of the states there would be no linear combination that would allow the states to be separated at either of the level crossings. The states on their own are entangled and have no common overlap so are orthogonal to each other, thus are differently entangled but without a factorisation point they can not break their entanglement. In the beginning of this chapter it was said that our definition of the ET requires the states to completely break entanglement at the transition. Unfortunately, for the axial plaquette the two lowest ground states will never fully decouple.

The energy spectrum for the axial hexagon resembles the spectrum for the anisotropic XY-model in the way that it is only the two lowest states that cross each other and they do this three times. It is not known whether they factorise at these level crossings, though the concurrence for these models is calculated at the end of this section. Before this, the gap for both the plaquette and hexagon are plotted in Fig.6.32 for a range of anisotropy γ_g.

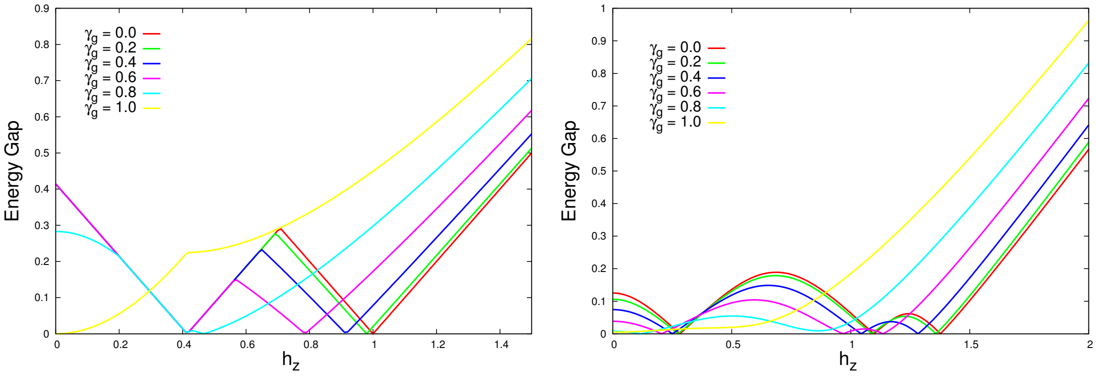

FIGURE 6.32: The energy gap between the two lowest states in the energy spectrum for the axial model plaquette (left) and hexagon (right) for a range of anisotropies.

The plaquette (left) shows two level crossings where the gap closes until the anisotropy becomes greater than $\gamma_g = 0.8$. The first level crossing appears to be stationary and the second level crossing appears to follow a familiar trend of $h_{LC2} = \sqrt{1-\gamma_g^2}$ so decreasing with higher anisotropy. As the second level crossing reaches the first the states do not cross. For $\gamma_g = 1$ the two states above the ground states cross causing an inflection in the gap as they cross over. Even though the states cross at the same value as the factorisation field for the anisotropic XY-model, this value is not a factorisation field for this model as it is based on assumptions for 1D antiferromagnetic chains. The same reasoning can not be applied to the axial model but it is an interesting similarity even if it's origins are unknown. As stated above, it is known that these states in the plaquette will not factorise.

The hexagon (right) has three level crossings, unlike the axial plaquette they do not converge on each other at higher anisotropies. It seems that none of the level crossings follow a known pattern or the factorisation field. As it difficult to discuss much more about the axial hexagon. The concurrence was plotted using the same reduced density matrix methods outline in the previous chapter.

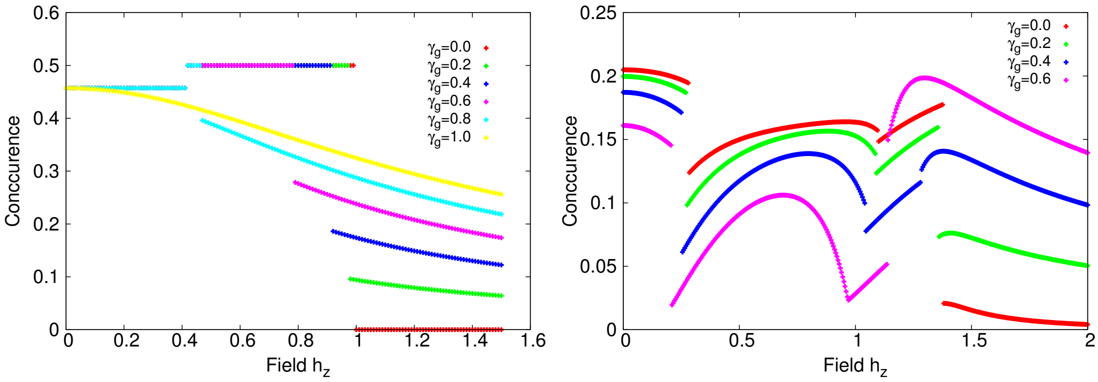

FIGURE 6.33: The ground state concurrence calculated for the axial model plaquette (left) and hexagon (right) for a range of anisotropy values.

Fig.6.33 shows the concurrence for a range of anisotropy values for the axial plaquette (left) and the axial hexagon (right). These ground state calculations show that the models experience a change over their level crossings though without studying thermal concurrence it is not possible to ascertain much about the nature of that change. By already being able to look at the states for the plaquette it is known that this model does not factorise and thermal calculations will not change this. With the anisotropic XY-model it was possible to see similarities and trends as the system size was increase, and it was a trivial matter (once coded) to calculate the Hamiltonian for a range of system sizes. In order to see any trends for the axial model we would need to calculate the Hamiltonian for at least $N = 8$ and $N = 10$, which would be interesting further work related to this project. As it stands, they are very little similarities between the axial plaquette and the axial hexagon. As speculation, we would predict that as system size increased the angle in which causes the cross-terms to appear from orbital overlap would get shallower, this could lead to a common trend in behaviour for larger molecules.

The next steps in exploring this model would be to produce neutron scattering predictions to see whether a greater understanding of the type of entanglement involved in the model can be found. Similarities to the anisotropic XY-model are still possible as the interactions in the Hamiltonian are still antiferromagnetic and at high enough fields the spins will align ferromagnetically. At the very least, the concurrence shows these systems to be quite strongly entangled. Further analysis into thermal concurrence would help to see if the hexagon model would factorise if concurrence tends to zero near a level crossing. It would be constructive to calculate thermal concurrence for all the models for comparison including open boundary conditions.

This section of the project details preliminary work and it offers an interesting alternative to interpreting small clustered quantum objects of $N = 4$ and $N = 6$, that with a full analysis would mean that in addition to the anisotropic XY-model/ XYZ-model would cover a wide range of clustered materials. The project has successfully demonstrated the experimental implication of identifying the entanglement transition in a range molecular magnets to a respectable temperature range. It should be noted that when searching for a real material to compare with, care should be taken to confirm which model best suits the material.

Chapter 7

Conclusions

7.1 Summary

The work presented in this thesis follows the logical journey made towards being able to identify the entanglement transition in small quantum spin clusters using neutron scattering techniques. The project draws from many areas of physics including Quantum Information, condensed matter theory and molecular magnets using new approaches developed in QI and applying it to small exactly solvable ring systems. By understanding the difficulties in detecting quantum phenomena like entanglement, discussed in Chapter 2 and being able to identify the potential in molecular molecules as reviewed in Chapter 3, it has lead to the foundations of this project. The entanglement transition has a strict definition that not only requires the change in the type of entanglement present in the system but the transition point to be synonymous with factorisation, such that the system becomes semi-classical and entanglement is broken.

We started our investigation by using the dimer model taking advantage of it's small Hilbert's space, documented in Chapter 4. The dimer allowed us to look at its individual eigen states and its whole energy spectrum, it was proven that the factorisation field introduced by Kurmann et al. was the product of a level crossing in the ground state for the dimer [18]. For this two-site model the entanglement transition is a simple process of an entangled singlet state being crossed by a ferromagnetically entangled state [2]. Despite the anisotropy effecting the proportions of the $|\uparrow\uparrow\rangle$ to $|\downarrow\downarrow\rangle$ in the ferromagnetically entangled state a calculation of concurrence shows that after the transition this state is still significantly entangled. At the factorisation field any linear combination of the two ground states are valid but a linear combination that cause the state to be separable at this point can be easily found. This means that the requirements for an entanglement transition are satisfied, where the dimer exhibits strong antiferromagnetic entanglement, factorises at the transition then recovers an amount of entanglement that is now ferromagnetically aligned with the applied field. The project progresses naturally by studying small finite-sized systems using exact diagonalisation to solve the anisotropic XY-model and it's $\gamma = 0$ and $\gamma = 1$ parameter counterparts for the isotropic and Ising model respectively. As the finite-sized calculations are exactly solvable we were also able to further explore the XYZ-model that also exhibits factorisation dependent on anisotropy parameters γ and Δ and an applied field. The flexibility of the calculations meant that the model could be adjustable boundary conditions that could relate to different type of models. Periodic boundary conditions have been used to describe bulk properties around factorisation and criticality [9] and form the core of the results in this thesis though with the purpose of modeling small molecular magnets. The calculations were kept to even number of spins in a system to avoid frustration where the boundary spins connected and where kept even for comparisons between open boundary conditions. The open boundary chains are related to doped systems, either a doped crystal of different chain lengths following a Poisson distribution, or carefully doped magnetic ring systems where a non magnetic doped ion within the ring breaks the connection but keeps the structure.

The finite-sized calculations, documented in Chapter 5 follows the same approach taken with the dimer, exploring the energy spectra of the models with different parameters and studying the level crossings in the ground state. It was found that the two lowest states cross multiple times with the relation $\frac{N}{2}$ where N is the system size. The last level crossing for systems with periodic boundary conditions always coincided with the factorisation field. It was shown, using the $N = 4$ spin system that only the level crossing that coincided with the factorisation field was factorisable and that the other level crossing was not [31]. This was done in the same way as the dimer by looking at the individual eigen states that make up the two lowest energy levels and calculating the conditions to find a linear combination of the two states that were separable. For larger systems the Hilbert space becomes unmanageable growing such as 2^N, thus for systems of $N = 6$ and above the absolute value correlation functions and the concurrence were calculated to assess the effects of factorisation in these systems. The nature of the calculations also allowed for finite-temperature calculation to study the effects of low temperatures on the correlation function before Chapter 6 builds on them to construct the neutron scattering function.

Chapter 6 gives the results for the main objective of the project which are the neutron scattering predictions for a range of small molecular magnets that give a clear signal of the entanglement transition at finite temperatures. Focusing mostly on the plaquette and hexagon models this chapter maps out the neutron scattering function for the orientation that the molecular lie in the 2D xy plane with the applied field perpendicular to the plane of the molecule in the z direction. The scattering function is calculated for steps in the applied field showing a significant change in the spectral weight across the entanglement transition with a break down of the function showing a mixture of the antiferro and ferromagnetic peaks originating form different interaction between the ions. For the anisotropic XY-model the transition was found to be robust to up to 10% the interaction energy J and the XYZ-model to be up to 15% the interaction energy, for the plaquette and hexagon. Using a common point in the scattering function graphs phase diagrams were plotted showing the curve of the factorisation field as a jump in the ferromagnetic peaks aligned with the field. This particular feature of the entanglement transition becomes less apparent with larger system sizes and it is thought that the behaviour of the thermodynamic limit can be commented upon with relatively small system sizes up to 12 spins.

Lastly, an alternative approach to modeling the plaquette and hexagon was proposed, that took potential cross-term interactions into consideration. This section of work was not completed to the same thorough level as the 1D Hamiltonian models were, but some interesting features were raised. This version of the plaquette, though similar in some ways to the anisotropic XY-model, was shown that because of the component parts of its eigen states that did cross in the energy spectrum, this system would never be able to truly factorise. The individual states that each in their turn occupy the ground state are strongly entangled in different ways as the concurrence calculations show, but with a factorised point to indicate the transition it is not thought that the entanglement transition could occur in this particular model. The same definitive conclusion can not be said about the hexagon, and further work would be required into an axial model approach to fully appreciate the potential of this approach to molecular magnets.

7.2 Achievements

The core objective of the collaboration is to experimentally detect the entanglement transition in a real material.This objective is yet to be fulfilled but this project makes substantial theoretical progress into the information needed before heading into an experiment. This work was tailored to explore finite-sized systems with the initial prediction that finite-sized chains might mimic ground state behaviour of the thermodynamic limit but at finite temperatures. The concept behind this was with the understanding that there could be a balance between the correlation length and the actual length of the chain that would allow the system to be more robust against thermal fluctuations. What was discovered was much more interesting. It was found that it was the differences between finite-sized systems and the thermodynamic limit, which made them better at detecting the entanglement transition above zero temperature. In the thermodynamic limit the ground state is doubly degenerate up to the critical field for the anisotropic XY-model: finite-sized systems are only degenerate at certain points where the two lowest energy levels cross. Therefore, the definition of the energy gap between the ground state and the first excited state has slightly different connotations. It is this definition of the gap that allows finite-sized system ground state behaviour apparent at higher finite temperatures than the thermodynamic limit.

The differences between open boundary conditions and periodic boundary conditions directed the project towards modeling molecular magnets. Initial analysis of the energy spectra showed that it was only the systems with periodic boundary conditions that had the correct conditions for a factorisation field. Further study using the four spin systems proved that it was only the level crossing that coincided with the factorisation field that could factorise and therefore be the best candidate to detect the entanglement transition with. Small open chains were too sensitive to boundary effects with some additional fluctuations destroying any long range order even in small chains. Despite the initial failings of the open chains there is some interesting observations to be had in respect to the thermodynamic limit that could be further explored.

Overall, the worked achieved here was able to to find a correct balance of parameters that provide the platform into find the entanglement transition in small quantum spin clusters using neutron scattering techniques.

7.3 Future Work

There are three main fractions of theoretical work that would warrant further investigation, and the identification of a real material that would be a suitable candidate for an experiment to be considered as future work.

For the collaboration to progress forward a deeper study into molecular magnets is required, with particular focus on molecules whose magnetic ions form a plaquette structure. These plaquettes would need to be isolated from each other to avoid any interaction between molecules and it would need to be determined that the 1D Hamiltonians would be a sufficient analogy to them. The key idea would be to avoid any cross-terms resulting from the overlap of different respect parts of the ion's orbitals. If a suitable material is found it could then be theoretically modeled with the correct parameters and with a known value of the interaction energy J then it could be determined whether a suitable temperature could be reached that would detect the entanglement transition and at the same time not change the phase of the material.

Continuing on with the theory side of the collaboration there are two more direct avenues of further work, which are the completion of some of the tangents around the main objectives of the work. Firstly, the concurrence calculations for the open boundary conditions were unexpected and could hold some interesting boundary effects, these were in Fig. 5.31. For the same parameters as the finite-sized calculations with periodic boundary conditions the open chains also found a common trend towards the thermodynamic limit with the plots for $N = 10$ and $N = 12$ converging on a common behaviour. For these slightly larger calculations the concurrence tends to zero at some common value of the field that does not coincide with the factorisation field for this model. When calculating concurrence the reduced density matrix was used to take sites 1 and 2 as a subsystem to indicate behaviour of the whole system. For periodic boundary conditions site 1 and 2 have no meaning with in the molecule, they are completely arbitrary, but for an open chain sites 1 and 2 mean an edge ion and its only neighbour. It could be interesting to calculate the concurrence for other pairs of sites with in a chain, including two sites in the middle of the chain and a center site to the edge of the chain. With this information calculated up to systems of 12 spins as before, it could be interesting to see whether different pairs are entangled differently and brings the concurrence towards zero at different values of the field or as the systems get bigger they find a common trend.

Concurrence proved a useful tool in understanding the entanglement in these systems but it was also one of the last calculations that was completed. Ideally calculations for thermal concurrence would have been completed also, this would be a natural progression for future work in this project [26].

Quite a substantial piece of further work would be to complete the analysis of the axial model started in section 6.7. This would involve the same processes employed to study the anisotropic XY-model, including studying the correlation functions and calculating the scattering function for zero temperature and finite temperatures. It would not be enough to complete this for just the plaquette and hexagon, but to extend it into larger molecules up to 10 or 12 spins to determine if any common behaviour becomes apparent. Also, it is speculated that as the molecules can larger and the angles that would cause the orbitals to overlap becomes less effective then they may tend towards the anisotropic XY or XYZ-model.

Bibliography

[1] A. Shimony T. K. Lo. Proposed molecular test of local hidden-variables theories. *Physical Review A*, 23(6), 1981.

[2] A. Candini, G. Lorusso, F. Troiani, A. Ghirri, S. Carretta, P. Santini, G. Amoretti, C. Muryn, F. Tuna, G. Timco, E. J L McInnes, R. E P Winpenny, W. Wernsdorfer, and M. Affronte. Entanglement in supramolecular spin systems of two weakly coupled antiferromagnetic rings (purple-Cr7Ni). *Physical Review Letters*, 104(3): 1–4, 2010. ISSN 00319007. doi: 10.1103/PhysRevLett.104.037203.

[3] R. Rossignoli, N. Canosa, and J. M. Matera. Factorization and entanglement in general XYZ spin arrays in nonuniform transverse fields. *Physical Review A - Atomic, Molecular, and Optical Physics*, 80(6), 2009. ISSN 10502947. doi: 10.1103/PhysRevA.80.062325.

[4] I. Siloi and F. Troiani. Detection of multipartite entanglement in spin rings by use of exchange energy. *Physical Review A*, 90(4):1–7, 2014. ISSN 1050-2947. doi: 10.1103/PhysRevA.90.042328. URL http://link.aps.org/doi/10.1103/PhysRevA.90.042328.

[5] H.A. Algra, L.J. de Jongh, H.W.J. Blöte, W.J. Huiskamp, and R.L. Carlin. Heat capacity of Cs\$_2\$CoCl\$_4\$ below 1 K, compared with the S=1/2 linear chain XY model. *Physica B+C*, 82(2):239–246, 1976. ISSN 03784363. doi: 10.1016/0378-4363(76)90186-8. URL http://dx.doi.org/10.1016/0378-4363(76)90186-8.

[6] Grigore a. Timco, Eric J. L. McInnes, and Richard E. P. Winpenny. Physical studies of heterometallic rings: an ideal system for studying magnetically-coupled systems. *Chem. Soc. Rev*, pages 1796–1806, 2013. ISSN 0306-0012. doi: 10.1039/c2cs35232j.

[7] Larry Engelhardt, Catalin Martin, Ruslan Prozorov, Marshall Luban, Grigore Timco, and Richard Winpenny. High-field magnetic properties of the magnetic molecule {Cr10Cu2}. *Physical Review B*, 79(1):1–8, 2009. ISSN 1098-0121. doi: 10.1103/PhysRevB.79.014404.

[8] Michael L. Baker, Oliver Waldmann, Stergios Piligkos, Roland Bircher, Olivier Cador, Stefano Carretta, David Collison, Felix Fernandez-Alonso, Eric J L McInnes, Hannu Mutka, Andrew Podlesnyak, Floriana Tuna, Stefan Ochsenbein, Roberta Sessoli, Andreas Sieber, Grigore a. Timco, Høgni Weihe, Hans U. Güdel, and Richard E P Winpenny. Inelastic neutron scattering studies on the odd-membered antiferromagnetic wheel Cr 8Ni. *Physical Review B - Condensed Matter and Materials Physics*, 86(6):1–11, 2012. ISSN 10980121. doi: 10.1103/PhysRevB.86.064405.

[9] Steve Campbell, Jonathan Richens, Nicola Lo Gullo, and Thomas Busch. Criticality, factorization, and long-range correlations in the anisotropic XY model. *Physical Review A - Atomic, Molecular, and Optical Physics*, 88(6):1–8, 2013. ISSN 10502947. doi: 10.1103/PhysRevA.88.062305.

[10] Eytan Barouch, Barry M. McCoy, and Max Dresden. Statistical mechanics of the XY model. I. *Physical Review A*, 2(3):1075–1092, 1970. ISSN 10502947. doi: 10.1103/PhysRevA.2.1075.

[11] Eytan Barouch and Barry M. McCoy. Statistical mechanics of the X y model. II. Spin-correlation functions. *Physical Review A*, 3(2):786–804, 1971. ISSN 10502947. doi: 10.1103/PhysRevA.3.786.

[12] O. Marty, M. Epping, H. Kampermann, D. Bruß, M. B. Plenio, and M. Cramer. Quantifying entanglement with scattering experiments. *Physical Review B - Condensed Matter and Materials Physics*, 89(12):1–13, 2014. ISSN 1550235X. doi: 10.1103/PhysRevB.89.125117.

[13] JM Yeomans. *Stastical Mechanics of Phase Transitions*. Oxford University Press, 1993. ISBN 978-0198517306.

[14] John Cardy. Scaling and Renormalization in Statistical Physics, 1996. ISSN 00319228. URL `http://link.aip.org/link/PHTOAD/v50/i11/p74/s1{&}Agg=doi`.

[15] Stephen M. Barnett. Quantum Information. *Condensed Matter Physics*, page 300, 2009. ISSN 0198527624.

[16] L. Amico, F. Baroni, a. Fubini, D. Patanè, V. Tognetti, and Paola Verrucchi. Divergence of the entanglement range in low-dimensional quantum systems. *Physical Review A - Atomic, Molecular, and Optical Physics*, 74(2):1–5, 2006. ISSN 10502947. doi: 10.1103/PhysRevA.74.022322.

[17] Luigi Amico, Rosario Fazio, Andreas Osterloh, and Vlatko Vedral. Entanglement in many-body systems. *Reviews of Modern Physics*, 80(2):517–576, 2008. ISSN 00346861. doi: 10.1103/RevModPhys.80.517.

[18] Muller Kurmann , Thomas. Antiferromagnetic long-range order. pages 235–255, 1982.

[19] W K Wootters and W K Wooters. Entanglement of Formation of an Arbitrary State of Two Qubits. *Phys. Rev. Lett.*, 80:2245, 1997. doi: 10.1103/PhysRevLett.80.2245.

[20] W. K. Wootters. Quantum entanglement as a quantifiable resource. *Philosophical Transactions of the Royal Society A: Mathematical, Physical and Engineering Sciences*, 356(1743):1717–1731, 1998. ISSN 1364-503X. doi: 10.1098/rsta.1998.0244. URL http://apps.isiknowledge.com/full{_}record.do?product=WOS{&}search{_}mode=GeneralSearch{&}qid=4{&}SID=3CTS1Sp13CqwqtPrQeR{&}page=8{&}doc=386$\delimiter"026E30F$nhttp://rsta.royalsocietypublishing.org/cgi/doi/10.1098/rsta.1998.0244.

[21] Valerie Coffman, Joydip Kundu, and William K. Wootters. Distributed Entanglement. *Physical Review A*, 61:052306, 2000. ISSN 1050-2947. doi: 10.1103/PhysRevA.61.052306. URL http://arxiv.org/abs/quant-ph/9907047.

[22] Otfried Gühne and Géza Tóth. Entanglement detection. *Physics Reports*, 474 (1-6):1–75, 2009. ISSN 03701573. doi: 10.1016/j.physrep.2009.02.004. URL http://dx.doi.org/10.1016/j.physrep.2009.02.004.

[23] Ryszard Horodecki, Paweł Horodecki, Michał Horodecki, and Karol Horodecki. Quantum entanglement. *Reviews of Modern Physics*, 81(2):865–942, 2009. ISSN 00346861. doi: 10.1103/RevModPhys.81.865.

[24] Sougato Bose. Quantum Communication through Spin Chain Dynamics: an Introductory Overview. 48(1):13–30, 2008. ISSN 0010-7514. doi: 10.1080/00107510701342313. URL http://arxiv.org/abs/0802.1224.

[25] Fabrizio Baroni, Andrea Fubini, Valerio Tognetti, and Paola Verrucchi. Two-spin entanglement distribution near factorized states. *Journal of Physics A: Mathematical and Theoretical*, 40(32):9845–9857, 2007. ISSN 1751-8113. doi: 10.1088/1751-8113/40/32/010. URL http://stacks.iop.org/1751-8121/40/i=32/a=010?key=crossref.cdb66c3896e747e73cc94f46e4f9a2a7.

[26] D. Gunlycke, V. Kendon, V. Vedral, and S. Bose. Thermal concurrence mixing in a one-dimensional Ising model. *Physical Review A*, 64(4):042302, 2001. ISSN 1050-2947. doi: 10.1103/PhysRevA.64.042302. URL http://link.aps.org/doi/10.1103/PhysRevA.64.042302.

[27] J. S. Bell. On the Einstein Podolsky Rosen paradox. *Physics*, 1(3):195–200, 1964. ISSN 01923188. doi: 10.1002/prop.19800281202.

[28] G. Lorusso, V. Corradini, A. Ghirri, R. Biagi, U. Del Pennino, I. Siloi, F. Troiani, G. Timco, R. E P Winpenny, and M. Affronte. Magnetic and entanglement properties of molecular Cr 2nCu 2 heterometallic spin rings. *Physical Review B - Condensed Matter and Materials Physics*, 86(18):1–10, 2012. ISSN 10980121. doi: 10.1103/PhysRevB.86.184424.

[29] I. Siloi and F. Troiani. Towards the chemical tuning of entanglement in molecular nanomagnets. *Physical Review B - Condensed Matter and Materials Physics*, 86 (22):1–5, 2012. ISSN 10980121. doi: 10.1103/PhysRevB.86.224404.

[30] Ilaria Siloi and Filippo Troiani. Quantum entanglement in heterometallic wheels. *European Physical Journal B*, 86(2):1–6, 2013. ISSN 14346028. doi: 10.1140/epjb/e2012-30681-1.

[31] Gian Luca Giorgi. Ground-state factorization and quantum phase transition in dimerized spin chains. *Physical Review B - Condensed Matter and Materials Physics*, 79(6):1–5, 2009. ISSN 10980121. doi: 10.1103/PhysRevB.79.060405.

[32] Peter Gibbins. *Particles and Paradoxes: The limits of quantum logic*. Cambridge University Press, first edition, 2008. ISBN 978-0521336918.

[33] W. H. Furry. Note on the quantum-mechanical theory of measurement. *Physical Review*, 49(5):393–399, 1936. ISSN 0031899X. doi: 10.1103/PhysRev.49.393.

[34] J. S. Bell. *Speakable and Unspeakable in Quantum Mechanics*, volume 57. 1989. ISBN <null>. doi: 10.1119/1.15983.

[35] Steven Weinberg. *Lectures on Quantum Mechanics*. Cambridge University Press, second edition, 2015. ISBN 978-1107111660.

[36] Paul Strange. Bell's Inequalities, 2010.

[37] Alastair IM Rae. *Quantum Mechanics*. CRC Press, fifth edition, 2007. ISBN 978-1584889705.

[38] Alain Aspect, Philippe Grangier, and Gerard Roger. (J = 1)-. 47(7), 1981.

[39] Alain Aspect, Jean Dalibard, and Gerard Roger. Experimental test of Bell's inequalities using time- varying analyzers. *Physical Review Letters*, 49(25):1804–1807, 1982. ISSN 00319007. doi: 10.1103/PhysRevLett.49.1804.

[40] Robert Garland Colodny and Arthur Fine. *Paradigms & paradoxes; the philosophical challenge of the quantum domain*. 1972. ISBN 082297598X.

[41] Shunsuke Furukawa and Grogoire Misguich. Topological entanglement entropy in the quantum dimer model on the triangular lattice. *Physical Review B - Condensed Matter and Materials Physics*, 75(21):1–10, 2007. ISSN 10980121. doi: 10.1103/PhysRevB.75.214407.

[42] Yuji Furukawa, Kazuki Kiuchi, Ken Ichi Kumagai, Yoshitami Ajiro, Yasuo Narumi, Masahiro Iwaki, Koichi Kindo, Alberto Bianchi, Stefano Carretta, Paolo Santini, Ferdinando Borsa, Grigore a. Timco, and Richard E P Winpenny. Evidence of spin singlet ground state in the frustrated antiferromagnetic ring Cr8 Ni. *Physical Review B - Condensed Matter and Materials Physics*, 79(13):1–7, 2009. ISSN 10980121. doi: 10.1103/PhysRevB.79.134416.

[43] M Barbieri, F De Martini, G Di Nepi, P Mataloni, G M D'Ariano, and C Macchiavello. Detection of entanglement with polarized photons: experimental realization of an entanglement witness. *Physical review letters*, 91(22):227901, 2003. ISSN 0031-9007. doi: 10.1103/PhysRevLett.91.227901.

[44] Mohamed Bourennane, Manfred Eibl, Christian Kurtsiefer, Sascha Gaertner, Harald Weinfurter, Otfried Gühne, Philipp Hyllus, Dagmar Bruss, Maciej Lewenstein, and Anna Sanpera. Experimental detection of multipartite entanglement using witness operators. *Physical review letters*, 92(8):087902, 2004. ISSN 0031-9007. doi: 10.1103/PhysRevLett.92.087902.

[45] Fernando G S L Brando. Quantifying entanglement with witness operators. *Physical Review A - Atomic, Molecular, and Optical Physics*, 72(2):1–15, 2005. ISSN 10502947. doi: 10.1103/PhysRevA.72.022310.

[46] J. Eisert, F. G S L Brandão, and K. M R Audenaert. Quantitative entanglement witnesses. *New Journal of Physics*, 9, 2007. ISSN 13672630. doi: 10.1088/1367-2630/9/3/046.

[47] Colin P Williams. *Explorations in Quantum Computing*. Springer, second edition, 2011. ISBN 978-1846288869.

[48] G. Karpat, B. Cakmak, and F. F. Fanchini. Quantum coherence and uncertainty in the anisotropic XY chain. *Physical Review B - Condensed Matter and Materials Physics*, 90(10):1–7, 2014. ISSN 1550235X. doi: 10.1103/PhysRevB.90.104431.

[49] Thiago R. De Oliveira, Gustavo Rigolin, Marcos C. De Oliveira, and E. Miranda. Symmetry-breaking effects upon bipartite and multipartite entanglement in the XY model. *Physical Review A - Atomic, Molecular, and Optical Physics*, 77(3): 1–12, 2008. ISSN 10502947. doi: 10.1103/PhysRevA.77.032325.

[50] O. Guehne, P. Hyllus, D. Bruss, a. Ekert, M. Lewenstein, C. Macchiavello, a. Sanpera, O Gühne, P. Hyllus, D Bruß, a. Ekert, M. Lewenstein, C. Macchiavello, and a. Sanpera. Detection of entanglement with few local measurements. *Phys. Rev. A*, 66:62305, 2002. ISSN 1050-2947. doi: 10.1103/PhysRevA.66.062305. URL http://arxiv.org/abs/quant-ph/0205089.

[51] Guifre Vidal and Rolf Tarrach. Robustness of entanglement. 59(1):27, 1998. ISSN 1050-2947. doi: 10.1103/PhysRevA.59.141. URL http://arxiv.org/abs/quant-ph/9806094.

[52] Michael Steiner. Genralized Robustness of Entanglement. (May):1–4, 2003. ISSN 1050-2947. doi: 10.1103/PhysRevA.67.054305. URL http://arxiv.org/abs/quant-ph/0304009.

[53] Takashi Uneyama and Yuichi Masubuchi. Multi-chain slip-spring model for entangled polymer dynamics. *Journal of Chemical Physics*, 137(15):1–25, 2012. ISSN 00219606. doi: 10.1063/1.4758320.

[54] Andreas Osterloh and Ralf Schützhold. The fourtangle in the transverse XY model. 4:1–7, 2015. URL `http://arxiv.org/abs/1512.06010`.

[55] M. Cerezo, R. Rossignoli, and N. Canosa. Nontransverse factorizing fields and entanglement in finite spin systems. *Physical Review B*, 92(22):224422, 2015. ISSN 1098-0121. doi: 10.1103/PhysRevB.92.224422. URL `http://link.aps.org/doi/10.1103/PhysRevB.92.224422`.

[56] Marcelo S. Sarandy, Thiago R. De Oliveira, and Luigi Amico. Quantum Discord in the Ground State of Spin Chains. *International Journal of Modern Physics B*, 27:1345030, 2012. ISSN 0217-9792. doi: 10.1142/S0217979213450306.

[57] Subir Sachdev. *Quantum Phase Transitions*. 2011. ISBN 9780521514682. doi: 10.1017/CBO9780511973765. URL `www.cambridge.org/9780521514682`.

[58] Tommaso Roscilde, Paola Verrucchi, Andrea Fubini, Stephan Haas, and Valerio Tognetti. Studying quantum spin systems through entanglement estimators. *Physical Review Letters*, 93(16):4–7, 2004. ISSN 00319007. doi: 10.1103/PhysRevLett.93.167203.

[59] Tommaso Roscilde, Paola Verrucchi, Andrea Fubini, Stephan Haas, and Valerio Tognetti. Entanglement and factorized ground states in two-dimensional quantum antiferromagnets. *Physical Review Letters*, 94(14):1–4, 2005. ISSN 00319007. doi: 10.1103/PhysRevLett.94.147208.

[60] M. Kenzelmann, R. Coldea, D. Tennant, D. Visser, M. Hofmann, P. Smeibidl, and Z. Tylczynski. Order to disorder transition in the XY-like quantum magnet Cs\$_2\$CoCl\$_4\$ induced by noncommuting applied fields. *Physical Review B*, 65 (14):144432, 2002. ISSN 0163-1829. doi: 10.1103/PhysRevB.65.144432. URL `http://link.aps.org/doi/10.1103/PhysRevB.65.144432`.

[61] D. Patanè, Rosario Fazio, and L. Amico. Bound entanglement in the XY model. *New Journal of Physics*, 9:1–7, 2007. ISSN 13672630. doi: 10.1088/1367-2630/9/9/322.

[62] Salvatore M. Giampaolo, Gerardo Adesso, and Fabrizio Illuminati. Probing quantum frustrated systems via factorization of the ground state. *Physical Review Letters*, 104(20):2–5, 2010. ISSN 00319007. doi: 10.1103/PhysRevLett.104.207202.

[63] S. M. Giampaolo and B. C. Hiesmayr. Genuine multipartite entanglement in the XY model. *Physical Review A - Atomic, Molecular, and Optical Physics*, 88(5): 1–10, 2013. ISSN 10502947. doi: 10.1103/PhysRevA.88.052305.

[64] W. W. Cheng, C. J. Shan, Y. X. Huang, T. K. Liu, and H. Li. Entanglement in the Heisenberg spin chain with multiple interaction. *Physica E: Low-Dimensional Systems and Nanostructures*, 43(1):235–238, 2010. ISSN 13869477. doi: 10.1016/j.physe.2010.07.012.

[65] H. Yoshizawa, G. Shirane, H Shiba, and K. Hirakawa. Neutron scattering study of a one-dimensional XY antiferromagnet Cs_{2}CoCl_{4}. *Physical Review B*, 28(7):3904–3908, 1983. ISSN 0163-1829. doi: 10.1103/PhysRevB.28.3904. URL http://link.aps.org/doi/10.1103/PhysRevB.28.3904.

[66] Birger Horstmann, J. Ignacio Cirac, and Geza Giedke. Noise-driven dynamics and phase transitions in fermionic systems. *Physical Review A - Atomic, Molecular, and Optical Physics*, 87(1), 2013. ISSN 10502947. doi: 10.1103/PhysRevA.87.012108.

[67] et all Rogério dos Santos Alves; Alex Soares de Souza. No Title No Title. *Igarss 2014*, 40(1):1–5, 2014. ISSN 13514180. doi: 10.1007/s13398-014-0173-7.2.

[68] Antonella De Pasquale and Paolo Facchi. XY model on the circle: Diagonalization, spectrum, and forerunners of the quantum phase transition. *Physical Review A - Atomic, Molecular, and Optical Physics*, 80(3), 2009. ISSN 10502947. doi: 10.1103/PhysRevA.80.032102.

[69] Home Search, Collections Journals, About Contact, My Iopscience, and I P Address. My IOPscience. 527, 1996.

[70] D. V. Dmitriev and V. Ya. Krivnov. Quasi-one-dimensional anisotropic Heisenberg model in a transverse magnetic field. 80(5):4, 2004. ISSN 00213640. doi: 10.1134/1.1825110. URL http://arxiv.org/abs/cond-mat/0407203.

[71] Elliott H. Lieb, Theodore Schultz, and Daniel Mattis. Two soluble models of an antiferromagnetic chain. *Annals of Physics*, 16(3):407–466, 1961. ISSN 00034916. doi: 10.1016/0003-4916(61)90115-4.

[72] Pierre Pfeuty. H = y - r 2 ci + ci - g E cci + - ci)(c ; + l + ci + l). 90:79–90, 1970.

[73] Marco Affronte and Filippo Troiani. *Molecular Magnets: Physics and Applications*, chapter Potentialities of Molecular Nanomagnets for Information Technologies, pages 249–273. Springer Berlin Heidelberg, Berlin, Heidelberg, 2014. ISBN 978-3-642-40609-6. doi: 10.1007/978-3-642-40609-6_10. URL `http://dx.doi.org/10.1007/978-3-642-40609-6{_}10`.

[74] F. Troiani, A. Ghirri, M. Affronte, S. Carretta, P. Santini, G. Amoretti, S. Piligkos, G. Timco, and R. E P Winpenny. Molecular engineering of antiferromagnetic rings for quantum computation. *Physical Review Letters*, 94(20):1–4, 2005. ISSN 00319007. doi: 10.1103/PhysRevLett.94.207208.

[75] Filippo Troiani and Marco Affronte. Molecular spins for quantum information technologies. *Chem. Soc. Rev.*, 40(6):3119–3129, 2013. doi: 10.1039/C0CS00158A. URL `http://dx.doi.org/10.1039/C0CS00158A`.

[76] Marzieh Asoudeh, Vahid Karimipour, and Afsaneh Sadrolashrafi. Exact dimer ground states for a continuous family of quantum spin chains and zigzag ladders. *Physical Review B - Condensed Matter and Materials Physics*, 76(6):25–30, 2007. ISSN 10980121. doi: 10.1103/PhysRevB.76.064433.

[77] Alexei A Belik, Hyun-joo Koo, Myung-hwan Whangbo, Naohito Tsujii, Hee Uni V, South Korea, North Carolina State, V Uni, and North Carolina. Magnetic Properties of Synthetic Libethenite Cu 2 PO 4 OH : a New Spin-Gap System. 46 (21):8684–8689, 2007.

[78] Xi Wen Hou, Jing Hua Chen, and Bambi Hu. Entanglement and bifurcation in the integrable dimer. *Physical Review A - Atomic, Molecular, and Optical Physics*, 71 (3):1–4, 2005. ISSN 10502947. doi: 10.1103/PhysRevA.71.034302.

[79] H G Paulinelli, S M de Souza, and Onofre Rojas. Thermal entanglement in an orthogonal dimer-plaquette chain with alternating Ising-Heisenberg coupling.

Journal of physics. Condensed matter : an Institute of Physics journal, 25(30): 306003, 2013. ISSN 1361-648X. doi: 10.1088/0953-8984/25/30/306003. URL `http://www.ncbi.nlm.nih.gov/pubmed/23822936`.

[80] S. Carretta, P. Santini, G. Amoretti, T. Guidi, J. R D Copley, Y. Qiu, R. Caciuffo, G. Timco, and R. E P Winpenny. Quantum oscillations of the total spin in a heterometallic antiferromagnetic ring: Evidence from neutron spectroscopy. *Physical Review Letters*, 98(16):1–4, 2007. ISSN 00319007. doi: 10.1103/PhysRevLett.98.167401.

[81] S Ghosh, T F Rosenbaum, G Aeppli, and S N Coppersmith. Entangled quantum state of magnetic dipoles. *Nature*, 425(6953):48–51, 2003. ISSN 0028-0836. doi: 10.1038/nature01888.

[82] W W Cheng, C J Shan, L Y Gong, and S M Zhao. Measurement-induced disturbance near Anderson localization in one-dimensional systems. *Journal of Physics B: Atomic, Molecular and Optical Physics*, 47(17): 175503, 2014. ISSN 0953-4075. doi: 10.1088/0953-4075/47/17/175503. URL `http://stacks.iop.org/0953-4075/47/i=17/a=175503?key=crossref.00e5e5ba44ed9ebf5849771cbd55c4b3`.

[83] R. Rossignoli, N. Canosa, and J. M. Matera. Entanglement of finite cyclic chains at factorizing fields. *Physical Review A - Atomic, Molecular, and Optical Physics*, 77(5):1–6, 2008. ISSN 10502947. doi: 10.1103/PhysRevA.77.052322.

[84] I. Hagymasi, J. Solyom, and O. Legeza. Interorbital interaction in the one-dimensional periodic Anderson model: Density matrix renormalization group study. *Physical Review B - Condensed Matter and Materials Physics*, 90(12): 1–9, 2014. ISSN 1550235X. doi: 10.1103/PhysRevB.90.125137.

[85] I. Hagymasi, J. Solyom, and O. Legeza. Competition between Hund's coupling and Kondo effect in a one-dimensional extended periodic Anderson model. *Physical Review B - Condensed Matter and Materials Physics*, 92(3):1–8, 2015. ISSN 1550235X. doi: 10.1103/PhysRevB.92.035108.

[86] Michael L. Baker, Tatiana Guidi, Stefano Carretta, Jacques Ollivier, Hannu Mutka, Hans U. Güdel, Grigore a. Timco, Eric J. L. McInnes, Giuseppe Amoretti,

Richard E. P. Winpenny, and Paolo Santini. Spin dynamics of molecular nanomagnets unravelled at atomic scale by four-dimensional inelastic neutron scattering. *Nature Physics*, 8(12):906–911, 2012. ISSN 1745-2473. doi: 10.1038/nphys2431. URL http://dx.doi.org/10.1038/nphys2431.

[87] M. L. Baker and H. Mutka. Neutron spectroscopy of molecular nanomagnets. *European Physical Journal: Special Topics*, 213(1):53–68, 2012. ISSN 19516355. doi: 10.1140/epjst/e2012-01663-6.

[88] Joseph W. Sharples, David Collison, Eric J. L. McInnes, Jürgen Schnack, Elias Palacios, and Marco Evangelisti. Quantum signatures of a molecular nanomagnet in direct magnetocaloric measurements. *Nature Communications*, 5:5321, 2014. ISSN 2041-1723. doi: 10.1038/ncomms6321. URL http://www.nature.com/doifinder/10.1038/ncomms6321.

[89] George Christou, Dante Gatteschi, David N Hendrickson, and Roberta Sessoli. S ingle-Molecule Magnets. (November):66–71, 2000.

[90] Stephen Blundell. *Magnetism in Condensed Matter*. Oxford University Press, 2000. ISBN 978-0198505914.

[91] P Kozlowski. Frustration and quantum entanglement in odd-membered ring-shaped chromium nanomagnets. *Phys. Rev. B*, 91(17):174432, may 2015. doi: 10.1103/PhysRevB.91.174432. URL http://link.aps.org/doi/10.1103/PhysRevB.91.174432.

[92] C Castelnovo, R Moessner, and S L Sondhi. Magnetic monopoles in spin ice. *Nature*, 451(7174):42–45, 2008. ISSN 0028-0836. doi: 10.1038/nature06433.

[93] Fabio Franchini. Lecture Notes solving analytically the anistropic XY-Model.

[94] Stephen Blundell Tom Lancaster. *Quantum Field Theory for the gifted amateur*. Oxford University Press, first edition, 2014. ISBN 978-0-19-969933-9.

[95] N B Christensen, H M Rønnow, D F McMorrow, a Harrison, T G Perring, M Enderle, R Coldea, L P Regnault, and G Aeppli. Quantum dynamics and entanglement of spins on a square lattice. *Proceedings of the National Academy of Sciences of the United States of America*, 104(39):15264–15269, 2007. ISSN 0027-8424. doi: 10.1073/pnas.0703293104.

[96] Guido Bellomo, Angelo Plastino, and Angel R. Plastino. Quantumness and the role of locality on quantum correlations. 2016. URL http://arxiv.org/abs/1601.01236.

[97] Luigi Amico Jorge Quintanilla, Toby Perring. Internal Corrrespondance, 2010.

[98] Robert M White. *Quantum Theory of Magnetism: Magnetic properties of materials*. Springer, third edition, 2010. ISBN 978-3642084522.

[99] D.S. Silvia. *Elementary Scattering Theory For x-ray and neutron users*. Oxford University Press, first edition, 2011. ISBN 978-0199228683.

[100] Stephen Lovesey. *Theory of Neutron Scattering from condensed matter*. Oxford University Press, 1986. ISBN 978-0198520283.

[101] J. M. Florez and P. Vargas. Factorizing magnetic fields triggered by the DzyaloshinskiiMoriya interaction: Application to magnetic trimers. *Journal of Magnetism and Magnetic Materials*, 324(1):83–89, 2012. ISSN 03048853. doi: 10.1016/j.jmmm.2011.07.052. URL http://dx.doi.org/10.1016/j.jmmm.2011.07.052.